Numerical simulation of Deflagration to Detonation Transition in Hydrogen Explosion

Ali Heidari

Thesis submitted for the Degree of Doctor of Philosophy of Kingston University of London

Faculty of Science, Engineering and Computing
Kingston University of London

June 2012

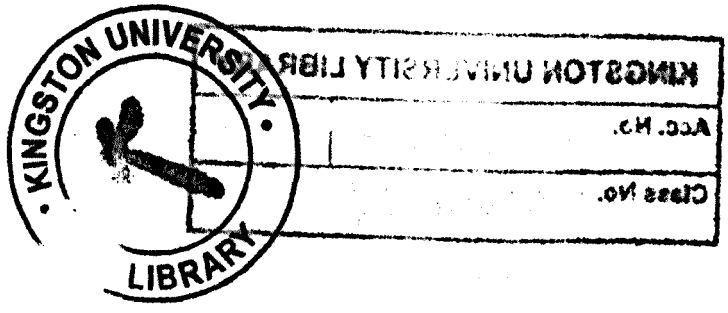

Abstract

The issue of deflagration to detonation transition (DDT) is one of the key factors influencing safety standards, risk assessment and risk managements in the petrochemical industries. It is also one of the most outstanding problems in combustion theory. Despite the efforts from a number of scientists around the world, numerical predictions of DDT is still an un-resolved problem due to the high level of complexities involved. Although there have been relatively more experimental efforts, a comprehensive database to assist model validation and development is still lacking.

The present thesis includes numerical analysis of a wide range of combustion regimes to establish the critical conditions under which transition from deflagration to detonation occurs.

In order to facilitate the study, new correlations for hydrogen burning velocity are derived from curve-fitting to experimental data from literature and implemented in the code for simulation of initial stages of flame acceleration and deflagration propagation. DetoFOAM, a code for solving transient and fully compressible Euler equations, has been developed within the framework of the OpenFOAM toolbox for numerical simulations of gaseous detonation. The detonation solver uses the total variation diminishing (TVD) numerical schemes which are suitable for shock capturing. A one step reaction mechanism has been developed following first principle and tuned for both small and large scale simulations.

Since the numerical solver for DDT simulations must be capable of handling both deflagration and detonation as well as the transition, a new solver, DDTFOAM, which is based on solving fully compressible and transient Navier-Stokes equations has also been developed. DDTFOAM also uses the TVD numerical schemes for shock capturing and uses the Implicit Large Eddy Simulation (ILES) approach as a compromise for accuracy and computational efficiency [131].

Implementing an adequate chemical reaction mechanism in the DDTFOAM has been challenging to ensure that the right amount of chemical energy release is supplied in the right place and at the right time. Incorrect models for chemical

energy release can significantly modify the flow behaviour. The available reactions in the literature are very limited and valid for limited range of conditions, e.g. for laminar flames only. A single step Arrhenius type reaction has been designed, tuned and implemented in DDTFOAM. The reaction mechanism has been carefully designed to reproduce flame properties e.g. laminar flame speed and thickness as well as detonation properties such as detonation thickness, propagation velocity, etc.

The main difference between DetoFOAM and DDTFOAM that the former is designed for supersonic combustions (detonations) only; therefore it neglects the diffusive effects and solves reactive Euler Equations, whereas in DDTFOAM full Navier Stokes Equations are solved. The detonation solver is mainly designed for large scale detonation simulations therefore the derived reaction mechanism for this solver is obtained trough slightly different procedure compared to the DDT solver. Obtaining the reaction mechanism for DDTFOAM is more challenging as it has to reproduce properties of deflagrations as well as detonations correctly.

The computational power which is required to carry out the simulations is extremely high. Different techniques have been employed to reduce the computational cost without compromising accuracy. These include using the ILES approach in cooperation with adaptive mesh refinement and multiple meshes.

Numerical predictions have been conducted for different combustion regimes including laminar flames, turbulent flames and detonations as well as the actually DDT processes. The predictions of deflagrations waves are found to be in reasonably good agreement with some published experiment data. In case of detonations, detailed studies have been conducted on the detonation front structure, cellular structures as well as large industrial scenarios. This work involved contributions to Buncefield explosion investigations [109-110].

Finally, numerical simulations of some standard DDT tests have been carried out. The predictions have again achieved reasonable agreement with published experimental data and previous simulations.

Successful simulations of large scale detonation in the present work represent the capability of the present study to address the increasing demands from the industries to study real scale accidental scenarios. Furthermore the obtained results for DDT

simulations compare well with the medium scale experimental works and provide a step forward towards large scale and unconfined DDT studies.

Dedicated to my wife Maryam

Acknowledgements

I would like to express my sincere gratitude to my supervisor, Professor Jennifer Wen for her continuous support and guidance throughout this study.

It has been said something as small as the flutter of a butterfly's wing can ultimately cause a typhoon halfway around the world.

- Chaos Theory

Contents

List of Figures

List of Tables

Nomenclature

A	Pre-exponential factor/ surface area
A_s	Reference Sutherland viscosity
a_i	JANAF coefficients
b	Regress variable
c	Progress variable
C_d	Drag coefficient
Co	Courant number
C_p	Specific heat at constant pressure
D_{CJ}	CJ detonation velocity
D_{Sp}	Explosion spreading speed
D_{tb}	Sub-grid turbulent diffusion coefficient
E	Energy
E_a	Activation energy
F	Force
$\acute{f}$	Fluctuating component
$\bar{f}$	Averaged variable/filtered variable
$\tilde{f}$	Mass-weighted Favre filtered
h	Enthalpy
I	Impulse
j	Flux
k	Turbulent kinetic energy
k	Thermal conductivity
m	Mass
n_f	Normal in the direction of flame propagation

n	Reaction order
n_i	Number of moles
p	Pressure
q	Total energy release per unit mass
$\mathbb{Q}$	Heat of chemical reaction per unit mass
$\dot{Q}$	Heat transfer rate
R	Specific gas constant
R_u	Universal gas constant
S_ψ	Source term
s_d	Flame displacement speed
S_u	Laminar flame speed
T	Temperature
t	Time
T_s	Sutherland temperature
TV	Total variation
t^l_{burn}	Burn time
U	Velocity
$\overline{U_s}$	Surface filtered local instantaneous velocity
$\overline{U_t}$	Surface filtered effective velocity
V	Volume
W	Work
W	Molar weight
x_i	Mole fraction
Y	Mass fraction
α	Under relaxation factor
α_b	Detonation progress variable

Φ	Equivalence ratio
ρ	Density
ρ_u	Unburned gas density
ε	Dissipation rate
υ	Kinematic viscosity
η	Kolmogorov length scale
Ψ	General variable
λ	Bulk viscosity/weighting factor
γ	Heat capacity ratio or Adiabatic index or Ratio of specific heats
Ξ	Sub-grid flame wrinkling
Σ	Flame surface density
μ	Dynamic viscosity
ζ	Face value of flux
τ_i	explosion time
τ_{ij}	Stress tensor
τ'_{ij}	Reynolds stress tensor
$\tau(T,Y)$	Induction time
Γ_Ψ	Diffusion coefficient
Ω_F	Total fuel consumption
μ_t	Turbulent viscosity
R_u	Reynolds number
Le	Lewis number
Pr	Prandtl number
R_η	Kolmogorov Reynolds number
Sc_t	Turbulent Schmidt number

Chapter 1

Introduction

1-1 Problem description

Hydrogen (H_2) has been known as an ideal fuel. Pollutants production in the hydrogen combustion is significantly low in comparison with fossil fuels.

Large amount of energy release per mass and wide range of flammability are also some factors which make H_2 a desirable fuel. Considering the fact that fossil fuels will diminish in the near future, there are great interests in industries to replace fossil fuels with a suitable fuel like hydrogen. This growing tendency and interest towards hydrogen as a fuel shows that its usage will be widespread in near future in many industrial applications like furnaces, engines, turbines etc.

However this growing interest means that this fuel must be stored and carried in very large amounts. Hydrogen is a very sensitive and reactive gas and a leakage and release of this gas into air will create a highly reactive mixture which can easily explode and cause serious and expensive damages to the surrounding facilities and humans [1]. Therefore important challenge related to the future wide use of hydrogen is to develop codes and standards as well as prevention and mitigation measure to address the safety issues [1].

From the past accidental explosions involving hydrogen, it is evident that serious explosion accidents involving hydrogen usually happened due to its massive release into congested environments with a high density of equipments and obstacles [1]. In such reactive mixture several mechanisms can lead to initiation of detonation. Lee et al. [2] explained different possible modes of detonation initiation in reactive mixtures. In practice direct initiation of detonation is highly unlikely to happen but deflagration to detonation transition has to be taken into account in safety analyses of hydrogen industry [3]. An ignition in a large explosive clouds forms high speed turbulent deflagrations which lead to formation of strong pressure waves. Transition to detonation in hydrogen air mixtures is also highly possible which can lead to severe blast damages to surrounding facilities and personnel. DDT in confined domains is more likely compared to unconfined environment. The accidental introduction of air into hydrogen storage vessels has been frequently reported. This

would lead to the formation of a highly reactive and confined mixture [1]. It is, therefore, very important for safety experts to have comprehensive knowledge of deflagration and detonation parameters of these reactive mixtures in all possible scenarios.

In general, explosion properties of an explosive mixture can be divided into equilibrium parameters (static parameters) and non-equilibrium parameters (dynamic parameters). Equilibrium parameters are calculated based on thermodynamics and can readily be determined using standard computer codes like STANJAN [4], CEA [5], GASEQ [6], GEC [92] etc. The constant volume and pressure explosions as well as Chapman–Jouguet detonation states can be all computed using equilibrium calculations. In contrast, the dynamic parameters including detonability limits, minimum initiation energy, critical diameter, cell size, etc. cannot be determined theoretically from first principle and thermodynamics alone. To determine these dynamic parameters, the description of the non-equilibrium chemical kinetics, turbulence and various transport, shock waves and non-linear instability processes involving the coupling between gas dynamics and thermo chemistry is required. Accordingly, in order to gain insight and predict the potential hazards of accidental hydrogen explosions, a good knowledge and ability to predict the high-speed deflagration and detonation dynamic parameters are required [1]. A comprehensive review of the dynamic parameters associated with hydrogen detonation can be found in Lee [8].

1-2 Background

In the past a number of numerical and experimental studies have been carried out to investigate the deflagration to detonation transition phenomenon, affecting parameters on DDT and criterions for onset of detonation [62]. Some of these works present useful information which help to shed light on this complicated phenomenon. DDT simulation is probably the most challenging problem in combustion field because of complex nonlinear interaction among different contributing physical processes such as turbulence, shocks, obstacle and flame

interaction and energy release [17]. Until now there has not been any successful, verifiable and reliable DDT simulation in the combustion community and scientists are not able to predict a priori whether DDT can occur in a reactive mixture or not. This is a consequence of incomplete knowledge of relevant parameters and scaling relationships to describe the fundamental processes of turbulent flame acceleration, auto ignition and onset of detonation [15], despite these problems, some of the previous works show promising results. Here a brief review of some of notable works is presented.

A brief review of some previous studies about DDT

Kratzel et al. [9], used a 2-D algorithm based on Direct Numerical Simulation and Including Large Eddy Simulation to calculate flame folding in the early phase of the process after ignition, to model DDT in Hydrogen-air mixture in a tube with obstacle. They used a random vortex method for the flame acceleration. As they concluded, the result of their numerical simulation for deflagration and detonation (separately) is promising in comparison with experimental data. But the transition process between these two modes of combustion (deflagration and detonation) is missing in their simulation. So they concluded further research efforts are needed to at least have a qualitatively correct model for these combustion processes [9].

Smirnov et al. [10], Simulated mixture ignition and flame acceleration in 1-D and 2-D and then presented some experimental tests to investigate several affecting parameters on the onset of detonation. They used a two step chemical kinetic model for combustion and a modified Godonov numerical scheme to solve governing Equations. They concluded from their 1-D results that the flow structure differs greatly with activation energy. For high E_a a region of constant flow which is followed by a combustion wave is created. For low E_a instantly (by ignition) a strong detonation wave is crated which eventually slows down to CJ condition. For intermediate E_a, initially a combustion wave is formed and the pressure in between precursor waves and flame front increases and flame acceleration rapidly forms a detonation.

In 2-D, they just show the flow structure of a detonation wave. Finally they show results of some experiments to investigate the effect of reflected shocks.

They concluded an acceleration of the reaction zone preceded by several shock waves can be a result of the interaction of the contact surface with the flame zone overtaking it [10].

Khokhlov and Oran [11-13], studied the role of hot spots and shock flame interactions in detonation initiation in the flame brush.

They developed a physical and numerical model to simulate the shock–flame interaction in the conditions of the reflected shock-tube experiments. The model includes a self-consistent description of processes of chemical reactions, molecular diffusion, viscosity, and thermal conduction in acetylene–air mixtures. It reproduces the laminar flame and detonation properties of acetylene–air initially at room temperature and in the pressure range 0.1–1 atm. The simulations were carried out using adaptive mesh refinement "*at a level that resolved the laminar flame and all of the chemical and physical processes associated with flame development, propagation, and interaction with shocks*" [12]. The model provides a resolved, multidimensional solution of the two dimensional reactive Navier-Stokes Equations.

Oran and co-workers subsequently used this model to carry out a series of DDT studies [11-13]. They initially investigated the interaction of a single shock with a sinusoidally perturbed flame and compared the results in two and three dimensions [12]. They examined a single shock–flame interaction and the resulting Richtmyer-Meshkov (RM) instability. The RM instability was found to form a funnel (also called a "spike") of unburned material extending into the burned region. As a result of the instability, the interaction increased the surface area of the flame, which increased the subsequent energy release. However, it was concluded that the single shock–flame interaction was not enough to create a flame brush that could lead to DDT.

The second paper [13] reported two-dimensional simulations of shock–flame interactions, including the effects on the flame of both the incident and reflects shocks. These simulations examined how this interaction generates a flame brush, amplify shocks, and leads to the high speed shocks observed in the experiments.

They found that the shock–flame interactions, through the RM instability, create and maintain a highly turbulent flame brush. The source of turbulence in these simulations was not a Kolmogorov cascade. The turbulence was driven at all scales by repeated shock–flame interactions. Multiple shock–flame interactions and merging shocks in un-reacted material led to the development of a high-speed shock that moved out in front of the turbulent flame. The region between this shock and the flame was subjected to intense fluctuations generated in the flame. They have performed the above simulations for incident shocks at two relatively low Mach numbers, Ms = 1.4 and Ms = 1.5. The Ms = 1.4 case did not show a transition to detonation. In the Ms = 1.5 case, pressure fluctuations generated in the region of the turbulent flame brush created, in turn, hot spots in un-reacted material. They observed that these hot spots led to detonation through the gradient mechanism in the region of unburned material between the flame brush and the high-speed shock. They resolved the process of DDT in a hot spot both in space and in time in this simulation. The characteristic time of the DDT was significantly shorter, of order a microsecond, than the time-scale of the Shock–flame interaction itself (approximately a millisecond). As a result, *DDT appeared as a sudden explosion.* They mentioned that the appearance of DDT ahead of the flame brush was in qualitative agreement with what was observed in certain ranges of Mach numbers in the experiments [11].

In the last paper of this series [11], they mentioned *that the mechanism by which a high speed deflagration becomes a detonation remains as an outstanding problem in combustion theory.* Also "*Exactly how DDT occurs is not clear from experiments, and seems to vary from event to event*". They observed two basic pictures of DDT: sometimes it happened inside the flame brush; sometimes it occurred in the preheated, compressed material between the leading shock wave and the flame brush. A prominent feature of all these experiments is the existence of a boundary layer, the role of which is not entirely clear [11].

Oran and Gamezo [14], in a comprehensive article demonstrate the result a 10-year theoretical and numerical effort to understand the deflagration-to-detonation transition (DDT). They mention that, to simulate DDT from first principles, it is necessary to resolve the relevant scales ranging from the size of the system to the flame thickness, a range that can cover up to 12 orders of magnitude in real systems.

This computational challenge resulted in the development of numerical algorithms for solving coupled partial and ordinary differential Equations and a new method for adaptive mesh refinement to deal with multi-scale phenomena. Insight into how, when, and where DDT occurs was obtained by analyzing a series of multidimensional numerical simulations of laboratory experiments designed to create a turbulent flame through a series of shock–flame interactions. Their simulations showed that these interactions are important for creating the conditions in which DDT can occur. They also found out that flames enhance the strength of shocks passing through a turbulent flame brush and generate new shocks. In turn, shock interactions with flames create and drive the turbulence in flames. They also believe *the turbulent flame itself does not undergo a transition, but it creates conditions in nearby un-reacted material that lead to ignition centres, or "hot spots," which can then produce a detonation through the Zeldovich gradient mechanism involving gradients of reactivity.* Obstacles and boundary layers, through their interactions with shocks and flames, help to create environments in which hot spots can develop. Other scenarios producing reactivity gradients that can lead to detonations include flame–flame interactions, turbulent mixing of hot products with reactant gases, and direct shock ignition. The most important unresolved questions in their work are about the properties of non-equilibrium, shock-driven turbulence, stochastic properties of ignition events, and the possibility of unconfined DDT.

Vaagsaether et al. [16], simulated the flame acceleration and DDT in hydrogen air mixture with a code based on flux limiter centred method for hyperbolic partial differential Equations. They calculated the energy source term by a Riemann solver for the inhomogeneous Euler Equations for the turbulent combustion and a two step reaction model for H_2-Air reaction. They filtered transport Equation for LES and used a transport Equation for turbulent kinetic energy to model the sub-grid scale turbulence. A G-Equation approach was used to track the flame interface. They used a second order accurate total variation diminishing (TVD) numerical scheme because a detonation wave is a shock and combustion wave which are coupled and a TVD numerical scheme ensures capturing of discontinuities in the solution. Although the 2^{nd} order centred scheme may smoothen shocks over more cells than upwind scheme, it was used for its simplicity and high speed.

They solved the governing Equations in a shock-tube shape computational domain with an obstacle to intensify turbulence, since they had pressure records for physical experiments performed using a shock tube with the same geometry they were able to compare numerical and experimental results. Although their numerical result matches the experimental result to some degree, as the flame gets closer to the obstacle the differences become more evident. They predicted a high pressure point which mimicked the transition point in the experiment but the corresponding time this occurred differed from the measured time. The detonation was predicted to occur far behind the obstacle while in the experiments it happened later. They attributed these discrepancies to poor flame obstacle interaction modelling or some problems in turbulence and flame models which were used in the study.

Khokhlov et al. [17], studied the possibility of detonation triggering in unconfined geometries. They based their study and simulation on 2 assumptions. *1- The gradient mechanism is the inherent mechanism that leads to deflagration to detonation transition in unconfined geometries. 2- The sole mechanism for preparing the gradient in induction time is by turbulent mixing and local flame quenching.* They investigated the criterion for DDT in terms of 1D detonation wave thickness, laminar flame speed and thickness. They believe that their study provides a lower-bound criterion for DDT in conditions where shock preheating, obstacle interactions and wall effects are absent. They mentioned that the in most cases the mechanism of onset of detonation is the explosion of a non-uniformly preconditioned region of fuel in which a spatial gradient of induction time has been created by turbulent mixing or shock heating or both. This mechanism was first suggested by Zeldovich for non-uniform temperature distribution and it was subsequently observed in photo initiation experiments by Lee [15] and was called SWACER. It is mentioned that different mechanisms such as shock waves, turbulence, photo-irradiation, intrinsic flame instabilities, rarefaction or a combination of these mechanisms can provide a gradient of induction time in the reactive mixture. They believe that it is very difficult to have DDT in unconfined geometries, because shock waves become weak and turbulence might damp due to expansions and usually there is no reflected shock and wall effects, therefore it is very difficult to precondition the mixture. They explain that based on the experiments done by Wagner et al., DDT in very large and unconfined vapour clouds and under right conditions is possible.

In their study, they investigated two fundamental questions. 1- What is the minimum size of mixed region capable for DDT, 2- what level of turbulence is required to create such a region.

They assumed that the non-uniformity in the region is due to mixing of high entropy products and low entropy reactants. And also for simplicity they assumed that this region is a one dimensional linear distribution of products. They explained the definition of spontaneous burning which was first introduced by Zeldovich. This definition says that explosion starts at the point of minimum induction time (τ) and spreads with the speed of D_{SP}, Eq. 1.1

$$D_{Sp} = \left(\frac{d\tau}{dx}\right)^{-1} \qquad 1.1$$

The difference between spontaneous wave and detonation is that there is no shock wave present in the former.

They also explain the probable mechanism by which a spontaneous wave can be converted to a detonation wave. In this situation the spontaneous wave velocity is initially higher than CJ speed, but then speed decreases and become less than CJ speed. When the spontaneous wave is moving exactly with the CJ speed, the products are moving with the local sound speed, so they tend to overcome the wave and create a shock wave. They believe if the spontaneous wave velocity changes become too steep, causing very steep gradient, the shock and reaction will separate and CJ detonation will not form. Therefore in this process the spontaneous wave velocity must change slowly enough so that shock and reaction do not separate. This means the non-uniform region must be large enough to satisfy this condition. Then they solved a 2 step chemical reaction along with the conservation Equations on the computational domain. They selected the grid sizes to have at least 10 cells within the detonation reaction zone. They introduced induction time as a function of temperature and fuel mass fraction by Eq. 1.2

$$\tau(T,Y) \approx \frac{1}{(\gamma-1)qY}\left(\frac{T^2}{E_a}\right)exp\left(\frac{E_a}{T}\right) \qquad 1.2$$

In Eq. 2, E_a is activation energy and q is total energy release per unit mass. Using this Equation it is possible to find the point at which induction time is minimum so

the explosion starts from there. By calculating the derivative of induction time with respect to x and using Eq. 1.1 It is possible to find spontaneous wave velocity in all points in the computational domain. By solving these Equations along with the conservation equation they investigated the conversion of spontaneous wave to CJ detonation and the minimum size of preconditioned region required to have a self sustained and non damping Detonation.

At the end, by solving several cases with different sizes and in different initial temperature, they found a minimum region size in which it is possible to have stable Detonation. They also concluded that the critical length for triggering DDT is highly dependent on initial temperature. According to their results they also concluded that a very large scale mixing is required to precondition the region for DDT.

Kratzel et al. [3] conducted 2-dimensional direct numerical simulation of DDT in hydrogen-air mixture in an obstructed tube. In their simulations, flame folding in the early phase of the process following ignition was modelled using large eddy simulation. The predictions were found to be in reasonable agreement with the experimental data for the actual deflagration and detonation but failed to capture the transition process from deflagration and detonation. Smirnov et al. [4] simulated mixture ignition and flame acceleration in 1-D. They also carried out 2-D detonation modelling with two-step combustion chemistry. A modified Godonov numerical scheme was used to solve the governing Equations. The predicted flow structures in the 1-D simulations were found to differ greatly with the change of activation energy (E_a). For high E_a, a region of constant flow was found to follow the combustion wave. For low E_a, a strong (over-driven) detonation wave was initiated following ignition and gradually slowed down to CJ detonation. For intermediate E_a, a turbulent combustion wave was initiated following ignition. This was followed by the gradual increase in the pressure in between the precursor waves and the flame front. The flame accelerated rapidly and underwent transition to detonation. It was postulated that the acceleration of the reaction zone preceded by several shock waves could be a result of the interaction of the contact surface with the flame zone overtaking it [4].

Zbikowski et al. [140], developed a large eddy simulation based model for numerical simulation of detonation. They used the progress variable equation and a gradient

method, based on a product of pre-shock mixture density and detonation velocity to model the source term in the progress variable equation. In this model the chemical kinetics enters the combustion model only through its influence on the detonation velocity and modelling of chemistry is omitted. They also verified their model against theoretical solution by the Zel'dovich–von Neumann–Doring (ZND) theory for a stoichiometric hydrogen–air detonation; however the applicability of this model for DDT and near transition regions simulations is not justified.

Lee et al. [18], in a paper titled "*Photochemical initiation of gaseous detonations*" introduced his famous SWACER mechanism for DDT.

Lee and Moen [15], in a very comprehensive article investigated and explained DDT from a physical point of view. Although they did not simulate DDT numerically and their article is completely based on their knowledge and experimental results, it provides us with the most comprehensive qualitative description of DDT. In this article Lee further introduced his famous SWACER theory for DDT. This bears close similarity to the induction time gradient theory developed by Zeldovich in 1970 [125] but offers more physical insight. The authors mention that due to incomplete physical knowledge DDT still it is not possible to have a reliable and quantitatively correct numerical simulation. The SWACER or "Sock Wave Amplification through Coherent Energy Release" implies that the formation of detonation requires amplification of shock waves through several localised auto explosion points. This mechanism was observed and suggested by Lee in his photo irradiation experiments. This mechanism is based on proper synchronisation of shock wave and chemical energy release applied to a single travelling pressure pulse. *The SWACER is based on the principle that the time sequence of chemical energy release is such that it is coherent with the shock wave it generates, so it strengthen the propagating shock.* According to the SWACER mechanism, the formation of detonation requires amplification of shock waves through several localised auto explosions.

Teodorczyk et al. [120], Carried out experimental studies of hydrogen-air flame acceleration and transition from deflagration to detonation in a 2 meter long square section (0.08 by 0.11 m) tube with the initial condition of 0.1 MPa pressure and 293 K temperature. They repeated the experiments for 3 different obstacle blockage ratio

(0.25, 0.5 0.75) and four different obstacle density. They also repeated the experiments in 3 different mixtures with 20%, 25% and 29.6% (Φ = 1) hydrogen mixture with air (percentages are based on volume). The results of flame acceleration and DDT were recorded using four pressure transducer and four in-house ion probes. They made the geometry to match the numerical work of Gamezo et al. [21].

In an earlier study, Teodorczyk et al. [121] (motivated by Gamezo et al. [21]) did flame acceleration and transition from deflagration to detonation experiments in 2m long tube with 0.11 m width and 1, 2, 4 and 8 cm height in 1cm no detonation, in 2 and 4 cm quasi-detonation and DDT and in 8 cm quasi-detonation, DDT and stable detonation was observed. They concluded as the size of domain increases the distance to the DDT (run up distance) also increases. They stated the same results are obtained qualitatively by Gamezo et al. [21].

There have been more studies and publications about DDT, however, due to the limited space here, only some of the most notable works on DDT are reviewed. The materials included in other valuable works are mostly covered in the articles which are reviewed here; this suffices at this point to choose these articles as a guide trough the rest of our work.

1-3 Objectives of the research

In spite of several attempts by combustion scientists to simulate deflagration to detonation transition numerically, there has not been any successful and reliable breakthrough so far. The most notable works in the past are carried out by Oran et al. [14, 21], but validation is lacking in these works and DDT remains an unresolved problem in combustion studies. This is mainly associated with the complex physics involved and extremely high computational power required.

Therefore the current work is mainly dedicated to developing models and solvers in order to carry out numerical simulations of deflagrations, detonations and transition from deflagrations to detonation. The complex physics involved implies that many commonly used combustion and turbulence models may not be applicable to DDT

studies. Therefore the current work is aimed at employing other alternatives without compromising the accuracy.

The high computational cost associated with such heavy simulations is extremely challenging. Therefore another objective of the present work is to develop and employ new approaches to reduce the computational costs to an affordable level while keeping high quality in the simulations.

It is also intended to compare the results of the current numerical work against some of the experimental works which are available in the literature to verify accuracy and reliability of the proposed approaches.

1-4 Research methodology

A numerical approach has been developed based on the use of the single step chemistry and the solution of the full Navier Stokes solver using the implicit large eddy simulation techniques implemented within the frame of open source CFD code, OpenFoam [35].

The OpenFoam toolbox contains several useful classes and functions that can be used to create new solvers. Additional governing Equations have been implemented in the present study to create solvers DDTFOAM capable of simulating flame acceleration, DDT and detonation.

1-5 Thesis Organisations

Chapter one provides the background to the research and brief review of previous related works. This is followed by the definition of the research objectives and an outline of the research methodology and approach.

Chapter two presents the governing Equations. Initially the physical model is described then the governing Equations for flow and flame simulations under given condition are described. A range of acceptable model simplifications and suitable boundary and initial conditions for the simulations are discussed.

Chapter three describes the solution methods for the governing Equations.

Chapter four is dedicated to numerical simulations of laminar flame, flame propagation and acceleration as well as turbulent flames using different techniques.

Chapter five reports on the numerical simulations of the detonation phenomenon in small, medium and large scales. The differences in the underlying physics between deflagration and detonation regimes as well as the numerical considerations are discussed.

Chapter six is dedicated to transition from deflagration to detonation. The simulations presented in this chapter are a continuation of the numerical studies Chapter 4, where flame acceleration continues to the final stages and DDT occurred.

Chapter seven reports on the model validation and verification using previously published experimental and numerical DDT results.

Chapter eight summarises the thesis and provides suggestion for future works.

Chapter 2

Governing Equations and Numerical methods

In this chapter, initially the physical model is described then the governing Equations for flow and flame simulations under different conditions are presented. A range of suitable simplifications, boundary and initial conditions for the simulations are discussed.

2-1 Physical model

If a flame triggers inside a reactive mixture passing through a pipe, the flame which is initially laminar and low speed, under proper condition, would gradually accelerate and becomes fast and turbulent.

Several parameters affect the acceleration of the flame such as the initial mixture condition and the presence of bends and junctions in the pipeline. If a flame accelerates enough, under proper condition it can undergo transition to a detonation wave which is a much more destructive combustion regime. As the detonation waves are the most violent and destructive types of combustion waves, extra care must be taken while designing a device which might need to withstand a detonation load such as a detonation arrester.

During the flame acceleration process the gases are pushed ahead of the flame due to the expansion in the products and it creates pressure waves moving ahead of the flame. When the reaction rate is high enough the fast energy release at the reaction front also creates pressure waves moving ahead. The reflection of these shocks hit the flame front and creates localised high pressure and temperature points called "hot spot". If temperature and induction time gradient in these hot spots is appropriate, it coherently leads to a series of localised explosions in the shock laden gas ahead of the flame or right at the flame brush. These explosions create secondary shocks that magnify each other and under appropriate condition they can trigger an overdriven detonation. The magnitude of the pressure for this overdriven detonation is potentially of the order of 100 bar. The overdriven detonation damps to a steady detonation with CJ condition right after the transition process. This overall process is

called Deflagration to Detonation Transition which is frequently referred to as DDT [2].

Previous experiments have shown that during the flame acceleration process, when the shock velocity reaches a critical value transition to detonation is inevitable [2].

Understanding the propagation mechanism of different combustion regimes is essential for deriving the governing equations for numerical simulations, it is also important in the practical works because the propagation mechanism gives us insight about the ways to alter the sustainability of different combustion waves and mitigate or quench them.

In case of deflagrations, the mechanism of propagation is based on the diffusion of mass and heat in the reaction zone which keeps the chain branching reactions sustained, turbulence also plays an important role in the rate of heat release and flame speed.

For detonations however, a totally different propagation mechanism exists. As the detonation wave passes through a mixture the shock heating increases the reactive mixture's temperature to the auto-ignition point and leads to the exothermic reaction [2]. On the other hand the heat release from the exothermic reaction feeds energy into the shock and keeps it sustained. Therefore decoupling the shock and combustion region in a detonation wave can effectively disrupt detonation wave propagation, although still deflagration waves might exist after detonation quenching, therefore for detonation waves the turbulence and diffusive terms are mostly negligible compared to shock effects.

2-2 Turbulence modelling

In order to simulate the DDT process due to high level of turbulence involved at some stages, the numerical approach should be able to resolve or model a very wide range of length scales ranging from a few microns up to a few centimetres or meters depending on the geometry conditions.

Here a brief description of the most widely used techniques for turbulence modelling is provided and the rationale behind our chosen approach explained.

2-2-1 RANS modelling

One approach for turbulence modelling is based on the solutions of the Reynolds-Averaged Navier-Stokes (RANS) Equations in which the instantaneous variables such as pressure and velocity are split into an averaged part ($\overline{f(x)}$) and a fluctuating component ($f(\acute{x},t)$).

$$\begin{cases} f(x,t) = \overline{f(x)} + f(\acute{x},t) \\ \overline{f(\acute{x},t)} = 0 \\ \overline{f(x)} = \lim_{\Delta t \to \infty} \frac{1}{\Delta t} \int_{t_0}^{t_0+\Delta t} f(t)dt \end{cases} \qquad 2.1$$

Applying this formula to fluid properties and substituting them in the Navier-Stokes Equations will result is some unknown variables such as Reynolds tensor which are products of averaged quantities and derivatives of the mean properties. The Reynolds tensor can be estimated using simple or high order closure models to close the set of governing equations and solve them numerically.

The benefit of the RANS approach is isolating and approximating un-known fluctuating parts while using a coarser grid to solve the time averaged parts.

The RANS method is applicable only if the mean flow is stationary, otherwise if the mean flow properties, $\overline{f(x)}$, are varying with time, it would be very difficult to separate $\overline{f(x)}$ and $f(\acute{x},t)$ which would lead to unavoidable errors [19].

In applications such as DDT modelling where the mean flow is not steady state RANS is not an appropriate method, also interpreting the time dependent variables in such highly unsteady problems is questionable.

2-2-2 Direct Numerical Simulation

The intrinsic shortcoming of the RANS approach in dealing with highly unsteady problems shows that a proper numerical approach should be able to resolve instantaneous flow properties. One alternative would be Direct Numerical Simulation (DNS) in which all of available length scales ranging from Kolmogorov scales to the largest available eddies most be resolved. Doing DNS requires a domain which is large enough to contain the largest length scales and a computational grid which is fine enough to resolve eddies in the Kolmogorov scales. As a result the DNS approach is limited to very low Reynolds numbers and very small computational domains.

DNS can also be called numerical experiment, the high accuracy and possibility of tracking very small details especially nonlinear behaviour of turbulent flows provides a benchmark for developing, calibrate and validating turbulence models. As result of the high resolution associated with DNS it can uncover very important and fine features of different fluid flow problems which are difficult or impossible to track in laboratories. However the extremely high computational cost associated with DNS simulations renders it unaffordable for most of practical applications.

2-2-3 Large Eddy Simulations

Large Eddy Simulation (LES) is based on splitting the available length scales into two parts e.g. $f(x,t) = \overline{f(x)} + f(\acute{x},t)$, large and macroscopic scales, $\overline{f(x)}$, which can be resolved using instantaneous Navier-Stokes Equations and small microscopic scales, $f(\acute{x},t)$, which cover all ranges smaller than the computational grid up to Kolmogorov length scale. In Large Eddy Simulations the variables are filtered either in spectral coordinates or space coordinates. Those eddies which are larger than the LES filter are resolved and the smaller ones which cannot be resolved using the computational grid are modelled using a Sub-Grid Scale Model (SGS model). The filtered quantities in LES read:

$$\begin{cases} \overline{f(x)} = \int f(x')F(x-x')dx' \\ \text{Gaussian filter} \\ \widetilde{F(x)} = F(x_1,x_2,x_3) = \left(\frac{6}{\pi\Delta^2}\right)^{\frac{3}{2}} exp\left[-\frac{6}{\Delta^2}(x_1^2+x_2^2+x_3^2)\right] \end{cases} \quad 2.2$$

Where $F(x-x')$ is the LES filter. The most widely used LES filters are introduced in [43, 130]. As an example the Gaussian filter in physical space is included in Eq. 2.2.

For compressible flows a mass-weighted Favre filtering [43] is introduced in Eq. 2.3:

$$\bar{\rho}\tilde{f}(x) = \int \rho f(x')F(x-x')dx' \quad 2.3$$

The main benefit of the LES methods is that the larger eddies which contain most of the turbulence energy are resolved properly and the smaller eddies which carry a much smaller proportion of turbulence energy are modelled using SGS models. Therefore high accuracy can be achieved provided the cut-off filter (mostly the grid size) is fine enough to resolve the energy carrying eddies and also a well calibrated SGS model is used. The sub-grid scale effects can be modelled either by use of Explicit SGS models or by Implicit treatments. The explicit SGS models are very well developed and widely used today [43, 130]. However, very recent researches have proved that the sub-grid scale modelling can be done implicitly by making use of the truncated terms in the numerical schemes [131, 141]. In these studies, by using modified equation analysis which quantifies the magnitude of truncated terms in each numerical system, it is proved that certain numerical schemes called NVF or Non-oscillatory Finite Volume schemes, which include Total Variation Diminishing schemes and some other Non-oscillatory methods, benefit from truncated terms which have the form of a built-in sub-grid scale model.

2-2-4 Implicit Large Eddy Simulation using monotone fluid-dynamic algorithms

Over the past years it is observed that monotone fluid-dynamic algorithms produce results that are in good qualitative and quantitative agreement with experimental results [7]. Monotone fluid-dynamic algorithms do not use explicit turbulence models. Even in some studies which include significant turbulence in sub-grid scales, the monotone fluid-dynamic algorithms have been found to produce reasonably accurate predictions [7, 14, 29, and 131].

There are interesting physical reasons which explain good performance of these methods as described by Oran [7] and Grinstein et al. [131].

Looking at Kolmogorov energy cascade diagram as shown in figure 2-1, the spectrum of the turbulent energy flow falls off quickly at small scales. Therefore the volume of kinetic energy contained in progressively smaller turbulent scales drops quite fast and as a result smaller scales (smaller than currently computationally resolvable scales) contain a significantly smaller portion of the turbulence kinetic energy [7], therefore the scales containing most of energy can be resolved using our current computational power. If the energy spectrum had a flatter trend then it would have meant a large volume of energy is contained in smaller eddies then it would have been necessary to fully resolve these small scales. However, these small eddies have a small turnover time and high rotational velocity which is high enough to mix with large scale in-homogeneities, produced in large scale flow.

It is also observed in DNS and theoretical studies [7] that the turbulent energy is transferred through a cascade from larger eddies to their neighbouring smaller eddies which are in contact and interacting, this turbulent cascade continues until the energy is dissipated in the smaller eddies [7, 21, 130 and 131].

Eventually the energy which is taken from a given eddy scale, is taken out due to the interactions with eddies in maximum one order of magnitude smaller [7] therefore the energy cannot be transferred directly from large and high energy eddies to the small energy dissipating eddies. If the smallest eddies could extract significant amount energy from large eddies then it would have been necessary to resolve all of the present scales for meaningful simulation. However the described turbulent

cascade guarantees that numerical simulation of a range of given eddy scales can accurately predict the rate of energy transfer out of those eddies, the predicted energy transfer can be used to match the sub-grid model to the resolved part.

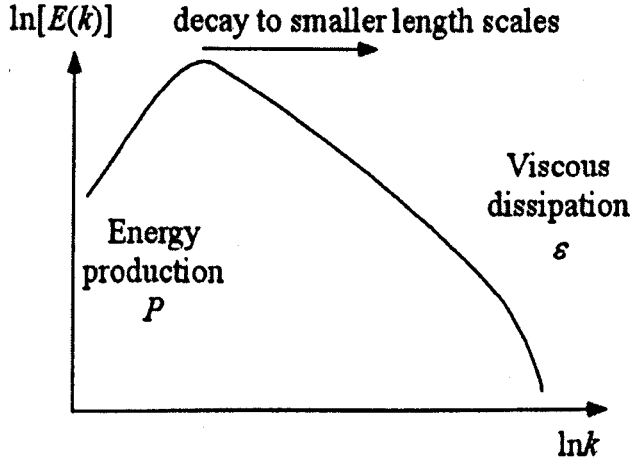

Figure 2-1 Kolmogorov energy cascade [19]

It is also evident that there is no important dynamics phenomenon happening in scales even more than 10 times larger than Kolmogorov length scale. Presence of significant dissipation effects leads to very small dynamics effects remaining at the scales well larger than Kolmogorov scales [7]. Studies carried out by Moin and Mahesh [122] and Vuillermoz and Oran [123] supports the absence of dynamic effects at small scales. This fact further support the significantly less importance of resolving very small scales [7].

Apart from the physical observations explained above, the numerical nature of the nonlinear monotone numerical methods exhibits some uniquely valuable properties which can be summarised in: conservation, and positivity which can be called monotonicity in general. It means this numerical methods, through their local dissipation, can smoothly connect the large scale, energy carrying, resolved eddies to the smaller unresolved scales, and this is done by the natural dissipation effects which is available in these methods. While using these methods in LES we can trust that they resolve the larger scales with the minimal affection from the numerical errors from the smallest resolved scales.

Above discussion around the monotone numerical methods and their capability to reproduce good results by only resolving energy containing scales, is valid for

reacting flows as well as non-reacting flows [7, 131]. In case of reacting flows, temperature increase leads to higher flow viscosity, υ, which reduces the Reynolds number and alters the dissipation scale. This means the Kolmogorov length scale, $\left(\frac{\upsilon^3}{\varepsilon}\right)^{\frac{1}{4}}$ and time scale, $\left(\frac{\upsilon}{\varepsilon}\right)^{\frac{1}{2}}$, are even larger in reacting flows and even lower grid resolution would be required compared to a low temperature flow [7].

2-2-5 Turbulence generation and flow instabilities

There are many factors which can help the turbulence generation process and formation of flow instabilities. These instabilities can lead to an increase in the flame surface area and mixing rate, resulting in a higher reaction rate. Higher heat release in turn leads to sharper density gradients and localised flow expansions which feed to flow instabilities and turbulence generation.

The two most common instabilities in compressible flows are Rayleigh-Taylor and the Kelvin-Helmholtz. The Rayleigh-Taylor instability is a result of heavier fluid acceleration through the lighter fluid. This would be observed in buoyancy driven flows and shock-flame interactions. Kelvin-Helmholtz instability happens when two flows with different velocity interact and subsequently the instability develops at their contact surface, this is mostly observed in jet flows. There are other types of flow instabilities such as thermo diffusive, chemical acoustic, Landau Darrieus and thermal instabilities [7].

In simulating reactive turbulent flows it is necessary to know the range of time and space scales which must be resolved to produce a reliable solution and then, how we can use the information about the scales and instabilities involved to make the simulations efficient. As a compromise between computational requirement and accuracy, it is decided to base the present study on LES techniques. In particular as discussed in the previous section, the ILES approach is particularly promising and will be adopted in the present study.

2-3 The Governing Equations

The deflagration to detonation transition covers a wide range of combustion regimes starting from very low speed laminar flames and ending at a supersonic combustion wave which might have a highly distorted surface. The propagation mechanism of each combustion regime might be fundamentally different from the others [41-42]; therefore the governing equations for such a phenomenon must be able to predict the behaviour of each combustion regime correctly.

In this chapter we introduce the fundamental equations which should be used for numerical simulations of reactive flows. Initially, equations are shown in their general forms, then later specific forms of governing equations are presented based on the specific application they are intended to be used for [39].

Fundamental equations for describing flow motion are normally derived using an infinitely small control volume through which the flow is passing. As a result the equations are presented in form of partial differential conservation equations.

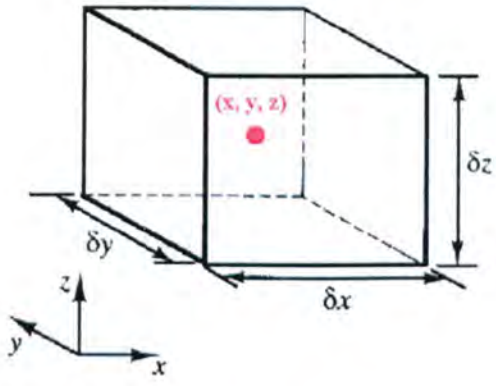

Figure 2-2 Infinitely small control volume for flow motion equation derivations

Substantial derivatives, Eq. 2.4, are used to show the net rate of variations in a variable.

$$\frac{D\Psi}{Dt} = \frac{\partial \Psi}{\partial t} + U.\nabla\Psi \qquad 2.4$$

It means that the net variation of the general variable Ψ in a fluid element is equal to the rate of time-variations of Ψ within that element plus the rate of Ψ flowing in and out of that element.

2-3-1 Continuity Equation

Applying Eq. 2.4 to the total mass of a system would help to derive one of the most fundamental fluid dynamics equations which is called continuity Equation. The continuity Equations is based on the physical fact that the mass is conserved, meaning that the summation of total mass coming in a domain and going out of the domain plus the variation of the mass inside the system is zero. This expression can be formulated using Eq 2.4 and rewritten in form of Eq. 2.5:

$$\begin{cases} \dfrac{Dm}{Dt} = 0 \\ \dfrac{\partial m}{\partial t} + U.\nabla m = 0 \end{cases} \qquad 2.5$$

For a small control volume such as the one presented in Figure 2.1, the mass, m, can be written as the product of density and volume:

$$\begin{cases} m = \rho V \\ V = \delta x \times \delta y \times \delta z \\ \Longrightarrow m = \rho \delta x \delta y \delta z \end{cases} \qquad 2.6$$

Substituting Eq. 2.6 in Eq. 2.5 results in the final form of continuity Equation which is most widely used in fluid dynamic problems:

$$\begin{cases} \dfrac{\partial \rho \delta x \delta y \delta z}{\partial t} + U.\nabla \rho \delta x \delta y \delta z = 0 \\ \Rightarrow \\ \dfrac{\partial \rho}{\partial t} + U.\nabla \rho = 0 \end{cases} \qquad 2.7$$

In the above Equations ρ, U, V and m represent density, velocity, volume and mass respectively.

2-3-2 Momentum conservation Equation

The momentum conservation law is derived mainly from the Newton's second law, meaning that the rate of variations of the momentum of a fluid element is equal to the resultant forces applied on that fluid element.

Incorporating Eq. 2.4 again to express the second Newton's law results in Eq. 2.8:

$$m\frac{DU}{Dt} = m\left(\frac{\partial U}{\partial t} + U.\nabla U\right) = F_{surface} + F_{body} \qquad 2.8$$

Taking the control volume presented at Figure 2.1 as the reference again, $F_{surface}$ represents the forces applied on the boundaries of this control volume such as viscous and pressure forces as well as the hydrostatic terms of stress tensor.

For the x direction on our reference control volume these forces can be written as:

$$F_{s-xy} = \left[\left(-\frac{\partial p}{\partial x} + \frac{\tau_{xx}}{\partial x}\right)\delta x\delta y\delta z + \left(\frac{\tau_{xy}}{\partial y}\right)\delta x\delta y\delta z + \left(\frac{\tau_{xz}}{\partial z}\right)\delta x\delta y\delta z\right] \qquad 2.9$$

Simplifying Eq. 2.9 and substituting in Eq. 2.8 for the momentum variations in the x direction results in:

$$\frac{\partial \rho u}{\partial t} + \nabla.(\rho u U) = \left(-\frac{\partial p}{\partial x} + \frac{\tau_{xx}}{\partial x}\right) + \left(\frac{\tau_{xy}}{\partial y}\right) + \left(\frac{\tau_{xz}}{\partial z}\right) + F_{body-x} \qquad 2.10$$

Since the dimensions of the reference control volume, $\delta x \times \delta y \times \delta z$, are cancelled out for the equation terms, the derived differential equation has a generalised form.

The same way we can derive the momentum conservation Equations in y and z directions which are presented as Eq. 2.11 and Eq. 2.12:

$$\frac{\partial \rho v}{\partial t} + \nabla.(\rho v U) = \left(-\frac{\partial p}{\partial y} + \frac{\tau_{yy}}{\partial y}\right) + \left(\frac{\tau_{xy}}{\partial x}\right) + \left(\frac{\tau_{yz}}{\partial z}\right) + F_{body-y} \qquad 2.11$$

$$\frac{\partial \rho w}{\partial t} + \nabla.(\rho w U) = \left(-\frac{\partial p}{\partial z} + \frac{\tau_{zz}}{\partial z}\right) + \left(\frac{\tau_{xz}}{\partial x}\right) + \left(\frac{\tau_{yz}}{\partial y}\right) + F_{body-z} \qquad 2.12$$

2-3-3 Energy conservation Equation

The energy conservation Equation is based on the first law of thermodynamics meaning that the rate of variation of energy in a fluid element is equal to the heat transfer to that fluid element plus the rate of work done on that element.

Using Eq. 2.4 the first law of thermodynamics can be written as Eq. 2.13:

$$m\frac{DE}{Dt} = m\left(\frac{\partial E}{\partial t} + U.\nabla E\right) = W + \dot{Q} \qquad 2.13$$

In Eq. 2.13 E, W and $\dot{Q}$ represent energy, work and heat transfer rate respectively.

The rate of energy transfer and work on the reference control volume can be expressed in terms of stresses (shear and normal) and temperature. For example the rate of heat flow in the x, y and z directions can be written as:

$$\begin{cases} -\frac{\partial q_x}{\partial x}\delta x\delta y\delta z \\ -\frac{\partial q_y}{\partial y}\delta x\delta y\delta z \\ -\frac{\partial q_z}{\partial z}\delta x\delta y\delta z \end{cases} \qquad 2.14$$

Therefore the total heat transfer to the control volume would be equal to:

$$-\frac{\partial q_x}{\partial x} - \frac{\partial q_y}{\partial y} - \frac{\partial q_z}{\partial z} = -\nabla.q \qquad 2.15$$

Using the Fourier law we can express the heat transfer as a function of temperature gradient and the fluid thermal conductivity:

$$q = -k\nabla T \qquad 2.16$$

Therefore, the total heat transfer to the control volume would be:

$$\dot{Q} = -\nabla.(k\nabla T)\delta x\delta y\delta z \qquad 2.17$$

The total rate of work which is being done on the control volume in the x direction can be expressed as:

$$W_x = \left[\left(\frac{\partial(u\tau_{xx} - up)}{\partial x} + \frac{\partial(u\tau_{yx})}{\partial y} + \frac{\partial(u\tau_{zx})}{\partial z}\right)\right]\delta x\delta y\delta z \qquad 2.18$$

The work in other directions follows the same structure as Eq. 2.18, therefore we can use the following generalised form for representing the work done on the fluid element:

$$W_{c.v} = \left(\frac{\partial(U_j\tau_{ij})}{\partial x_i} - \nabla.(pU)\right)\delta x\delta y\delta z \qquad 2.19$$

Substituting Eq. 2.19 and Eq. 2.17 into Eq. 2.13 and replacing m with $\rho\delta x\delta y\delta z$ results in the final form for the energy conservation Equation:

$$\frac{\partial\rho \mathrm{E}}{\partial t} + \nabla.(\rho U\mathrm{E}) = \frac{\partial(U_j\tau_{ij})}{\partial x_i} - \nabla.(pU) + \nabla.(k\nabla T) + w_{body} \qquad 2.20$$

In Eq. 2.20, w_{body} represents the works done by body forces on the fluid element.

If the flow is compressible we can use the total enthalpy instead in the energy Equation, the total enthalpy is:

$$h_0 = e + \frac{p}{\rho} + \frac{1}{2}(u^2 + v^2 + w^2) = E + \frac{p}{\rho} \qquad 2.21$$

Substituting Eq. 2.21 into Eq. 2.20 results in the enthalpy based form of the energy conservation Equation:

$$\frac{\partial\rho h_0}{\partial t} + \nabla.(\rho U h_0) = \frac{\partial(U_j\tau_{ij})}{\partial x_i} + \frac{\partial p}{\partial t} + \nabla.(k\nabla T) + w_{body} \qquad 2.22$$

2-3-4 Species conservation Equation

One can write conservation equation for each chemical spices available in the system on the same bases as the mass, momentum and energy conservation equations by taking into account the rate of chemical spices entering and exiting a reference control volume in the flow as well as the production and consumption rate of each chemical spices available in the system. The species conservation is of more

importance in reacting flows where production and consumption of chemical spices exist. The species conservation equation is presented in Eq. 2.23:

Species conservation:

$$\frac{\partial \rho Y_k}{\partial t} + \frac{\partial(\rho(U_i + V_{k,i})Y_k}{\partial x_i} = \omega_k \qquad 2.23$$

2-3-5 Simplified from of the Equations

The above equations are derived for general types of flow. For the specific types of application here the following simplifications can be made based on the physical nature of the phenomenon of interest.

1- Ideal gas behaviour

This is characteristic for low-medium pressure flows and is formulated using the ideal gas Equation of state as in Eq. 2.24

$$p = \rho RT \qquad 2.24$$

Equation 2.24 is valid as long as the flow is not under very high pressure and is not about to change to the condensed phase. For non-Ideal gas conditions other types of gas Equation of states or so-called real gas Equations of state are available in the literature.

2- Newtonian fluid

This assumption is used for modelling the viscous terms in the equations. In a Newtonian flow, the shear forces have a linear dependent on the velocity gradient and the dynamic and bulk viscosity of the fluid, therefore the share stress for the Newtonian flow can be expressed as:

$$\tau_{ij} = \mu\left(\frac{\partial(U_j)}{\partial x_i} + \frac{\partial(U_i)}{\partial x_j}\right) + \lambda\delta_{ij}(\nabla . U) \qquad 2.25$$

In Eq. 2.25 μ and λ represent the dynamic and bulk viscosity of the flow. The characteristics of the bulk viscosity are not very well understood yet and it is common to use $\lambda = -\frac{2}{3}\mu$ and also the second term in Eq. 2.25 is normally very small therefore many of the fluid mechanics scientists has proposed to totally neglect [33, 34] the second term in Eq. 2.25.

3- Pressure and temperature dependence of fluid thermo-physical properties

Generally the enthalpy, viscosity and thermal diffusivity of the gases have strong temperature dependency. This is particularly important in reactive flows where sharp temperature changes exist. These properties have much less pressure dependency and in most thermophysical problems, they are proposed as functions of temperature only.

The enthalpy variations of the flow can be determined as a function of the specific heat at constant pressure, C_p, and the temperature variations:

$$\Delta h = C_p \Delta T \qquad 2.26$$

The specific heat at constant pressure, C_p, itself is a function of temperature.

$$C_p = R(a_4 T^4 + a_3 T^3 + a_2 T^2 + a_1 T + a_0) \qquad 2.27$$

The Eq. 2.27 [35] is commonly used to determine specific heat of gasses. There are a number of coefficients, a_i which are available in JANAF thermodynamic tables and are developed by NASA [132]. These data include a set of 14 coefficients for each gas. The first 7 are used for high temperature conditions normally ranging from 1000 K to 6000 K while the second set of the numbers are for low temperature condition normally ranging from 200 K to 1000 K. For calculating C_p, only the first 5 number of each set, $a_0 \ldots a_4$ are used as presented in Eq. 2.27. The remaining two numbers, a_5 and a_6 are used in the calculations of entropy and enthalpy as a function of

temperature. In fact a_5 is called the Low/High temperature enthalpy offset and a_6 is called the Low/High temperature enthalpy offset.

For the viscosity the Sutherland correlation [133] is used which gives the flow viscosity as a function of temperature:

$$\mu = \frac{A_s\sqrt{T}}{1+\frac{T_s}{T}} \qquad 2.28$$

A_s and T_s are the constants which have to be taken from standard thermodynamics data bases in order to have an accurate approximation of the viscosity for each gas.

The Prandtl number is determined using Eq. 2.29:

$$Pr = \frac{\mu C_p}{\kappa} \qquad 2.29$$

By having the value of Prandtl number or assuming unity Prandtl number and calculating μ and C_p from the above correlations, the thermal conductivity, κ, of each gas can be derived.

Applying the above initial simplifications results in the following general form for the flow governing Equations:

$$\frac{\partial \rho}{\partial t} + \frac{\partial(\rho U_i)}{\partial x_i} = 0 \qquad 2.30$$

$$\frac{\partial \rho Y_k}{\partial t} + \frac{\partial(\rho(U_i + V_{k,i})Y_k}{\partial x_i} = \dot{\omega_k} \qquad 2.31$$

$$\frac{\partial(\rho U_i)}{\partial t} + \frac{\partial(\rho U_i U_j)}{\partial x_j} = -\frac{\partial p}{\partial x_i} + \frac{\partial}{\partial x_i}\left(\mu\left(\frac{\partial U_i}{\partial x_j} + \frac{\partial U_j}{\partial x_i}\right) - \frac{2}{3}\mu\delta_{ij}\frac{\partial U_j}{\partial x_j}\right) + F_b \qquad 2.32$$

$$\frac{\partial \rho h_0}{\partial t} + \frac{\partial(\rho h_0 U_j)}{\partial x_j} = \frac{\partial}{\partial x_j}\left(k\frac{\partial T}{\partial x_j}\right) + \frac{\partial p}{\partial t} + \mu\left[\frac{1}{2}\left(\frac{\partial U_i}{\partial x_j} + \frac{\partial U_j}{\partial x_i}\right)^2 - \frac{2}{3}(\nabla.\vec{U})^2\right] + S \qquad 2.33$$

In very high velocity flows e.g. supersonic flows such as detonation, depending on the application, further simplification of the governing equations is possible. In such

conditions the viscous effects are negligible and the flow can be described using reactive Euler Equations. Therefore, the flow can be described using the inviscid, non-conducting, Euler Equations in conservative form:

Mass conservation:

$$\frac{\partial \rho}{\partial t} = -\nabla(\rho U) \tag{2.34}$$

Momentum conservation:

$$\frac{\partial \rho U}{\partial t} = -\nabla(\rho UU) - \nabla p \tag{2.35}$$

Energy conservation:

$$\frac{\partial \rho E}{\partial t} = -\nabla(\rho EU) - \nabla(\mathrm{U}p) \tag{2.36}$$

E in Eq. 5.3 can be expressed as:

$$E = -\alpha \mathbb{Q} + \frac{p}{[\rho(\gamma - 1)]} + \frac{U^2}{2} \tag{2.37}$$

where $\mathbb{Q}$ is the heat of chemical reaction per unit mass.

Chapter 3

The numerical techniques

Having a closer look at the governing equations, which are derived in chapter 2, reveals that we are dealing with coupled non linear partial differential equations. In majority of the cases these equations, even in their most simple form, cannot be solved analytically.

The alternative approach to the analytical solution is the numerical solution which in the category of fluid mechanics is referred to as Computational Fluid Dynamics or CFD.

The purpose of Computational Fluid Dynamics is to turn the highly non-linear coupled fluid motion governing equations into sets of linearised discrete algebraic equations. The solution of these equations results in the determination of the results of the original governing equations at a number of pre-determined locations (grid points) and times (time steps) inside the computational domain.

From the above description, it is clear that there are two main steps in the discretisation process, firstly to discretise the governing equations to derive the sets of linearised algebraic equations and secondly to discretise the computational domain and define the pre-determined locations which are called control volumes or computational cells. In case of unsteady solution the time also should be divided into relatively small time steps for the solution.

There are different approaches for discretising the equations and domain such as finite element, finite difference and finite volume.

The finite difference method linearises the partial differential equations using truncated Taylor series expansions which are solved on a number of grid points in the computational domain. The main benefit is that high order schemes can be achieved however the application of finite difference method is limited to the structured grids and more importantly it does not comply with the conservation of the quantities.

The finite volume method discretises the domain into a number of finite volumes. The values are determined at the centroid of each computational cell and the quantities are interpolated to determine the values at the shared faces between two cells. Since the integral of quantities at the shared faces between two neighbouring cells is the same, this method keeps the conservation of the quantities. Because of

the differentiations, integrations and interpolations involved in the finite volume method, it is very difficult to construct schemes higher than second order.

The finite element method is similar in many ways to the finite volume method except that there are weight functions obtained from the quantities at cell corners which are used while integrating the partial differential equation to help minimising the residuals. However, the efficient solution of the resulting set of matrixes could be very difficult.

OpenFOAM toolbox [35], which is used as the main framework for the code developments in the present work, is based on the finite volume method.

3-1 Discretisation

3-1-1 Discretisation of time and domain

The discretisation of the numerical domain produces the computational mesh which is a set of control volumes. The control volumes or cells can have any shape, as in Figure 3-1, and only the coordinates of the cell centre, corners, constructing faces should be accurately determined as in input to the discretised equations, which will be explained later. There are codes which can only deal with structured mesh, such as cubic cells, however the flexibility and the quality of the computational mesh would be very limited in these codes.

The time behaves as a parabolic coordinate [36] therefore the computational solution is obtained from marching on time, beginning from an initial condition at start time.

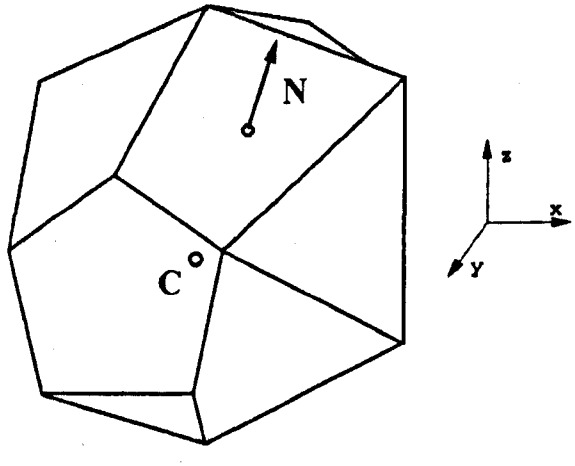

Figure 3-1 Random shape computational cell, control volume

In the general control volume presented in figure 3-1 the centroid of the cell is shown by point C and the cell has a number of surfaces which are shared with other cells except for the faces at the domain boundaries. The normal vector to one of the faces is shown by vector N.

As the computational domain is decomposed to a finite number of control volumes, the computational cells may not fully cover the computational domain. The uniformity of the computational domain depends on how coarse/fine the computational cells are and whether the mesh is structured or unstructured.

3-1-2 Discretisation of the Equations

A typical transport Equation for the arbitrary quantity Ψ is presented in Eq. 3.1:

$$\underbrace{\frac{\partial \rho \Psi}{\partial t}}_{\text{Time derivative}} + \underbrace{\nabla.(\rho U \Psi)}_{\text{Convection term}} + \underbrace{\nabla.(\rho \Gamma_{\Psi} \nabla \Psi)}_{\text{Diffudion term}} = \underbrace{S_{\Psi}}_{\text{source term}} \qquad 3.1$$

Eq. 3.1 is a second order equation because the second derivative of Ψ is present in the equation. In order to get a reasonably accurate result we need to have a discretisation method which is at least at the same order as the transport equation, here in this case second order discretisation schemes are required.

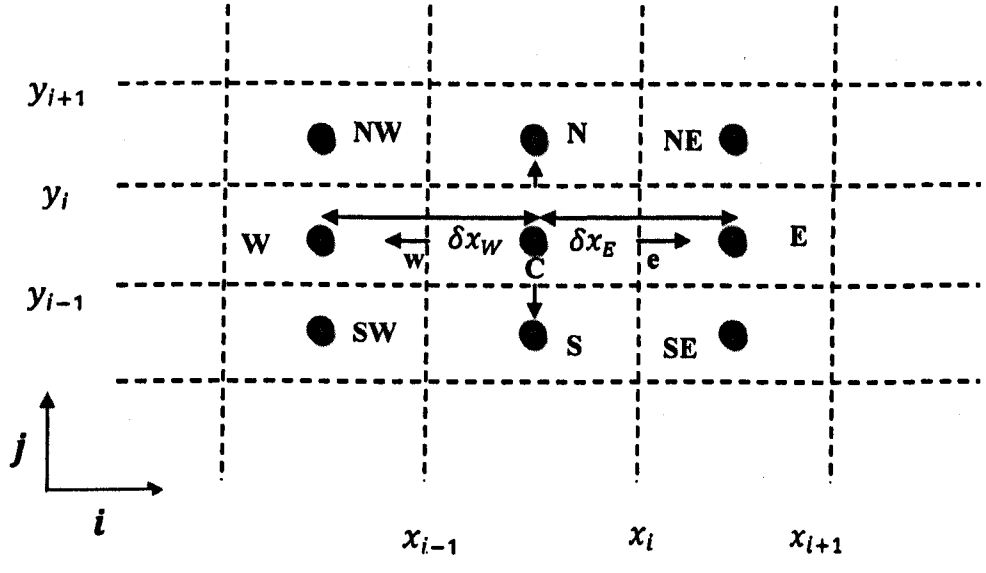

Figure 3-2 Computational cell and the neighburing control volumes

The general diffusive term presented in Eq. 3.2 can be discretised as on the above domain [36]:

$$\begin{cases} \dfrac{\partial}{\partial x}\left(\Gamma_\Psi \dfrac{\partial \Psi}{\partial x}\right) = S_\Psi \\ \left(\Gamma_\Psi \dfrac{\partial \Psi}{\partial x}\right)_E - \left(\Gamma_\Psi \dfrac{\partial \Psi}{\partial x}\right)_W = \int_W^E S_\Psi \, dx \\ \left(\dfrac{\Gamma_{\Psi E}(\Psi_E - \Psi_C)}{\delta x_E}\right) - \left(\dfrac{\Gamma_{\Psi W}(\Psi_C - \Psi_W)}{\delta x_W}\right) = \overline{S_\Psi}\Delta x \end{cases} \qquad 3.2$$

The diffusion term in y and z direction can be discretised similarly as presented in Eq. 3.2.

The discretisation example which is presented in Eq. 3.2 is a very simplistic case. More complex schemes depending on the flow condition and the simulation requirements can be adopted.

The source term in Eq. 3.2 is replaced with an average value, $\overline{S_\Psi}$. In more complex situations proper treatments are required for the source term [36]. One may also replace $\overline{S_\Psi}$ with the value of the source term at the cell centre, $S_{\Psi C}$. This is only accurate if the source term, follows a linear trend within the cell.

Determining the surface integrals

The overall flux for each cell is the summation of fluxes from all faces of that cell [36, 7].

$$\int_s J.n \; dS = \int_s J_n \; dS = \sum_i \int_{si} j \, dS = \sum_i \zeta_k \qquad 3.3$$

To calculate the fluxes on each cell, one needs to determine the approximate values using the quantities at the nodes. Therefore the face values should be approximated using the nodal values and the face integral should be determined using the approximated face values.

For example for finding the fluxes at face e, Figure 3.2, we may define the face value, ζ_k, using fixed cell value or average of cell vertexes or the combination of face centre and vertex values or by using the Simpson's rule, as in Eq. 3.4:

$$\begin{cases} \zeta_k = j_e S \\ \zeta_k = \frac{S}{2}(j_{ne} + j_{se}) \\ \zeta_k = \frac{S}{6}(j_{ne} + 4j_e + j_{se}) \end{cases} \quad 3.4$$

The flux j, in Equations 3.3 and 3.4 consists of two terms, the diffusive flux and the convective flux.

The diffusive flux integrals over the surface can be formulated as in Eq. 3.5

$$\begin{cases} \int_s \rho\Gamma_\Psi \frac{\partial\Psi}{\partial x}\, dS = \sum_i S_i \left(\rho\Gamma_\Psi \frac{\partial\Psi}{\partial x}\right) = \sum_i S_i (\Gamma_\Psi \rho)_i \left(\frac{\partial\Psi}{\partial x}\right) \\ \left(\frac{\partial\Psi}{\partial x}\right)_e = \frac{\Psi_E - \Psi_C}{x_E - x_C} \end{cases} \quad 3.5$$

It is also possible to find the values of the Ψ gradient on points E and C and then interpolate it to the face e [33].

The discretisation and surface integration of the convective fluxes can also be formulated as in Eq. 3.6:

$$\begin{aligned} \int_s \rho\Psi(U.n)\, dS &= \sum_i S_i (\rho\Psi U_n)_i \\ &= \sum_i S_i \Psi_i (\rho U_n)_i = \sum_i \Psi_i f_i \end{aligned} \quad 3.6$$

In Eq. 3.6 for convective fluxes, the main challenge is determining the Ψ_i, from the node values, proper interpolation and differentiation schemes are required to handle this.

The main functionality of the interpolation schemes is to determine the quantities of interest in different locations using the values at the nodes. A number of most widely used interpolation schemes are briefly reviewed here.

Central difference/Linear interpolation

The linear interpolation is probably the simplest approach and is base on the simple assumption of the linear variation of the values between two computational cell centres. Similar scheme exist in finite difference concept.

In the linear interpolation, naturally, the distance of each node from the target point change the significance of the effect of that node on the interpolated value, therefore the distance from each cell works as a weight function. Therefore for the sample computational mesh presented in Figure 3.2, in order to determine Ψ_e, the value at point e, using linear interpolation, Eq. 3.7 would be used:

$$\begin{cases} \Psi_e = (1-\delta_e)\Psi_C + \delta_e \Psi_E \\ \delta_e = \dfrac{x_e - x_C}{x_E - x_C} \end{cases} \qquad 3.7$$

Comparing Eq. 3.7 with the Taylor expansion for the linear Ψ variations at point C reveals that the expression in Eq. 3.7 is second order accurate. Since the numerical diffusion is taken out in Eq. 3.7, compared to the Taylor expansion, this scheme may result in oscillations in the result, however, due to the simplicity this scheme is very widely used [33].

The Taylor expansion is presented in Eq. 3.8:

$$\Psi_e = \Psi_C + (x_e - x_C)\left(\frac{\partial \Psi}{\partial x}\right)_C + \frac{(x_e - x_C)^2}{2}\left(\frac{\partial^2 \Psi}{\partial x^2}\right)_C + O(H) \qquad 3.8$$

Upwind scheme

The idea of upwind scheme is based on the fact that in a convection dominant flow the values at each point can be predicted using the upstream values. This means that the quantities are dominantly convected from the upstream cell to the target cell and the downstream cell has negligible effect on the target cell. For each computational cell, depending on the flow direction the left or right neighbouring cell could be the determining cell.

$$\begin{cases} \Psi_e = \Psi_C & if\ U_n > 0 \\ \Psi_e = \Psi_E & if\ U_n < 0 \end{cases} \qquad 3.9$$

The upwind method is very stable in simulations but comparing it with the Taylor expansion reveals that all terms of the Taylor expansion except the first term are eliminated therefore this scheme first order and is very diffusive.

The second term of the Taylor expansion which is neglected in upwind scheme shows diffusion like behaviour, $\Gamma_e \left(\frac{\partial \Psi}{\partial x}\right)_e$, and the coefficient of diffusion in this term is proportional to the distance of the cell centre and the target point, in other words it depends on the grid size, therefore, very fine mesh is required to keep this term small and avoid high numerical error.

Blended differencing/Self filtered centred scheme

This scheme is designed to hold the advantages of both upwind and central differencing. Therefore it is supposed to have the stability and boundedness of the upwind scheme as well as the accuracy of the central scheme. To achieve this, the blended scheme is formulated as a combination of both upwind and central differencing and there is a weighting factor, determining which scheme plays the dominant role from time to time.

$$\Psi_e = (1-\lambda_e)\Psi_{central\ difference} + \lambda_e \Psi_{upwind} \qquad 3.10$$

Therefore:

$$\Psi_e = \left[(1-\lambda_e)\, max(sgn(U),0) + \lambda_e \frac{x_e - x_C}{x_E - x_C}\right]\Psi_C + \left[(1-\lambda_e)\, max(sgn(U),0) + \lambda_e \frac{x_e - x_C}{x_E - x_C}\right]\Psi_E \qquad 3.11$$

When there is a sharp discontinuity in a flow λ_e should be unity or close to unity so that the scheme would be dominantly central differencing and when the flow is more uniform λ_e should be close to zero so that the upwind part of the scheme dominant. λ_e variations determines how much numerical diffusion is added to the system. These changes are required to achieve desirable result from the blended method. This is the main weak point of this scheme as a new nonlinear and Ψ depended parameter is added to the equations.

The above methods are for discretising the convection terms of the transport equations. Similarly, as a simple example is presented in Eq. 3.2, discretisation schemes have been developed for the diffusion schemes, based on the linear variation of the quantities. The diffusion terms discretisation and handling of the

accuracy level on non-orthogonal meshes is discussed with more details by Hrvoje Jasak [37].

Total variation diminishing scheme

The total variation diminishing (TVD) schemes were first introduced by Ami Haretn [38], and are designed to produce oscillation free flux limited schemes. The flux limited schemes are higher order compared to the first order schemes while the oscillations observed in normal second order schemes, such as central differencing, are removed.

To construct a TVD scheme first we need to determine the total variation of the solution as in Eq. 3.12

$$Total\ variation\ for\ \Psi = \mathrm{TV}(\Psi) = \sum_{f} |\Psi_E - \Psi_C| \qquad 3.12$$

E and C are the points around the face f.

A scheme is total variation diminishing if the following condition is satisfied:

$$\mathrm{TV}(\Psi^{t_{i+1}}) \leq \mathrm{TV}(\Psi^{t_i}) \qquad 3.13$$

In other words if the solution of the convection equation for the independent variable, Ψ, changes from time t_i to t_{i+1}, the total variation of Ψ which could be represented as $\int \left|\frac{d\Psi}{dx}\right| dx$ must satisfy the $\left(\int \left|\frac{d\Psi}{dx}\right| dx\right)^{t_{i+1}} \leq \left(\int \left|\frac{d\Psi}{dx}\right| dx\right)^{t_i}$ condition. The total variation diminishing condition in the discretised form reads: $(\sum_{i=1}^{N-1}|\Psi_{i+1} - \Psi_i|)^{t_{i+1}} \leq (\sum_{i=1}^{N-1}|\Psi_{i+1} - \Psi_i|)^{t_i}$ [141].

However, it is possible to maintain the TVD property and build higher order numerical schemes, this is achieved through incorporation of nonlinear functions, called limiters, to bound the solution of the independent variable, Ψ. Since these functions are intended to limit the gradients by modifying the fluxes, they are normally referred to as flux limiters [141]. The flux limiters only operate when sharp gradients and discontinuities exist in the domain. If the wave front changes

smoothly, the flux limiters would not operate and the space derivatives can be discretised using higher order schemes without nonphysical oscillations.

Source term

The source term in the transport equation, Eq. 3.1, needs special treatments. Any quantity in the transport equation which does not have the form of convection, diffusion or temporal varying term would be included in the source term. In Eq. 3.2 the source term is simply replaced by an average value over the computational cell. However, the source term is normally a function of Ψ and special treatment is required for that [36]. Since the system of equations is discretised to fit in a linear framework, the source term must be linearised as well. Linearising the source term is better than treating it as a constant term.

The linearised source term would be in the form of Eq. 3.14:

$$S_\Psi = S_T \Psi + S_c \qquad 3.14$$

The coefficients S_T and S_c may also be functions of Ψ, depending on the nature of the source term, in this case the S_T and S_c should be recalculated using the new values of Ψ. The linearization proposed in Eq. 3.14 must closely represent the relationship between S_Ψ and Ψ. Furthermore, the contribution of the source term must increase the diagonally dominance of the resulting matrix of coefficients. It is known as a rule [36] that the slope of the linearised source term, S_T, must be negative otherwise it could result in unacceptable values in the coefficients of discretised equations and lead to divergence. However, one can select different negative slopes for the source term. Steeper slopes would slow down the convergence and less steep slopes may fail to converge. The best slope is that of the tangent line to the given curve of the source term.

Integrating the linearised source term over the cell volume results in:

$$\int S_\Psi \, dV = S_T \Psi V_C + V_C S_c \qquad 3.15$$

So far the discretisation approach for convective, diffusive fluxes and the source term are briefly discussed, this involve determining the face values using the cell

centre values and discretising surface and volume integrals. For transient problems the values are changing with time and temporal discretisation is required to break the time unsteady term into discretised terms and since the time is a one way coordinate we should march in time starting from a given initial condition until the solution at target time is achieved.

Unsteady terms/temporal discretisation

Taking the integral of the general transport equation, presented in Eq. 3.1leads to:

$$\int_{t_i}^{t_{i+1}} \left[\frac{\partial}{\partial t}\left(\int (\rho\Psi)\, dV\right) + \int \nabla.(\rho U\Psi)\, dV + \int \nabla.(\rho\Gamma_\Psi \nabla\Psi)\, \mathrm{dV}\right] dt = \int_{t_i}^{t_{i+1}} \left(\int S_\Psi\, dV\right) dt \qquad 3.16$$

Substituting the convective and dissuasive terms from Equations 3.5, 3.6 and 3.15 results in the semi-discretised form as in Eq. 3.17:

$$\int_{t_i}^{t_{i+1}} \left[\left(\left(\frac{\partial \rho\Psi}{\partial t}\right)_c V_c\right) + \sum_f (\Psi S)_f (\rho U_n)_f + \sum_f (\Gamma_\Psi \rho)_f S.\left(\frac{\partial \Psi}{\partial x}\right)_f\right] dt = \int_{t_i}^{t_{i+1}} (S_T \Psi V_C + V_C S_c)\, dt \qquad 3.17$$

To convert the above equation into a fully discretised format, the convection and diffusion term can be substituted from the previously drived schemes but we leave them in their current format here and concentrate on the temporal discretisation. The target for the temporal discretisation is to find the value of Ψ at the next time step (time $(t_i + \Delta t)$ or t_{i+1}) by using the values at the current time (time t_i).

The first two terms of the Taylor expansion of $\Psi_{t_{i+1}}$ around t_i read as:

$$\Psi^{t_{i+1}} = \Psi^{(t_i+\Delta t)} = \Psi^{t_i} + \Delta t \left(\frac{\partial \Psi}{\partial t}\right)^{t_i} \qquad 3.18$$

By rearranging Eq. 3.18, the time derivative of Ψ can be formulated as:

$$\left(\frac{\partial \Psi}{\partial t}\right)^{t_i} = \frac{\Psi^{t_{i+1}} - \Psi^{t_i}}{\Delta t} \qquad 3.19$$

Therefore:

$$\left(\frac{\partial \rho \Psi}{\partial t}\right)_C^{t_l} = \frac{(\rho\Psi)_C^{t_{l+1}} - (\rho\Psi)_C^{t_l}}{\Delta t} \qquad 3.20$$

In order to determine the integral of the unsteady term we need to make an assumption about how the Ψ value is changing between times t_l and t_{l+1}, as in Eq. 3.21:

$$\int_{t_l}^{t_{l+1}} \Psi^{t_l}\, dt = [\lambda \Psi^{t_{l+1}} + (1-\lambda)\Psi^{t_l}]\Delta t \qquad 3.21$$

λ in Eq. 3.21 is a weighting factor which varies between 0 and 1 and determines how much role the current time and old time play in calculating the time integral [36].

If the value λ is taken as 0 the scheme would be fully explicit and it is equal to 1 the scheme is fully implicit. Taking λ equal to 0.5 leads to a well-known scheme called Crank-Nicolson which is formulated in Eq. 3.22 [36]:

$$\int_{t_l}^{t_{l+1}} \Psi^{t_l}\, dt = (0.5\Psi^{t_{l+1}} + 0.5\Psi^{t_l})\Delta t = \left(\frac{\Psi^{t_{l+1}} + \Psi^{t_l}}{2}\right)\Delta t \qquad 3.22$$

Now, substituting Eq. 3.20 into Eq. 3.17, using the Crank-Nicolson scheme and assuming the density is constant, the Eq. 3.17 can be written as:

$$\begin{aligned} &\frac{(\rho\Psi)_C^{t_{l+1}} - (\rho\Psi)_C^{t_l}}{\Delta t} V_C + \frac{1}{2}\sum_f \left(\Psi_C^{t_{l+1}} S\right)_f (\rho U_n)_f + \frac{1}{2}\sum_f \left(\Psi_C^{t_l} S\right)_f (\rho U_n)_f \\ &\quad - \frac{1}{2}\sum_f \left(\Gamma_{\Psi_C^{t_{l+1}}\rho}\right)_f S.\left(\frac{\partial \Psi_C^{t_{l+1}}}{\partial x}\right)_f - \frac{1}{2}\sum_f \left(\Gamma_{\Psi_C^{t_l}\rho}\right)_f S.\left(\frac{\partial \Psi_C^{t_l}}{\partial x}\right)_f \qquad 3.23 \\ &\quad = \left(S_T \frac{\Psi_C^{t_{l+1}}}{2} V_C + S_T \frac{\Psi_C^{t_l}}{2} V_C + V_C S_C\right) \end{aligned}$$

The discretised form of the transport equation, presented in Eq. 3.23 is second order in terms of accuracy. The cell and face values for previous and current time step are required for solving the above equation. The values $(\Psi_C\, S)_f$ and $\left(\frac{\partial \Psi_C}{\partial x}\right)_f$ also depend on the neighbouring cell values, therefore one can write the:

$$\begin{cases} a_C \Psi_C^{t_{i+1}} + \sum_N a_k \Psi_k^{t_{i+1}} = S_{\Psi C} \\ [A][\Psi] = [S_{\Psi C}] \end{cases} \quad 3.24$$

Therefore the Eq. 3.24 shows that $\Psi_C^{t_{i+1}}$ for every single cell depends on the Ψ in the neighbouring cells.

In Eq. 3.24 $[A]$ is the matrix of coefficients which has the a_C on the diagonal and a_k values on the other elements of the matrix. $[\Psi]$ is the matrix of Ψ values for all computational cells and the goal is to calculate it in the new time step. $[S_{\Psi C}]$ represents the vector for source term.

The coefficient a_C is a combination of all the coefficients coming from the convective, diffusive and temporal term for the cell at which $\Psi_C^{t_{i+1}}$ is being calculated and the a_k is the coefficient for the k^{th} cell which is sharing a face with the target cell.

The Crank-Nicolson scheme presented in Eq. 3.22 and Eq. 3.23 is known as unconditionally stable [36], this however, does not guarantee achieving physically realistic results regardless of the mesh size and the time step. Therefore one might observe oscillatory behaviour and physically unrealistic results using the Crank-Nicolson scheme. The stability however, implies that the oscillations will eventually disappear [36].

If we neglect the temporal variations of face values, as it has been common [36] the Eq. 3.23 would be reduced to:

$$\frac{(\rho\Psi)_C^{t_{i+1}} - (\rho\Psi)_C^{t_i}}{\Delta t} V_C + \sum_f (\Psi_C\, S)_f (\rho U_n)_f - \sum_f \left(\Gamma_{\Psi_C} \rho\right)_f S. \left(\frac{\partial \Psi_C}{\partial x}\right)_f = (S_T \Psi_C\, V_C + V_C S_C) \quad 3.25$$

In Eq. 3.25 if the face values are determined using the old time step the scheme would be called Explicit and is equivalent to the situation where f is equal to zero in Eq. 3.21 and if the face values are determined using the new time step the scheme would be called Euler Implicit and is equivalent to the situation where f is equal to 1:

$$\begin{cases} a_C \Psi_C^{t_{i+1}} + \sum_N a_k \Psi_k^{t_i} = S_{\Psi C} \rightarrow Explicit \\ a_C \Psi_C^{t_{i+1}} + \sum_N a_k \Psi_k^{t_{i+1}} = S_{\Psi C} \rightarrow Implicit \end{cases} \quad 3.26$$

Expanding the Eq. 3.26 shows that a_k coefficients has to be positive otherwise an increase in Ψ in the neighbouring cells would have negative effect on the Ψ value in the target cell.

From the Equation 3.26 it is clear that in explicit scheme the value of Ψ at the new time step only depends on the values at the old time step, therefore there is no need to form the matrix of equations as presented in Eq. 3.24 and solve the resulting set of algebraic equations. This makes the explicit scheme much simpler and more effective in terms of computational cost; however the explicit method is limited by the Courant–Friedrichs–Lewy (CFL) condition.

The CFL condition

The CFL condition requires that if there is a flow which is travelling across a discrete spatial grid and we are willing to numerically compute the flow on a discrete time step, then the time step must be smaller than the time that takes for the flow to travel the length of the spatial grid. The CFL condition can be formulated as:

$$Co = \frac{u\Delta t}{\Delta x} \leq 1 \quad 3.27$$

The term introduced in Eq. 3.27 is called the Courant number and is an important limiting factor in explicit CFD calculations.

For three dimensional geometries where there is the spatial discretisation in 3 direction of the coordinate system, the Courant number and CFL condition can be expressed using the Eq. 3.28:

$$Co = \left[\frac{u_x\Delta t}{\Delta x} + \frac{u_y\Delta t}{\Delta y} + \frac{u_z\Delta t}{\Delta z}\right] \leq 1 \quad 3.28$$

Enforcement of the CFL condition is a necessary measure but does not guarantee the convergence and quality of the results.

3-2 Boundary and initial conditions

Discretising the computational domain results in a number of computational cells which are placed at the domain boundaries. On the boundary-facing side, the cells do not host shared faces with other computational cells. This may not look restricting at the beginning but reviewing Eqs. 3.5 to 3.11 as well as Eq. 3.24 shows that for each cell the diffusive and convective terms depend on the values at the neighbouring cells and for the cells at the boundaries there is no neighbouring cell at the boundary side, therefore special treatments are required to pass the information from the boundaries to associated cells and keep the required data set complete. The provided boundary information must represent the physical behaviour of system as closely as possible to the real situation.

Generally, the boundary conditions can be categorised as either physical boundary conditions or numerical boundary conditions. There two types of numerical boundary conditions; the first type specifies the values at the boundaries directly and is called the Dirichlet boundary condition. The second numerical boundary condition specifies the gradients of variables at the boundaries and is called the Von-Neumann boundary condition. The Dirichlet condition is straight forward to use in the discretised equations because the Ψ value is given, whereas in Von-Neumann condition only the flux for Ψ is given and an extra equation for Ψ must be constructed by integrating the differential equation over half of the first computational cell at the vicinity of the boundary [36].

The physical boundary conditions are associated with the physical state at which the system is being held, such as wall, outlet, symmetry plane, inlet, etc. For each physical boundary condition a set of numerical boundary conditions can be used to describe each variable at that boundary, for example in a flow, for a wall boundary at no-slip condition the Dirichlet condition applies to the velocity (zero-velocity at the wall) and at the same time we may have fixed heat flux (the temperature gradient at the wall is given) which is a Von-Neumann condition for the temperature variation at the wall-flow interface.

Here some of most widely used physical boundary conditions are briefly explained:

Wall/no slip boundary

The wall boundary condition imposes fixed value for the velocity and fixed gradient for the pressure at the wall surface. As it is evident from the physics of a solid wall in a flow, there would be no flux passing through the wall, furthermore the fluid layers right at the wall surface are attached to the wall due to viscous forces between the fluid and the wall. This means that the fluid velocity at the wall surface is exactly the same as the velocity of the wall itself. In most practical cases stationary walls exist in the domain which means zero velocity in all directions should be imposed on the flow. Zero gradient pressure condition is also imposed on the flow in case of wall boundary which is consistent with the physics of a fluid flowing over a wall.

Inlet boundary

The inlet boundaries are mostly constructed on the basis of a priori known flow velocity at the inlet. Therefore fixed velocity at the inlet would be impost and to keep the physical consistency zero gradient condition should be used for the pressure.

Outlet boundary

For the outlet boundary condition it is crucial to make the adjustments so that the total mass of the system is kept constant. This can be done by adjusting the outgoing flow velocity. The velocity adjustment should guarantee the conservation of mass in the system, while the pressure is kept at zero gradient condition. However, this may cause instabilities where there are local inflows at the outlet boundary.

The more convenient approach for determining the outlet boundary condition is using the fixed value pressure at the outlet; this condition, in most practical cases, is a physically valid assumption meaning that the flow pressure right at the outlet would be equal to the ambient pressure. The zero gradient condition would be applied to the velocity in this case and the pressure Equation enforces the conservation of total mass for the system [37].

Symmetry plane boundary

The symmetry plane boundary condition is applicable to the cases where there is an axisymmetric condition in the geometry leading to the possibility to model only half of the domain and mirror the results to the other half, which can cause considerable reduction in computational cost.

The symmetry boundary can be interpreted in numerical form as a situation in which the normal components (with respect to the boundary plane) of the parameters gradients are equal to zero, whereas the tangent components of the gradients are mirrored from inside to the outside of the domain [37].

3-3 Solution of the resulting algebraic Equations

So far different techniques for discretising the transport equations are briefly reviewed in previous sections. The discretisation procedure is aimed at linearizing the highly non-linear governing equations over a discretised computational mesh, which results in a set of algebraic equation. These equations can be formulated as in Eq. 3.24 and solved either by a direct approach or an iterative procedure.

The direct method is suitable for finding the solution of relatively small sets of equations but the number of computational operations increases dramatically with number of equations consequently the direct method is not feasible for large systems of equations.

The iterative method starts the solution with a guess for the result and in an iterative procedure keeps improving the initial guess until it converges to the actual solution. A predetermined tolerance for the solution is used as a criterion to determine when the convergence is achieved and no more iteration is required.

In contrast to direct method the iterative methods are much easier to extend to larger systems, they can also preserve the sparseness of the coefficient matrix, as it is the case in most of CFD problems and it significantly reduces the occupied memory and computational cost, therefore the iterative approach is the suitable choice for CFD problems.

To have an effective iterative solution and smooth convergence the matrix of coefficient must be diagonally dominant. This means that the element on the diagonal of the matrix must be larger than the summation of other elements on the corresponding row or column.

This condition can be expressed as:

$$|a_C| > \sum_N |a_k| \qquad 3.29$$

Higher diagonally dominance results in better convergence therefore it would be helpful to alter the source term linearization, as in Eq. 3.14 in a way that the S_T gets a negative value and consequently increases the $|a_C|$ in the Eq. 3.29. Although the diagonal dominance of matrix would help better convergence, it does not guarantee convergence of the solution.

While the discretisation of convective and diffusive term usually weakens the diagonal dominance, the discretised temporal term only contributes to the source and diagonal terms and increases $|a_C|$. It has actually been observed in practice that only the linear parts of the source term and the temporal term make a positive contribution to the diagonally dominance of the system.

Under relaxation

When dealing with steady state problems the temporal terms do not exist in the system therefore their positive contribution is absent therefore extra treatments are required to compensate this and increase the diagonal dominance of the system. Using the under relaxation factor is widely used approach to achieve this.

This is done via adding an extra term to both sides of the equations. This term is a fraction of the diagonal elements of the matrix from the previous iteration. Applying this to Eq. 3.24 results in:

$$\left[\left(\frac{1-\alpha}{\alpha}\right) a_C \Psi_C^{t_{i+1}}\right] + a_C \Psi_C^{t_{i+1}} + \sum_N a_k \Psi_k^{t_{i+1}} = \left[\left(\frac{1-\alpha}{\alpha}\right) a_C \Psi_C^{t_i}\right] + S_{\Psi C} \qquad 3.30$$

Simplifying Eq. 3.30 leads to:

$$\frac{a_C}{\alpha}\Psi_C^{t_{i+1}} + \sum_N a_k \Psi_k^{t_{i+1}} = \left[\left(\frac{1-\alpha}{\alpha}\right) a_C \Psi_C^{t_i}\right] + S_{\Psi C} \qquad 3.31$$

The $\Psi_C^{t_i}$ is the value at the previous iteration and the α is the under relaxation factor and its value varies between 0 to 1, $(0 < \alpha < 1)$.

α can not take the zero value because it leads to the division by zero error and unity α is equivalent of no relaxation condition. Smaller α values impose stronger relaxation to the system leading to slower but more stable convergence. A proper value which results in stable convergence while having reasonable convergence speed may be achieved by try and error as there is no standard procedure to determine best relaxation factor and it varies from case to case.

3-4 Numerical error

The computational solution of the transport equations over a discretised domain results in some errors associated with the discretisation process. These errors can be categorised as the Equation discretisation errors and domain discretisation errors.

Earlier in Eq. 3.8 and Eq. 3.18, the Taylor expansions of the temporal and spatial terms are presented explaining the essence of eliminating higher order terms of the Taylor expansion to derive the Equation discretisation schemes. For example the upwind scheme only keeps the first term of the Taylor expansion and the central scheme keeps the first two terms of the Taylor expansion and the rest of the terms are eliminated. Although the eliminated terms are quite smaller in magnitude compared to the remaining terms, they still introduce an error to the system of the equations compared to the exact solution of the equations.

The second source of error in CFD comes from domain discretisation and is directly linked to the computational mesh quality. Low resolution, high aspect ratio, non-orthogonality, high skewness, etc are all considered as computational mesh flaws which can result in generation of large computational errors. Generating a high quality mesh is one of the biggest challenges in the numerical simulations as the target is to generate low aspect ratio, low skewed and uniform mesh as well as imposing high resolution at the areas of interest while keeping the total number of

cells as low as possible to achieve affordable computational cost. Achieving all these at the same time may seem out of reach at some cases but an experienced user usually can manage to impose all these criterions effectively. Therefore the mesh generation concept needs extra care and it has direct effect on the reliability of the results.

The computational mesh can be either in structured form, meaning that the grid points are created from intersection of group of well ordered lines. For a 3D mesh each grid point is generated from the intersection 3 different lines whereas in 2D the 2 lines intersecting form the grid point. In contrast the unstructured mesh is made of arbitrary control volumes (computational cells) which share faces one with another and cover the whole domain but the lines forming the grid points do not follow any specific pattern and can go in any direction to make the mesh consistent.

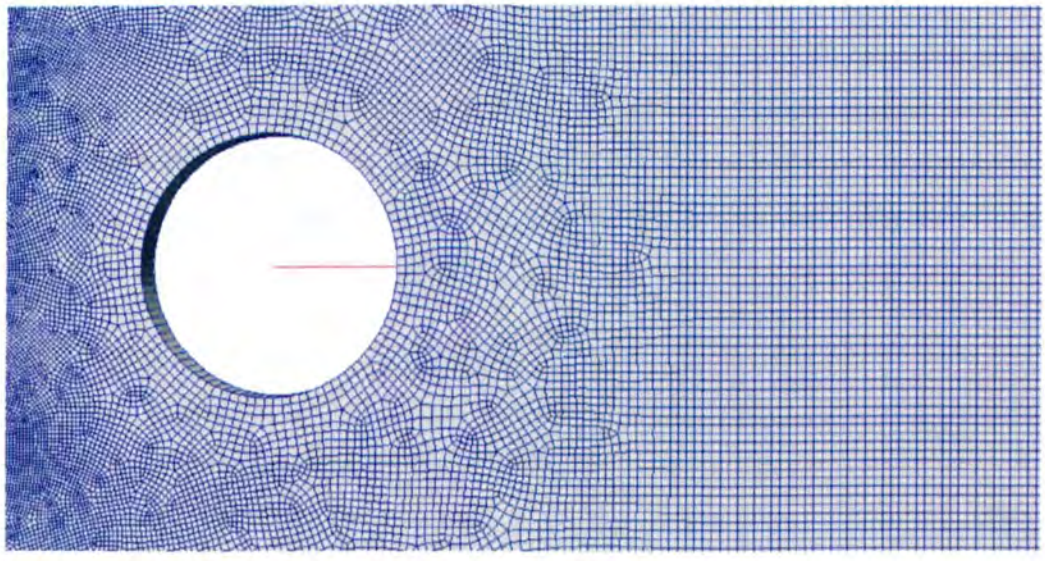

Figure 3-3 Example of structured (right side) and unstructured (left side) computational mesh

Figure 3-3 shows example of structured and unstructured mesh at a single domain, in the right side of the domain the mesh is formed by well ordered lines whereas in the left side arbitrary volumes pave the domain.

Both structured and unstructured, as long as they have enough resolution and low aspect ratio, non-orthogonality and skewness are suitable and produce negligible discretisation error.

The discretisation schemes presented so far which are mainly used in the rest of this work are at maximum second order accurate. Achieving higher order schemes in finite volume approach is challenging and difficult to implement due to numerical difficulties, whereas in finite difference approach higher order schemes are much easier to build, therefore higher mesh resolution may be required to reduce the numerical error and compensate limitations of the order of accuracy in finite volume discretisation schemes.

3-5 Adaptive mesh refinement (AMR)

The idea of using adaptive mesh refinement is mainly driven by the desire to keep high grid resolution at regions of interest, while keeping low resolution at other places to make the computations affordable in terms of time and cost. The regions of interest are mainly the places where sharp gradients exist in the field quantities such as the flame fronts, shock waves and boundary layers. In transient problems the high gradient regions move from one location to another while the process is progressing, therefore it would be impossible to use a fixed mesh with high resolution and achieve cost efficiency at the same time

An adaptive grid automatically rearranges the grid spacing and breaks down the coarser grid to finer ones based on the solution of the flow field. This means that a mesh manipulation algorithm is fitted in the solver and linked to the solution at every time step. The flow field at each time step is then analysed by the AMR function and the regions with high gradients of pressure, temperature, velocity etc. are marked for resolution enhancement. As an example, one needs to keep at-least 10-20 grid points across the half reaction length to resolve the detonation front; this would generate a grid size of about 20 micron for hydrogen detonation which is unaffordable in most scenarios, whereas a AMR solver can track the detonation front (associated with high pressure gradient) and keep high resolution there while having much lower resolution elsewhere. The solver should be capable of reversing the procedure by merging the fine grids and making coarse ones when it is viable to reduce the resolutions in regions which were refined before but no longer contain any high gradients as the simulation progress.

When bigger computational cells are broken to smaller ones the surface areas between the cells are changing as a result the fluxes keep changing and a well developed AMR algorithm must re-calculate the fluxes at the manipulated regions after each time the refinement or coarsening takes place.

Adaptive mesh refinement capability is developed and impalement in OpenFOAM solver for the present work. Figure 3-4 shows an example of the flame propagation at the vicinity of solid walls. The image illustrates how the solver tracks the flame surface and refines the mesh in regions with high temperature gradients.

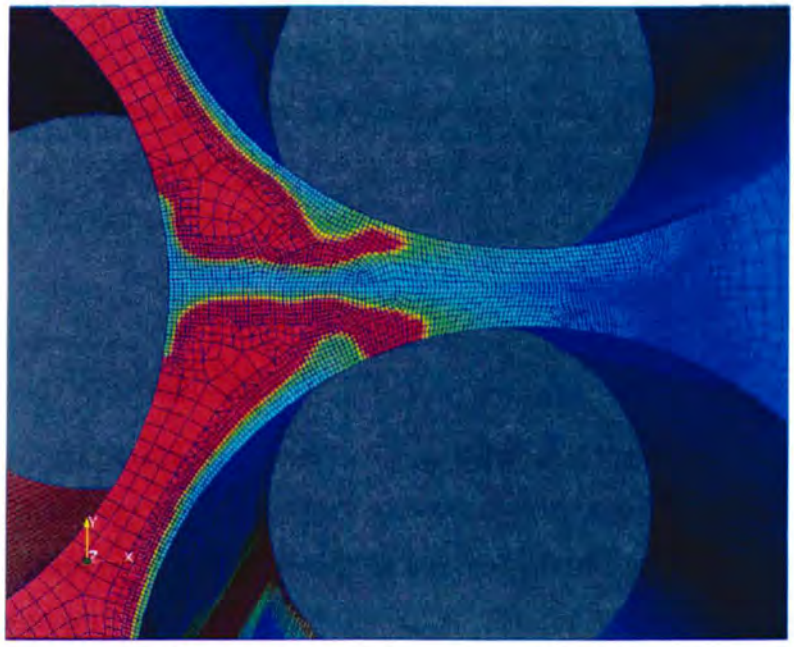

Figure 3-4 Adaptive Mesh refinement algorithm employed in deflagration simulations, the solver automatically tracks the flame surface and refines the mesh there.

The AMR technique implemented in the present work can carry out two levels of refinement meaning in 1-D, a grid spacing would be refined into 4 new grids while in 2-D each computational cell would be divided into 16 new cells and in 3-D each cell would be refined to 64 new computational cells. This is schematically shown in Figure 3-5.

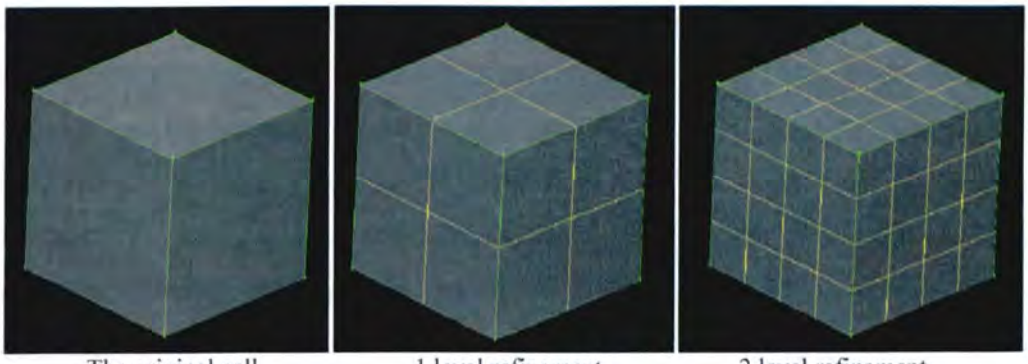

The original cell 1 level refinement 2 level refinement

Figure 3-5 Two level mesh refinement in 3D

From Figure 3-5 one can imagine that the solver can use an initial mesh which is 64 times coarser and still achieve the same resolution and quality. Therefore the employed AMR technique adopted here could potentially reduce the computational cost by 64 times in 3-D simulations. However in reality the extra load imposed by the AMR function and the increase in the number of the grids at the refined areas makes this ratio smaller. But still the computational efficiency would be increased by more than 30-40 times in most case.

3-6 Numerical viscosity

As previously mentioned, the numerical error which is a result of truncating higher order terms in the Taylor series expansion of the discretised term, can be regarded as numerical diffusion. This is mainly because the truncated term behaves like numerical viscosity in the equation. From Eq. 3.8, the second order term, which would be eliminated in the discretisation, reads as:

$$\frac{(x_e - x_C)^2}{2}\left(\frac{\partial^2\Psi}{\partial x^2}\right)_C = \Gamma_{\text{err-c}}\left(\frac{\partial^2\Psi}{\partial x^2}\right)_C \qquad 3.32$$

Eq. 3.32 shows that the first eliminated term in a second order scheme has the characteristics of a diffusive flux, this is also referred to as false diffusion [36], As a result, the numerically discretised form of the equations slightly differ from the original partial differential equations because of the extra numerically added viscosity. However, in ILES approach, the numerical diffusion is used to compensate the sub-grid scale effects.

One should keep in mind that numerical diffusion happens when the direction of the flow is parallel to the direction of cell normal vector, the magnitude of the numerical diffusion can be reduced by using a fine grid and trying to keep the cell surfaces perpendicular to flow direction. In fluid flow the numerical viscosity is small compared to the physical viscosity. Central differencing produces very low numerical viscosity, consequently, unrealistic results may be produced, especially at high Peclet numbers [36].

3-7 Flow field simulations

So far the discretisation of the transport equation for a general variable, Ψ, is briefly discussed. However the flow field (velocity and density fields) was assumed to be priori determined, whereas in CFD problems the velocity and density fields are a part of the solution and cannot be determined without solving the whole set of the coupled governing equations.

3-7-1 Discretisation of the Navier-Stokes Equations

For the fluid flow problems, as mentioned earlier, the Navier-Stokes Equations including the conservation of mass, momentum and energy are the governing equations. Discretising the Navier-Stokes Equations in a way which is appropriate for an iterative solution procedure is rather more complex compared to the simple case of a single transport equation. Therefore we shall start with the incompressible case for the sake of simplicity. The flow governing equations for an incompressible flow are:

$$\begin{cases} \nabla . U = 0 & \rightarrow \quad mass\ conservation \\ \dfrac{\partial U}{\partial t} + \nabla . (UU) = \nabla . (\nu \nabla U) - \nabla p & \rightarrow \quad momentum\ conservation \end{cases} \qquad 3.33$$

The main issues in the above equations are the coupling of pressure and velocity in the momentum Equation as well as the nonlinearity.

The convection term $\nabla.(UU)$, represents the convection of velocity by velocity and the resulting algebraic Equation from its discretisation is a quadratic nonlinear term. Discretisation of the velocity convection term reads as:

$$\nabla.(UU) = \sum_f S(U)_f(U)_f = \sum_f F\ (U)_f = a_C U_C + \sum_k a_k U_k \qquad 3.34$$

In Eq. 3.34 the parameters a_k, a_C and F are functions of U as well. The main difficulty is due to dependence of the flux, F, to the velocity which makes the resulting equations highly nonlinear. The nonlinear solution methods are complex and computationally heavy especially for large sets of equations. Therefore it is worth to take the linearization approach and try to solve the linearised equations.

For linearising the $\nabla.(UU)$ term, it is required to use the consistent flow field (satisfying the continuity Equation) at the current time step to determine the parameters a_k, a_C and F.

The above measure would not make any problem for steady state problems as the lag in the flow field used in the nonlinear term would be insignificant when the convergence is achieved, however for the transient problems one could either neglect this lag or take an iterative approach on the nonlinear term until it is fully corrected. The corrective approach may cause significant increase in computational cost especially when the time step is large because the flow field would have a large lag over a longer time step. Therefore, if for a case it is required to fully resolve the temporal space, meaning a very small time step is used, the difference in flow field from one time step to the next one would not be significant and ignoring the flow field lag can produce satisfactory results as well as significant cost reduction compared to corrective approach.

In the present study the SIMPLE algorithm, proposed by Patankar [36] is used for steady state and the PISO algorithm, proposed by Issa [40], is used for handling the transient problems. The details of these algorithms will be discussed briefly, but at first we need to study the pressure velocity coupling and derive the pressure Equation.

3-7-2 Pressure Equation

The partially discretised from of the momentum Equation which is presented in Eq. 3.35 can be used to derive the pressure Equation:

$$a_C U_C = H(U) - \nabla p \qquad 3.35$$

Eq. 3.35 is derived from the integral form of the momentum Equation and the pressure gradient term is not discretised at this stage.

The $H(U)$ term is made of two term, first is the source term from the temporal term and the other source term, the second part includes the product of the matrix of all neighbouring cell coefficients and the corresponding velocities:

$$H(U) = \frac{U^0}{\Delta t} - \sum_k a_k U_k \qquad 3.36$$

Discretising the incompressible form of the continuity Equation results in:

$$\nabla . U = \sum_f S . U_f = 0 \qquad 3.37$$

U_C can be extracted from Eq. 3.35:

$$U_C = \frac{H(U)}{a_C} - \frac{\nabla p}{a_C} \qquad 3.38$$

Eq. 3.38 represents the velocity at cell centre, point C, however the surface velocities can be derived from surface interpolations:

$$U_f = \left(\frac{H(U)}{a_C}\right)_f - \left(\frac{\nabla p}{a_C}\right)_f \qquad 3.39$$

The velocity obtained in Eq. 3.39 will be used to determine the fluxes.

Substituting Eq. 3.39 into Eq. 3.37 results in the pressure Equation:

$$\nabla . \left(\frac{\nabla p}{a_C}\right)_f = \nabla . \left(\frac{H(U)}{a_C}\right)_f = \sum_f S . \left(\frac{H(U)}{a_C}\right)_f \qquad 3.40$$

The discretised form of the Navier-Stokes Equations can be expressed in the following form:

$$\begin{cases} a_C U_C = H(U) - \sum_f S(p)_f p & \rightarrow momentum\ equation \\ \sum_f S.\left(\frac{\nabla p}{a_C}\right)_f = \sum_f S.\left(\frac{H(U)}{a_C}\right)_f & \rightarrow\ pressure\ equation \end{cases} \quad 3.41$$

The fluxes at the cell faces can be obtained from:

$$F = S.U_f = S.\left[\left(\frac{H(U)}{a_C}\right)_f - \left(\frac{\nabla p}{a_C}\right)_f\right] \quad 3.42$$

3-7-3 Velocity-pressure coupling

The final discretised form of the Navier-Stokes Equations presented in Eq. 3.41 shows that the velocity is a linear function of the pressure and pressure is also a function of the velocity. This coupling between pressure and velocity makes the situation more complex and needs extra measures.

The most efficient way for handling the coupling problem is called segregated approach. Among the segregated approaches the PISO algorithm by Issa [40] and SIMPLE by Patankar [36] are most widely used and will be discussed and used in this thesis.

3-7-4 SIMPLE algorithm

For steady state problems it is not required to fully resolve the velocity-pressure coupling because the changes from one iteration to the next is not small any more, meaning the effective time step is quite large compared to transient cases and the nonlinearity has a higher significance. The SIMPLE algorithm, proposed by Patankar [36], is believed to be very efficient and the most widely used algorithm for handling the velocity-pressure coupling in steady state situations. SIMPLE stands for "Semi-Implicit Method for Pressure Linked Equations" and the algorithm consists of the following steps:

- The pressure field from previous iteration or an initial guess for the pressure field (only for the first iteration) is used to solve the momentum Equation, presented in

Eq. 3.41, and obtain a prediction of the velocity field. At this stage under-relaxation factor for velocity is used to smoothen the velocity convergence.

- The pressure Equation, presented in Eq. 3.41, is solved to find a new prediction of the pressure field.

- Using Eq. 3.42 the new fluxes are calculated. The transport equations for other parameters which might have any effect on the flow filed are solved.

- The pressure Equation must be solved again while taking into account the nonlinear effects because they are much more significant compared to transient situation, therefore, the term $H(U)$ is updated using the latest update for pressure and used to update the pressure field again. The pressure correction procedure is based on the following formulation [35]:

$$p^n = p^O + \alpha_p(p^p - p^O) \qquad 3.43$$

p^n, p^0, p^p and α_p are the latest prediction of pressure for using in the momentum Equation, previous prediction of pressure used in the momentum Equation, pressure prediction obtained from the pressure Equation and the pressure under relaxation factor respectively.

- The velocities are calculated explicitly using Eq. 3.38 before solving the momentum Equation again.

3-7-5 PISO algorithm

PISO stands for "Pressure Implicit with Splitting of Operators" and was first proposed by Issa [40] to handle the pressure velocity coupling in the transient form of Navier-Stokes Equations.

The PISO algorithm consists of the following steps:

- The pressure field from the previous time step is used to solve the momentum Equation as the first step. This step provides a prediction of the new velocity field by solving Eq. 3.41 and substituting the pressure field from the previous, therefore it is called the momentum predictor.

- The predicted velocity from the momentum predictor is used to update $H(U)$ and solve the pressure Equation to predict the pressure at the current time step. Therefore this step is known as the pressure solution.

- Using the new pressure and Eq. 3.42 the fluxes are calculated. The velocity field is corrected based on the new pressure field obtained at previous step. Correction of the velocity is done explicitly by using Eq. 3.38 this means that only the updated pressure term in Eq. 3.38, $\frac{\nabla p}{a_C}$, is used for the correction and the influence of the updated neighbouring velocity, $\frac{H(U)}{a_C}$, is neglected in the correction.

- In previous step it is assumed that all the velocity error is due to the pressure term which is not correct, therefore the $H(U)$ term must be updated to correct the pressure Equation and repeat the whole procedure until a priori determined tolerance is achieved.

To put it in simple words, the PISO algorithm is made of one implicit velocity predictor as well as a series of pressure correction and explicit velocity corrections which are iterated until the error goes below the tolerance. During this procedure, the coefficients in $H(U)$ can be updated due to the new fluxes (each time the pressure is corrected) but the effect is assumed to be negligible and the $H(U)$ coefficients are only updated during momentum prediction step.

3-7-6 Solution algorithm

Having introduced the PISO and SIMPLE algorithms, it is now possible to present the step by step solution procedure for steady state and transient problems.

For an incompressible steady state flow the steps by step solution can be summarised as:

1- Define the initial conditions for all the parameters.

2- Solve the momentum predictor for the time step the loop is in (it would be [0+Δt] for the first iteration).

3- Update the pressure field using the pressure field solution and proper under relaxation as presented in Eq. 3.43.

4- Update the velocity field explicitly

5- Solve the transport Equations for other parameters using the obtained pressure and velocity fields from the previous steps and a proper under relaxation.

6- If the target tolerance is not achieved go to step 2.

The procedure for the transient problems is different as there is time marching and convergence is achieved in every time step. The solution step for transient solutions based on PISO algorithm can be summarised as:

1- Define the initial conditions for all the parameters.

2- Solve the momentum predictor for the time step the loop is in (it would be [0+Δt] for the first iteration).

3- Iterate the PISO loop until the target tolerance for pressure and velocity is achieved, then updated the fluxes for the current time step.

4- Update the turbulence properties based on the obtained flow fields at the step 3.

5- If the current time is smaller than the end time for the solution go to step 2.

3-8 OpenFOAM

The OpenFOAM (Open Field Operation and Manipulation), is an open source and object-oriented CFD toolbox [35] that contains several CFD functions and classes that can be used to create new continuum solvers.

The main package of OpenFOAM contains some solvers for chemical reactions, turbulence and heat transfer, solid dynamics, electromagnetic [35]. All these solvers are created using several function and classes that are available in the main source.

The CFD parts of OpenFOAM are based on finite volume numerical approach. During past few years OpenFOAM users has been increased dramatically and

thousands of researchers are involved in research developments by this toolbox. The available solvers for combustion simulation in OpenFOAM can be used to simulate simple phenomenon such as low speed deflagrations and simple laminar and turbulent flames. However, to simulate more complex phenomenon like high-speed deflagrations and detonations, new solvers must be developed.

OpenFOAM can be called a high-level and advanced programming language that is specifically developed for computational fluid dynamics. In simple programming languages the developer has access to some mathematical operators such as add, subtract, power..., however OpenFOAM users have access to high-level operators like, divergence, gradient, laplacian,... this way developers can create more efficient and reliable solvers in shorter time. The object-oriented structure of OpenFOAM helps the developers to follow a very organized and standard pattern in their code developments.

Weller et al. [59-61] provided good insight to the main code structure and abilities.

Considering the benefits of using such a powerful package as the base of a research work, the author of the current work, used OpenFOAM toolbox to develop CFD solvers for simulating different combustion regimes and specially the DDT phenomenon.

Chapter 4

Numerical Simulation of Turbulent Deflagrations

The most common scenario in DDT related studies is based on ignition of a reactive mixture by a spark which leads to an initially low speed and laminar flame, after a short period of time due to the interaction of this laminar flame with obstacles and walls, the flame surface become distorted and wrinkled and the flame becomes turbulent. These wrinkling in the flame surface increases the flame surface area so the energy release per unit volume and flame speed both increase, these in turn cause more distortion in the flame surface. This positive feedback continues and the flame accelerates. The accelerating flame generates several pressure waves which propagate through the mixture. When the pressure waves hit the walls, obstacles and possibly closed ends of the tube, they are reflected and travel back towards the flame. The interaction of these reflected pressure or shock waves with the flame induce even more turbulence in the flame and further increases the rate of energy release and flame speed. In case of sustained influence of these mechanisms, the flame continues to accelerate up to the point at which there is a very high speed flame with several local auto explosions and hot spots. Such a high speed deflagration can precondition the reactive mixture in a way that transition from the high speed deflagration to detonation can occur.

As it can be seen from the above explanation, to study DDT one needs to study, laminar flame, turbulence inducing mechanisms, turbulent flame, flame acceleration [75-77], transition mechanisms and detonation wave. Therefore DDT simulation covers a wide range of combustion waves at which different physical mechanisms are dominant and the propagation mechanism is completely different in some cases. Therefore a numerical code which is expected to simulate this phenomenon should be developed and tested very carefully so that it can cover all these ranges of combustion. For example in laminar and low speed deflagration the pressure changes across the flame are negligible but in detonation an abrupt and large change in the pressure exists across the detonation wave. The mechanism of deflagration propagation is diffusion of heat and reactive radicals toward unburned mixture, but detonation propagates due to shock-heating up to the auto ignition point. All these differences should be studied, investigated and applied carefully to the numerical work to assure a reliable result.

In this chapter, turbulent deflagrations are studied numerically as a first step towards a reliable simulation of DDT phenomenon.

4-1 Governing Equations for Laminar premixed deflagrations

Governing Equations for deflagrations are fully compressible Navier-Stokes Equations that are usually written in the conservation form. Earlier in chapter 2 standard and simplified forms of these equations are presented [43-47].

In the numerical solution of the Equations 2.30 to 2.33, depending on the combustion regime some terms might be either neglected or modelled to reduce complexities and solution time.

Laminar flames are the most basic combustion regimes that are simulated by these equations in the literature [43-47].

4-2 Deflagration propagation mechanism

The starting point for most combustion phenomena is a laminar propagating deflagration which is triggered from an ignition point. Laminar flames are also considered as "elementary building blocks of turbulent flames" [43], especially for development of more complex models such as flamelet models for turbulent flame simulations.

The propagation of low speed deflagration is dominantly controlled by diffusion of heat and mass. The flame front in low speed deflagration waves can be divided into two layers; the first layer which is the front layer of the flame is the preheated zone and is dominantly controlled by mass and heat diffusion. The second layer is a very thin reaction zone in which sequences of chain branching reactions take place leading to substantial energy release. This whole process can be simulated using Equations 2.30 to 2.33 provided that a proper reaction mechanism is employed. Due

to the complexities involved there is no analytical solution for the deflagration problems. Under some specific conditions some simplifications may be done to derive semi-analytical solutions. However this is limited to very simple cases with no practical application. In almost all engineering problems, numerical computation is the only plausible approach.

Practically, across the reaction zone a very sharp gradient of temperature and species concentration, as presented in Figure 1, is formed which results in numerous difficulties in experimental and numerical studies of this region. Due to very sharp jump of properties across a very short distance, it is hard to observe and record the details in practice and it is also difficult to resolve the process in numerical investigations. However, the pressure variations across the flames are mostly negligible as long as the deflagration wave is in low speed phase.

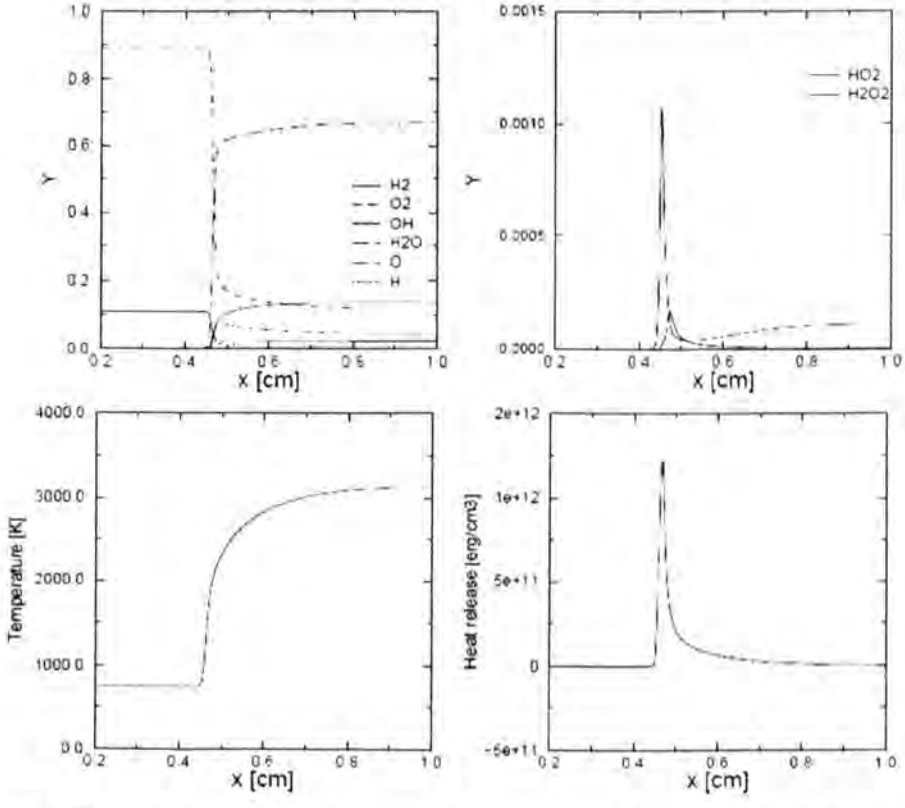

Figure 4-1 Computations of one-dimensional premixed stoichiometric H_2-O_2 laminar flame using PREMIX code, reproduced from [43].

The other difficulty associated with flame simulations lies in the large difference in the time scales involved. The time scales associated with the flow dynamics are generally considerably larger than the reactions time scale, making it difficult to resolve flow dynamics and reactions in the same time marching process. This is

often referred to as the reaction stiffness problem. To overcome such problems and the associated difficulties with simulation of turbulent flames, several simplified models are proposed and successfully used in the past.

An example of laminar spherical flame propagation simulated using a flame model is presented in Figure 4-2. The Figure shows temperature field for a flame propagating from an ignition centre (in the front corner of the domain) that is simulated by using a flamelet model. Since the geometry is symmetric, only $\frac{1}{8}$ of the domain is modelled to reduce the solution time.

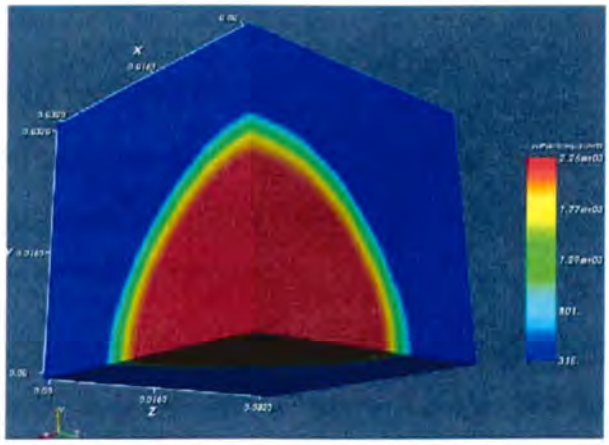

Figure 4-2 Temperature field in spherical laminar flame propagation, $\frac{1}{8}$ of domain.

This case is solved for propane-air mixture in stoichiometric mixture and standard condition. The obtained flame temperature is in agreement with propane flame temperature [48].

A laminar flame reaches a constant moving velocity (when the flame is steady and before the flame acceleration process starts). In this situation, Eq. 2.30 can be

$$\rho u = \rho S_u = Constant \qquad 4.1$$

simplified to Eq. 4.1 [43]:

where S_u is the laminar flame speed.

Another insightful formula for laminar burning velocity can be obtained by simplifying species and energy conservation equations [43]:

$$\begin{cases} \rho_1 S_u Y_F^1 = -\int_{-\infty}^{+\infty} \dot{\omega}_F \, dx = \Omega_F \\ \rho_1 S_u C_p (T_2 - T_1) = -\mathbb{Q} \int_{-\infty}^{+\infty} \dot{\omega}_F \, dx = \mathbb{Q}\Omega_F \end{cases} \quad 4.2$$

In Eq. 4.2, Ω_F is the total fuel consumption and the equation shows that the whole fuel which is entering the domain ($\rho_1 S_u Y_F^1$) is burnt in the flame front to Ω_F. It also shows that by integrating a proper reaction mechanism over the domain one can determine the laminar burning velocity of a fuel.

4-3 Turbulent premixed flames

When the flow field is turbulent the flame passing through the field would not have a uniform laminar structure. The flame surface starts to wrinkle and the reaction zone spreads over a distorted surface area.

When dealing with a turbulent flow there are random fluctuations and perturbations in flow properties such as temperature, density, species concentration etc. This makes studying turbulent flow alone a very complex subject. When it comes to turbulent combustion, the level of complexities further increases. Due to the coupling of the turbulent flow field and turbulent reactions, the turbulent flow field modifies the reaction process and the heat release from the reaction modifies the turbulence in the flow field. The flame induces "flame generated turbulence" and on the other hand changes viscosity as a result of temperature variations which modifies the turbulence damping process. On the other hand the turbulence increases the reacting surface area leading to higher reaction rate and heat release [43].

Turbulent reactive flow contains numerous random fluctuations and perturbations in flow properties. Completely resolving small scale fluctuations is computationally unaffordable for problems of practical interest, simplified approaches have been developed to numerically simulate turbulent combustion processes. These approaches are linked with RANS, LES, ILES and DNS of turbulent flows described in Chapter 2.

4-3-1 RANS simulations for turbulent combustion

As mentioned earlier the RANS approach solves for averaged quantities over time, the flow quantities in Equations 2.30 to 2.33 need to be time averaged. This means any quantity f would be spited into mean and fluctuating part using the Favre averaging:

$$\begin{cases} f = \tilde{f} + f'' \\ \tilde{f} = \dfrac{\overline{\rho f}}{\bar{\rho}} \\ \widetilde{f''} = 0 \end{cases} \qquad 4.3$$

The averaging process results in the following RANS Equations:

Mass conservation:

$$\frac{\partial \bar{\rho}}{\partial t} + \frac{\partial \bar{\rho}\tilde{u}_i}{\partial x_i} = 0 \qquad 4.4$$

Species conservation:

$$\frac{\partial \bar{\rho}\tilde{Y}_k}{\partial t} + \frac{\partial (\bar{\rho}\tilde{u}_i\tilde{Y}_k)}{\partial x_i} = -\frac{\partial (\overline{Y_k V_{k,i}} + \bar{\rho}\widetilde{Y_k'' u_i''})}{\partial x_i} + \overline{\dot{\omega}_k} \qquad 4.5$$

Momentum conservation Equation:

$$\frac{\partial \bar{\rho}\tilde{u}_j}{\partial t} + \frac{\partial \bar{\rho}\tilde{u}_i\tilde{u}_j}{\partial x_i} = -\frac{\partial \bar{p}}{\partial x_j} + \frac{\partial (\overline{\tau_{ij}} - \bar{\rho}\widetilde{u_j'' u_i''})}{\partial x_i} \qquad 4.6$$

Energy conservation Equation (based on enthalpy):

$$\frac{\partial \bar{\rho}\widetilde{h_s}}{\partial t} + \frac{\partial \bar{\rho}\tilde{u}_i\widetilde{h_s}}{\partial x_i} = \overline{\dot{\omega}_T} + \frac{\overline{Dp}}{Dt} + \frac{\partial}{\partial x_i}\left(\lambda\frac{\overline{\partial T}}{\partial x_i} - \overline{u_i'' h_s''}\right) + \tau_{ij}\frac{\overline{\partial u_i}}{\partial x_j} \quad \frac{\partial \overline{\sigma_{ij}u_i}}{\partial x_j}$$

$$+\frac{\partial}{\partial x_i}\left(\overline{\rho\sum_1^N V_{k,i}Y_k h_s}\right) \qquad 4.7$$

The main goal in turbulence combustion modelling is to propose closure for unknown terms in the above equations. These terms are Reynolds stresses ($\widetilde{u_j'' u_i''}$), species and enthalpy fluxes ($\widetilde{Y_k'' u_i''}$, $\widetilde{u_i'' h_s''}$) and species chemical reaction ($\overline{\dot{\omega}_k}$).

The fluxes are most of the times modelled using a simple gradient term [43]:

$$\widetilde{\bar{\rho} Y_k'' u_i''} = -\frac{\mu_t}{Sc_{kt}} \frac{\partial \tilde{Y}_k}{\partial x_i} \tag{4.8}$$

The turbulent Reynolds stresses are normally modelled using viscous tensor τ_{ij}, similar to Newtonian fluids [43]:

$$\overline{\rho u_j'' u_i''} = \bar{\rho} \widetilde{u_j'' u_i''} = -\mu_t \left(\frac{\partial \tilde{u}_j}{\partial x_i} + \frac{\partial \tilde{u}_i}{\partial x_j} - \frac{2}{3} \delta_{ij} \frac{\partial \tilde{u}_k}{\partial x_k} \right) + \frac{2}{3} \bar{\rho} k \tag{4.9}$$

In Eq. 4.13, μ_t is the turbulent viscosity and k is turbulent kinetic energy:

$$k = \frac{1}{2} \sum_{k=1}^{3} \widetilde{u_j'' u_i''} \tag{4.10}$$

At this stage one needs to make an assumption for the turbulence viscosity to close the Eq. 4.9. There are 3 main approaches to evaluate μ_t which are referred to as algebraic methods, one Equation closure and two Equation closure.

Two Equation closure is the most widely used approach in combustion modelling and among two Equation models $k - \varepsilon$ has been successfully used for long time. Here the $k - \varepsilon$ is briefly expressed in Eqs. 4.11 to 4.14.

The turbulence viscosity (μ_t) is evaluated using Eq. 4.11:

$$\mu_t = \bar{\rho} C_\mu \frac{k^2}{\varepsilon} \tag{4.11}$$

In Eq. 4.11 k and ε come from Eqs. 4.12 and 4.13:

$$\frac{\partial \bar{\rho} k}{\partial t} + \frac{\partial \bar{\rho} \tilde{u}_i k}{\partial x_i} = \frac{\partial}{\partial x_i} \left[\left(\mu + \frac{\mu_t}{\sigma_k} \right) \frac{k}{\partial x_i} \right] + P_k - \bar{\rho} \varepsilon \tag{4.12}$$

And for ε:

$$\frac{\partial \bar{\rho} \varepsilon}{\partial t} + \frac{\partial \bar{\rho} \tilde{u}_i \varepsilon}{\partial x_i} = \frac{\partial}{\partial x_i} \left[\left(\mu + \frac{\mu_t}{\sigma_\varepsilon} \right) \frac{\varepsilon}{\partial x_i} \right] + C_{\varepsilon 1} \frac{\varepsilon}{k} P_k - C_{\varepsilon 2} \bar{\rho} \frac{\varepsilon^2}{k} \tag{4.13}$$

The $k - \varepsilon$ model constants are usually taken as:

$$C_\mu = 0.09 \quad \sigma_k = 1.0 \quad \sigma_\varepsilon = 1.3 \quad C_{\varepsilon 1} = 1.44 \quad C_{\varepsilon 2} = 1.92 \tag{4.14}$$

The above equations suffice for modelling a non-reacting flow. In order to simulate a reacting flow, it is crucial to propose a reliable model for mean reaction rate ($\overline{\omega_k}$). One option would be to use averaged from of the Arrhenius reaction, but the applicability of this approach is limited to the cases in which the turbulent time scale is smaller than all chemical time scales. In contrast there are more complicated approaches for mean reaction rate modelling with much wider applicability. Because of the similarities, some of these methods are explained here in LES section.

4-3-2 LES simulations for turbulent combustion

The filtered balance equations for LES can be formulated as:

Mass conservation:

$$\frac{\partial \bar{\rho}}{\partial t} + \frac{\partial \bar{\rho}\tilde{u}_i}{\partial x_i} = 0 \qquad 4.15$$

Species conservation:

$$\frac{\partial \bar{\rho}\tilde{Y}_k}{\partial t} + \frac{\partial (\bar{\rho}\tilde{u}_i\tilde{Y}_k)}{\partial x_i} = -\frac{\partial\left[\overline{Y_k V_{k,i}} - \bar{\rho}(\widetilde{u_i Y_k} - \tilde{Y}_k\tilde{u}_i)\right]}{\partial x_i} + \overline{\omega_k} \qquad 4.16$$

Momentum conservation Equation:

$$\frac{\partial \bar{\rho}\tilde{u}_j}{\partial t} + \frac{\partial \bar{\rho}\tilde{u}_i\tilde{u}_j}{\partial x_i} = -\frac{\partial \bar{p}}{\partial x_j} + \frac{\partial\left[\overline{\tau_{ij}} - \bar{\rho}(\widetilde{u_i u_j} - \tilde{u}_i\tilde{u}_j)\right]}{\partial x_i} \qquad 4.17$$

Energy conservation Equation (based on enthalpy):

$$\frac{\partial \bar{\rho}\widetilde{h_s}}{\partial t} + \frac{\partial \bar{\rho}\tilde{u}_i\widetilde{h_s}}{\partial x_i} = \overline{\omega_T} + \frac{\overline{Dp}}{Dt} + \frac{\partial\left[\lambda\frac{\overline{\partial T}}{\partial x_i}(\widetilde{h_s u_i} - \tilde{u}_i\widetilde{h_s})\right]}{\partial x_i} + \overline{\tau_{ij}\frac{\partial u_i}{\partial x_j}} + \frac{\partial}{\partial x_i}\left(\overline{\rho\sum_1^N V_{k,i}Y_k h_s}\right) \qquad 4.18$$

$$\frac{\overline{Dp}}{Dt} = -\frac{\partial \bar{p}}{\partial t} + \overline{u_i\frac{\partial p}{\partial x_i}} \qquad 4.19$$

The flow quantities in above formulations are instantaneous rather than averaged and the terms which have to be modelled (SGS terms) are different and include:

- Unresolved Reynolds stresses $(\widetilde{u_i u_j} - \tilde{u}_i \tilde{u}_j)$
- Unresolved species fluxes $(\widetilde{u_i Y_k} - \tilde{Y}_k \tilde{u}_i)$
- Unresolved enthalpy fluxes $(\widetilde{h_s u_i} - \tilde{u}_i \widetilde{h_s})$
- Filtered laminar diffusion fluxes $(\overline{Y_k V_{k,i}})$ and $\left(\lambda \frac{\overline{\partial T}}{\partial x_i}\right)$
- Filtered chemical reaction rate $(\overline{\dot{\omega}_T})$
- The pressure velocity term $(u_i \frac{\partial p}{\partial x_i})$

Modelling of the above unresolved terms for LES is explained in detail by Poinsot and Veynante [43] and also in [128-129]. Here only the two models used in the present study for the filtered chemical reaction rate are briefly described.

The Two Equations Turbulent Deflagration Models [86]

The premixed flame thickness is generally much smaller than the LES mesh size. Hence the flame front cannot be resolved in the computation. To overcome this difficulty, simulation of artificially thickened flame or G-Equation method or filtering with Gaussian filter larger than the mesh size are adopted [43]. Another alternative approach is solving a balance Equation for sub-grid scale flame wrinkling developed by Weller et al. [59-61] and available in the released version of OpenFOAM.

Flame wrinkling model:

The flamelet concept simplifies the turbulent combustion treatment by separating the combustion modelling from the analysis of the turbulent flow field by assuming that reaction takes place in relatively thin layers that separate regions of unburned and fully burned gases. The unburnt zone volume fraction can be denoted by regress variable (b), taking values 1 and 0 in unburnt and fully burnt region. The chemical source term in the flame wrinkling model is mainly developed and implemented in OpenFoam by Henry Weller [59-61] and is based on flame surface density concept.

In this approach "b" values specify the margin between unburned and burnt cells in the domain. The source term for this method is expressed as:

$$\overline{\omega_{\tilde{T}}} = -\nabla.(\bar{\rho}\tilde{U}\tilde{b}) - \bar{\rho}\Xi\widetilde{S_u}|\nabla\tilde{b}| \qquad 4.20$$

The transport Equation for the regress variable is given as:

$$\frac{\partial\bar{\rho}\tilde{b}}{\partial t} + \nabla.(\bar{\rho}\tilde{U}\tilde{b}) - \nabla.(\bar{\rho}\widetilde{D_{tb}}\nabla\tilde{b}) = -\overline{\rho_u}\Xi S_u|\nabla\tilde{b}| \qquad 4.21$$

Where Ξ is sub-grid flame wrinkling, ρ is the density, ρ_u is unburned gas density, $S_u$is laminar flame speed and D_{tb} is the sub-grid turbulent diffusion coefficient. Symbols ($\bar{}$) and ($\tilde{}$) represent the filtered and the density weighted filtering operations respectively. The closure for the sub-grid wrinkling is provided by a balanced transport Equation

$$\left(\frac{\partial\bar{\rho}\Xi}{\partial t}\right) + \overline{U_s}.\nabla\Xi = \bar{\rho}\overline{U_t}G\Xi - \bar{\rho}R(\Xi - 1) + \bar{\rho}\max\left[\sigma_s - \sigma_t\right]\Xi \qquad 4.22$$

Where $\overline{U_s}$ is the surface filtered local instantaneous velocity of the flame, $\overline{U_t}$ is the surface filtered effective velocity of the flame surface, σ_s and σ_t are resolved strain rates relating to $\overline{U_s}$ and $\overline{U_t}$. $G\Xi$ and $R(\Xi - 1)$ are sub-grid turbulence generation and removal rate, with G and R as rate coefficients requiring modelling.

The modelling for the respective terms in Eq. 4.23 is given below:

$$\begin{cases} \sigma_t = \frac{1}{2}\left\|\nabla\overline{U_t} + \overline{U_t}^T\right\| \\ \sigma_s = \frac{1}{2}\left\|\nabla\overline{U_s} + \overline{U_s}^T\right\| \\ G = R\frac{\Xi_{eq} - 1}{\Xi_{eq}} \\ R = \frac{0.28}{\tau_n}\frac{\Xi_{eq}^*}{\Xi_{eq}^* - 1} \\ \Xi_{eq}^* = 1 + 0.26\sqrt{\frac{\acute{u}}{S_u}}R_\eta \\ \Xi_{eq} = 1 + 2(1 - \bar{b})(\Xi_{eq}^* - 1) \end{cases} \qquad 4.23$$

where $\tau_n$is the Kolmogorov time scale, $\acute{u}$ is the sub-grid turbulence intensity and R_η is the Kolmogorov Reynolds number.

The surface filtered velocity of the flame $\overline{U_s}$ is given as:

$$\overline{U_s} = \tilde{U} + \left(\frac{\overline{\rho_u}}{\rho} - 1\right) S_u \Xi n_f - \frac{\nabla.(\bar{\rho} D \nabla \tilde{b})}{\bar{\rho}|\nabla \tilde{b}|} n_f \qquad 4.24$$

Eq. 4.22 can be simply written as:

$$\left(\frac{\partial \Xi}{\partial t}\right) + \overline{U_s}.\nabla\Xi - \nabla.\overline{D_l}\nabla\Xi = G\Xi - R\Xi^2 + \Xi\hat{n}.\nabla\widehat{U_t}\hat{n} - \frac{1}{\Xi}\hat{n}.\nabla\overline{U_s}\hat{n} + \left(\Xi\widehat{S_l}\left(\Xi - \frac{1}{\Xi}\right) + \overline{D_l}\nabla\Xi\right).\frac{\nabla|\nabla\bar{b}|}{|\nabla\bar{b}|} \qquad 4.25$$

where n_f is normal in the direction of flame propagation.

In order to capture the filtered strain and curvature effects on the laminar flame speed [9], the transport Equation for filtered laminar flame speed is solved:

$$\left(\frac{\partial S_u}{\partial t}\right) + \overline{U_s}.\nabla S_u = -\sigma_s S_u + \sigma_s {S_u}^{\infty}\left(\frac{{S_u}^0 - S_u}{{S_u}^0 - {S_u}^{\infty}}\right) \qquad 4.26$$

where ${S_u}^{\infty} = {S_u}^0 max\,(1 - \frac{\sigma_s}{\sigma_{ext}}, 0)$ and σ_{ext} is the strain rate at extinction.

More details and the derivation of the above equations are discussed in details by Weller et al. [59-61].

The Coherent Flame Model

The Coherent Flames Model (CFM) has been widely used in RANS with different source term formulations [63...66, 72]. CFM simplifies the turbulent combustion problem by separating the combustion modelling from the analysis of the turbulent flow field. Considering a single step chemistry, unity Lewis number and flamelet regime, the thermo chemistry of the reacting flow may be described by the progress variable "c" of the reaction (c = 0 in fresh gases and c = 1 in fully burnt gases) according to Eq. 4.27:

$$\frac{\partial \bar{\rho}\tilde{c}}{\partial t} + \nabla.(\bar{\rho}\tilde{U}\tilde{c}) - \nabla.\left(\sigma_c \frac{\bar{\rho}\widehat{\upsilon_t}}{Sc_t}\nabla\tilde{c}\right) = \rho_u S_u \overline{\Sigma_c} \qquad 4.27$$

where $(\overline{\Psi})$ denotes a filtered quantity and $(\widetilde{\Psi})$ a mass weighted filtered quantity $(\overline{\rho\Psi} = \bar{\rho}\widetilde{\Psi})$. $\widehat{\upsilon_t}$ is sub-grid turbulent viscosity $(\widehat{\upsilon_t} = C\widehat{u'}\hat{\Delta},\ C = 0.12)$, Sc_t is turbulent Schmidt number, S_u is the laminar flame speed which will be addressed later. ρ_u is the unburned gases density, $\overline{\Sigma_c}$ is the filtered flame surface density defined as $\overline{\Sigma_c} = \bar{\Sigma} + \nabla.\left((\bar{c} - \tilde{c})N\right)$ and $\bar{\Sigma} = |\overline{\nabla c}|$, $\tilde{c}$ is estimated from the Bray-Moss-Libby (BML) expression $(\bar{c} = \tilde{c}\frac{\bar{\rho}}{\rho_b})$, the BML is a flamelet based combustion model [41-43]. N in the $\overline{\Sigma_c}$ equation is the normal to the iso-surface of the filtered progress variable, ρ_b is burned gas density. The closure for the filtered Flame Surface Density $\overline{\Sigma_c}$ is given through a phenomenological transport equation [13]:

$$\frac{\partial\overline{\Sigma_c}}{\partial t} + T_{res} + T_{sgs} = S_{res} + S_{sgs} + C_{res} + C_{sgs} + P \qquad 4.28$$

$$\begin{aligned}\frac{\partial\overline{\Sigma_c}}{\partial t} + \nabla.(\tilde{u}\overline{\Sigma_c}) - \nabla.\left(\sigma_c\,\frac{\widehat{\upsilon_t}}{Sc_t}\nabla\overline{\Sigma_c}\right) \\ = \nabla.(\nabla.\tilde{u} - NN{:}\nabla\tilde{u})\overline{\Sigma_c} + \Gamma\left(\frac{\widehat{u'}}{S_u},\frac{\hat{\Delta}}{\sigma_l}\right)\frac{\widehat{u'}}{\hat{\Delta}}\frac{\overline{\Sigma_c}}{\sigma_c} \\ + \beta S_u\frac{c^* - \bar{c}}{\bar{c}(1-\bar{c})}\left(\overline{\Sigma_c} - \overline{\Sigma_c^{lam}}\right)\overline{\Sigma_c} - \nabla.(s_d N\overline{\Sigma_c})\end{aligned} \qquad 4.29$$

where Γ is efficiency function accounting the ability of all vortices to wrinkle the flame, $\widehat{u'}$ is turbulent velocity fluctuation at filter size $\hat{\Delta}$, $\Sigma_c^{lam} = \overline{|\nabla c|} + (\bar{c} - \tilde{c})\nabla.N$, flame displacement speed is defined as $s_d = (1 + \tau\tilde{c})S_u$, $\left(\tau = \frac{\rho_u}{\rho_b} - 1\right)$ is thermal expansion rate, $\beta = \frac{4}{3}$ and $c^* = 0.5$ are modelling constant. In Eq. 4.28, T_{res}, S_{res}, C_{res} and P are respectively, the transport, strain, curvature and propagation terms due to resolved flow motions, and T_{sgs}, S_{sgs}, C_{sgs} are respectively the unresolved transport, strain and curvature terms.

The CFM formulation described is based on the work of Richard et al. [63]. It has been implemented and used in the current work.

4-4 Modelling the laminar burning velocity

The laminar flame speed is a key parameter in the simulation of all deflagration regimes. The laminar flame speed or laminar burning velocity depends on the fuel, pressure, temperature and mixture equivalence ratio.

Several numerical and experimental studies have been carried out to investigate laminar burning velocities of different fuels and the effects of pressure, temperature and equivalence ratio on laminar flame speeds [49...58].

Because the flame speed can affect the propagation pattern of the flame significantly, selecting a reliable correlation for laminar flame speed is crucial in numerical simulations of turbulent deflagrations. A low speed deflagration can accelerate, becoming turbulent and converting to a high-speed propagating combustion wave that can eventually converts to detonation. Several key factors can increase the turbulence intensity in the flame surface and affect the flame acceleration process. A good understanding of these processes is essential for simulation of DDT.

4-4-1 Hydrogen burning velocity Correlation

As mentioned earlier, laminar flame speed is one of key affecting parameters in combustion simulation. Currently the Gulder correlation for flame speed is available in OpenFOAM. However, this correlation was originally developed for internal combustion engine applications involving fuels like propane, isooctane etc. It is not applicable for hydrogen. In order to simulate hydrogen deflagration, it is necessary to implement an appropriate flame speed correlation.

Several correlations for hydrogen flame [49...58] have been implemented in the code. By comparing the predictions with experimental results, the most accurate correlations have been selected for the subsequent study.

The chosen flame speed correlations consists of two formulas; the first part gives the flame speed in the standard condition as a function of equivalence ratio and the second part corrects the results of the first formula to predict the flame speed when the mixture pressure and temperature are different from standard condition. In the present work, the first part of the correlation is obtained by curve fitting a 6^{th} order polynomial (Figure 4-4) to the experimental results (Figure 4-3) [57] for hydrogen burning velocity at 100 KPa and 25°C. Similar correlations are derived by curve fitting polynomials to other experimental data [49...58]. Since most of these derivations reproduce equally good predictions of the flame speed, only one of these correlations which is based on [57] is presented and used here.

The resulting formula obtained from curve fitting reads:

$$Su_0 = 0.022\Phi^6 - 0.316\,\Phi^5 + 2.757\,\Phi^4 - 10.51\,\Phi^3 + 15.06\,\Phi^2 - 4.886\,\Phi + 0.516 \qquad 4.30$$

By substituting the equivalence ratio "Φ"in Eq. 4.30, the laminar flame speed in reference condition"Su_0" can be obtained.

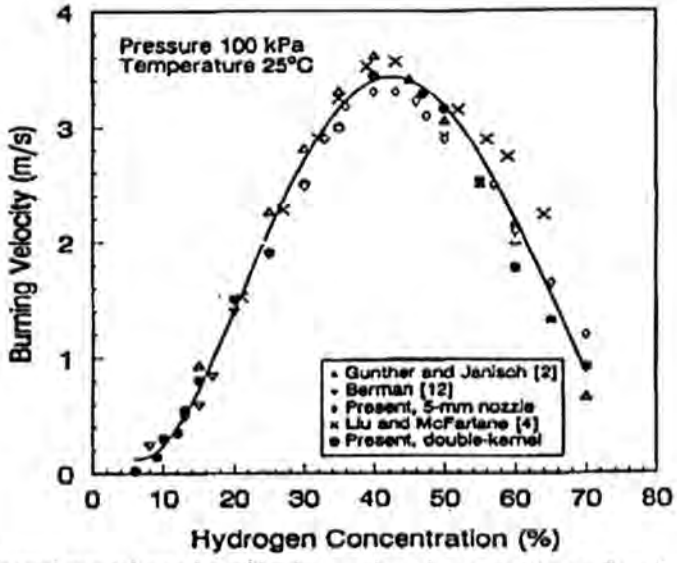

Figure 4-3 Experimental results of hydrogen burning velocity as function of hydrogen concentration, reproduced from [57].

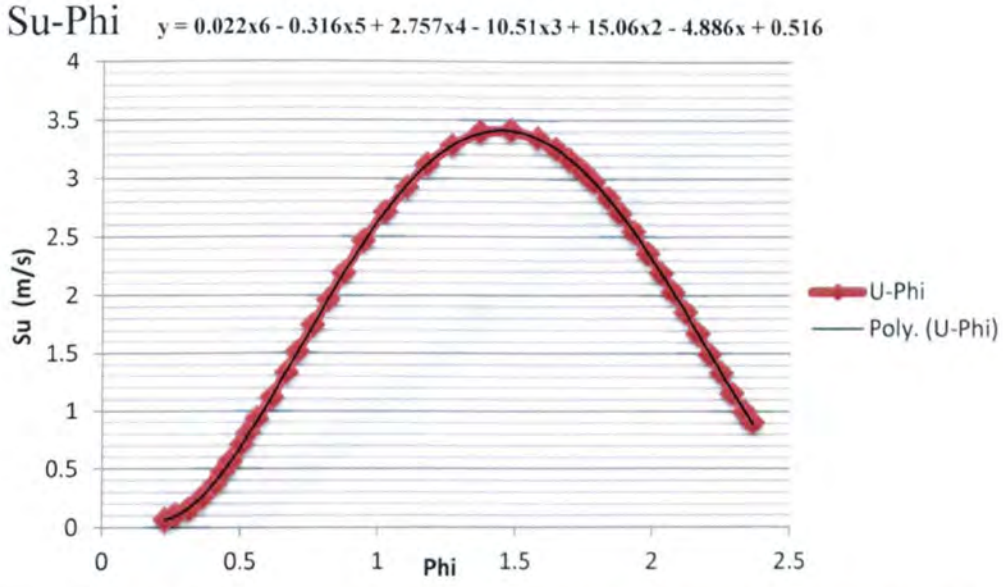

Figure 4-4 Curve fit of 6th order polynomial to experimental results of hydrogen burning velocity as function of hydrogen concentration, used as a part of flame speed correlation.

The second formula reads [52]:

$$Su = Su_0 \left(\frac{T}{T_0}\right)^{\alpha} \times \left(\frac{P}{P_0}\right)^{\beta} \qquad 4.31$$

By substituting Su_0 from Eq. 4.30 into Eq. 4.31, one can obtain the total laminar burning velocity in a specified pressure, temperature and equivalence ratio.

The above correlation is implemented in the current work. As illustrated in Figure 4-5, to investigate the accuracy of the correlation, the results of flame radii via time for a laminar spherical flame propagation of hydrogen-air mixture have been validated against the experimental results [58].

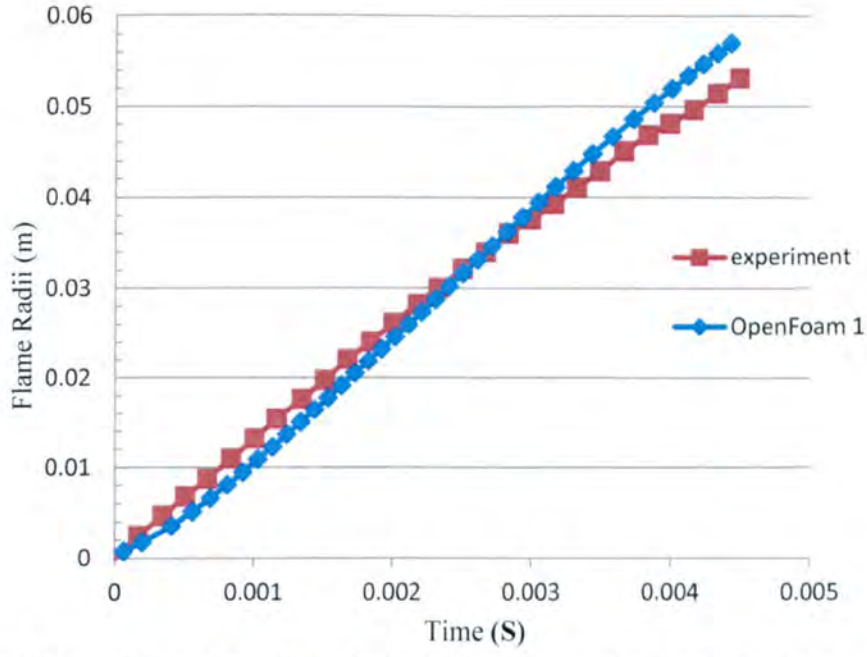

Figure 4-5 Validation of results for flame radii via time against experimental results in spherical flame propagation to investigate the accuracy of new implemented hydrogen burning correlation.

Figure 4-5 shows excellent agreement between numerical and experimental results meaning implemented correlations in the current work are reliable for hydrogen combustion simulations.

4-5 Flame acceleration process

Having validated the laminar flame simulations, a number of case studies have been conducted for flame acceleration and turbulent deflagration.

Undesired deflagration/explosion incidents in an industrial places start from an accidental release and ignition of a reactive gas. Subsequently, a deflagration wave propagates in the reactive mixture. The flame which is initially laminar could be well simulated using the Navier-Stokes Equations and a simple reaction mechanism. However the laminar stage does not last long. A series of processes influence the flame causing flame wrinkling, transforming the flame to a turbulent flame and enhancing the turbulence level. The most likely cause of turbulence induction into a

flame is interaction with obstacle located within the path way of the flame propagation, causing considerable turbulence intensity increase in the flame front.

Flame obstacle interaction wrinkles the flame surface and increases the flame surface area per unit volume [67], resulting in increases in the energy release and acceleration of the deflagration wave. There is a positive feedback between flame speed and turbulence intensity in the flame surface.

The high-speed deflagration wave forms strong pressure waves, which can magnify one another and create stronger pressure and shock waves. The reflected shock waves from the surrounding walls interact with the flame front and make it more distorted and wrinkled [42]. In addition, the passage of hot jets of burnt gasses through the narrow parts of the channels can also increase the turbulence intensity and flame distortion.

All these processes increase the rate of energy release in the flame surface and cause higher flame velocity and more turbulence intensity.

In this chapter large eddy simulation approach based on the formulation derived earlier in this chapter is used to simulate deflagration propagation and acceleration process.

Starting from a simple test case for code validations a spherical propagating flame in an initially turbulent reactive mixture is studied using OpenFoam two-equation combustion model.

Figure 4-6 shows the predicted velocity fields. It can be observed that the flame surface is distorted and wrinkled. Figure 4-7 shows that there is reasonably good agreement between the predicted and measured flame radii vs time [71].

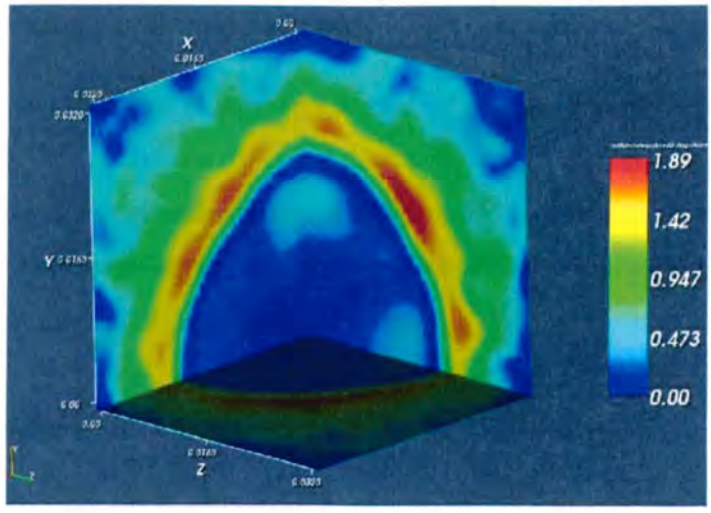

Figure 4-6 Pressure field in spherical turbulent flame propagation $\frac{1}{8}$ of domain

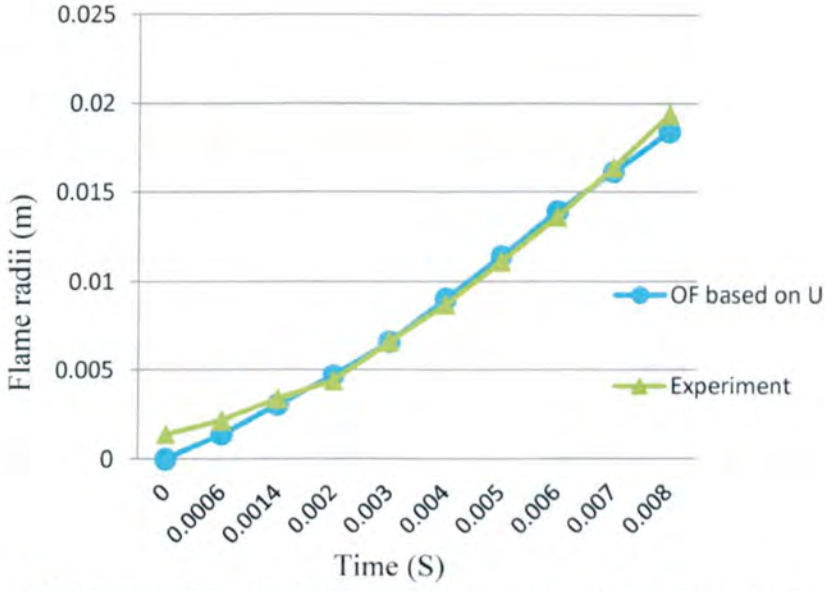

Figure 4-7 Validation of results for flame radii via time against experimental results in spherical flame propagation

Having tested the code performance against this simple experimental test case, more complex flame acceleration and turbulent deflagration processes are simulated to aid understanding about the condition under which transition from deflagration regime to detonation regime can occur.

4-6 Deflagration simulation-test cases

The first test is based on experimental case of Renou and Boukhalfa [71] and reported in [86, 89]. This case is based on the same experimental work as the one presented in previous section but here the CFM model and effects of spark wrinkling are presented. The reactive mixture was injected through a turbulence grid into a channel where a thin spark plug ignited the mixture. The turbulence was found to be nearly isotropic (PIV and laser tomography imaging) and hardly decayed during the flame kernel growth.

In Fig. 4-8, comparison is made between the measurements of Renou and Boukhalfa [71] and the predictions from the original two Equation deflagration model in OpenFoam and the modified version with CFM implemented by the authors [86]. In this simple case, both models are found to be in reasonably good agreement with the data apart from the initial stage. As the flame was initially laminar in this case, it was found necessary to retain a model evolution equation for the spark wrinkling equation and define a local flame surface density for the CFM. The predictions with the modification are shown in Fig. 4-8 as "CFM Lam Ign" and are found to be in good agreement with the data.

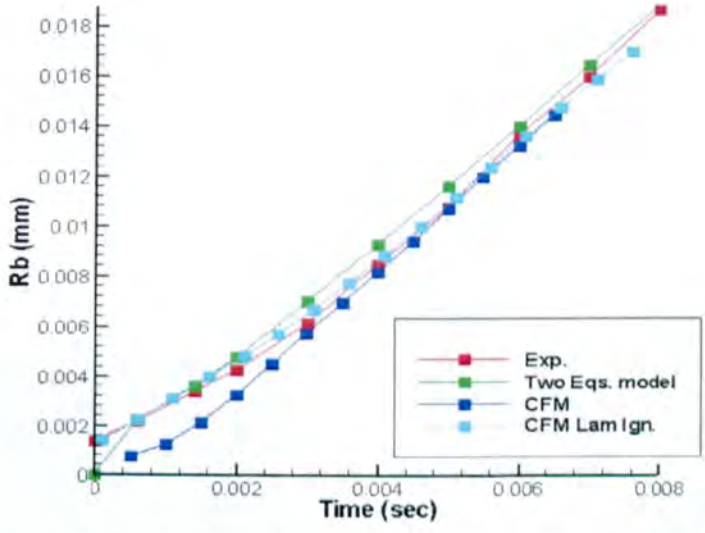

Figure 4-8 Evolution of the mean flame radii – comparison between the predictions of different models and experiment data in [74, 86].

The second case is based on the experiments of Patel et al. [69, 73] for deflagration in a semi-confined explosion chamber. Laser diagnostics techniques were used to

investigate flame propagation past multiple obstacles mounted in the chamber. Pressure was measured at two locations within the combustion chamber. The computational domain, as shown in Figure 4-9-(a), is 150 x 150 x 500 mm with average mesh size of 2mm. The maximum Courant number used for this case is 0.2. The computational domain consists of 0.5M grid cells in total and as shown in Figure 4-9-(a), it is extended both vertically and horizontally beyond the opening of the chamber. The stoichiometric methane and air mixture has an initial temperature of 300K and pressure of 1 bar.

In Figure 4-9-(b), comparison is made between the predicted and measured overpressure at different times. The newly implemented model has demonstrated improvement over the original two Equation turbulent deflagration model in OpenFoam. Even more encouraging agreement is seen in Figure 4-10 when comparison is made between the predicted and measured flame front speed at different locations from the ignition end.

In Figure 4-11, comparison is made between the present predictions with the measurement and RANS simulations of Patel et al. [73]. Here the right hand side column of results is from the present study. The middle column shows the experimental results and the left column shows numerical results of simulations by Patel et al. It can be seen that the predictions in current work are in good agreement with experimental measurement.

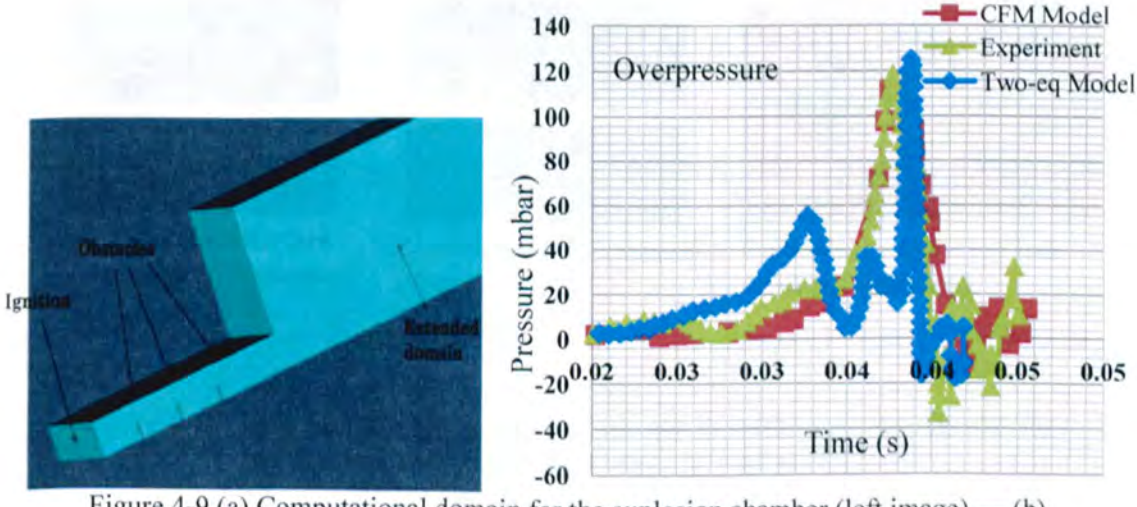

Figure 4-9 (a) Computational domain for the explosion chamber (left image) — (b) Comparison between predicted and measured overpressure (right image).

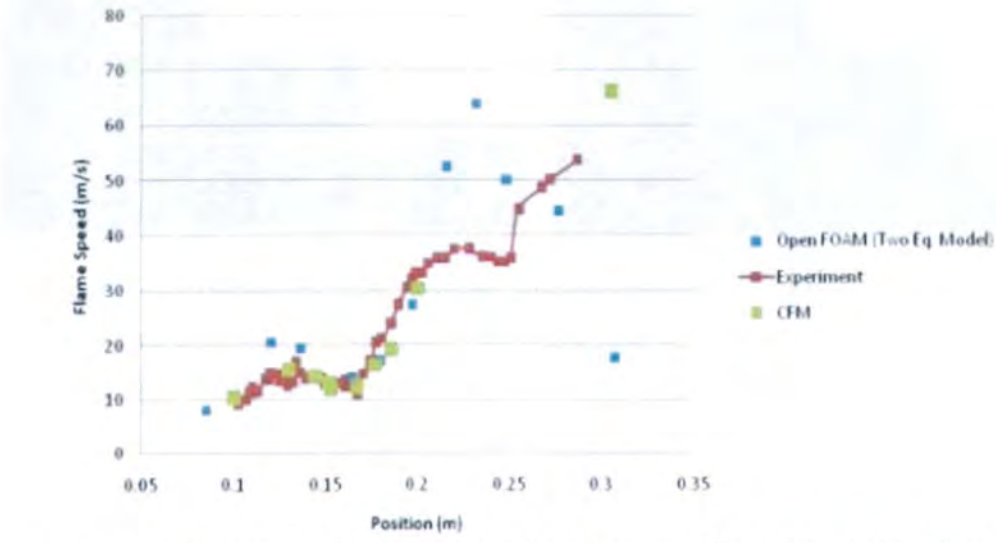

Figure 4-10 Comparison between predicted and measured flame front speed values at different locations from the ignition end.

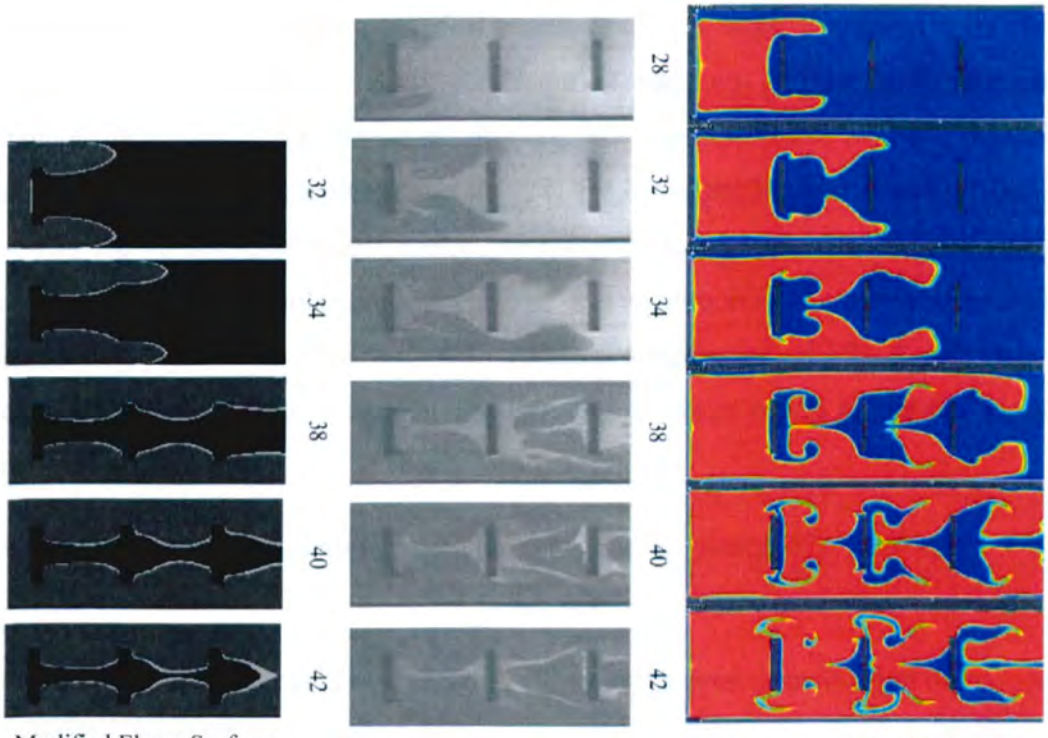

Modified Flame Surface Density-RANS simulation of Patel et al. [73]

Experimental Measurements of Patel et al. [73]

Predictions by LES-CFM code developed in this work

Figure 4-11 Flame evolutions – comparison between the present predictions with the measurement and RANS simulations of Patel et al. [73]

(a) (b)

Figure 4-12 Comparison of the predicted and measured flame propagation patterns; (a) Sequence of shadow photographs of flame propagation in 10% H_2–air mixture with blockage ratio of 0.6, Channel width is 80mm. Times after ignition in ms are shown on the right; (b) the present predictions.

The third case study is based on the experimental work of Ciccarelli et al. [79] demonstrating the flame Propagation in an obstructed channel filled with hydrogen-air. Figure 4-12 shows the numerical result from this work compared with the measurements of Ciccarelli et al. for flame propagation through an obstructed channel filled with 10% hydrogen-air mixture. Here the correlation which is derived based on the work of Lamoureux et al. [78] for hydrogen laminar flame speed is used in the combustion model, using other flames speed correlations e.g. Koroll, would result in very similar predictions. The grid resolution is 1 mm structured. All the boundary conditions are wall with constant temperature of 293 K and zero-velocity in all directions or no slip. The initial temperature is 293 K and the initial pressure is 1.013 bar.

Figure 4-12 shows qualitatively the predictions are in reasonably good agreement with the experiments.

Several numerical test cases revealed that although the present model can reproduce reasonable results for low speed and to some extent fairly high speed deflagration waves, the models suffer from considerable deviations when applied to highly turbulent and fast deflagrations which are about to undergo transition to detonation. This is mainly because many of the underlying assumptions are not valid in near DDT combustion regimes. For example due to flame thickening, the standard flamelet assumption is not valid near a wall when highly turbulent deflagration wave

is interacting with an obstacle. This could significantly alter the prediction of hot spot formations when the deflagration waves are hitting an obstacle.

Therefore it is decided from this point onwards; the efforts towards simulating DDT are carried out without using the traditional flamelet based combustion model and rather by using Arrhenius type reactions and full instantaneous Navier-Stokes Equations with the ILES approach

4-7 Wall flame interaction

For combustion in confined geometries, the deflagration wave passes through a vessel/container which might contain a number of solid obstacles. Even in unconfined geometries, walls or solid boundaries may be in the pass way of a deflagration wave. The DDT phenomenon which is studied in later chapters of this work may also be affected by the wall-flame interaction as the deflagration wave passes through the obstacles. Therefore studying the behaviour of the flame at the vicinity of solid boundaries is of considerable importance. The presence of a wall in the way or the side of a deflagration wave may significantly influence the behaviour of the flame, its propagation pattern, energy release rate and consequently the overall performance of the combustion system. Even in accidental combustion and explosion scenarios, presence of solid boundaries may trigger extinction or excitation of the explosion wave passing through the solid walls.

Despite the importance of the subject, very little work is done on flame wall interaction and phenomenon is not very well understood [43]. The present work uses DNS and ILES to avoid the use of combustion models when dealing with flame-wall interaction during flame acceleration through obstacles.

Chapter 5

Numerical Simulation of Detonations

5-1 Background

In contrast to deflagration waves, which are sub-sonic, the detonation waves are extremely violent and supersonic, moving with a velocity of about 2000m/s in gaseous reactive mixtures. The detonation waves consist of a very thin shock wave, known as *von Neumann spike,* and a combustion region which are coupled and moving together. In fact a detonation wave can be referred to as a reactive shock wave. There is a very sharp change in the thermodynamic state across a detonation wave and reactants are converted to product with energy release across reaction zone. Since the detonation is moving with a supersonic speed, the reactive mixture ahead of the wave would not be able to see the effect of the detonation therefore the flow ahead of the wave would remain undisturbed until the detonation wave reaches there.

Able [74] was probably the first one who discovered detonation phenomenon and measured the detonation velocity. Since then several experimental, theoretical and numerical studies about detonation have been carried out to shed light on different aspect of detonation waves. The first theory about detonation was suggested separately by Chapman in 1899 and Jouguet in 1905. Later the theory was called Chapman- Jouguet or CJ theory.

CJ theory assumes that detonation is a one dimensional steady state and zero thickness phenomenon so it does not really explain the structure of the detonation front and the affecting parameters in the reaction region. Instead it is based on the equilibrium parameters of detonation which can be determined by solving one dimensional Euler Equations from knowing the initial thermodynamic state of the detonable mixture plus enforcing the CJ condition (sonic condition). The parameters that can be determined by CJ theory are called thermodynamic or static parameters of detonation, which include detonation pressure, temperature, propagation velocity (CJ velocity), etc. The theory also assumes that the detonation products right after the detonation wave move with the sonic velocity with respect to the detonation

front. This assumption is called CJ condition and is essential for calculating other CJ parameters in a detonation.

When the detonation products are moving with sonic velocity with respect to the shock, it is simply called a CJ detonation, otherwise if the products velocity is supersonic it is called a weak detonation which requires certain properties on Hugoniot curve [6]. Weak detonations are not quite stable, therefore they are not normally observed. In reality, free moving detonations are normally CJ detonations [6].

Despite its simplicity, the CJ model has proved to be very accurate. In some studies it is proven that the CJ theory can reproduce the pressure and propagation velocity with an accuracy of about 99% compared to the experimental measurements [93]. However, the CJ theory ignores the detonation reaction zone and is unable to explain the details of real detonation waves and their behaviours such as formation of the cellular pattern in detonations or the prediction of the maximum quenching distance etc.

A more comprehensive detonation theory was later proposed independently by Zeldovich [137] in 1940, von Neumann [138] in 1942 and W. Doering [139] in 1943, and was later known as ZND theory. It assumes a one dimensional model for detonation but unlike CJ theory, the reaction zone thickness is not zero. Therefore, the detonation front structure includes a leading shock which is followed by a reaction zone. At the end of the reaction zone the CJ condition exists. Based on the ZND theory, right after the shock a delay time exists in which the pressure and temperature remains constant, meanwhile reactive radicals are formed due to high pressure and temperature. After the delay zone, the reaction zone starts where the radicals react and release energy. Figure 5-1, shows temperature and pressure profile for propane-oxygen detonation obtained by ZND theory [96] which is computed by Schultz [94] using a code developed by Shepherd [95]

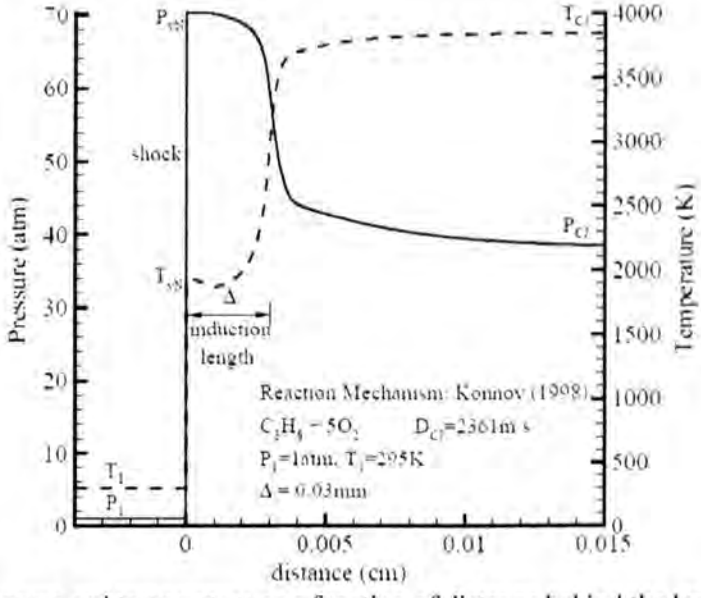

Figure 5-1 Pressure and temperature as a function of distance behind the leading shock, for propane-Oxygen detonation, obtained using ZND theory [96]

Despite its superiority to CJ model, the ZND model is also unable to fully predict the detailed behaviour and structure of a real detonation wave as it assumes that detonation waves are one dimensional and steady state phenomenon, whilst it is observed in experiments that detonation is an unsteady and three dimensional phenomenon [6].

Although CJ and ZND models can provide valuable information about detonation pressure, temperature and propagation velocity in 1-D, in order to simulate the behaviour of a real detonation wave and capture the details of detonation structure, one needs to solve three dimensional Navier–Stokes Equations for flow hydrodynamics along with a set of detailed kinetic mechanisms for the reaction zone. The viscous terms in the Navier–Stokes Equations can be neglected for detonation simulations, leaving only the Euler Equations to be solved. This simplification is justified because very high velocity of detonation waves makes the diffusion and heat conduction effects negligible. DNS of detonations requires extremely high grid resolutions to resolve the shock front and tremendous amount of computational time. A 3-D detonation simulation by DNS is almost beyond the reach of today's computing power. Reaction mechanisms can also be simplified. Detailed studies of a complete set of reaction mechanism can show the level of

importance of each reaction equation. The species which have a very small mass fraction in the mixture and reactions that do not affect the overall mechanism significantly can be eliminated from the reaction list. However, simplification of reaction mechanisms is a very sensitive subject and needs to be carried out with extra care to guarantee production of reliable results by the final simplified reaction mechanism. Such simplified reactions are normally referred to as reduced reaction mechanisms.

Detailed reaction mechanisms either full or reduced are generally required for studies which involve tracing the generation of pollutions such as NO_X, which is not of primary importance in safety studies. Here the primary concern is the static or dynamic state of the combustion regime (pressure, temperature, detonation cell pattern, etc.) which can be captured by a single step reaction mechanism. In an extensive study by Oran et al. [14], they successfully used a single step reaction to simulate DDT.

5-2 Governing Equations

As mentioned earlier detonation is a shock wave which is followed by a combustion region. The shock and the flame front are coupled and move together. In other words detonation is a supersonic combustion wave [6]. The velocity of gaseous detonation wave is around 2000 m/s. In such condition the viscous effects are negligible and the flow can be described using reactive Euler Equations. Consequently the sub-grid scale effects are negligible as well and usually no turbulence modelling is required. The flow can be described using the inviscid, non-conducting, reactive Euler Equations in conservative form as presented in Equations 2.34 to 2.37. In the present work, a numerical solver, called DetoFOAM, is developed to solve these equations along with appropriate reaction kinetics for the underlying combustion process. These reactions model the consumption and production of each chemical element (Y_i) which is present during the detonation process. As explained earlier, detailed reaction mechanisms describe the consumption and production rate of tens or hundreds spices during the reaction. Tracking the consumption and production most of these spices is absolutely unnecessary in detonation studies in the context of risk assessment, on the other

hand experience has proved simple approaches to reaction modelling can produce even better results compared to the detailed reaction mechanisms. One simple method to describe the chemistry is to use a $\{reactant \rightarrow product\}$ approach. This means the fuel-oxidiser mixture is considered as one specie called reactants and all the products are treated as a single specie called products. To formulate this, the parameter α_b which is called the detonation progress variable may be used. α_b is zero where all the mixture is unburned and is 1 where the mixture is burnt. Solving a transport equation for α_b helps to track the margin between burnt and unburnt gasses, this is also the location of detonation front:

Reaction progress Equation:

$$\frac{\partial \rho \alpha_b}{\partial t} = -\nabla(\rho \alpha_b U) + \rho\omega \qquad 5.1$$

In Eq. 5.1, ω represents the reaction rate and is modelled using a single step Arrhenius type reactions which will be explained later in Eqs. 5.6 and 5.7. The equation of state is required to close the above set of governing equations. For gaseous detonation, the pressure range is low enough to keep the ideal gas assumption valid and hence adopted in the present study.

Equation of state:

$$\frac{P}{\rho} = \frac{RT}{M} \qquad 5.2$$

By using the rate of production and consumption of each element and the resulting change in the enthalpy, it is possible to calculate the energy source term and the progress rate of reaction.

The above equations are discretised using the finite volume methods with the explicit Euler scheme for the time derivatives [98]. For shock capturing, the Van Leer flux limited method which is a total variation diminishing scheme is used [97]. It can be expressed by the following formulation:

$$u_i^{n+1} = u_i^n - \lambda(\hat{f}^n_{i+\frac{1}{2}} - \hat{f}^n_{i-\frac{1}{2}}) \qquad 5.3$$

$$\hat{f}^n_{i+\frac{1}{2}} = \frac{1+\eta_i^n}{2}\hat{f}^{L-W}_{i+\frac{1}{2}} + \frac{1-\eta_i^n}{2}\hat{f}^{B-W}_{i+\frac{1}{2}} \qquad 5.4$$

$$u = \begin{bmatrix} \rho \\ \rho u \\ \rho e \end{bmatrix} \quad \text{and} \quad f = \begin{bmatrix} \rho u \\ \rho u^2 + p \\ (\rho e + p)u \end{bmatrix} \qquad 5.5$$

Further details about the scheme can be found in reference [97].

For accurate simulations of the fine structures in detonation, it is necessary to capture the shock waves. This requires very fine grid resolutions typically in the order of microns. The current computer power still restricts the use of such fine resolutions in large scale detonation studies but very fine mesh, e.g. 20-30 grid points across detonation half reaction length can be used to study the detonation wave structure in very small scales in the order of a few centimetre or millimetre. Such fine resolutions are used in the present study when the structure of the detonation front is of interest.

For larger scale studies, an approach has been developed which is based on tuning the reaction model so that it can produce the right CJ parameters with relatively large grid size and still captures the correct pre- and post- detonation states as well as the correct energy release. The speed of the detonation wave can be computed as part of the overall coupled fluid/reaction simulation. It should be acknowledged that a coarse-grid simulation will not capture the internal structure of the detonation wave, e.g. the detonation cellular structure. However, if adequately tuned, it is capable of capturing the moving detonation front and hence the detonation wave speed pressure and temperature. Nevertheless, the downside of using relatively coarse grids is that the shock wave will be smeared over at least that distance and more typically 3 or 4 cells. In summary, based on the application and the level of details required, different grid sizes have been used in the present study. For detonation structure studies the grid must be fine enough to resolve the detonation front, it is normally suggested to put 20 grids across the detonation half reaction length if resolving the detonation front is desired. In larger scale applications grids which are hundreds and thousands of times bigger than the half reaction length may be used but special treatments are required to ensure correct results are produced.

5-3 Detonation wave structure

As discussed earlier, detonation is a shock induced combustion wave. The 1-D theories such as CJ and ZND can produce a surprisingly good prediction of its static

parameters. However, experimental observations have shown that the multi-dimensional structure of the detonation front is not planar and there are multi-dimensional instabilities in the form of perpendicular shock waves (with respect to propagation direction) at the detonation front. The intersection of the transverse shocks and detonation leading shock forms triple points where the pressure and temperature and consequently the reaction rate are increased significantly. Recording the triple point trajectories produces a "fish-scale" sketch, which is called detonation cellular pattern. The cellular patterns of different mixtures are distinguished with the cell's characteristic length L, width λ and the irregularity of the pattern.

As mentioned earlier, to capture correctly the details of detonation structure a fine mesh resolution is required, it is normally suggested to put at least 20 grids within the detonation half reaction length (HRL) to resolve the detonation front. Studying finer details such as Kelvin-Helmholtz or Richtmyer-Meshkov instabilities requires even finer grid resolution. Mahmoudi and Mazaheri [19] recently analysed high resolution 2-D numerical simulations of gaseous detonations both in high and low activation energies. They found that in the case of high activation energy, $\frac{E_a}{RT_0} = 20$, (irregular detonation structure) much higher grid resolution (300 per half reaction length) is required to study the effect of KH and RM hydrodynamic instabilities in detonation propagation whereas in lower activation energies, $\frac{E_a}{RT_0} = 10$, (regular structure) due to absence of fine scale structures, using 50 grids per HRL suffices for capturing most of the details.

In the present study, a relatively high resolution 2-D simulation of hydrogen-air detonation in a 3 by 10 cm tube is conducted; the detonation is initiated using an initial high pressure and temperature region in the domain and as it is presented in Figure 5-2 it propagates from left to right. This test case is conducted to study the performance of DetoFOAM code in predicting the fine structure of hydrogen detonation. The half-reaction length and detonation cell size for hydrogen-air (H_2-air) mixture are about 167.3μm and 1-2 cm, respectively. A 5μm grid size is chosen which gives about 33 cells per half reaction length. The courant number is kept less than 0.1 to avoid large time steps during the solution.

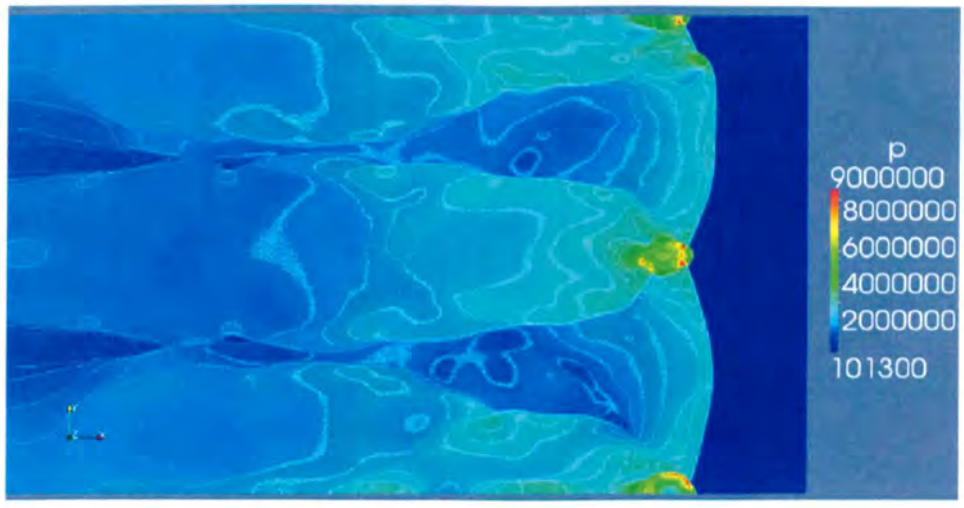

Figure 5-2 High resolution detonation simulation, 33 point within the half reaction zone.

Figure 5-2 shows a snapshot of the detonation wave front (pressure field) and the transverse waves behind the detonation front. The schematic of triple point is presented in Figure 5-3 showing the Mach reflection and the undisturbed detonation front which is called the incident shock, while the transverse wave works as the reflected shock. The triple point is driven forward by a strong shock wave, called Mach stem. Mach stem and reflected shock enclose the slip line and the contact discontinuity. *"The shock front inside the detonation cell propagates as two Mach stems from point A to the line BC. In the points B and C the triple point configuration is inverted nearly instantaneously and the front in the cell becomes the incident shock. Along the symmetry line AD the change is smooth and the shock strength decreases continuously. In D the two triple points merge exactly in a single point. The incident shock vanishes completely and the slip line, which was necessary for a stable triple point configuration between Mach stem and incident shock, is torn off and remains behind. Two new triple points with two new slip lines develop immediately after" [99]*

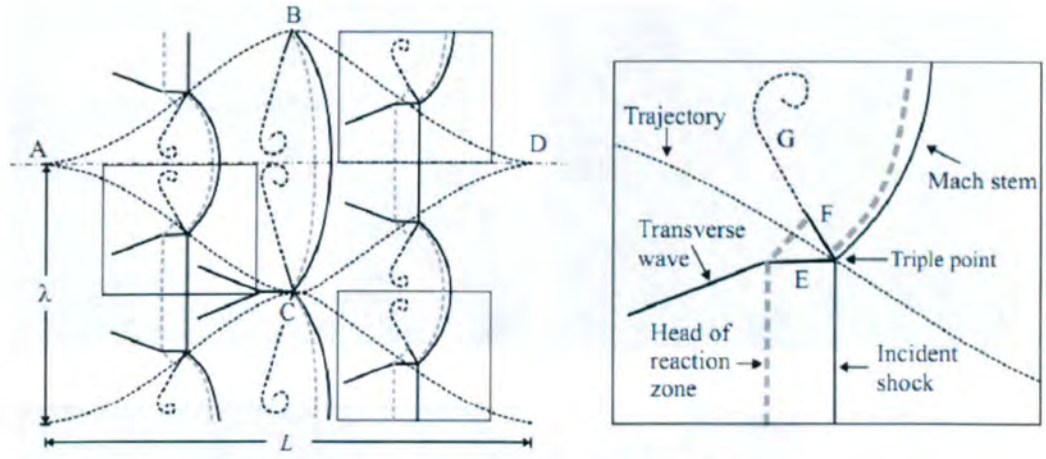

Figure 5-3 The schematic of triple point [100].

Figure 5-4 The triple point, mach stem, transverse wave and the incident shock.

As shown in Figure 5-4, the predictions have captured the structure of the detonation front including the triple point, mach stem, transverse wave and the incident shock. In 3-D plots the transverse shocks travelling normal to the detonation direction and moving inwards from both sides, sweep across the leading detonation front. The transverse waves reflect from each other and in the same time the leading shock front moves between being the Mach stem and the incident shock of a triple point shock structure, in this structure the transverse waves propagate in between the collisions [100-101]. Figure 5- 5 shows that this phenomenon is captured by the present simulations in comparison with the Schlieren photograph of a detonation front propagating in a thin channel with an accompanying sketch by Radulescu et al. [102]. It should be pointed out that the predictions in Figure 5-5 are not for the same configurations. The comparison is hence only qualitative.

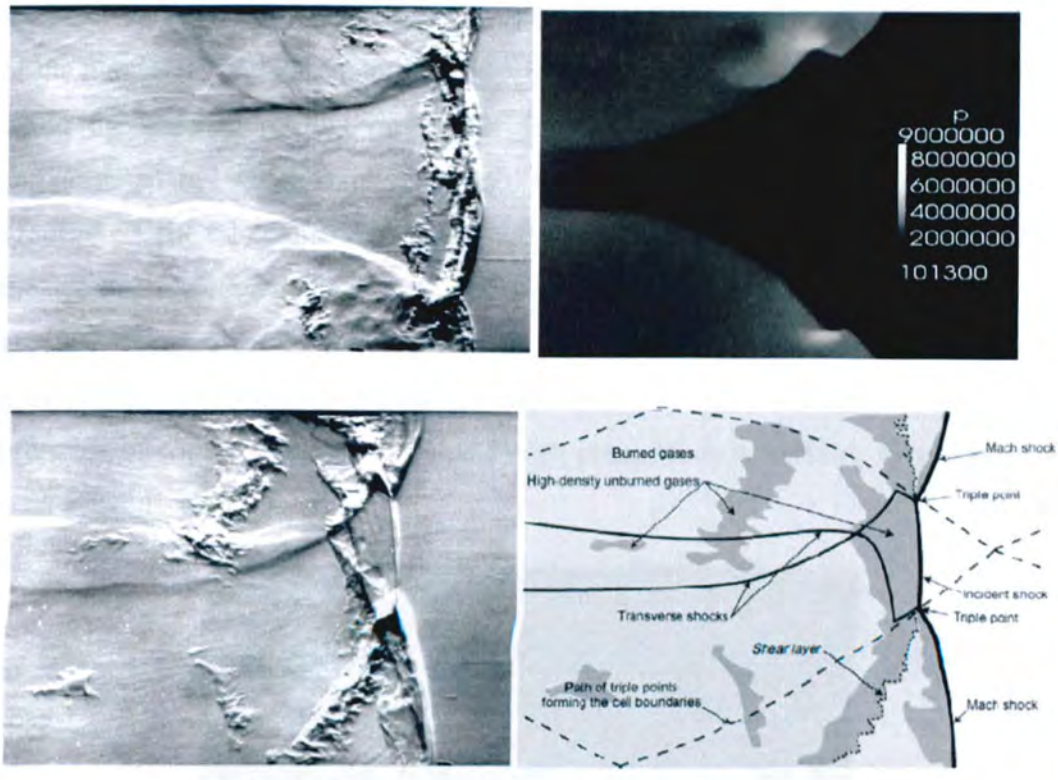

Figure 5-5 CFD results for detonation front (top-right image) and the Schlieren photograph of a detonation propagating in a thin channel, with an accompanying sketch (Radulescu et.al [102]), bottom images.

As mentioned earlier the triple point trajectories produce a "fish-scale" pattern, which is called detonation cellular pattern. In experiments a soot covered foil is normally fitted inside the detonation chamber so when the detonation propagates over the foil the triple point trajectories scratch the soot layer and leave the fish-scale cellular pattern on the foil. This is presented in Figure 5-6 which is obtained in the experiments by Shepherd et al. [95]:

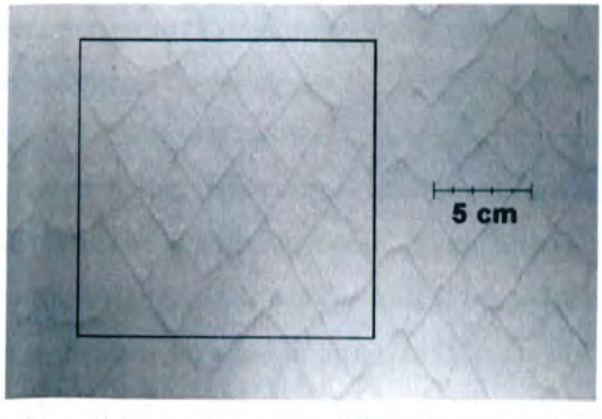

Figure 5-6 Detonation cellular pattern on soot foil experiment by Shepherd et al. [95].

In the present work the detonation cellular pattern is recorded by tracking the locus of the maximum pressure points (triple points) as they are sweeping over the domain while the detonation front propagates forward. An example of this for a high activation energy which results in relatively irregular cellular pattern is presented in Figure 5-7. The CJ detonation velocity for the studied mixture is D_{CJ}=1980 m/s [93], the average recorded detonation velocity in our high resolution studies simulation is D=1997m/s which is in good agreement with CJ predictions. The CJ theory only provides a fixed value 1-D peak pressure but in 2 and 3-D simulations due to presence of triple point and associated high pressure, it is difficult to validate the peak pressure with CJ results.

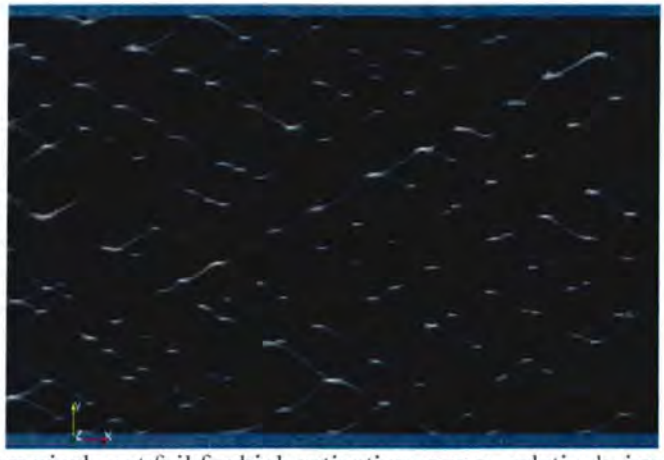

Figure 5-7 Numerical soot foil for high activation energy, relatively irregular cellular pattern.

5-4 Detonation propagation in a bifurcated Tube

Wang et al. [103] carried out a series of experiments to study detonation propagation in bifurcated tubes filled with hydrogen-oxygen mixtures diluted with argon gas. The experiments were performed in a 40mm×40mm square cross section detonation tube [103]. The experimental apparatus is shown in Figure 5-8. The apparatus presented above includes driver sections and very long initial tube for establishing a self-sustained detonation wave, however in the numerical work a very well established and self sustained detonation wave can be initialised in a very short distance. Since the primary aim of the work is to study the detonation behaviour in the bifurcated section, there is no need to simulate the tubes in parts I, II and III. Therefore it suffices to set up a numerical domain only including parts IV and V,

provided that a self sustained detonation wave is successfully initiated and entered the test section. They used pressure sensors, soot foil and schlieren photography to record the results. They also carried out numerical simulations of detonation propagation using detailed chemistry in low pressures (8 kPa). They found that the detonation wave experiences strong disturbance, failure and re-ignition while passing through the bifurcated tube.

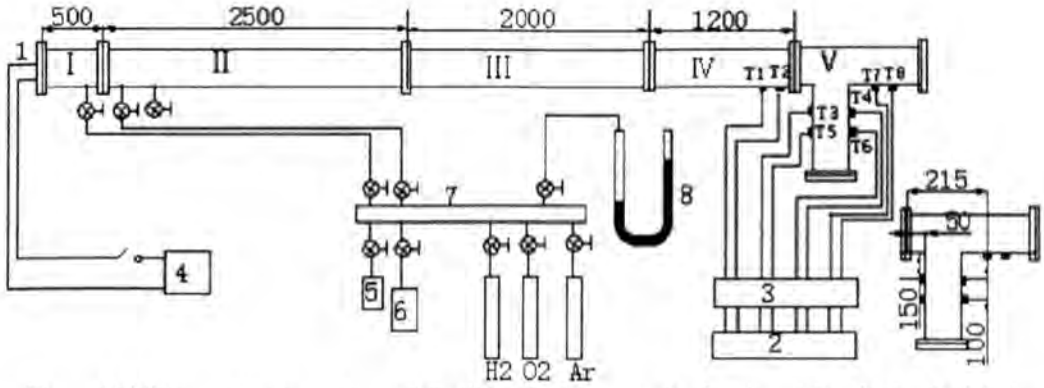

Figure 5-8 Schematic of experimental facilities for Wang et al., showing :1 Spark plug 2 digital oscilloscope 3 Charge amplifier 4 AC power 5 premixed gas tank 6 Vacuum pump 7 Gas distributor 8 Vacuum gauge T1_T8 pizeo-electric transducers I driver section II,III driven sections IV, V test sections (Reproduced from [103])

In the present work 2-D numerical simulations of the above explained experiments are carried out to evaluate the performance of DetoFOAM solver in predicting behaviour of medium scale detonations. For these simulations a 0.2 mm grid size is used. The size of numerical domain exactly matches the size of parts IV and V in the experiment and there is no need to simulate the other parts. The simulations are carried out using parallel processing on 32 processors.

Figure 5-9 shows the numerical results for the detonation wave and the triple points before entering the bifurcated section, the experimental results of Radulescu [6] for the same test condition are included for qualitative comparison of the predicted wave front. As the detonation wave moves onward (from left to right) the trajectories of the triple points sweep over the domain and leave the cellular pattern behind. This is recorded in simulations by tracing the maximum pressure points (triple points) and recording the history of their location over the domain as the simulations go on. When the detonation wave reaches the bifurcated section the leading wave diffracts

from the bifurcated corner. Consequently the leading shock wave and the combustion region decouple due to the detonation wave diffraction. The bottom part of the wave experiences the diffraction first, therefore the maximum flame shock decoupling happens at the areas around the diffraction corner, the top areas of the wave see the effect of the diffraction much later and are least affected by the bifurcated section. This process is illustrated in Figure 5-10, where the top 3 images show the experimental data by Wang et al. and bottom images show the temperature field obtained from the numerical work in the present work. In Figure 5-10, red and yellow areas show the burned regions and the light green areas are the preheated regions due to shock passage. At the bifurcated section the shock-heated region is separated from the reacted region and moving ahead of the flame front, this represents the shock flame decupling and detonation failure due to wave diffraction. The disappearance of the detonation cellular pattern in bifurcated section, as shown in Figure 5-11, confirms the detonation failure at this region.

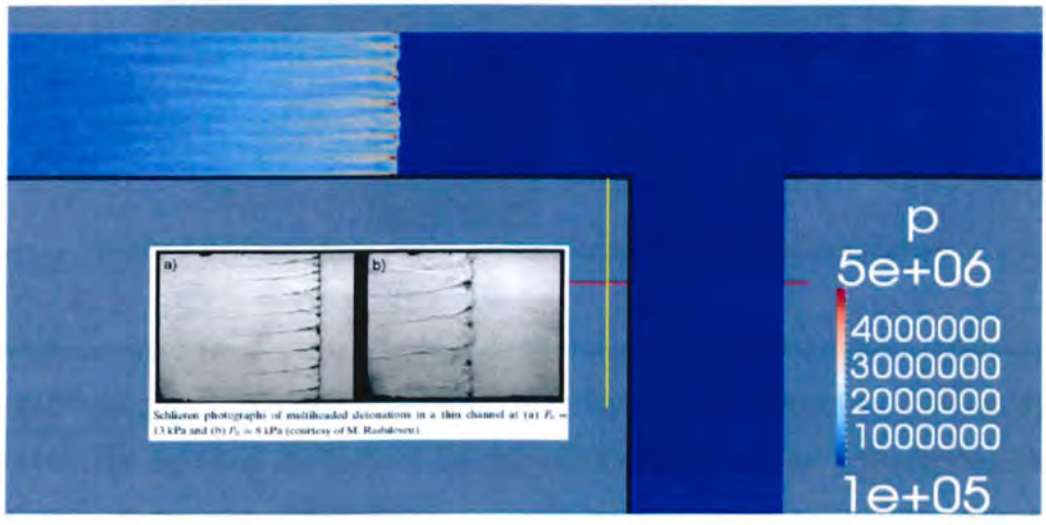

Figure 5-9 Pressure field for detonation propagation in bifurcated tube from present work (top image) schlieren photography of detonation front by Radulescu, (bottom left image) [6]

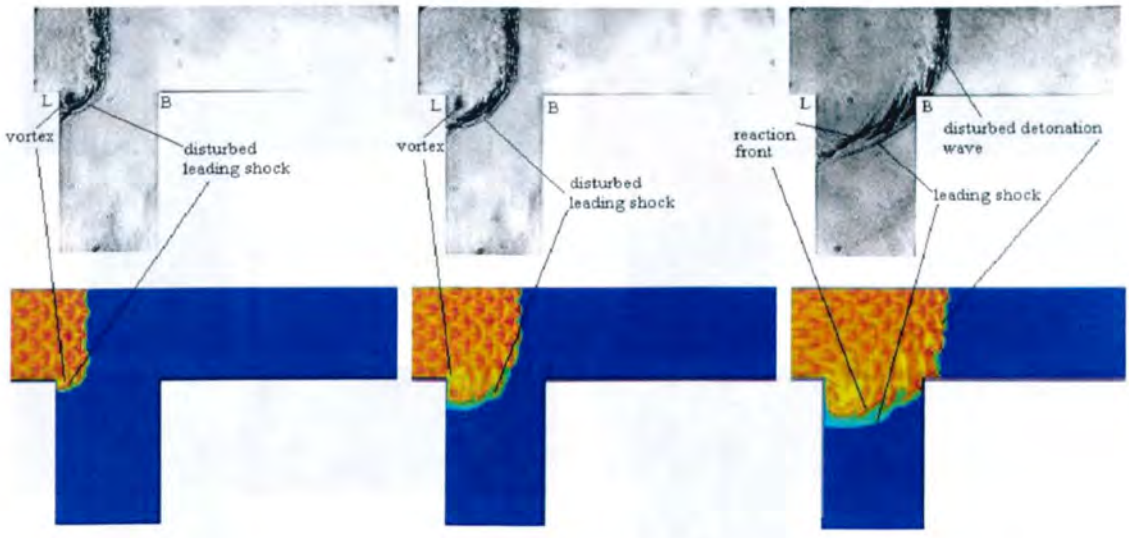

Figure 5-10 Detonation wave diffraction while passing through bifurcated section (the results of current work compared with Wang et al. [103].

Figure 5-11 Detonation cellular pattern vanishing at the bifurcated section.

When the wave front reaches the opposite corner of the bifurcated section, the wave hits the tube wall and reflects back forming a high pressure region around the tube corner. The reflected shock from the right corner of the vertical tube causes rapid increase in pressure, temperature, chemical reaction and consequently leads to detonation re-initiation. This phenomenon is simulated in the present work and compared with the experimental and numerical results of Wang et al. In Figure 5-12. The detonation passing through the horizontal tube only experiences minor disturbance which are not strong enough to extinct the detonation but in the vertical tube the temporary detonation failure due to diffraction persists for some times until the re-initiated detonation grows again. The re-initiation is due to the collision of the reflected shock from the right wall and the decoupled leading shock, this collision results in a self sustained detonation propagating through the rest of the tube.

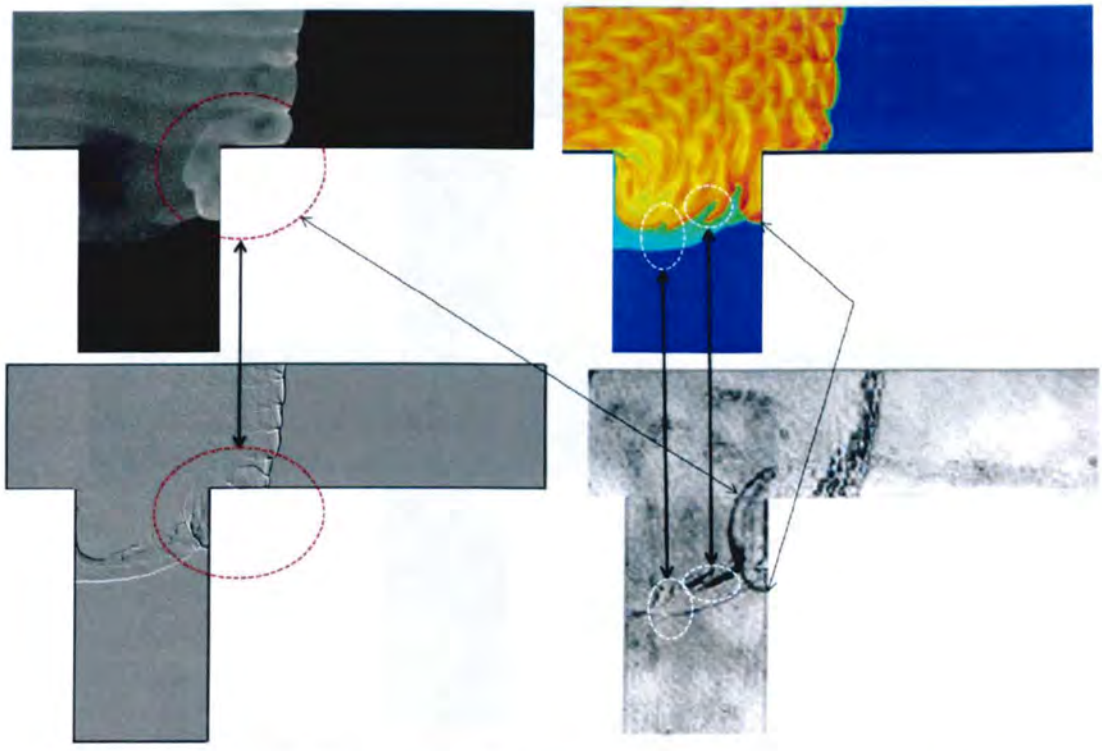

Figure 5-12 The present work results for the detonation propagation, diffraction, failure, reflection and detonation re-ignition in a bifurcated tube compared with Wang et al. experimental and numerical results [103].

Figure 5-13 shows the numerically recorded detonation cellular pattern in the present work compared with the soot-foil detonation cell recordings of Wang et al. [103]. It shows that the detonation wave moving in the horizontal direction never failed but experienced some strong disturbance which is recognisable through the irregularity of detonation cells at the areas around and after the vertical tube. However, in the vertical tube the cellular pattern has completely vanished and does not re-appear for some time which confirms the detonation failure in the vertical tube. When the reflected shock from the right corner of the vertical tube catches up with the decoupled leading shock wave in the vertical tube, a self sustained detonation is formed which propagates through the rest of the vertical tube. This is illustrated in Figure 5-14 which shows the experimental result of Wang et al. [103] (left image) compared with the numerical results of present work for the pressure field (right image) which represents a good agreement in predictions.

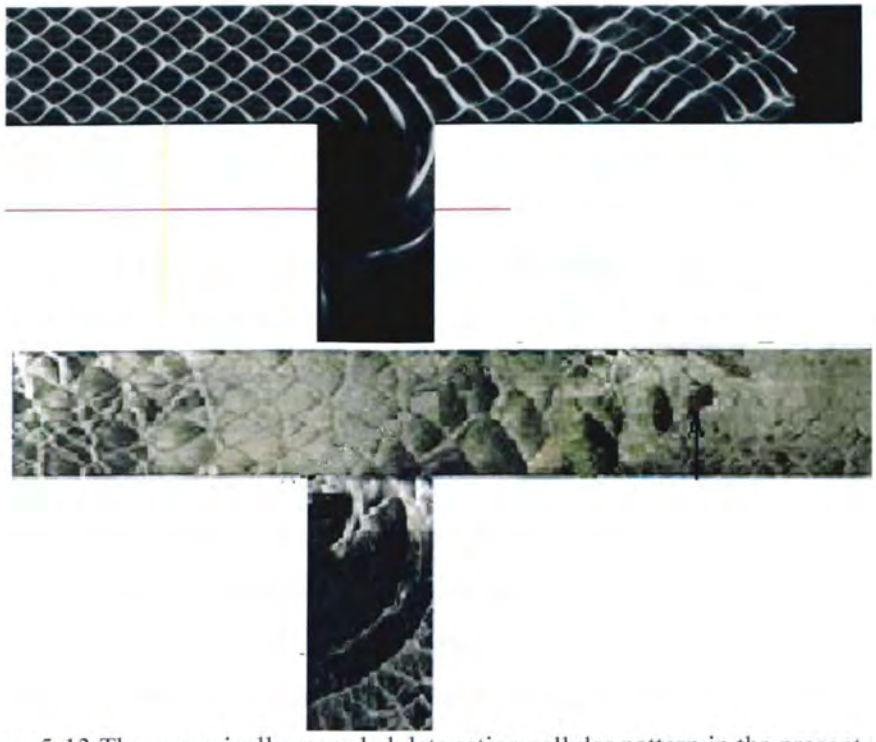

Figure 5-13 The numerically recorded detonation cellular pattern in the present work compared with the soot-foil detonation cell recordings of Wang et al. [103].

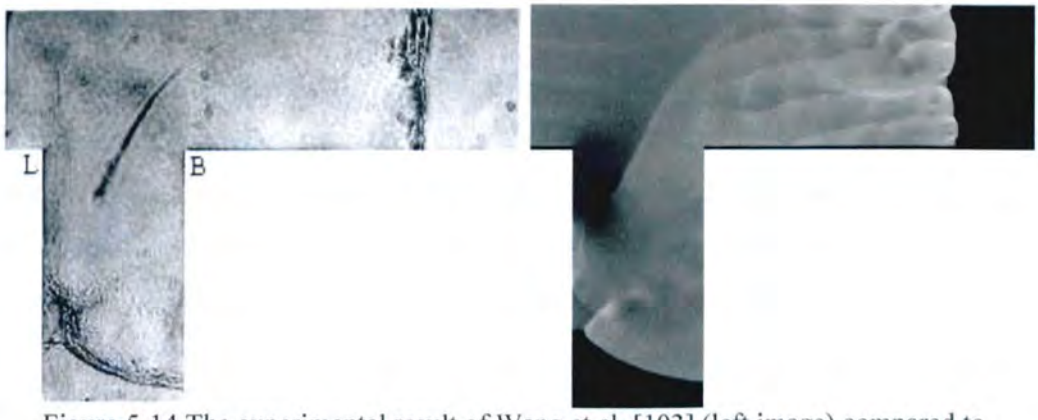

Figure 5-14 The experimental result of Wang et al. [103] (left image) compared to numerical results of present work for the pressure field (right image).

5-5 Diverging detonation and diffraction over the obstacles

Another test study which is carried out in the present work is about the propagation of diverging detonation and their interaction with obstacles. This scenario is particularly of interest for risk assessments in accidental detonations in industrial facilities. In open space or large space geometries such as industrial facilities, a spherical detonation diverges as it expands outwards from the ignition centre. The resulting detonation wave would interact with equipments which might be present at

the vicinity of the incident location. Therefore simulating and analysing the free-propagating diverging-detonation and its interaction with obstacles would be required for such scenarios.

One hypothetical 2-D example is chosen to simulate diverging detonation numerically and provide a brief qualitative description of detonation behaviour in such scenarios. The selected test case is a 0.4m by 0.4m box which includes 3 obstacles and is filled with stoichiometric hydrogen air mixture. Similar to section 5.4, a 0.2 mm grid resolution is used here. The mixture is initially at standard pressure and temperature. This hypothetical cloud is ignited at the centre of the domain and consequently a diverging detonation propagates outwards. The ignition is induced by using a small region of high pressure and temperature (20 bar and 2000 K) at the centre of the domain. The induced detonation wave propagates freely downwards whereas in upward direction 3 obstacles are place in detonation pathway.

Figure 5-15 shows the pressure (right image) and temperature (left image) fields for this simulation. The triple points are distinguishable in pressure field as lighter colour points (high pressure points). The wave at the top of the domain experiences diffraction as it passes over the obstacles, this leads to flame shock decoupling which can be clearly observed in the temperature field. The decoupled pressure waves moving behind the middle obstacle hit each other later on and initiate an overdriven detonation right behind the middle obstacle. Tracking the triple points as the wave propagates outwards sketches the cellular pattern of the diverging detonation. The resulting pattern forms two intersecting sets of logarithmic spirals which are illustrated in Figure 5-16 (left).

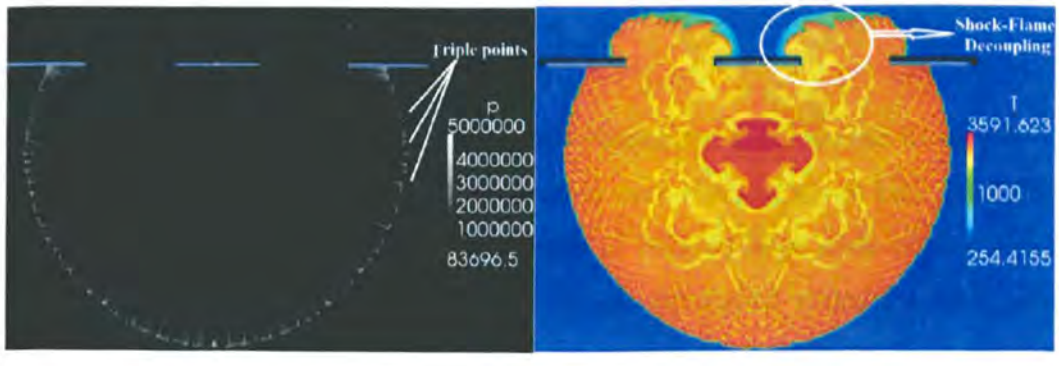

Figure 5-15 Pressure and temperature fields for diverging detonation interaction with obstacles – flame shock decoupling after wave diffraction over the obstacles

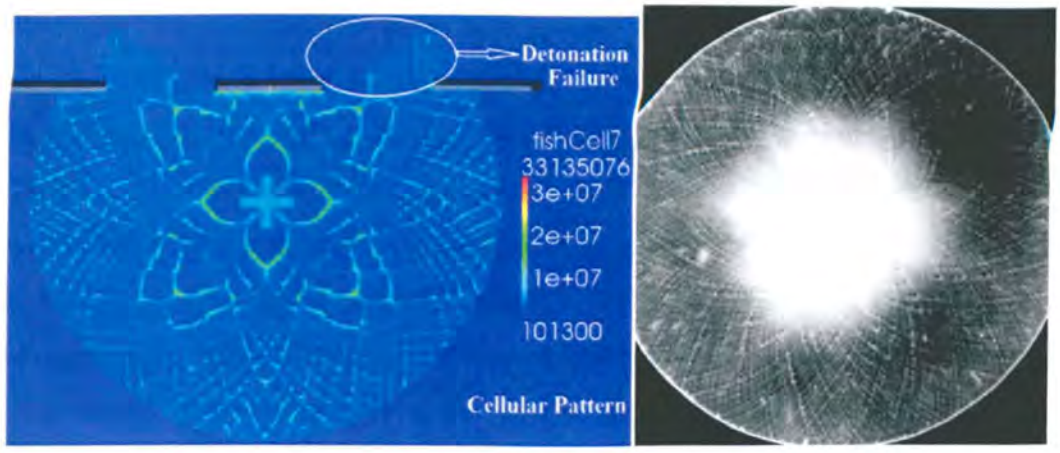

Figure 5-16 Numerical result of the present work for cellular pattern of the diverging detonation compared with Open-shutter photograph of a diverging cylindrical detonation, by Lee [6].

The detonation cellular pattern for the diverging cylindrical detonation experiments, initiated by a powerful ignition source is included in Figure 5-16 to make a qualitative comparison with the current work. Although the two cases are not identical, the two intersecting sets of logarithmic spirals which are formed by trajectories of the transverse waves creating the detonation cell structure can be compared qualitatively. A strong ignition source is required to initiate detonation in both numerical and experimental studies therefore it takes a while until a stable and self sustained outwards-propagating detonation wave is established, as a result no clear cellular pattern is formed at the centre areas of the domain. The disappearance of the cellular pattern right over the obstacles, confirms the detonation failure at those areas which was also predicted earlier from temperature field showing flame-shock decoupling.

5-6 Large scale detonations

The above comparison has demonstrated the capability of our model to reproduce the fine structure of a detonation front. However such simulations on high resolution mesh is costly. This section includes a number of selected large scale studies which are intended to demonstrate applicability of the developed codes for real scale accidental detonation studies.

There are certain difficulties when dealing with large scale simulations which may not be encountered in small scale studies. The large scale geometry and limited computational power mean that relatively coarse grid resolutions need to be used. However, the downside of using relatively coarse grids is that the shock wave will be smeared over at least that distance - and more typically 3 or 4 cells once a curved shock wave is (inevitably) captured oblique to the mesh. In such case, it would also be necessary to implement treatment to avoid artificial acceleration of the detonation wave due to numerical diffusion. The detonation front is artificially thickened by adjusting the chemistry so the available grid can resolve the artificially thickened wave front. The main difficulty arising here is the lack of a proper reaction mechanism which works on such coarse grids. Consequently the reaction mechanism would be grid-resolution dependent and grid independency studies are not applicable. However, reactions are tuned and validated for different grid resolutions and the results can be verified against experimental and analytical studies therefore the grid independency concept does not need to be followed.

5-6-1 Reaction mechanism for large scale scenarios

The available reaction mechanisms in the literature are mainly proposed for DNS simulations and are not applicable in coarse grids. Moreover, there is the possibility of stiffness problem when using detailed reaction mechanism. Therefore, the best option would be to adopt a simple one step global chemistry to avoid stiffness and high computational cost. One could then safely run a coarse grid simulation in a reasonable time at a Courant–Friedrichs–Lewy condition (CFL) of less than 1 and capture the overpressure generated by the detonation wave as well as pressure behind the wave as long as the energy balance (not the kinetic pathway) is maintained.

A modelling approach is hence developed which combines the use of single step chemistry with grid resolutions in the order of millimetres. The chemical reaction which is used here is a single step Arrhenius reaction which can be written as:

$$\omega = A(1 - \alpha_b)exp(-\frac{E_a}{RT}) \qquad 5.6$$

where α_b, ω, A and E_a are progress variable, reaction rate, pre-exponential factor and chemical activation energy, respectively. Standard forms of these reactions can be found in the literature [11-14]. However, for the present study, which involves very large scales and relatively coarse mesh, the reactions have to be tuned to control the source term behaviour so that the solver can capture the pressure and velocity time-history correctly. During this process, it is essential to ensure that the rate of energy release should be correct.

Given the Chapman-Jouguet (CJ) wave speed, which freely propagating waves tend to assume, depends upon the heat release alone, the key effect of the concentration gradient due to dispersion can be captured with the single step model.

Numerical tests were hence systematically conducted to tune the reaction constants in Eq. 5-10 in order to ensure the code can correctly predict detonation parameters compared to CJ values. The CJ pressure for Hydrogen and propane are 15 and 17.5 atmospheres and the propagation velocities are 1980 and 1800 m/s, respectively. Preliminary calculations were firstly conducted for small domains with both relatively fine grids and coarse grids to ensure that the reaction schemes have been properly tuned for different grids to capture the correct detonation pressure, temperature and velocity. Since the reaction parameters depend on the grid size, the values obtained for a specific grid size range might not be suitable for another grid with very different size. Therefore, for each case, depending on the grid size several initial tuning steps are done to pick the most appropriate reaction parameters for the case. To verify the results of the tuned reactions, the predictions for pressure, velocity and other static parameters of detonation were compared with C-J parameters calculated from an in-house equilibrium code [91-93]. This led to a set of pre-exponential factors and activation energies for Eq. 5.7. The values for three different grid sizes are present here as examples:

$$\omega = 2 \times 10^9 \times (1 - \alpha_b) exp(-\frac{10000}{T}) \quad \text{For 0.2 mm grid size}$$

$$\omega = 6 \times 10^{12} \times (1 - \alpha_b) exp(-\frac{12000}{T}) \quad \text{For 10 mm grid size} \qquad 5.7$$

$$\omega = 9 \times 10^{13} \times (1 - \alpha_b) exp(-\frac{14000}{T}) \quad \text{For 50 mm grid size}$$

The performance of the above reactions has been tested on several 1, 2 and 3D simple validation cases.

Using this approach, a number of real scale detonation simulations have been carried out and described in this section.

5-6-2 RUT experiments

The first large scale simulation presented here is for validation purpose only [88, 90] and is intended to reproduce the predictions of detonation experiments carried out at RUT facilities in Russia.

There was a series of detonation tests carried out at the RUT tunnel facilities in Russia, which is one of the standard test cases selected for International Association for Hydrogen Safety (HYSAFE). A part of the RUT facilities is steel-lined reinforced concrete channel with 263 m^3 volume [104]. Schematic of the test channel is shown in Figures 5-17. The dimensions of the tunnel and the ignition location are shown in the Figure 5-17. The tunnel was filled with hydrogen-air mixture with 25% hydrogen. Ignition was started at one end of the tunnel as shown in Figure 5-17. The detonation was started by direct initiation [2] with a high explosive charge of 200 g weight as the initiator [104]. Overall, twelve monitoring points were selected and pressure gages were used to record pressure-time history at these locations. As shown in Figure 5-18, the gauges were placed at the opposite end (with regard to the ignition point) of the tunnel. Pressure measurements are available for 5 of the 12 monitoring points, i.e. points 7 to 11. The present 3-D predictions are compared with these measurement as well as the numerical predictions of Kotchourko [105] for the same set up.

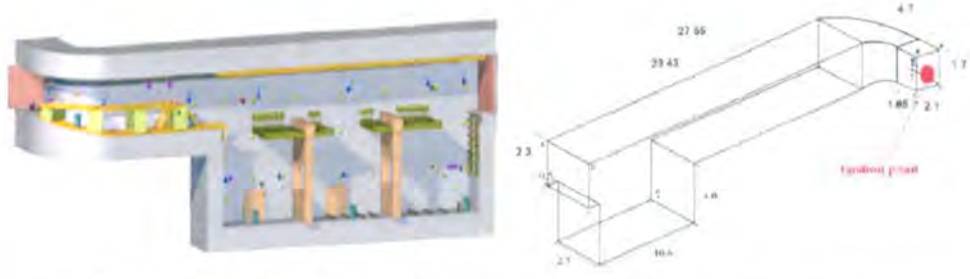

Figure 5-17 The experiment channel and the tunnel dimensions (reproduced from [105])

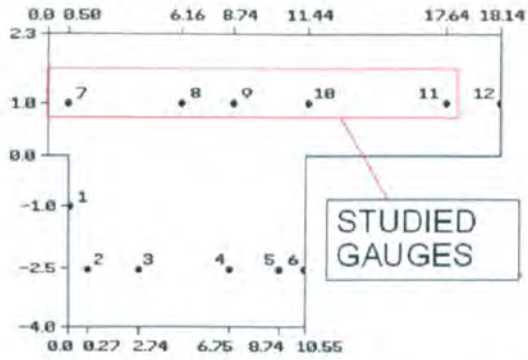

Figure 5-18 Locations of the monitoring gauges (reproduced from [105]).

A structured 3-D hexahedral mesh is used in the domain. The average grid size is 5 cm. Since the domain is uniformly filled with the reactive mixture, it is necessary to keep approximately the same mesh size equally throughout the computational domain. The total number of grids is around 2.2 million. The domain is decomposed into 20 sub-domains for parallel processing. Since the domain is a closed enclosure and the reactive mixture is completely confined, all the boundary conditions are set to wall. The initial temperature is 300 K and initial pressure 1 atm. Ignition was initiated by adding a small region of very high temperature and pressure around the ignition point. The values for the ignition pressure and temperature should be in a reasonable range, if the values are much lower than the CJ detonation values for pressure and temperature, it would either fail to initiate detonation or lead to oscillations prior to establishing a stable detonation wave. On the other hand applying very high initiation pressure and temperature would create an overdriven detonation wave at the beginning before transition to a stable detonation wave. To avoid theses oscillations it is recommended to set the ignition pressure and temperature roughly equal to the CJ values. The pressure and temperature used for initiation in the present work are 15 atm and 3000 K. The volume of the initial hot region for ignition initiation was selected carefully such that the energy added equals to the ignition energy in the experiments.

Following ignition, the simulation was run for 22 milliseconds, which was long enough for the detonation to reach the opposite end of the tunnel and burn out all the mixture. The predictions were then compared with the measurements and predictions of Kotchourko [105].

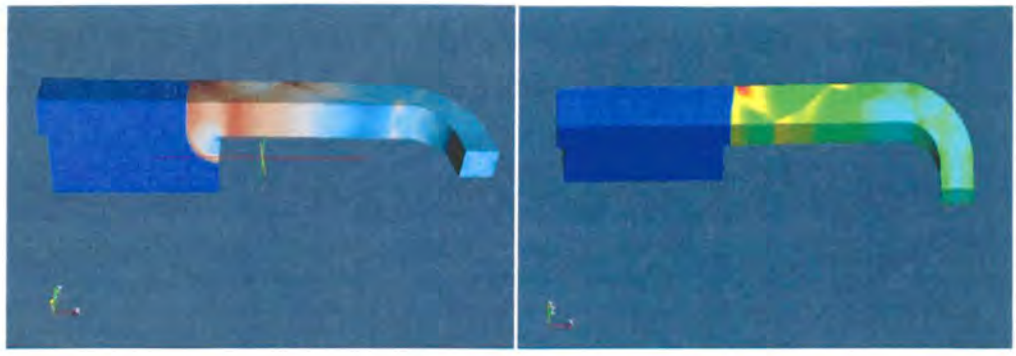

Figure 5-19 The predicted pressure field

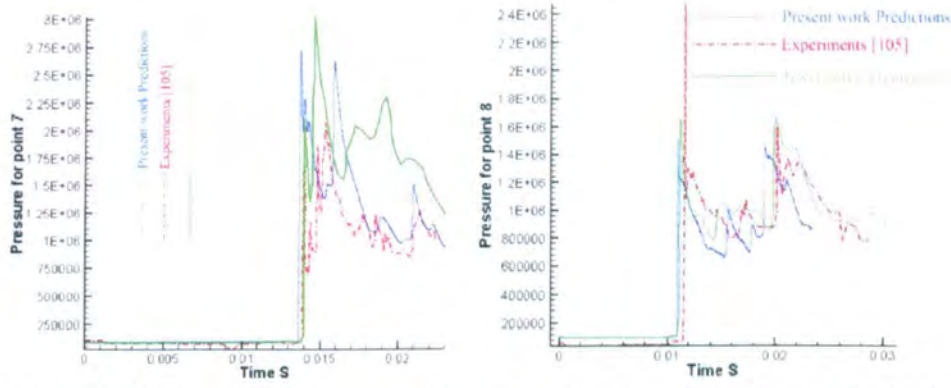

Figure 5-20 The predicted pressure (Pascal) vs time for points 7 (left) and 8 (right).

Two snapshots of predicted pressure fields at two different time instance by using different colour spectrums are presented in Figure 5-19. In both plots, the reflections of shock waves from the side walls are visible. In some areas these reflected shocks create regions with pressure higher than the leading detonation. The diagrams of pressure via time for the selected monitoring points are shown in Figures 5-20 and 5-21, where the red dash-dotted line represents the experimental results; the green lines are the predictions of Kotchourko [105] while the blue dotted lines are the present predictions. It can be seen that the present predictions have followed the same trend as the experiment. It is expected that the predicted peak pressure would be lower than the measurement as the grid resolution was not designed to capture the leading spike. Even at the peak, the present predictions are higher than those of Kotchourko [105]. It should also be pointed out that the measured peak pressure here

was actually higher than the von-Neumann spike due to the reflections of shock waves which further amplified the peak pressure. The predictions are broadly in line with the measurements in terms of the pressure decay following the shock, the arrival of the shock and the actual values of the overpressure at different times.

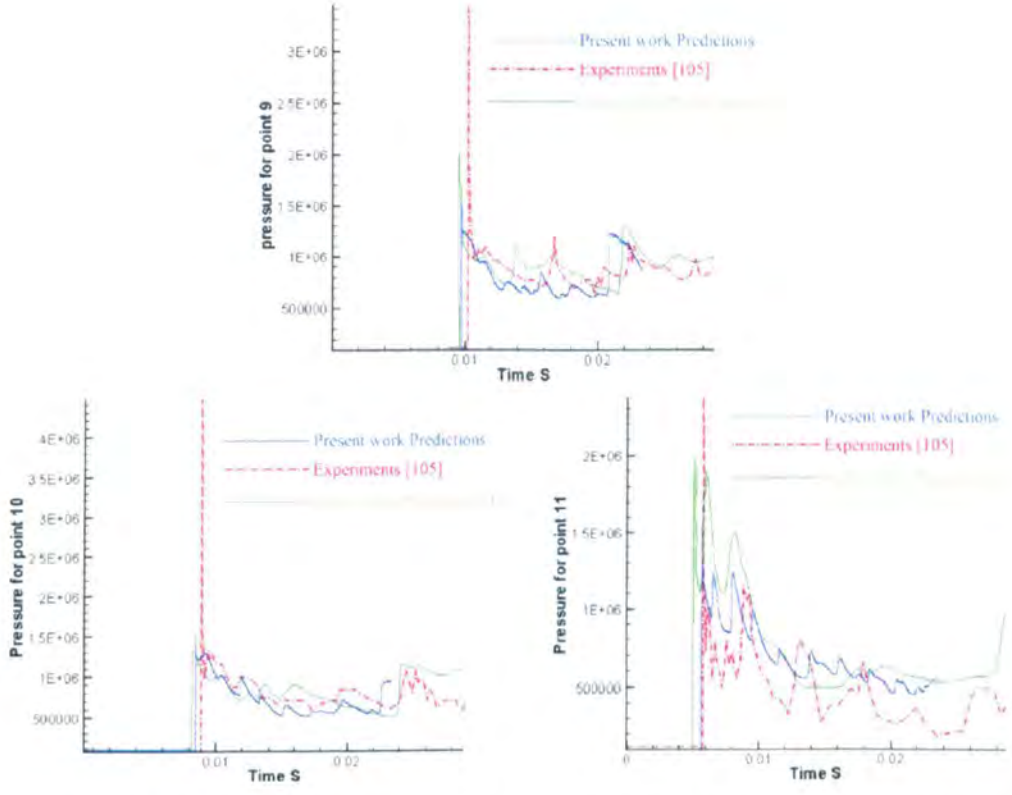

Figure 5-21 The predicted pressure (Pascal) vs time for point 9 (top), 10 (bottom left) and 11 (bottom right)

5-6-3 U-bend shock tube detonation tests

The next test case which is again carried out for code validation is aimed to reproduce the measurements of Frolov et al. [106] for detonation propagation in a U-bend shock tube. Despite the smaller size of the geometry the physics involved in this case is more complicated due to the presence of the U-bends in detonation path way.

The test tube, as schematically shown in Figure 5-22 [106], the total length of the tube is 3 m and has 3 straight sections which are connected by 2 U-bends; therefore the beginning and end of the shock tube are 1.5 m away. The tube is fixed at the experimental stand. The ignition is generated by a shock generator which has 22 cm^3

volume and transmits the ignition via a 14 mm nozzle into the main tube. The shock generator is placed at the left end of the tube, the location of the shock generator (SG) and monitoring points are also shown in Figure 5-22. The tube inner diameter is 51 mm and the tube is fully equipped with measurement gauges and data acquisition systems for data collection. The tube was filled with stoichiometric propane-air mixture at normal atmospheric condition. Ignition was started at left side of the tube. The detonation was initiated with 2.5 g solid propellant [106]. Pressure measurements were reported for 9 out of the 11 monitoring points, i.e. points 2 to 10. In the tests, the solid propellant generates an initial overdriven detonation which later stabilises (1800–2000 m/s) at the first straight segment. The detonation decelerates (may even partially fail) due to the diffraction while passing through the U-bends and re-accelerates again in each of the two straight sections [106].

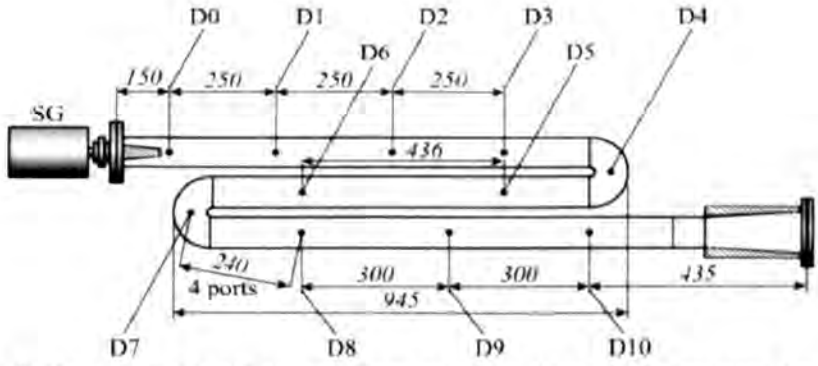

Figure 5-22 The schematic of the shock tube with two U-bends (reproduced from [106])

For the numerical simulations, due to the relatively uniform shape of the geometry, a structured hexahedral mesh with an average grid size of 0.2 mm is used which results in approximately 3 million grid points. As the domain is uniformly filled with the reactive mixture, it is necessary to keep approximately the same grid resolution equally throughout the computational domain. The domain is decomposed into 60 sub-domains to execute parallel processing. Since the domain is a closed enclosure and the reactive mixture is confined, all the boundary conditions are wall. The initial temperature is 300 K and initial pressure 1 atm. Ignition was initiated by adding a small region of very high temperature and pressure around the ignition point. As explained earlier the ignition pressure and temperature must be set carefully to avoid oscillations before establishing a stable detonation wave. Therefore, the ignition pressure and temperature were set close to the CJ values at 20 atm and 3000 K.

Following ignition, the simulation was run for 1.7 milliseconds, which was sufficiently long for the detonation wave to reach the opposite end of the tube and burn out all the reactive mixture.

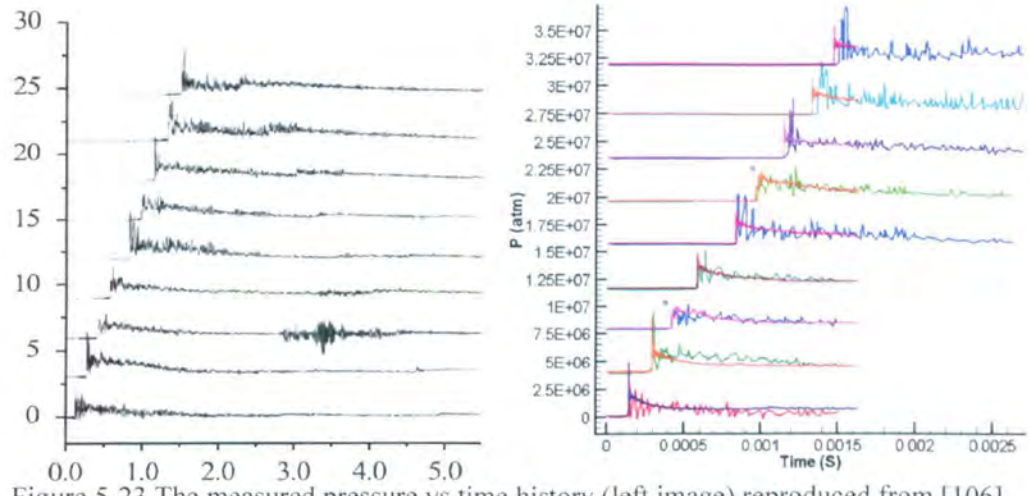

Figure 5-23 The measured pressure vs time history (left image) reproduced from [106], Comparison of the predicted and measured pressure vs time history (right image)

Although Frolov et al. [106] also conducted numerical simulations of detonation in the same U-bend tubes; they did not include any conclusive numerical result or comparison between the predictions and experimental data in their publication, therefore, here we have only compared the current work's results with their experimental measurements. The measured pressure histories at nine monitoring points (D_2 to D_{10}) are presented in Figure 5-23/left where the horizontal axis indicates time (ms) and the vertical axis shows electrical signal recorded by the pressure gauges which is converted to pressure by using the conversion ratio of the gauge and re-plotted in Figure 5-23/right. In Figure 5-23/right, comparison is made between the predicted and measured pressure-time history. Here the horizontal axis is changed from millisecond to second for clarity. The results for the gauges D_4 and D_{10} which are in the first and second bend of the tube are marked with * sign. The start time in Figure 5-23/right is the time of detonation arrival at gauge D_1 meaning when the wave is at D_1, time is equal zero. The exact time of wave arrival at gauge D_2 is equal to 0.000144 s and the distance between D_1 and D_2 is 25 cm. The predicted detonation propagation velocity is hence approximately 1736 m/s, which is within 3% of the theoretical CJ velocity of 1804 m/s. The peak pressure at D_2 is about 40 bar which is consistent with Von-Neumann peak pressure in an overdriven

detonation. It can also be seen that the peak pressure dropped in the U-bend sections while the von-Neumann peak was not captured in the measurements. Frolov et al. [106] observed that the fish cell pattern of detonation vanished in the bend part indicating that the detonation wave was temporarily extinguished for a very short period of time due to the wave diffraction at the bent section. However the results at the next monitoring points show that the detonation has recovered due to re-initiation in the next straight section of the tube.

The predicted pressure history and time of arrival for the first six points match quite well with the measurements. There are some discrepancies for points 7-9 which are thought to be caused by the local detonation deceleration at the U-bend and the subsequent re-acceleration. As mentioned earlier, the current numerical approach is tuned for the consequence analysis of detonation and it may not be entirely accurate when dealing with predictions of such salient features which require resolving the wave front. Nevertheless, the comparison shows that this model can predict with reasonable accuracy the detonation propagation speed and overpressure which are key for safety analysis.

5-6-4 Hemispherical detonations

So far the presented simulations have been mostly in 2D domains, except for the RUT simulations. This might raise the question about applicability of the current work to the 3D geometries. From the technical point of view, since fully compressible 3D governing equations are being solved, there should not be any problem in code performance as it is observed in the RUT simulations. However the author decided to further validate the 3D results of the current work against an experimental case study which is carried out in a hemispherical geometry. Therefore, numerical simulations of large scale hydrogen-air and propane-air detonations in a hemispherical geometry with 300 m^3 volume were carried out. The numerical domain around the hemispherical vapour-cloud is extended in all directions to record the resulting blast pressure and impulse following the detonation phase. Due to the relatively large size of the domain, relatively large grid size is used to render the computation affordable. AMR is used to track the leading wave and

refine the mesh at the shock front. The chemical reaction is grid dependent and is tuned prior to the numerical simulations.

The relatively coarse mesh means that the fine details of the detonation waves such as cell patterns cannot be captured. However the aim of this case study is to investigate the resulting pressure and impulse from large scale hemispherical detonations which is useful for risk assessment and safety investigations. The key objective is to validate the modelling approach for detonation propagation pattern, pressure and velocity for addressing safety issues in real scale accident scenarios. The results of 3D hemispherical stoichiometric hydrogen-air detonation are compared with experimental results of Groethe et al. [107] which were carried out in the same geometry as the current simulations. Further comparisons are made between hemispherical and vapour cloud detonations in stoichiometric propane-air mixture, to investigate the possible deviations in 2 and 3D.

The schematic of the domain and mesh is presented in Figure 5-24. The volume of the cloud is 300 m3 which is equivalent to 10.5 m diameter for the cloud. The domain is extended to longer distance specifically at one side to cover a distance of about 20 m away from the ignition centre. The results are recorded at a monitoring point placed 15.61m away from the ignition centre to compare the predictions with the measurements of Groethe et al. [107].

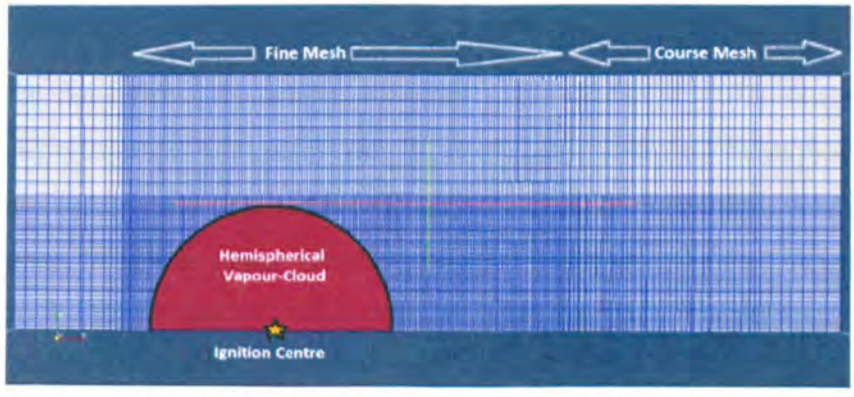

Figure 5-24 The Numerical domain and the Mesh

In Figure 5-24, the red circle shows the location of the hemispherical cloud and the ignition point is shown by a star. The mesh is also shown in Figure 5-24, which is finer at the vicinity of the vapour cloud with grid size of 6 to 8 cm and it is coarser at

locations farther from the cloud. The total number of cells is about 5.5 million. Due to 3D nature of the simulations, it is computationally unaffordable to use finer mesh for the above domain, therefore AMR is used to track and refine mesh at the wave front. The mesh at these areas is refined up to two levels therefore the minimum grid size is about 1.5 to 2 cm. Figure 5-25 (left) shows that the mesh is finer at the wave front and coarser at the other areas with low pressure gradient.

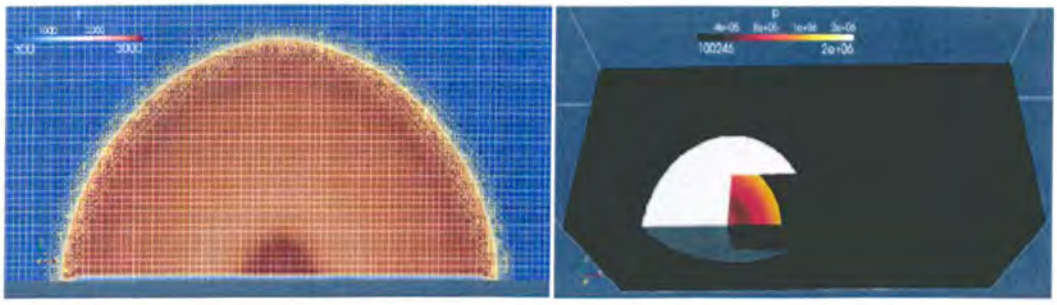

Figure 5-25 The AMR at the shock front (left), detonation in the hemispherical cloud (right)

The detonation wave is initiated by using a small region of high pressure and temperature at the ignition point. The initial pressure and temperature of the ignition point are selected to be roughly equal to CJ values for each reactive mixture. The simulation is run for 0.12 second. Figure 5-25 (right) shows 3D view of the domain cut. The white region shows the cloud location and the red-yellow spectrum shows the pressure field propagating inside the cloud.

Figure 5-26 (top) shows the images recorded by Groethe et al. [107] illustrating the detonation propagation in experiments. Figure 5-26 (middle and bottom) shows the numerical results for temperature and pressure fields at the same time intervals as in the top image. In bottom image the cloud location is shown at left half of each frame to provide a better view of cloud location and make the comparison with the experimental results easier.

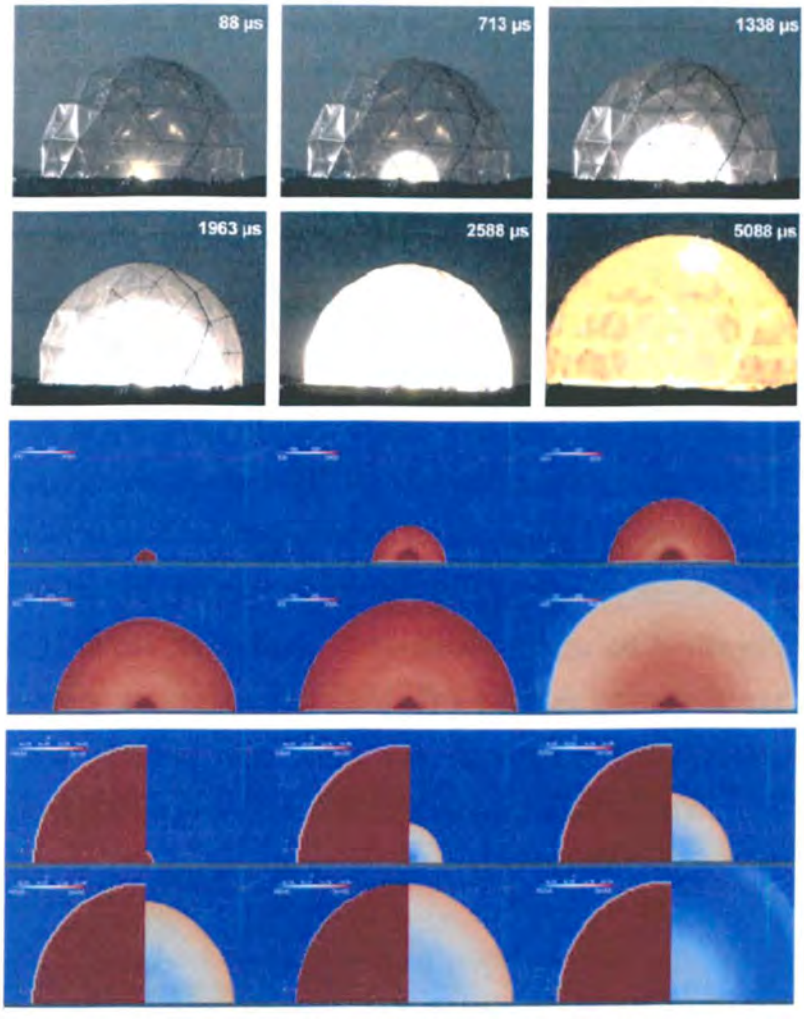

Figure 5-26 The experimental images from Groethe et al. [107] (top image), the temperature fields at the same time intervals (middle image), the pressure field and cloud position (bottom image)

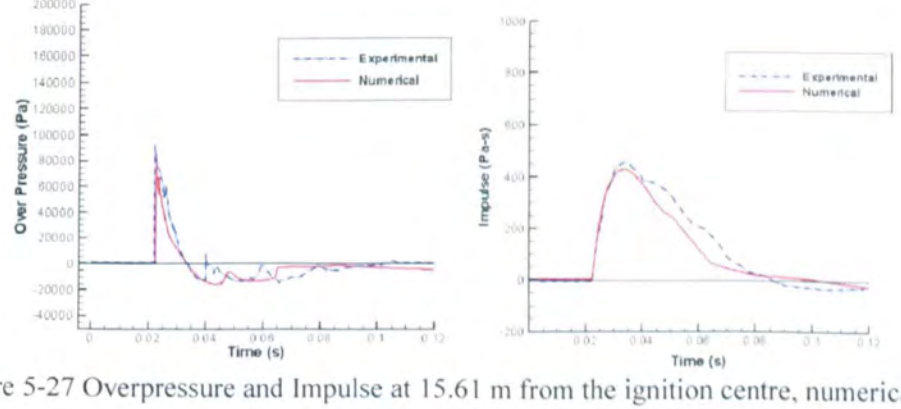

Figure 5-27 Overpressure and Impulse at 15.61 m from the ignition centre, numerical and experimental results.

Figure 5-27 shows the recorded pressure and impulse at a monitoring point located 15.61m away from the ignition centre. The timing of wave arrival and the pressure history shows good agreement with the experimental results. However the numerical peak pressure is slightly lower than the measured value. The numerical and experimental results for impulse are also in good agreement. There is a small deviation after about 0.04s time which is a result of small differences in aftershock expansion.

Detonation of propane-air mixture is also simulated in the same hemispherical domain as presented in Figure 5-24. The equivalence ratio of the mixture is equal to 1 and the initial pressure and temperature for the ignition of the mixture are roughly equal to CJ values. For propane air mixture the P_{CJ}, T_{CJ} and D_{CJ} are about 17.5 atm, 2810 K and 1800 m/s respectively. Detonation propagation is shown in Figure 5-28/(left) by using the temperature field. The left side of each image shows the location of the cloud in white color and the right half shows the location of detonation front. 8 time steps from 0.05 to 5 ms are presented here.

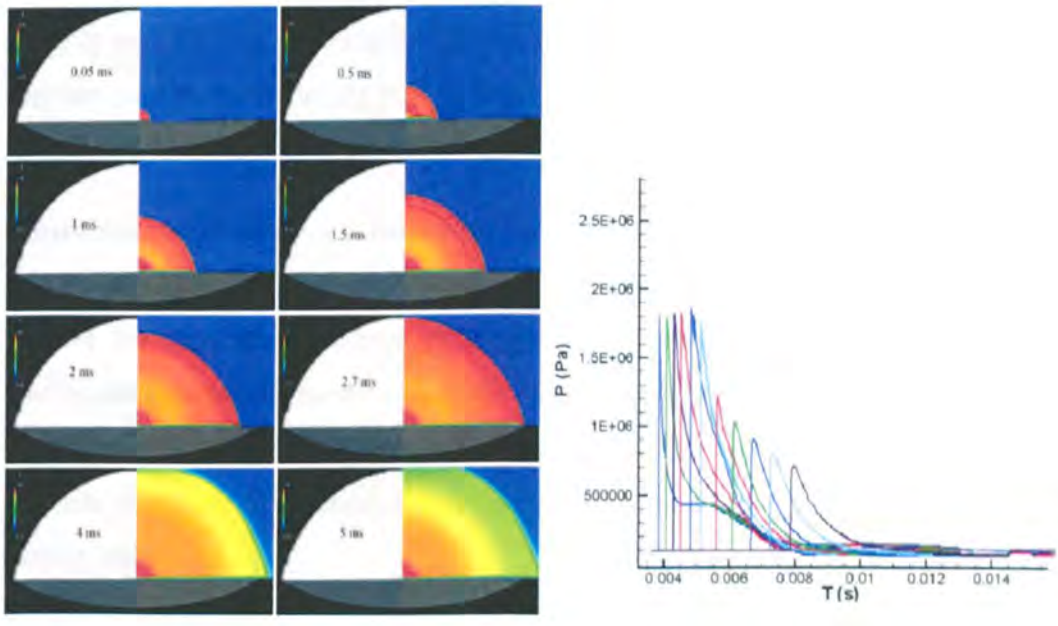

Figure 5-28 The temperature fields at 8 times between 0.05-5 ms (right), Pressure diagram via time (right)

The overall propagation pattern is similar to hydrogen case, but hydrogen detonation velocity is about 9% higher than propane velocity and the wave position via time is slightly different in two cases.

As presented in Figure 5-28/(right) the peak pressure in hemispherical simulation is between 17 to 18 atm which is in agreement with CJ pressure and predictions from 2-D rectangular (2×20 m) vapor cloud simulations [84].

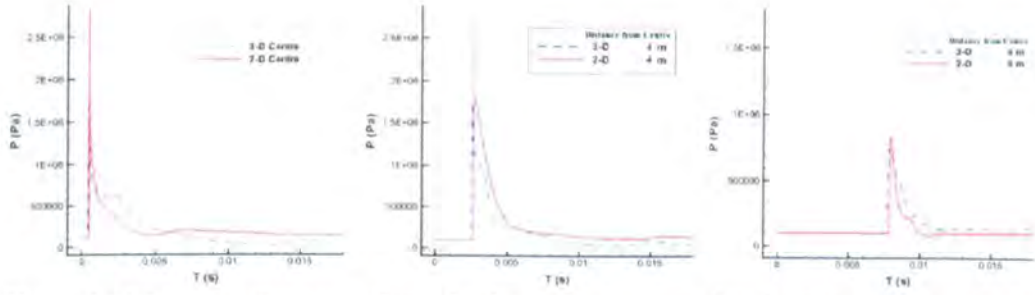

Figure 5-29 Pressure diagram at 3 monitoring points, vapour cloud results (solid-red line) compared with hemispherical results (blue-dashed line).

To compare the results of vapor cloud [84-87] and hemispherical detonations 3 monitoring points, one close to the cloud centre, one close to cloud edge and one at about 5 meter away from the cloud edge are selected and the results for pressure, velocity and impulse are compared at these 3 points. Figure 5-29 shows the pressure diagram for the 3 monitoring points. In all 3 points the time of shock arrival and the peak CJ pressure for vapor cloud and hemispherical results are in good agreement.

Horizontal velocities (U_x) at the monitoring points are compared in Figure 5-30. As it is explained in author's previous research on large scale vapor cloud detonations [84-87], the detonation products experience a long period of high negative velocity shortly after the initial positive velocity phase. This is due to high pressure gradient behind the detonation wave which forces the detonation products to move in opposite direction of detonation and compensates the pressure gradient behind the leading shock.

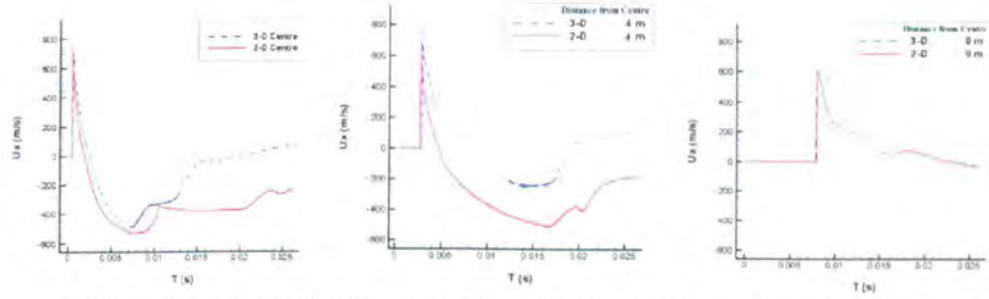

Figure 5-30 Horizontal velocity diagram at 3 monitoring points, vapour cloud results (solid-red line) compared with hemispherical results (blue-dashed line)

Figure 5-30 shows that the recorded positive peak velocity in vapor cloud and hemispherical case is consistent but transition to the negative phase is sharper in the vapor cloud and the magnitude of negative velocity is higher in vapor cloud detonation. This is possibly because the vapor cloud simulations are done for a planar detonation in which the vertical velocity is negligible but in hemispherical simulation a point ignition and radial propagation exist, therefore the vertical component plays an important role. The other reason is the third component of velocity vector in hemispherical geometry which contributes to the overall kinematic energy of the gases.

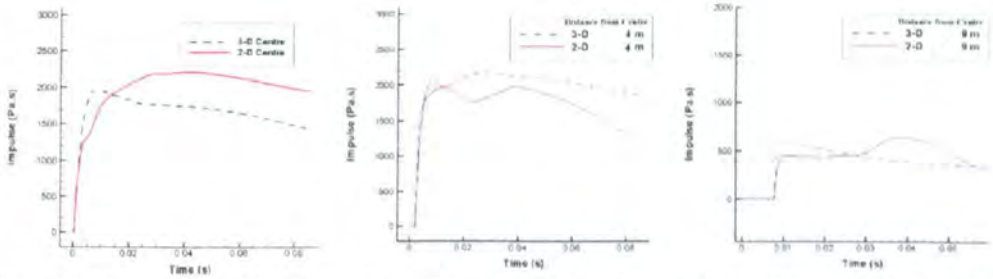

Figure 5-31 Impulse at 3 monitoring points, vapour cloud results (solid-red line) compared with hemispherical results (blue-dashed line).

In Figure 5-31, the overall impulse in vapor cloud and hemispherical detonation are consistent especially right after the shock arrivals and this confirms the Thomas et al. [108] opinion about little effect of Von-Neumann peak compared to CJ peak and aftershock expansion on overall impulse.

5-7 Buncefield incident

The Buncefield depot explosion on 11 December 2005 resulted in the largest fire in Europe since World War II. The severity of the explosions challenges our current understanding of such large scale explosion accidents and as Buncefield Explosion Mechanism Advisory Group admitted, it uncovers design implications which warrant timely consideration by industry [109]. Following the initial investigation, the Explosion Mechanism Group Phase I preliminary research was initiated which concluded that the most likely scenario at Buncefield was a deflagration outside the emergency pump house that changed into a detonation due to flame acceleration in the undergrowth and trees along Three Cherry Trees Lane. The detonation extended to a significant part of the remaining vapour cloud [110]. CCTV images suggested that the cloud was pancake shaped with an average depth of 2m. Based on inventory information, the chemical composition of the cloud is similar to butane or propane in terms of reactivity [110, 111]. It was identified that little was known about the pressure fields caused by detonation of low-lying vapour clouds in the open or when they impinged on buildings [111] while it is known that this configuration effectively maximises the blast damage for a given amount of explosion energy by keeping the energy release near the ground. Sichel and Foster [112] carried out an analysis of planar detonation and found that the pressure behind the detonation front decreases quite rapidly and the positive phase duration near the centre of the cloud is extremely long even though the pressure is relatively low. Fishburn et al. [113] conducted theoretical and experimental studies of the blast effect from a pancake shaped fuel drop-air cloud detonation. The HEMP hydrocarcode, which is based on the CJ-volume burn method which assumes that the flow is one dimensional and the front of the detonation is a jump discontinuity with infinite reaction rate [114], was used to simulate centrally initiated detonation in a cloud

A number of numerical simulations in vapour clouds and pancake clouds have been carried out [80-85] for consequence analysis of medium and large scale hydrogen-air and propane-air planar cloud detonations using the modelling approach developed here. The predictions demonstrated sharp fall of overpressure at the edge of the cloud. In contrary to common belief that the impulse of all explosions will push

objects away from the epicentre, the predictions have revealed the existence of high negative drag impulse within the detonated cloud. Such impulse was also found to vary with heights. The findings from the analysis were in line with the forensic evidence on damages in some historic accidents and challenges previous analysis of the Ufa train disaster which led to liquefied petroleum gas explosion killed 575 and wounded 623 [115], the forensic evidence suggested localised detonation but it was considered as the consequence of fire storms by the investigation team [116].

There were a number of objects (*e.g.* switch boxes, oil drums, cars) distributed across the site and immediate surrounding areas. The condition of these objects after the explosion provided an indication of the overpressure magnitude at the location of these objects. In order to do the numerical simulations, a hypothetical vapour cloud is studied; the shape and dimensions of the geometry are based on the CCTV images right before the explosion.

5-7-1 Planar propane-air cloud

Two-dimensional simulations were carried out for the detonation of a hypothetical propane-air cloud to examine the propagation of the resulting blast wave in the surrounding air and the pressure impulse. Predictions were conducted for clouds of different aspect ratios to investigate the effect of cloud height on the drag impulse generated by high speed gasses that follow the detonation waves. Here just the pressure, velocity and drag impulse for one of the aspect ratios are presented.

The drag impulse can be determined using the Morrison Equation [117]:

$$I = \int f_D dt = \int_0^{t_i} \left\{ \left(\frac{1}{2} C_d \times \rho \times A \times Ux \times |Ux| \right) + \rho \frac{dU_x}{dt} \right\} dt \qquad 5.8$$

The second term inside the integral is called unsteady impulse which is generally much smaller than the steady (first) term so the Morrison Equation can be rewritten in the following simplified form:

$$I = \int f dt = \int_0^{t_i} \left(\frac{1}{2} C_d \times \rho \times A \times Ux \times |Ux| \right) dt \qquad 5.9$$

Simulations were carried out for the detonation of a planar propane cloud which is surrounded by air. The computational domain is of rectangular shape with dimensions of 160 × 70 m as shown in Figure 5-32:

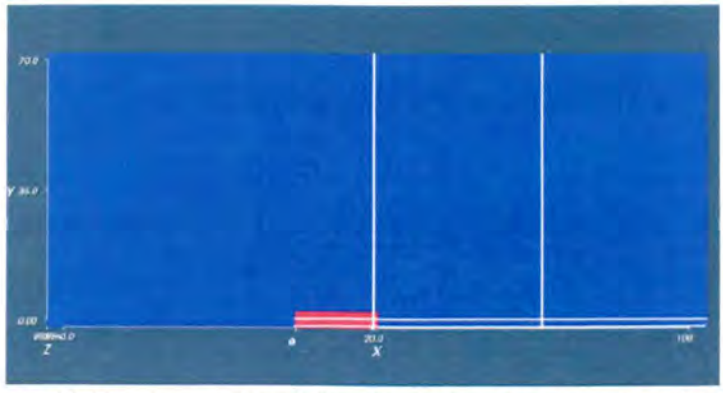

Figure 5-32 The computational domain for the planar propane-air cloud.

The extent of the stoichiometric propane-air cloud is 20 × 2 m (red box) placed at the origin of the domain. The rest of the domain (the blue colour region) is filled with air.

Due to the relatively large size of the domain, it is necessary to divide the domain into several sections and use appropriate grid resolution and pattern for each region based on its relative level of importance. For example, inside the cloud a finer structured mesh (10 mm) is used. From the edge of the cloud and its immediate surrounding where the blast wave is expected to be strong, the mesh resolution is only decreased slightly. Further out, the unstructured mesh gradually becomes coarser. Figure 5-33 shows the mesh pattern in the immediate region around the cloud, where the mesh inside the cloud is so fine that the grids are almost un-distinguishable. As discussed, such grid resolution will not resolve the shock waves but should predict with reasonable accuracy the pressure decay and propagation pattern with the tuned chemistry.

Figure 5-33 The mesh pattern around the cloud.

A hot high pressure region was used to initiate the detonation. This consisted of a vertical line of cells along the left edge of the cloud set to 3000 K and 20 atm. Pressure, density, velocity and temperature were monitored at selected points along several horizontal and vertical lines. Results are analysed in particular for several points along the monitoring line which is placed 1 m above ground for estimation of potential damage at this level through analysis of the pressure, velocity and drag impulse at 5 monitoring points. The coordinates of these points are given in Table 5-1.

Table 5-1 Coordinates of the monitoring points

Monitoring points	Coordinates
1	(0.2 1.0)
2	(5.0 1.0)
3	(10 1.0)
4	(12 1.0)
5	(19 1.0)

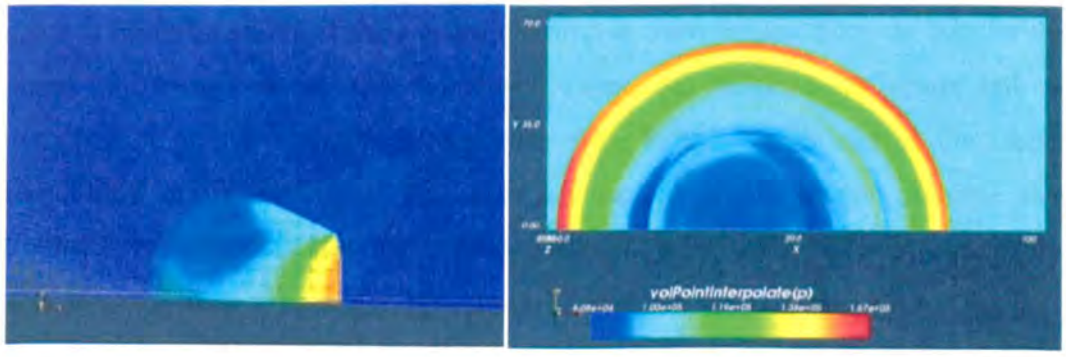

Figure 5-34 The predicted pressure field for the planar detonation (left) The predicted pressure field for the blast wave (right).

The pressure field for detonation and blast wave propagation are shown in Figure 5-34. Following initiation, a planar detonation propagates towards the right. When the detonation reaches the right edge of the cloud, the mixture is all burned and the blast wave propagates into the surrounding air and decays rapidly with distance from the initial cloud. As the detonation wave propagates through the propane-air mixture and then transmits from the cloud to air, due to the free boundary on the top of the cloud, the detonation wave diffracts. In addition, due to high pressure of detonation products, the shock wave propagates outwards from both the top and left of the cloud.

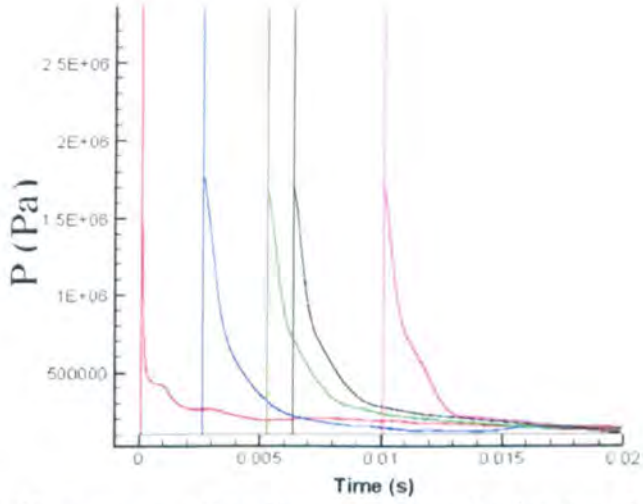

Figure 5-35 The pressure vs time diagram at selected points 1 m above the ground

The pressure diagram for the monitoring points are shown in figure 5-35 with predictions for points 1 to 5 shown in red, blue, green, black and pink colour, respectively. Figure 5-36 shows more points along the monitoring line 1m above the ground. It can be seen that there is a sharp drop in overpressure from the edge of the cloud (0.01 ms) where the aftershock expansion starts. Such sharp fall of overpressure at the cloud edge is in-line with forensic evidences in the recent Buncefield depot explosion. As explained earlier, it is thought possible that transition to detonation is the most likely scenario, when the initial explosion of the very large gasoline vapour cloud accelerated through a line of trees.

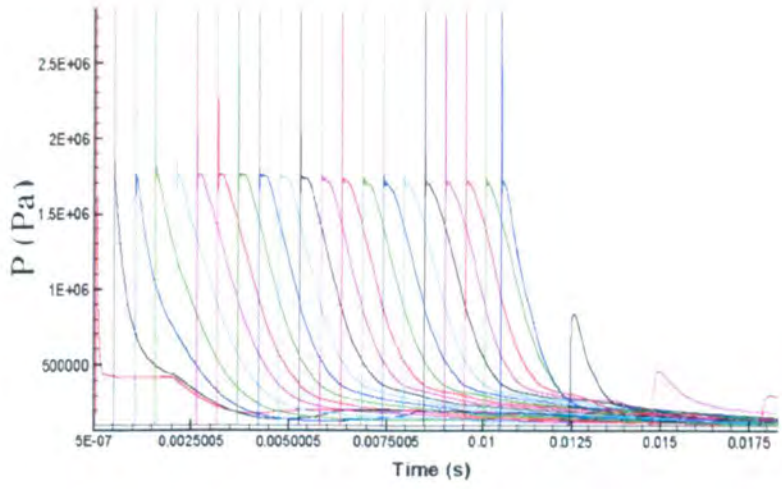

Figure 5-36 The pressure vs time diagram along the monitoring line 1 m above the ground

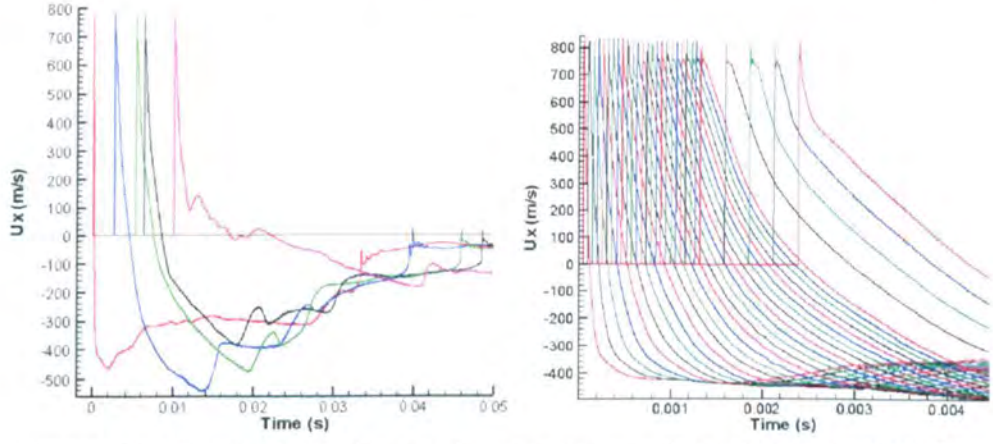

Figure 5-37 The velocity vs time at selected points 1 m above the ground (left), The velocity vs time, 1 m above the ground (right)

Figure 5-37 (left) shows the velocity *vs* time at monitoring points 1 to 5 while the right image shows more points along the monitoring line 1m above the ground. It can be seen that immediately following the initiation of detonation, there is a very short period where the gas velocity shots up to very high values of about 800 m/s which is quite consistent with the CJ theory which states that the detonation products right after the detonation wave travel with sound speed with respect to the leading shock. This is followed by a relatively longer period of negative velocity. While the shock propagates towards the left and the detonation propagates towards the right, the product expands and then over-expands between them. In order to match the high pressure behind the shock or the detonation wave and the over-expanding low pressure region, secondary shocks form and propagate inwards, leading to a relatively longer period of negative velocity. With time elapsing, in the product

region, there exist shock-shock interaction and shock-expansion wave interaction, etc.

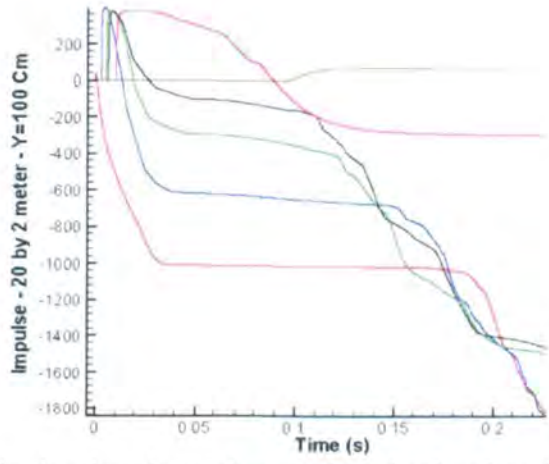

Figure 5-38 The drag impulse vs time at selected points 1 m above the ground

The drag impulse *vs* time for points 1 to 5 is plotted in Figure 5-38, where the sequence and colour of the curves is the same as in Figure 5-35. The drag impulse is calculated using the simplified Morrison Equation, Eq. 5-9, based on a cumulative total for each time step. The results show that within the cloud, the drag impulse is predominantly negative (towards the left) while outside the cloud the impulse is positive (towards the right). This finding has important implications when examining forensic evidence following explosion accidents. The negative impulse is caused by high negative velocities of the gasses in the opposite direction of the detonation wave which last for a relatively longer period of time in comparison with the expansion in the direction of detonation wave. This happens shortly after the detonation passage at each point. When the detonation passes a reference point, it forces the products behind it to move in the positive direction with the sound speed relative to the shock (CJ theory). This leads to creation of high pressure gradient behind the detonation wave. When the detonation is far enough and the gasses cannot see its effect this pressure gradient forces the gasses to move in the opposite direction and compensate the pressure gradient behind the shock, which is caused by the forced movement of products by detonation. The result is a relatively long period of negative velocity after the shock passage and the generation of a strong negative impulse. Weather the overall impulse is positive or negative depends on the position of the monitoring point. As shown in Figure 5-37, nearer to the origin of detonation the negative velocities last much longer and are of higher values, leading to higher

negative impulse. But for the points which are further away from the origin, the positive phase is dominant producing an overall positive impulse. In most detonation studies, the focus has been on the pressure impulse. The present work has demonstrated high speed gasses can generate a significant drag impulse that has more determining influence on the damages following a detonation accident. This point is of important implications for accidental investigations. The misconception exists that the over pressure from an explosion will impact on the objects in the outward direction, only the drag forces induced by fire storms would be inwards. A particular example is the published analysis of the Ufa Train Disaster [115, 116], which happened on June 4, 1989 near the town of Asha in the Soviet Union. A liquefied petroleum gas explosion killed 575 and wounded 623, making it the most deadly railway accident in Soviet history as two trains passing each other throwing sparks near a leaky pipeline. The explosion, estimated to be 10 kilotons of TNT, was so powerful that it blew out windows in Asha, eight miles (13 km) from the epicentre. Photographic records illustrated the breaking and blowing down of the trees in the large forest [116]. It was also reported that the trunks of the trees were snapped at about one-third of their heights by the high-velocity wind which bent the crowns, and the treetops were directed toward the epicentre [116]. Previous analysis attributed this to fireball-induced wind partly because of the directional indicator which is pointing to significant drag force towards the epicentre [116]. However, it is unlikely that fireballs can generate such huge drag impulse. While the drag impulse from an explosion will be directed away from the epicentre, the present work has shown that in the event of detonation (even if the transition to detonation is just at a localised level), significant drag impulse can be directed towards the epicentre.

5-7-2 Planar hydrogen-air cloud

Numerical simulations for hydrogen-air detonation in the same cloud as previous section are also carried out to study the hydrogen detonation behaviour. All the settings are the same as the ones explained above and only the mixture is different. Pressure velocity, drag impulse etc are monitored at the points presented in table 5-1

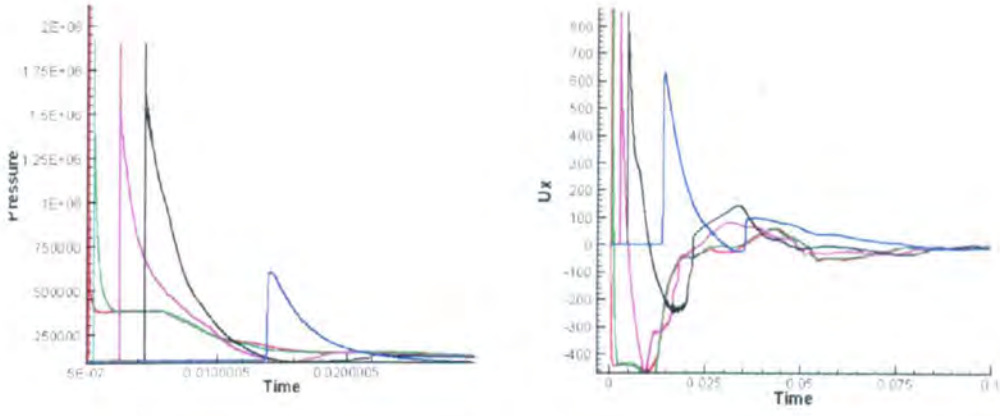

Figure 5-39 The pressure-time diagram the line 1 m above the ground, P unit is Pascal (left) -- The velocity-time diagram at selected points 1 m above the ground, U unit is meter per second (right).

The pressure and velocity diagrams for the monitoring points are shown in Figure 5-39. Predictions for points 1- 5 are shown in red, green, purple, black and blue colour, respectively. It can be seen that, similarly to the propane case, immediately following the initiation of detonation, there is a very short period where the gas velocity shots up to very high values. This is followed by a relatively longer period of negative velocity which is explained in the previous section.

Figure 5-40 shows the drag impulse which is again predominantly negative (towards the left) while outside the cloud the impulse is positive (towards the right). The negative impulse is caused by high negative velocities of the gasses in the opposite direction of the detonation wave which last for a relatively longer period of time in comparison with the expansion in the direction of detonation wave. Again, weather the overall impulse is positive or negative highly depends on the position of the monitoring point. As shown in Figure 5-40, nearer to the origin of detonation the negative velocities last much longer and are of higher values, leading to higher negative impulse. But for the points which are further from the origin, the positive phase is dominant producing an overall positive impulse.

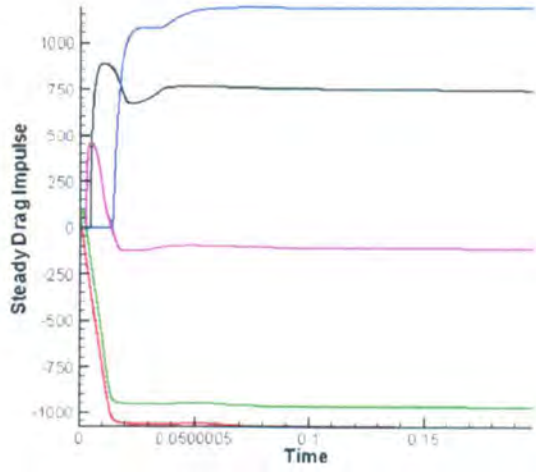

Figure 5-40 The drag impulse vs time at selected points 1 m above the ground

5-7-3 Pancake shaped cloud, Fishburn, 1981

As explained in pervious sections, the author has carried out a series of studies to understand the Buncefield explosions [109, 110]. The main bulk of these studies were carried out to aid understanding of the severe damages which indicated overpressures well above those in an open turbulent deflagration. These involved numerically simulating the detonation of pancake shaped clouds using similar settings and configurations as those experimentally tested by Fishburn [113]. This is presented here in this section. To expand the work and analyze the loading effects on equipments a second series of studies involving experimental and finite element (FE) analysis of lightweight metal boxes, similar to the lightweight steel junction boxes on the site located within the area covered by the gas cloud at Buncefield are jointly done [85]. The FE analyses are not presented here.

Fishburn et al. [113] conducted theoretical and experimental studies of the blast effect from a pancake shaped fuel drop-air cloud detonation. The HEMP hydrocarcode, which is based on the CJ-volume burn method which assumes that the flow is one dimensional and the front of the detonation is a jump discontinuity with infinite reaction rate [114], was used to simulate centrally initiated detonation in a cloud. The numerical simulations were conducted for a pancake-cylindrical case with 128 m diameter and 4.57 m height in 2-D while the experiment was conducted with an irregular shaped cloud of approximately 70 m diameter and 5.8 m thick detonated from two corners near the cloud edge. The theoretical results compared satisfactorily with pressure data obtained from detonation of a large (~70m nominal

diameter) hydrocarbon fuel-air cloud. They have mentioned that the pressure profile does not depend on the radius, except for the outer edges

In the current work, the previously explained numerical approach is used to predict the experimental works of Fishburn et al. [113]. Computations were set up based on the experimental configurations of Fishburn et al. [113]. As shown in Figure 5-41, the experimental domain was a non-uniform cloud, being nominally 70 m in diameter and 5.8m thick, created from fuel vaporisation from the 4 points which are marked in red. Ignition was started from the two points at two opposite corners of the cloud and the resulting detonation started to move inwards. Computations were set up for a cylindrical-pancake cloud shape of 80 m diameter with one ignition in the centre of the cloud. In order to save computational time, the cloud is assumed to be axisymmetric and wedge boundary conditions are used.

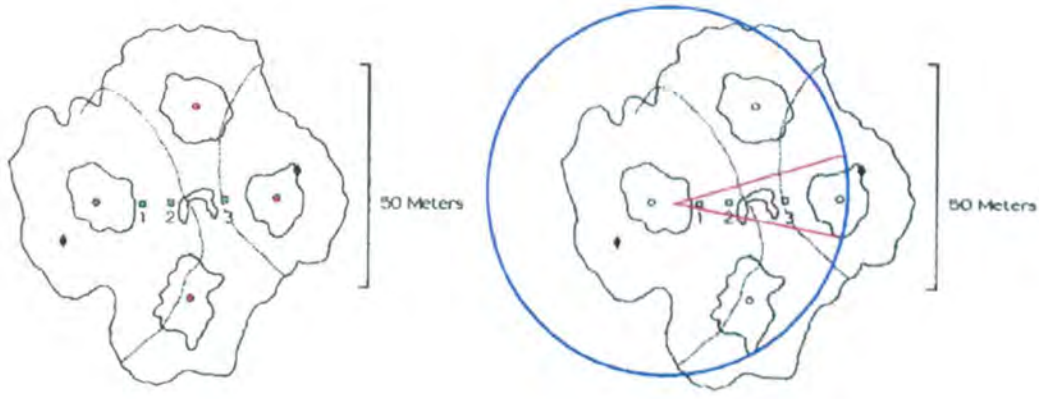

Figure 5-41 Overhead view of experimental cloud (reproduced from [113]) and the wedge shaped computational domain.

Measurements are available for pressure and impulse at the 3 monitoring points shown in Figure 5-41.

In Figure 5-42, comparison is made between the predicted and measured impulses at these points and shows reasonably good agreement. The predicted pressure-time history at 13 monitoring locations of which 7 are within the cloud, are plotted in Figure 5-43 (left). It can be seen that there is a sharp drop in overpressure from the edge of the cloud where the aftershock expansion starts. Such sharp fall of overpressure at the cloud edge is in line with some forensic evidence at Buncefield. As shown in Figure 5-43 (right), among the lines of the crushed cars, the rest of

them were much more significantly damaged than the one in the front. This is thought to be an indication that there was a sharp fall in the pressure wave between the location of front car and the one behind.

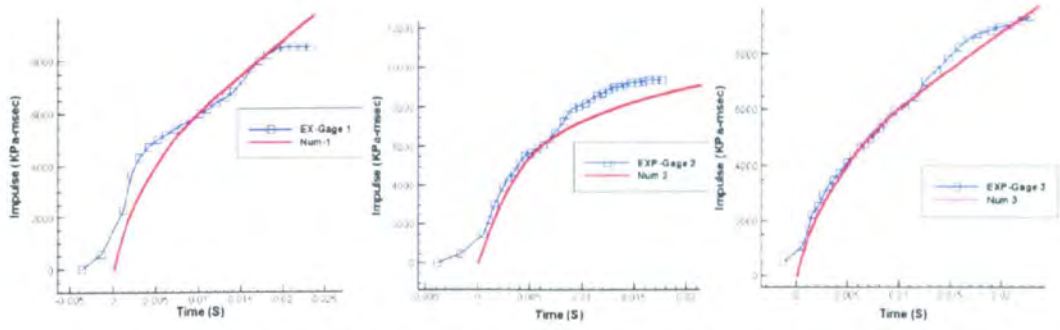

Figure 5-42 Comparison of the predicted and measured drag impulse for the three monitoring points

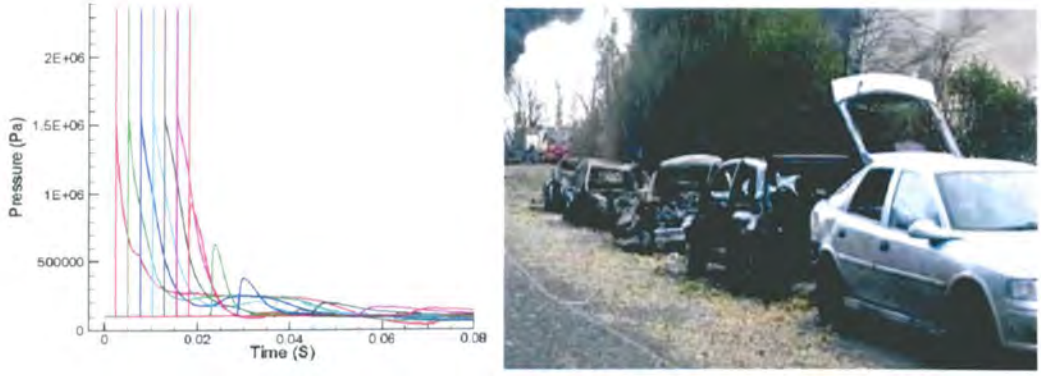

Figure 5-43 The predicted overpressure at the monitoring points (left), Lines of crashed cars at Buncefield site (reproduced from [109]) (right)

Comparison is made between the measured and predicted pressure-time history in Figure 5-44. Both show very similar trends and give the same maximum close to the CJ value. There are, however, some discrepancies which might be partly caused by the assumption of uniform fuel concentration in the numerical simulations while the actual fuel concentration in the cloud was non-uniform in the experiment. In the measured pressure-time history for the second monitoring point, a second pressure peak which is significantly lower than the first peak can be seen. As mentioned earlier, there were two ignition points on the two corners of the cloud; this is thought to be possibly the result of the blast wave generated by the second detonation wave

coming from opposite direction moving towards the second monitoring point. As the wave reached this location, the local fuel was already consumed by the first detonation wave and what was recorded was just the blast wave propagating through the burnt products. However since we are modelling a uniform cloud with one ignition point in the centre, this second peak does not exist in the current simulations.

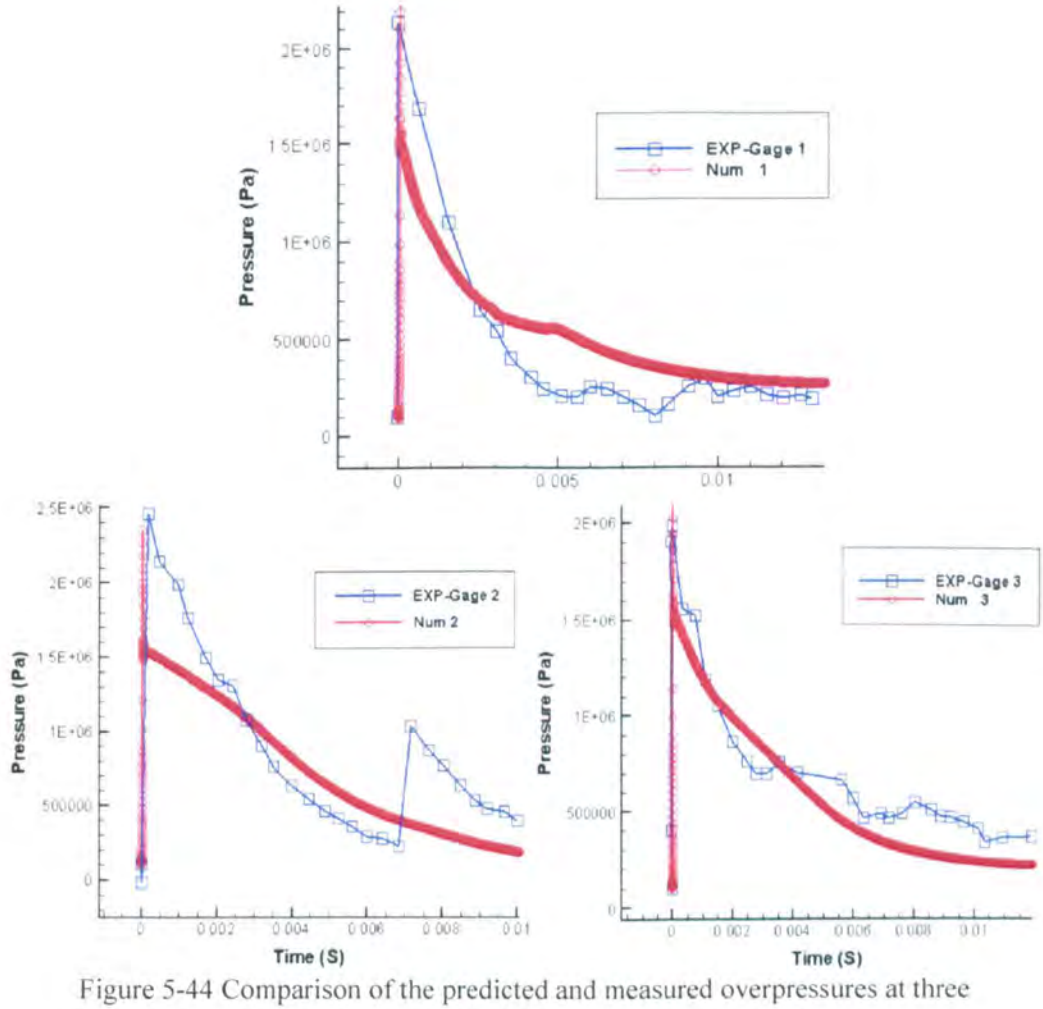

Figure 5-44 Comparison of the predicted and measured overpressures at three

5-8 CJ Burn method and detonation shock dynamics

As mentioned earlier, Fishburn et al. [113] used the HEMP hydrocarcode, which is based on the CJ burn method. The CJ burn method is based on 1-D CJ solution of detonation in which it is assumed that the flow is one dimensional and the detonation front is a jump discontinuity with infinite reaction rate [114]. However this is

extended to 2D and 3D geometries, meaning that CJ burn codes assume that the detonation wave propagates in all directions with CJ velocity.

In the CJ burn method no chemistry is involved therefore only shock dynamics and flow field is solved with a forced discontinuity (as the detonation front) in the domain. The benefit is that the solver can run faster and larger computational grid may be used, this is all because the reaction mechanism is ignored and a fixed moving wave is imposed on the flow field. As a result the CJ burn method has become popular especially for industrial applications. However there are very significant shortcomings in CJ burn method which may result in extremely wrong predictions.

In order to illustrate this, a code based on CJ burn method has been programmed. Its prediction for a detonation in a hypothetical geometry is compared with the reactive Euler equations approach.

The CJ burn method and detonation shock dynamics (DSD) is based on Constant velocity for detonation propagation ($U = D_{CJ}$) in all directions. The way it works is that, the solver analyses the domain at the beginning of the solution and determines the distance of each computational cell, l^i, to the ignition point or pre-existing detonation front at start time. Based on theses distances and the CJ velocity and using Eq. 5.10, a burn time, t^i_{burn}, is assigned to each computational cell.

$$t^i_{burn} = \frac{l^i}{D_{CJ}} \qquad 5.10$$

t^i_{burn} represents the time when the detonation wave reaches the i^{th} cell. As the solver marches on time the solver compares the t^i_{burn} for each computational cell with the flow time. If the time reaches the t^i_{burn} for any computational cell, that cell would considered as a burned cell. The whole procedure is more complex as in fact for most cells at any time step only a fraction of cell may be burnt and this should be taken into account.

In a free uniform domain this may seem straight forward but in presence of obstacles the problem is more challenging because the obstacle may stay in the way of detonation propagation towards a large number of computational cells and the

finding l^i is more challenging. This problem is mainly sorted out by employing Huygens construction [119].

CJ burn method which is also called programmed burn method has been modified and improved over the time and in its most advanced form takes into account the effect of detonation curvature, κ. The detonation curvature could have significant effects especially when the wave is bending over an obstacle in this case the actual detonation velocity, D, is calculated using Eq. 5.11:

$$D_{CJ} - D = f(\kappa) \qquad 5.11$$

More details on Eq. 5.11 and physics involved can be found in literature [118, 119].

Despite being promising, the programmed burn method is very simplistic mainly because the chemistry is ignored in the physics of detonation wave and assumes a persistent CJ like detonation propagation. However as Tariq et al. Stated; "*Detonation velocities have been observed to change by as much as 40% due to multi-dimensional effects. Failure of detonation waves has also been observed experimentally. Some other dynamic effects of detonation cannot be predicted by such a simple propagation rule*", [118].

Most significant shortcomings of programmed burn method appear in domains with obstacles and when the wave is bending around the obstacles, therefore a hypothetical cylindrical domain with 6 obstacles is selected as the test case to assess the CJ burn performance compared to the reactive Euler based solver.

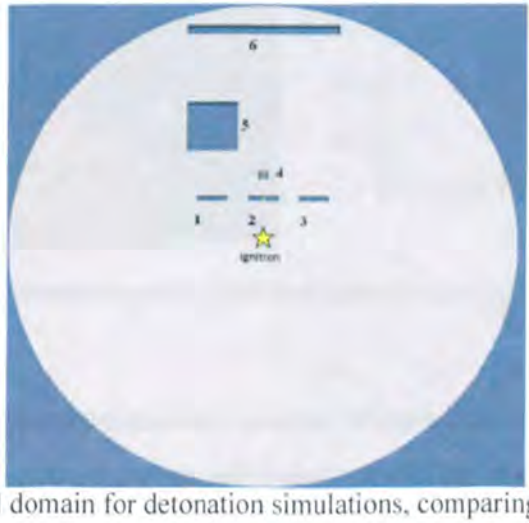

Figure 5-45 Numerical domain for detonation simulations, comparing CJ burn and reactive Euler methods

The domain is presented in Figure 5-54 in which the obstacles are numbered and the ignition point is marked with a star at the centre of the domain. The detonation is initiated at the ignition centre and starts to propagate outwards. As presented in Figure 5-45 all obstacles are placed at the top side of the domain and at the bottom part both codes are expected to predict similar, CJ like, propagation due to absence of any obstacle. However the results at the top part reveal interesting differences.

Figure 5-46/left compares the predicted detonation propagation around obstacle number 4. As it was expected the programmed burn method predicts uniform undisturbed wave propagation around the obstacles, where as in reality the wave diffraction around the obstacles cause temporary shock-flame decoupling and detonation failure around the obstacles. This is experimentally proved; an example of this phenomenon is discussed earlier in this text when studying detonation propagation in bifurcated tubes. In contrast to programmed burn method, the reactive Euler method which benefits from a temperature dependent reaction mechanism can predict detonation decoupling around the obstacles.

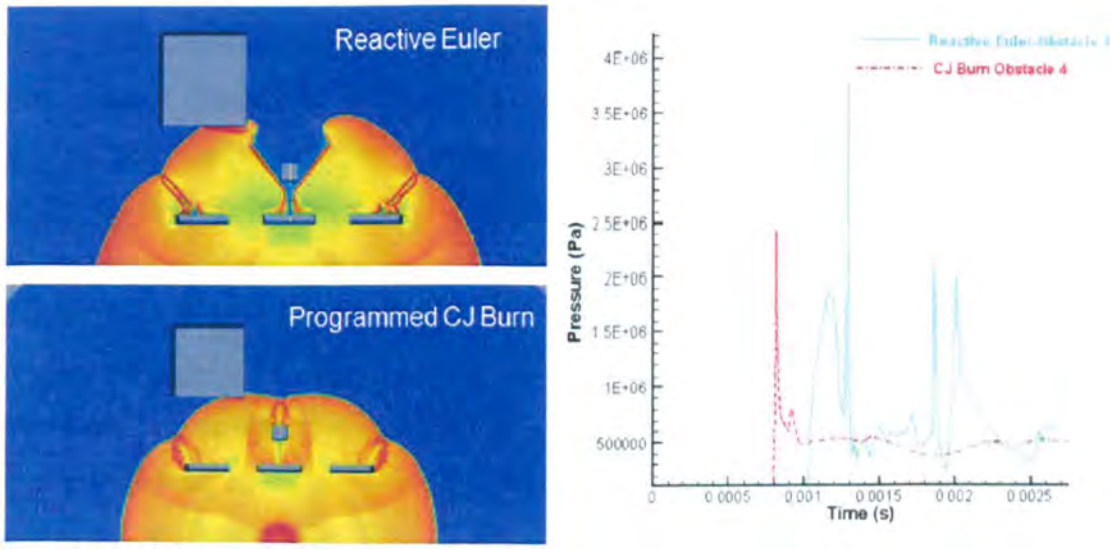

Figure 5-46 Comparison of the predicted pressure loadings on obstacle 4

Figure 5-46/right compares the pressure loading on back side of obstacle 4. Since the programmed CJ burn method cannot adequately model the detonation diffraction, it predicts an earlier detonation arrival at the obstacle. Moreover, the predicted peak

pressure and pressure history by the Euler solver are much more complex in comparison with that by the programmed CJ burn method. In accidental investigations, this difference could lead to misinterpretation of forensic evidences in terms of time and damage patterns.

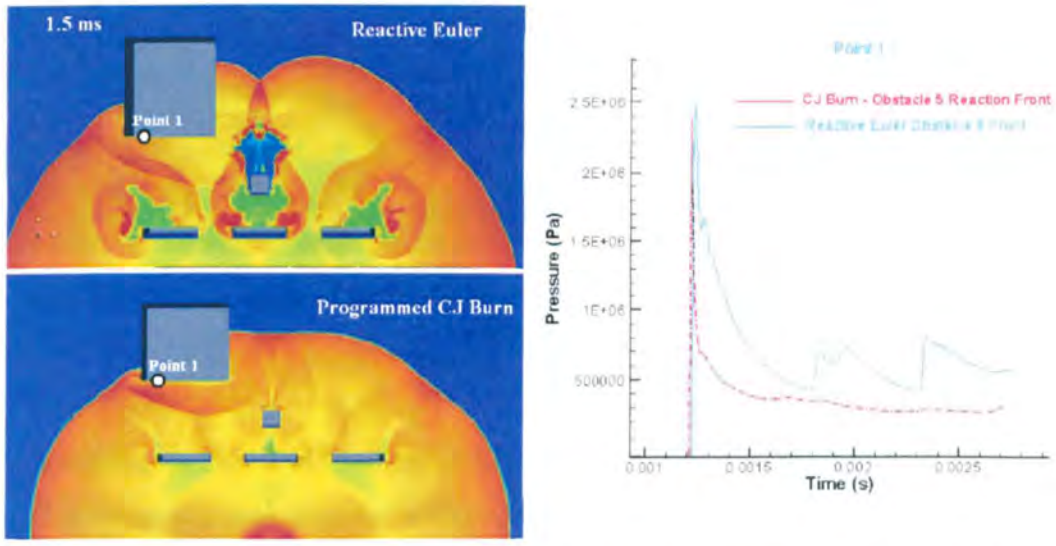

Figure 5-47 Comparison of the predicted pressure loadings at monitoring point 1 on the front side of obstacle 5.

Figure 5-47 shows the predicted detonation propagation and pressure loadings on the front side of obstacle 5. As expected, the programmed CJ burn method predicts uniform detonation propagation at approximately the CJ velocity. But the predictions of the reactive Euler solver have captured more complex phenomena. The shock diffraction around obstacle 4 has weakened the leading shock in these areas and the detonation is locally quenched for a short while behind obstacle 4, resulting in a pocket of unburned fuel-air mixture left for a short while behind obstacle 4. However, subsequent collision of the two shock waves coming from opposite direction behind obstacle 4 generate a hot spot and a localized explosion behind obstacle 4, as illustrated in Figure 5-48.

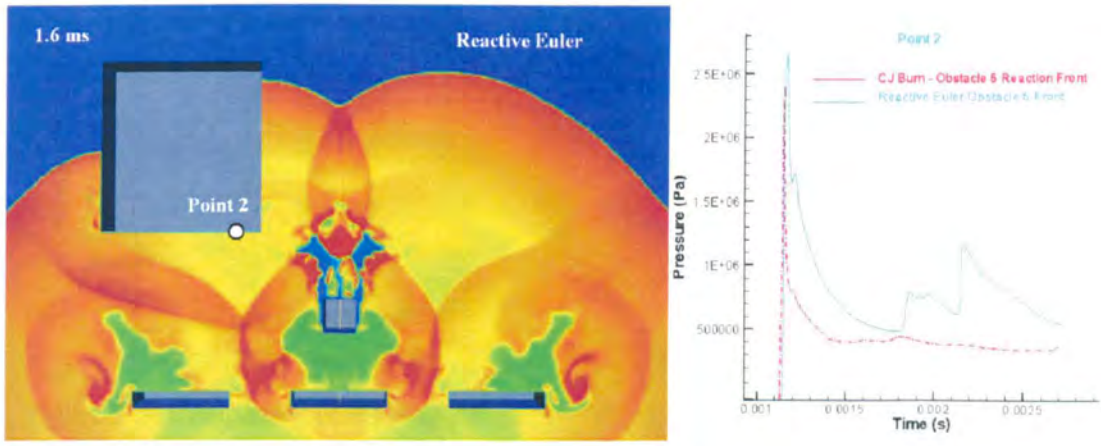

Figure 5-48 Comparison of the predicted pressure loading at point 1 on the front side of obstacle 5.

As a consequence of this localized explosion, a secondary shock wave hits obstacle 5. This secondary peak pressure is recorded in the pressure diagrams predicted by the reactive Euler solver but completely missing in the predictions of the programmed CJ burn method. This is expected as the later is a very simplistic approach mainly designed for calculating the blast waves generated by solid explosives and unable to capture the dynamic interactions between the obstacles and the combustion processes in vapor cloud explosions.

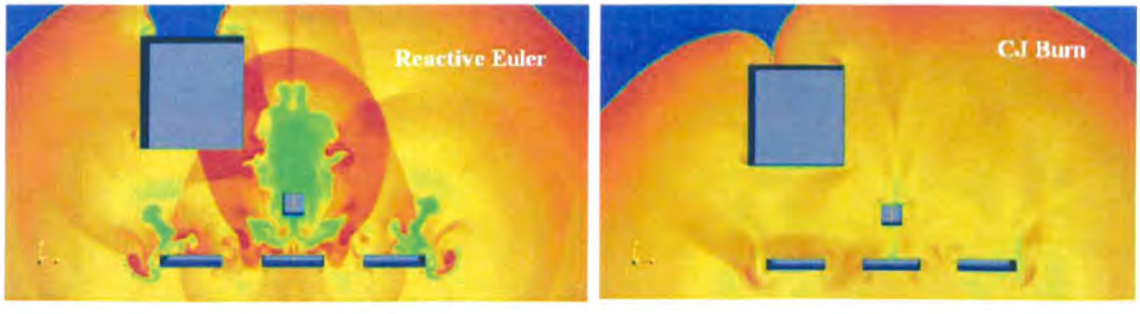

Figure 5-49 Comparison of the predicted pressure loadings on the back side obstacle 5.

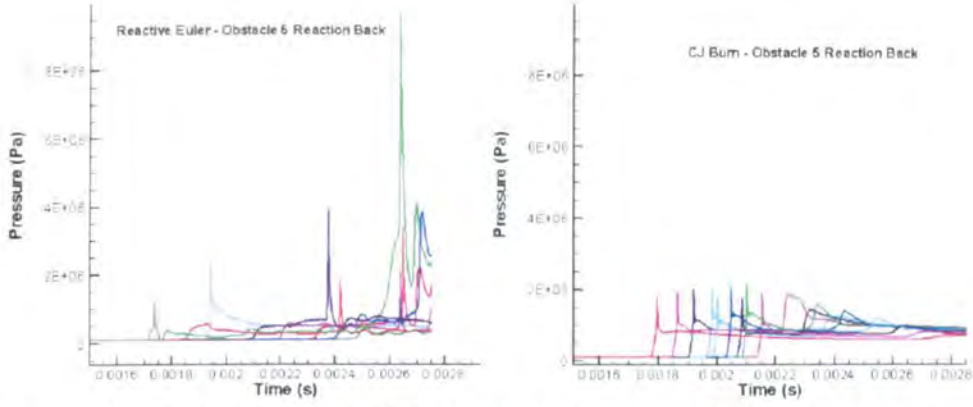

Figure 5-50 Comparison of the predicted pressure loadings on the back side of obstacle 5

Figures 5-49 and 5-50 show the detonation propagation and pressure loadings on the back side of obstacle 5. Again, while the CJ burn method predicts a simple, more or less uniform pressure distribution, the reactive Euler solver predicted much more complex pressure distributions. The difference in the predicted pressure loadings by the two methods implies that the predicted impulse which is an important parameter in risk assessments and safety analyses would be different using the two presented methods here. To investigate further, the predicted impulse using the two methods in two monitoring points, one on obstacle 4 and another one on obstacle 5 are compared in Figure 5-51. The corresponding pressure diagrams in these two points are presented and compared in Figures 5-46 and 5-47.

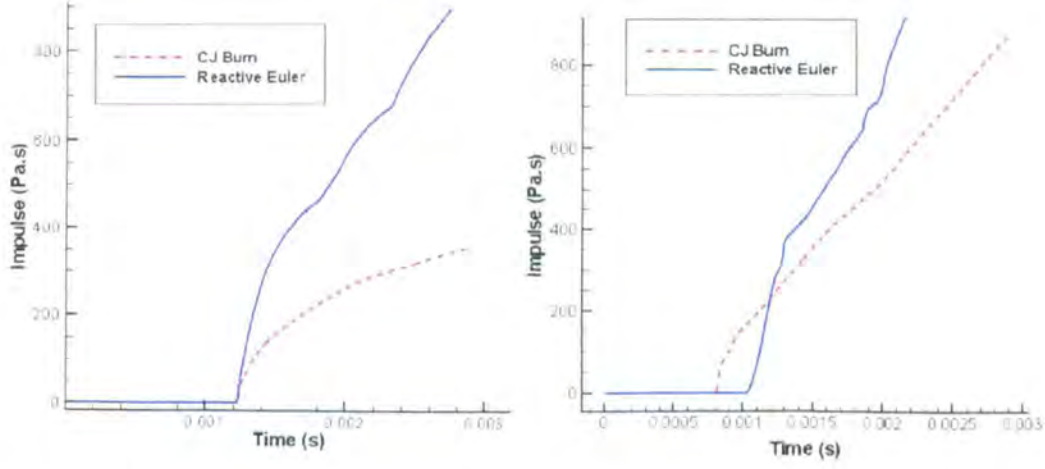

Figure 5-51 Comparison of the predicted impulse on obstacles 4 (right) and 5 (left) by the CJ burn and reactive Euler methods

The impulse per unit area is calculated integrating the pressure load over time, $I = \int_0^t P dt$. As expected from the pressure diagram in Figure 5-46, the CJ burn method predicts an earlier impulse building up on obstacle 4 starting 0.8 ms after the ignition, whereas the reactive Euler solver predicts a later shock arrival roughly at about 1 ms after ignition. However the predicted impulse using the Euler method has a higher growth rate leading to about 50% higher impulse at about 2.2 ms time. The predicted impulse on obstacle 5 shows an even bigger difference. Despite similar shock arrival time, the resulting pressure loading on obstacle 5 and corresponding impulse by using the Euler method are predicted to be twice more compared to the CJ burn results. The observed differences are thought to be due to the simplifications in the CJ burn approach which neglect the dynamic interaction between combustion and fluid dynamics as well as fluid obstacle interaction. In accidental investigations, this difference could lead to misinterpretation of forensic evidence in terms of time and damage patterns.

Chapter 6

DDT and the development of a reaction mechanism for its Simulation

6-1 Introduction to DDT

The two main combustion modes of concern in this thesis, deflagrations and detonations can be distinguished in several ways. Deflagration is a subsonic, expanding wave which propagates through diffusion of heat and mass whereas the detonation wave is supersonic compression wave which propagates through mixture ignition due to adiabatic shock heating in which the shock is sustained by the combustion energy release [6]. To initiate a deflagration wave, a fraction of one mill-joule energy is sufficient, whereas in detonations the required ignition energy might be as high as kilojoules [6]. A deflagration wave is the most likely form of combustion occurring in real life. However, deflagration waves are generally unstable and under certain conditions they can accelerate up to a point where transition to detonation occurs. The transition to detonation normally happens at the flame zone, provided that critical condition is achieved and it is generally independent of the process through which the critical condition is achieved. This implies that, there is no specific path and one can not specify a critical/maximum deflagration speed prior to the onset of detonation. Transition to detonation can occur at any point and stage provided that the critical condition is achieved [6]. Although the classical DDT experiments show that a deflagration wave normally accelerates to a maximum velocity as high as half CJ speed and then spontaneous localized explosion cause onset of detonation, this cannot be used as a reliable and accurate approach for prediction of DDT.

From the theoretical point of view, the deflagrations and detonations can be illustrated using Rankine-Hugoniot curve. The Rankine-Hugoniot curve is obtained when the energy equation is satisfied in addition to the continuity and momentum equations in 1-D steady state condition and by using ideal gas relations [6]. The deflagration waves are the areas located at the lower branch of the Hugoniot curve and the detonations are the regions located on the upper branch of the Hugoniot curve, CJ condition is the point where the Rayleigh line (combined form of continuity and momentum equations) is tangent to the Hugoniot curve and it corresponds to the minimum possible velocity for a detonation wave. DDT can be

interpreted as a sharp jump from lower branch to the upper of the Hugoniot curve. The difficulty here is that the precursor shocks which are generated by deflagration waves and move ahead of the flame, disturb the flow condition ahead of the flame and consequently a different Hugoniot would be achieved leading to continuous change in the Hugoniot solution throughout the process. The readers are referred to the book "The detonation phenomenon" [6] for further details of the derivation and interpretations associated with Rayleigh line and Hugoniot curve.

The whole DDT process consists of two parts, flame acceleration and detonation initiation. The onset of detonation occurs at the critical accelerated flame where localized explosion points or hot spots develop an overdriven detonation which later decays to a CJ detonation. In the flame acceleration stages the whole range of mechanisms such as turbulence generation, flame instabilities, pressure waves etc. can contribute to the acceleration process. It is not clear how much each mechanism contributes. This is also expected to vary from case to case depending on the initial and boundary conditions [6]. On the other hands, there have been considerable efforts to at-least provide a qualitative description of the later stage of DDT (onset of detonation) by the pioneering scientists in this field.

At the first stage of DDT, due to the expansion, the density and pressure of products are smaller than the initial conditions ahead of the flame. The combustion region keeps propagating with a subsonic velocity, meaning that the downstream boundary condition can effect condition ahead of the flame, for example if the flame is initiated at the close end of a tube, the gas expansions behind the flame pushes the reactants ahead like a piston, the specific volume increase behind the flame also forms compression waves moving ahead of the flame and modifies the flow ahead of the flame even before the flame reaches to those locations. In contrast, in the detonations, which are supersonic in nature, the flow ahead of the wave would not see any effect from the downstream conditions prior detonation arrival.

For the deflagration waves in closed end tubes, the compression waves generated by the flame catch up with each other and form stronger shock waves ahead of the flame. A deflagration wave will eventually turn into precursor shocks which are followed by a combustion region. This means that the flame is propagating in a flow which is disturbed and compressed by the leading shock instead of the undisturbed initial flow field. Behind the flame the particle velocity is zero to satisfy the closed

end boundary condition. As the flame propagates the strength of the precursor shock changes and the flow condition ahead of the flame keeps changing meaning that the Huguenot curve keeps changing. In fact the flow state ahead of the flame can be predicted using the conservation equations presented in Chapter 2.

Upon reaching the critical condition for transition to detonation, the onset of detonation can occur in many different ways depending on the specific case and the particular condition in the flame brush leading to onset of detonation [6].

Figure 6-1 Transition from deflagration to detonation is happening due to a small jet of hot products from a small orifice, reproduced from Lee et al. [6].

Figure 6-1 depicts the experimental result by Lee et al. [6] showing the instance when transition from deflagration to detonation is happening due to a small jet of hot products from a small orifice. The location where the wave undergoes transition to detonation is marked with * sign. At this point an overdriven detonation is formed and later decays to a CJ detonation as the wave is moving towards the left side in the image. The distance from the flame initiation location, which is at the bottom far-right of this image, to the transition point is called the induction distance which is also referred to as the run-up distance. The run-up distance depends on various parameters such as mixture thermophysical properties as well as the ignition location, ignition strength, boundary conditions, geometry and so on. Therefore trying to predict the run-up distance only by using the mixture properties would not be meaningful at all. An important characteristic of an accelerating deflagration wave is generation of pressure waves due to the increase in the energy release rate. Figure 6-2 shows the high speed schlieren photographs of flame acceleration and formation of pressure waves ahead of the flame carried out by Lee et al. In Figure

6.2 as the flame accelerates further stronger compression waves are formed ahead of the flame and they catch up with the leading wave and form a stronger shock wave ahead of the flame. Figure 6.3 shows later stages of flame acceleration illustrating very high velocity and highly turbulent flame with strong pressure waves moving ahead. The third frame shows formation of two localized explosions at the bottom of the tube which develop towards the leading shock but they are not strong enough to trigger the detonation wave. Later on third localized explosion occurs and sends one shock wave towards the flame font direction trigging the detonation and also sends a second shock backwards. The backwards shock is called retonation wave.

The experimental results by Lee [6], shows an example of DDT process but it has to be kept in mind that this process is not unique and in different cases and conditions, different mechanisms or combination of different mechanisms may lead to onset of detonation, this is the main reason why it is not possible to develop a general theory to predict transition to detonation even qualitatively [6].

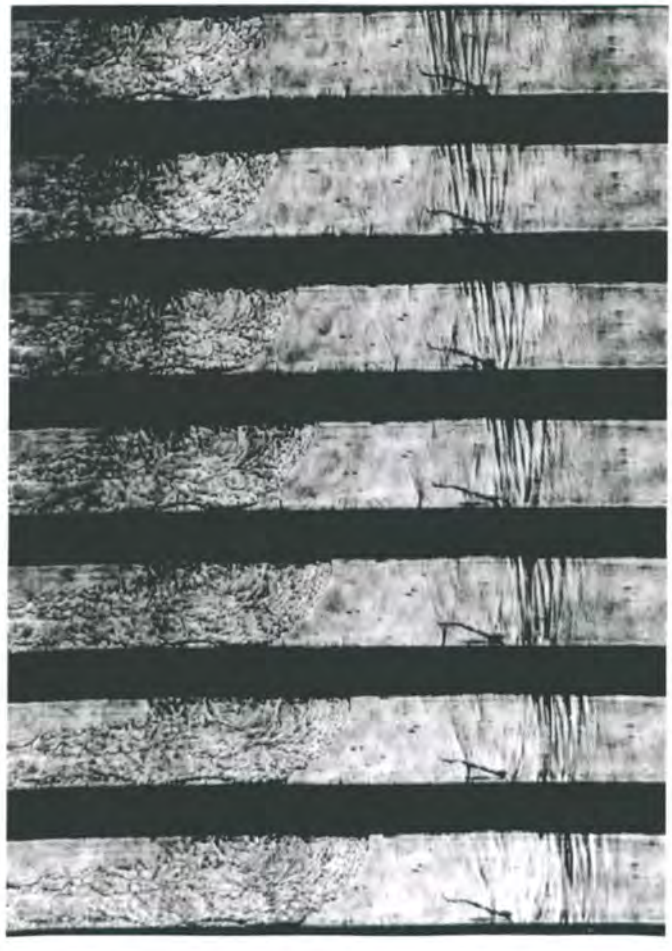

Figure 6-2 Schlieren photographs of flame acceleration and formation of pressure waves ahead of the flame carried out by Lee et al, (reproduced from [6]).

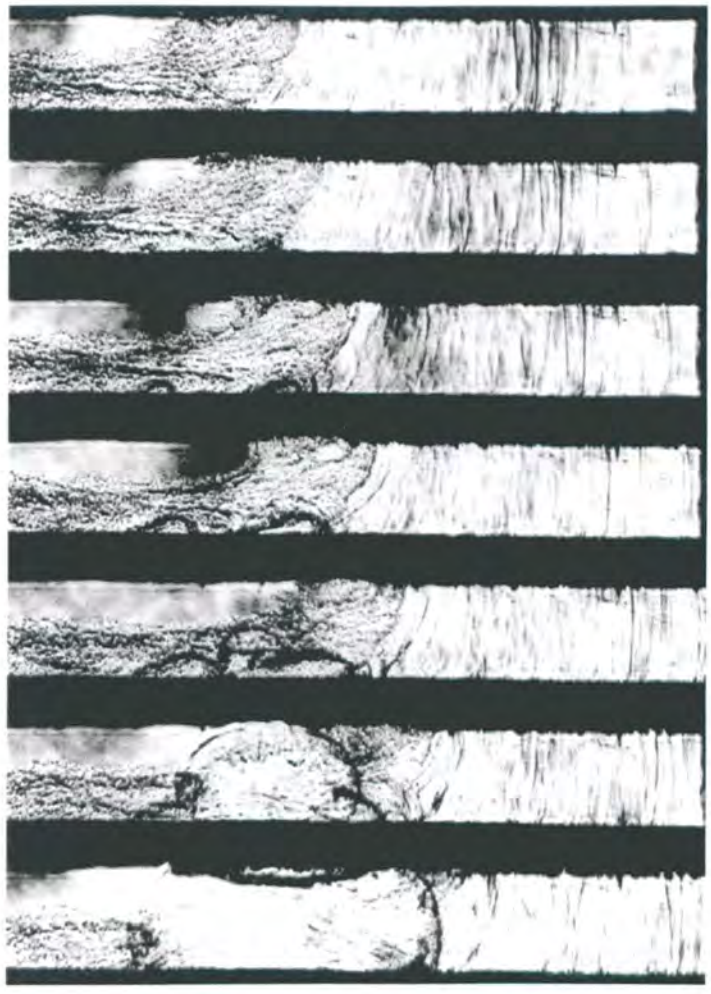

Figure 6-3 Schlieren photographs of flame acceleration and formation of localised explosion in highly accelerated flame, carried out by Lee, (reproduced from [6]).

The transition to detonation happens when a critical condition at the flame brush region is achieved. The process for onset of detonation is independent of the flame acceleration process, meaning that different flame acceleration mechanisms may finally lead to the desired critical condition for detonation initiation, however in most practical scenarios the flame is observed to be accelerated to some critical velocity which is close to the half CJ velocity for that Mixture. Once the detonation is triggered there must be an abrupt switch in the propagation mechanism, changing from diffusion based propagation to shock ignition.

There are some valuable set of experimental works in literature especially those published by Lee [6], showing the onset of detonation at different locations in the turbulent flame brush, however it is concluded that the turbulent flame generation

and formation of the pressure waves is highly nonlinear and irreproducible, therefore the transition to detonation cannot be a unique phenomenon. It should also be noted that the detonation should not necessarily start in the flame brush; it is sometimes observed that the onset of detonation occurs at the contact surface of two merging shock waves, the transition may also occur at other locations such as the point where the shock wave hits the obstacle corners as predicted by Oran et al. [14].

Despite different path ways leading to the critical condition it has been observed that DDT always happens through "an explosion within the explosion" (this expression was firstly used by Oppenheim [134] to explain the localized explosion in the flame brush). These localized explosions or hot spots form a highly overdriven detonation wave as well as retonation and transverse waves. One may compare these hot spots with direct initiation of detonation using a strong energy source term, however the strength of the shock produced by a constant volume explosion is well below the observe strength of overdriven detonations produced by these hot spots. This suggests that there is a very effective amplification mechanism that amplifies the constant volume explosion and turns it to an overdriven detonation in a very short time [6].

Lee et al. [18] proposed the SWACER mechanism to explain this amplification process which essentially results in transition from deflagration to detonation. SWACER stands for Shock Wave Amplification through Coherent Energy Release. The SWACER mechanism is based on effective synchronization of energy release in the critical region in a way that leads to formation of compression waves which amplify each other in a same way as in resonant coupling of oscillations in a system. It was suggested that there should be a gradient of induction time in the critical region to achieve this resonant through synchronized or coherent energy release. The concept of induction time gradient as an essential condition for transition to detonation was also suggested by Zeldovich et al. [125] who was a pioneering and distinguished scientist in this field.

Today the complex process of flame acceleration and transition to detonation is still not fully understood. Although there have been a number of efforts to shed light on salient features of this phenomena, only limited success has been achieved either numerically or experimentally. Development of analytical and empirical models is

out of question because it is not meaningful or possible to define the criterion for flame acceleration as whole spectrums of different mechanisms are involved. There have been some efforts by Lee et al. [8], Knystautas et al. [68], Peraldi et al. [135], and Lee [136], to propose a criterion which can at-least facilitates the prediction of the onset of the detonation but the results revealed that these criterions are case dependent and change from one condition to the other; and the predictions are strongly influenced by the boundary conditions. The only viable approach towards understanding and predicting DDT is numerical simulations. This is, however, limited by the computational power. The whole spectrums of different mechanisms involved in flame acceleration and onset of detonation requires a large portion of energy containing scales in the flow being resolved. This would make numerical simulations for cases bigger than a few centimeters or maximum a few meters impossible even with the largest available supercomputers today. In the mean time, numerical investigations on DDT which suffer from low grid resolution are not of any practical or scientific value. This essentially means that predicting DDT in large scale domains and open space geometries is out of reach with today's computing power. Oran and co-workers [14, 21] have made the most promising contributions to understanding and predicting DDT phenomena numerically. It has therefore been decided that a similar numerical approach will be followed in the present study.

The numerical approach in the present work is based on relatively high resolution solution of Navier-Stokes Equations using the ILES approach which is explained in Chapter 2 and incorporating a one-step Arrhenius type reaction. This whole set of numerical equations and techniques are implemented in a solver developed in C++ within the OpenFOAM toolbox. The outcome is used to solve some test cases which will be discussed in the next chapter. Much effort has been devoted to deriving an effective and accurate reaction mechanism, which will be described in the following section.

6-2 Single step chemistry reaction development

Employing a suitable reaction mechanism is one of the most crucial steps in order to ensure a reliable prediction of flame behaviour.

The right amount of chemical energy release needs to be injected, through the reaction mechanisms, in the right place at the correct time otherwise the dynamic of

the flow would be adversely affected. There are a number of proposed single and multi step reactions proposed in literature [14, 21] for flame and detonation propagations.

Preliminary studies have, however, shown that most of the proposed reactions in the literature fail to reproduce reasonable behaviour for the whole range of combustion regimes that is of interest to the present study.

Previous experiences of ourselves and other investigators have revealed the drawbacks of using detailed reaction mechanisms for DDT simulation especially when there is pressure increase in some parts of the domain. It is believed that the known drawbacks of the simplified reaction mechanisms are quite often because they are developed and validated only for a limited range of flow conditions such as pressure, temperature; turbulence intensity etc. Their use out of this range would result in non-physical reaction predictions. In order to overcome such limitations, it is necessary to develop a reaction mechanism which is able to reproduce reasonable behaviour throughout the whole range of conditions associated with the DDT phenomenon.

6-2-1 Predicting the reaction order [24]

The enthalpy in a constant volume explosion is a constant value and can be expressed as a function of temperature and mass fraction Eq. 6.1.

$$Enthalpy = h(T,Y) \tag{6.1}$$

We can differentiate the enthalpy with respect to time to derive the relationship between mass fraction and temperature.

$$\frac{dh}{dt} = \frac{\partial h}{\partial T}\frac{dT}{dt} + \frac{\partial h}{\partial Y}\frac{dY}{dt} = c_p\frac{dT}{dt} - q\frac{dY}{dt} \tag{6.2}$$

In Eq. 6.2 q, Y, T, t and c_p represent heat release per unit mass, mass fraction, temperature, time and specific heat at constant pressure respectively.

$$\frac{dY}{dt} = \frac{W\dot{\omega}}{\rho} \tag{6.3}$$

The Arrhenius equation presented in Eq. 6.4 is used to describe the products molar production rate per unit volume.

$$\dot{\omega} = A[O]^{nO}[F]^{nF} exp\left(\frac{-E}{\tilde{R}T}\right) \qquad 6.4$$

In Eq. 6.1, [O] and [F] represent the oxygen and fuel molar concentrations, n_O and n_F show the reaction empirical orders; using the ideal gas equation of state we can express the concentration of the i^{th} species as a function of density, Eq. 6.5.

$$[i] = \frac{n_i}{V} = \frac{p_i}{\tilde{R}T} = \frac{x_i p}{\tilde{R}T} = \frac{x_i}{W_i}\rho \qquad 6.5$$

x_i, W_i and p_i represent mole fraction, molar mass and partial pressure for the i^{th} spices respectively.

By substituting Eq. 6.5 into Eq. 6.4 we can obtain the following formula for molar production rate per unit volume

$$\begin{aligned}\dot{\omega} &= A\left[\frac{x_O}{W_O}\rho\right]^{nO}\left[\frac{x_F}{W_F}\rho\right]^{nF} exp\left(\frac{-E}{\tilde{R}T}\right) \\ &= \left[A\frac{x_O^{nO}x_F^{nF}}{W_O^{nO}W_F^{nF}}\right]\rho^{nO+nF} exp\left(\frac{-E}{\tilde{R}T}\right)\end{aligned} \qquad 6.6$$

Eq. 6.6 can be re-written in the following form:

$$\frac{dY}{dt} = \frac{W\dot{\omega}}{\rho} = \left[AW\frac{x_O^{nO}x_F^{nF}}{W_O^{nO}W_F^{nF}}\right]\rho^{nO+nF-1} exp\left(\frac{-E}{\tilde{R}T}\right) \qquad 6.7$$

We can simplify the Eq. 6.7 further by taking the reaction order $n = n_O + n_F$, replacing the bracket above with $\mathbb{Z}$ and substituting $\frac{dT}{dt}$ from Eq. 6.2 and express the temperature variations against time as in Eq. 6.8:

$$\frac{dT}{dt} = \mathbb{Z}\frac{q}{c_p}\rho^{n-1} exp\left(\frac{-E}{\tilde{R}T}\right) \qquad 6.8$$

Using Frank-Kamenetskii approximation and assuming small temperature increase, $T = T_0 + T'$ and $T_0 \gg T'$ we can re-write Eq. 6.8 as:

$$\frac{dT'}{dt} = \mathbb{Z}\frac{q}{c_p}\rho^{n-1} exp\left(\frac{-E}{\tilde{R}T_0\left(1+\frac{T'}{T_0}\right)}\right) \qquad 6.9$$

Using Furrier expansion for $\frac{1}{1+\frac{T'}{T_0}}$ around $T' = 0$ and neglect the third term onward

we would have:

$$\frac{dT'}{dt} = \mathbb{Z}\frac{q}{c_p}\rho^{n-1}exp\left(\frac{-E}{\tilde{R}T_0}\left(1-\frac{T'}{T_0}\right)\right) = \mathbb{Z}\frac{q}{c_p}\rho^{n-1}exp\left(\frac{-E}{\tilde{R}T_0}\right)exp\left(\frac{-E}{\tilde{R}T_0^2}T'\right) \quad 6.10$$

We can define a variable Φ as:

$$\begin{cases} \Phi = \frac{E}{\tilde{R}T_0^2}T' \\ \frac{d\Phi}{dt} = \frac{E}{\tilde{R}T_0^2}\frac{dT'}{dt} \end{cases} \quad 6.11$$

Substituting $\frac{dT'}{dt}$ from Eq. 6.11 to Eq. 6.10 results in:

$$\begin{cases} \frac{d\Phi}{dt} = \mathbb{Z}\frac{q}{c_p}\rho^{n-1}\frac{E}{\tilde{R}T_0^2}exp\left(\frac{-E}{\tilde{R}T_0}\right)exp(\Phi) = \frac{1}{\tau_i}exp(\Phi) \\ \tau_i = \frac{1}{\mathbb{Z}}\frac{c_p}{q}\rho^{-n+1}\frac{\tilde{R}T_0^2}{E}exp\left(\frac{E}{\tilde{R}T_0}\right) \end{cases} \quad 6.12$$

τ_i is known as explosion time. Differentiating τ_i with respect to density in constant T_0, we have:

$$\left(\frac{\partial\tau_i}{\partial\rho}\right)_{T_0} = \frac{-n+1}{\mathbb{Z}}\left(\frac{c_p}{q}\frac{\tilde{R}T_0^2}{E}\right)\rho^{-n}exp\left(\frac{E}{\tilde{R}T_0}\right) = \left[\frac{1}{\mathbb{Z}}\frac{c_p}{q}\frac{\tilde{R}T_0^2}{E}\rho^{-n+1}exp\left(\frac{E}{\tilde{R}T_0}\right)\right]\frac{-n+1}{\rho} = \frac{\tau_i}{\rho}(-n+1) \quad 6.13$$

The effective reaction order can be extracted from Eq. 6.13:

$$n = -\frac{\rho}{\tau_i}\left(\frac{\partial\tau_i}{\partial\rho}\right)_{T_0} + 1 \quad 6.14$$

The constant pressure explosion approach can be used to determine reaction order for hydrogen-oxygen reaction. The calculated reaction order against the equivalence ratio is plotted in Figure 6.4 [23].

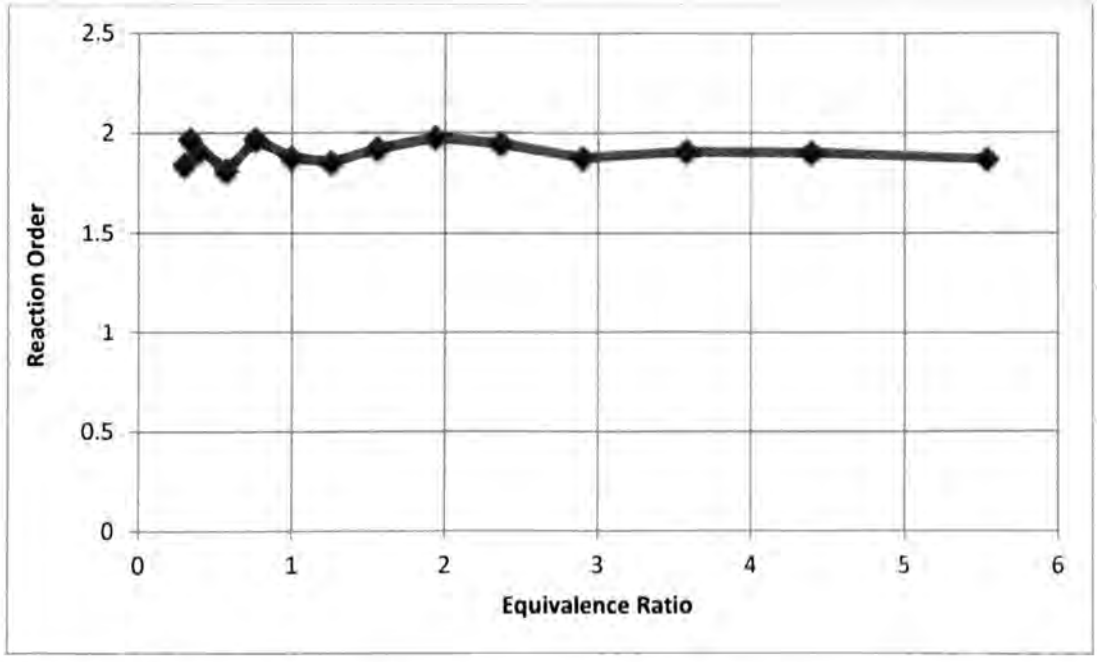

Figure 6-4 Reaction order against equivalence ratio for hydrogen-air mixture obtained using constant pressure explosion calculations [23]

6-2-2 Calculating adiabatic index (γ) and chemical energy release (q)

Heat release can be written as the difference of reactant's and product's enthalpy. By knowing the burned products temperature, T_b, we can express the heat release using Eq. 6.15[23-24]:

$$q = \Delta h = C_p \Delta T = C_p(T_b - T_0) = \frac{R(T_b - T_0)}{(1 - \frac{1}{\gamma})} \qquad 6.15$$

The detonation velocity can also be expressed with Eq. 6.16:

$$D_{CJ} = \left(\frac{\gamma^2 - 1}{2} q + C_0^2\right)^{0.5} + \left(\frac{\gamma^2 - 1}{2} q\right)^{0.5} \qquad 6.16$$

From Eqs. 6.15 and 6.16 and by knowing the products temperature and detonation velocity from CJ calculations [93], we can draw $\left(\frac{qM}{RT_0}\right)$ graph against γ in fixed D_{CJ}

and T_b, Figure 6-5. The intersection of two graphs shows the right γ and q for obtaining correct CJ velocity and temperature.

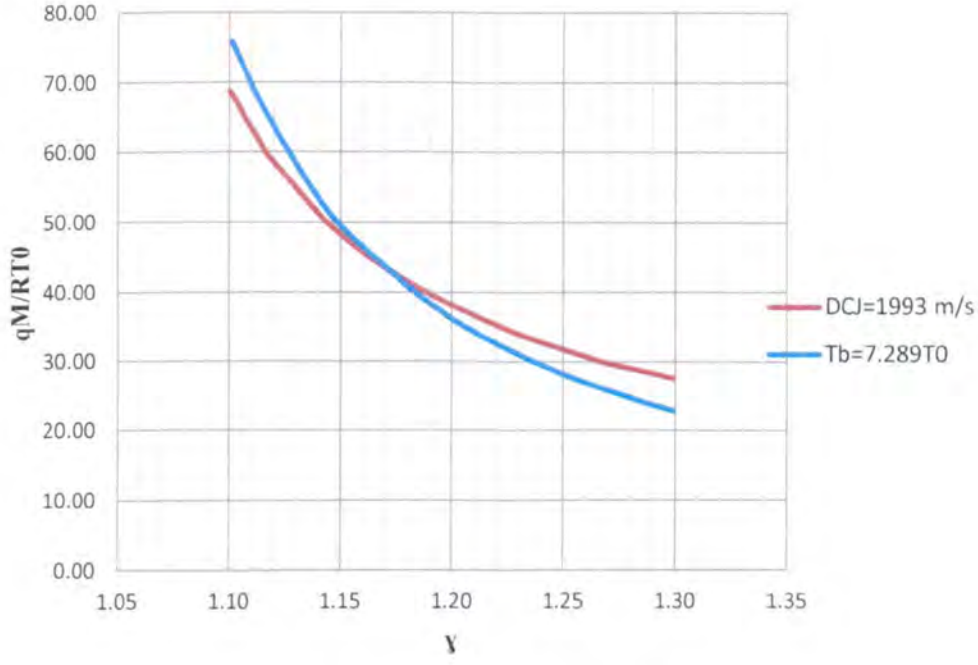

Figure 6-5 $\left(\frac{qM}{RT_0}\right)$ graph against γ in fixed D_{CJ} and T_b

6-2-3 Determining the activation energy

By using the ideal gas equation of state the Eq. 6.12 can be rewritten in the following format [24]:

$$\tau_i = \frac{1}{\mathbb{Z}}\frac{c_p}{q}\frac{\tilde{R}T_0^2}{E}\left(\frac{p}{\tilde{R}T_0}\right)^{-n+1} exp\left(\frac{E}{\tilde{R}T_0}\right) = \frac{1}{\mathbb{Z}}\frac{c_p}{q}\frac{\tilde{R}T_0^{n+1}}{E}\left(\frac{p}{\tilde{R}}\right)^{-n+1} exp\left(\frac{E}{\tilde{R}T_0}\right) \quad 6.17$$

Differentiating τ_i with respect to T_0 in a constant pressure condition leads to Eq. 6.18:

$$\left(\frac{\partial \tau_i}{\partial T_0}\right)_p = \frac{1}{\mathbb{Z}}\frac{c_p}{q}\frac{\tilde{R}T_0^{n+1}}{E}\left(\frac{p}{\tilde{R}}\right)^{-n+1}\left(-\frac{E}{\tilde{R}T_0^2}\right)exp\left(\frac{E}{\tilde{R}T_0}\right)$$
$$+\frac{1}{\mathbb{Z}}\frac{c_p}{q}(1+n)\frac{\tilde{R}T_0^{n}}{E}\left(\frac{p}{\tilde{R}}\right)^{-n+1}exp\left(\frac{E}{\tilde{R}T_0}\right)$$
$$=\left[\frac{1}{\mathbb{Z}}\frac{c_p}{q}\frac{\tilde{R}T_0^{n+1}}{E}\left(\frac{p}{\tilde{R}}\right)^{-n+1}exp\left(\frac{E}{\tilde{R}T_0}\right)\right]\times\left(-\frac{E}{\tilde{R}T_0^2}\right) \qquad 6.18$$
$$+\left[\frac{1}{\mathbb{Z}}\frac{c_p}{q}\frac{\tilde{R}T_0^{n+1}}{E}\left(\frac{p}{\tilde{R}}\right)^{-n+1}exp\left(\frac{E}{\tilde{R}T_0}\right)\right]\times\frac{n+1}{T_0}$$
$$=\left(-\frac{E}{\tilde{R}T_0^2}\right)\frac{\tau_i}{T_0}+(n+1)\frac{\tau_i}{T_0}$$

Therefore the activation energy could be described as:

$$E = RT_0\left(-\frac{T_0}{\tau_i}\left(\frac{\partial \tau_i}{\partial T_0}\right)_p + (n+1)\right) \qquad 6.19$$

Using constant pressure explosion approach we can calculate the activation energy as presented in Figure 6.6:

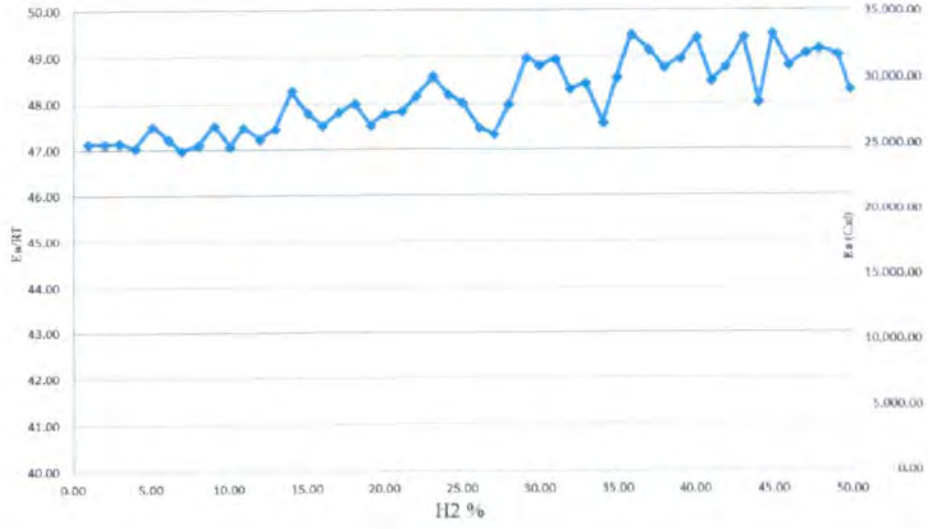

Figure 6-6 Activation energy for Hydrogen-air mixture obtained from Eq. 6.19

6-2-4 Calculating the pre exponential factor

So far the reaction order, gamma, reaction heat release and the activation energy for hydrogen-air reaction are determined in the previous sections. Now by using ZND model one can determine the pre-exponential factor of the reaction in a way that correct half reaction length would be predicted for the detonation waves. This is

carried out through adjusting pre-exponential then modelling the detonation wave propagation and checking the half reaction length until the correct result is achieved [23-24]:

$$ZND\ Model \begin{cases} w\frac{d\rho}{dx} + \rho\frac{dw}{dx} = 0 \\ \rho w\frac{dw}{dx} + \rho\frac{dp}{dx} = 0 \\ w\left(\frac{d\rho}{dx} + \frac{dp}{dx}\right) = \rho a_f^2 \dot{\sigma} \\ w\frac{dY_i}{dx} = \dot{\Omega}_i \end{cases} \quad 6.20$$

6-2-5 Determining viscosity, thermal and mass diffusivity

Eventually, the viscosity, thermal and mass diffusivity are adjusted by assuming unity Lewis and Prandtl Numbers [23], in order to match the laminar flame propagation velocity with the experimental results given in the literature [25-32].

$$\begin{cases} \mathrm{Le} = 1 \\ \mathrm{Pr} = 1 \\ \mu = \rho D = K/C_p \end{cases} \quad 6.21$$

Oran et al. [21] used Eq. 6.22 to find the viscosity, thermal and mass diffusivity and match the results.

$$\mu = \rho D = \frac{K}{C_p} = z_0 T^{0.7} \quad 6.22$$

Eq. 6.22 is derived by curve fitting the equation to NASA libraries for transport properties.

Wang [23] carried out some preliminary calculations and showed that in constant species mole fractions and by assuming that half of the reactants are converted to products results in the following equation:

$$\mu = 2.94 \times 10^{-6} T^{0.71355} \left(\frac{g}{cm}.s\right) \quad 6.23$$

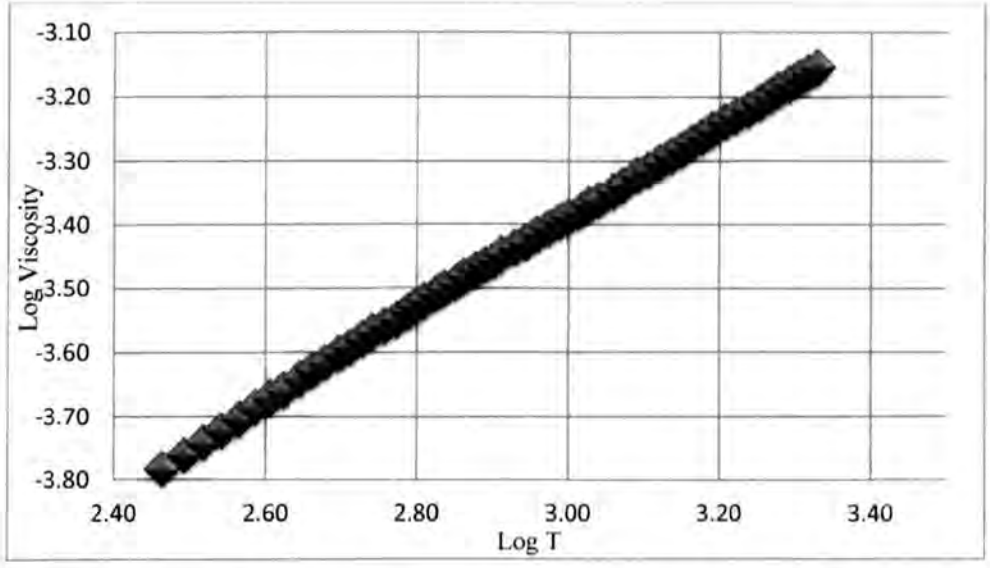

Figure 6-7 Viscosity vs temperature, in logarithmic scale [23]

Equation 6.23 is derived by curve fitting of the polynomial presented in Figure 6.7. Its predictions are close but slightly different from Oran's suggested correlations. The final step is validating the derived reaction mechanism to make sure it would produce correct results for different flame and detonation parameters.

6-3 Reaction validation

In order to validate the derived reaction mechanism a set of test runs for flame and detonation propagation in a 1-D domain is carried out.

The target is to verify the flame temperature, propagation velocity, detonation pressure and detonation propagation velocity. These parameters can represent how closely each reaction mechanism can predict the flame and detonation behaviour in comparison with the measurements in the literature.

Having a 1-D domain permits us to use a very fine grid size for the validation. A 5 cm long domain and a 1 μm grid spacing is used here.

The first test is flame propagation in a 1-D pipe. Stoichiometric hydrogen-air mixture is used and it is assumed that half of the domain (right side) is already burned and the flame is in the middle of the domain (2.5 cm away from each end) and propagating towards the left side. To measure the flame speed, an inlet flow of the reactive mixture is enforced on the left boundary and the right boundary is set to

outflow so the burned expanded products can exit freely. By adjusting the inlet flow velocity, it is possible to keep the flame position stationary at the middle of the domain.

If the inlet velocity is smaller than the burning velocity the flame would gradually move towards the inlet and if the inlet velocity is higher than the brining velocity it would push the flame front towards the outlet.

Finding the right flame velocity is somewhat tricky because there are some small oscillations in the flame behaviour especially at the beginning of the solution until the flame is fully stabilised therefore the test must be run long enough to make sure the flame is stabilised and is not moving for reasonably long time. The case was firstly run for 500 milliseconds to capture flame movement to either side of the domain. A total of 12 different inlet velocities are tested to find the right burning velocity. The measured flame velocity and temperature for the proposed reaction mechanism are listed in Table 6-1:

Table 6-1 Flame parameters, present work compared with measurements.

Stoichiometric hydrogen-air mixture	Current work	Experimental from literature [57]
Flame temperature	2491 K	2483 K
Burning velocity	2.95 m/s	2.9 m/s

Of course, an alternative method to find the flame velocity is to solve free flame propagation without having the inlet velocity and then determine the velocity by dividing the flame displacement by the elapsed time. However, a much longer numerical domain would be required. To be more precise, to run the case for 500 milliseconds the domain should have been about 150 cm long and the number of grids would have increased to 1.5 million. Our approach requires only one tens of the computational cost and provides better accuracy as we only need to set and record the inlet velocity rather than tracking the flame front and measuring the displacement in different time intervals.

The predicted flame temperature and velocity are in very good agreement compared to experimental results from literature [57]. This verifies that the derived reaction

mechanism can be safely used for the flame propagation solution but it still needs to be tested for detonation condition. A similar test case is set up. This time a detonation wave (by setting CJ condition) is created at the right half of the domain and the case is solved for 2 milliseconds to find the propagation velocity. The stabilised peak detonation pressure and velocity are listed in Table 6-2. The predicted detonation parameters are again in very good agreement with CJ results [93].

Table 6-2 Detonation parameters, present work compared with measurements.

Stoichiometric hydrogen-air mixture	Current work	CJ values [93]
Peak pressure	15.9 atm	15.447 atm
Propagation velocity	1997 m/s	1980 m/s

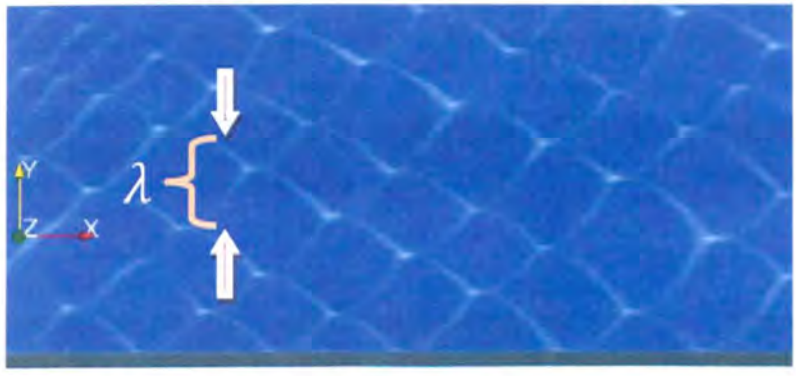

Figure 6-8 Recorded detonation cellular pattern.

Using the derived reaction, simple 2D detonation propagations are also simulated to evaluate the formation and size of the detonation cellular shapes. Formation of the detonation fish-cell pattern is recorded by tracking the position of the triple point. The recorded cell width varies from 0.5 to 2 cm and the average recorded cell width is $\lambda \approx 1.5$ m/s which is again within the expected range.

6-4 Grid independency test

A set of consistent 2D numerical simulations in a small tube filled with obstacles are carried out to investigate the issue of grid independency and formulate recommendation on the desirable grid resolution to achieve grid independent predictions. Stoichiometric hydrogen-air mixture is used for the simulations. Six different grid resolution are studied, i.e. 100, 50, 25, 15, 10 and 5 microns.

The domain is a symmetrical tube of 3 cm long and 1 cm wide filled with 5 obstacles. Due to axisymmetric condition, only half of the domain is modelled and the top boundary in Figure 6-9 is a symmetric boundary. The right boundary is an opening boundary and the rest of the boundaries are set to be wall. A flame is induced at the left end (closed end) of the domain by using hot burned region of products and the propagation of the flame, flame temperature, velocity and flow pattern are compared for three cases with exactly the same setting only with different grid sizes.

Figure 6-9 Numerical domain for grid independency studies

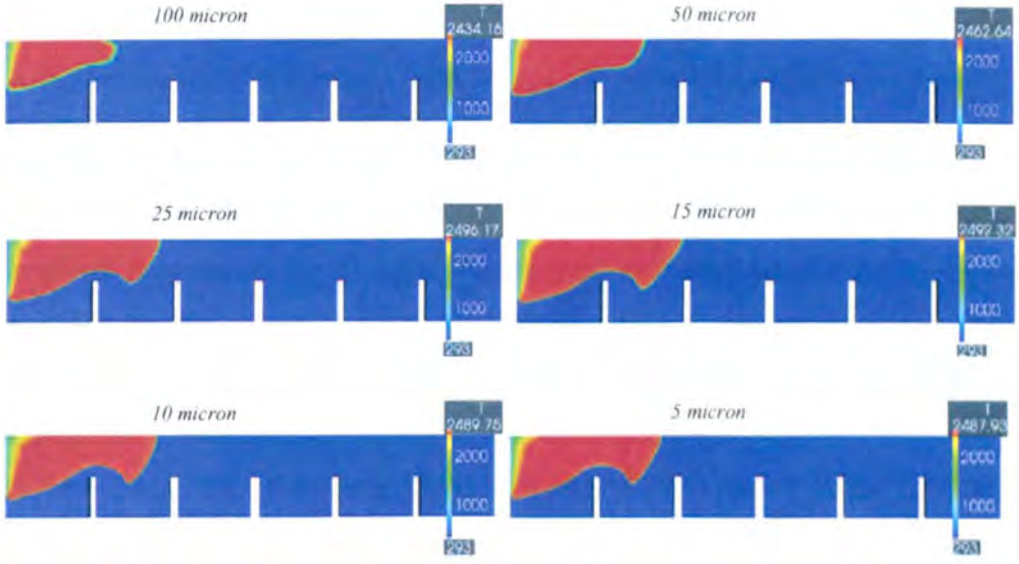

Figure 6-10 Grid independency studies, grid sizes of 100, 50, 25, 15, 10 and 5 microns

Figure 6-10 compares the flame propagation at exactly the same time, 2.5 ms after ignition, for different grid resolutions. Comparing the results for grid dependency in Figure 6-10 reveals that refining the grid size from 100 micron to 50 micron results in a notable change in the flame propagation pattern. Similarly, refining the grid size from 50 to 25 micron makes some changes in the predicted flame behaviour but the changes are less significant compared to the previous step. Further refining of the

grid to 15 micron also results in some slight changes in the shape and location of the flame front. The results for the 10 micron grid are very close to the ones obtained on the 15 micron grid. The location and shape of the flame is in good agreement and the predicted maximum flame temperature is 4 K lower for the 10 micron grid. Further refinement to 5 micron produces a result identical to 10 micron one, no difference can be observed and the predicted flame temperature is less than 1.8 K different, this is equivalent to 0.07% difference in predicted temperature which can be safely considered as zero. Figure 6-10 clearly shows that refining grid size from 10 to 5 micron does not make any difference in the predictions. The predicted flame and flow behaviour are exactly identical for the grid resolutions smaller than 10 micron. Therefore it is concluded that it is safe to use grid resolutions smaller than 10 micron for our simulations without worrying about the grid dependency of the results. Furthermore, the 15 micron grid can also be used with a small degree of error but the author selects to use the 10 micron grid due to the high complexity and sensitivity of the DDT process and importance of high resolution.

A further question that might raise here is the issue of resolving the Kolmogorov length scale and extremely fine turbulence length scales.

This question is addressed in Chapter 2 where the use of ILES is described and justified. It is reasonable to argue that as long as the energy containing eddies are resolved and the results are grid independent, there is no justification to use finer grid size which could also be computationally unaffordable even using the biggest available supercomputers. For the case of detonation it is suggested in the literature to have about 20 grid points across the detonation half reaction length [23, 103]. For stoichiometric hydrogen-air mixture the detonation half reaction length is about 0.2 mm therefore the 10 micron grid size puts exactly 20 grid points across the detonation half reaction length as suggested in literature [23, 103].

In the present study, adaptive mesh refinement with one and two levels of refinement is also used for some simulation leading to the minimum grid size of 2.5 to 5 micron which is equivalent to 40 to 80 grid points across the half reaction length and is well above the required grid resolution. Oran et al. [21] used 39 gird points across the half reaction length for their simulations of DDT in stoichiometric hydrogen-air mixture which is equivalent of 5.13 micron grid size.

Chapter 7

DDT case studies and validation

Grid independency studies in the previous chapter revealed that very fine computational grid with a grid size of a few microns is required to have a reasonable DDT simulation. Such resolutions mean that the total number of the grid points would exceed 10-40 million in most of the cases. To help shedding light on the salient features of DDT process as well as providing validation evidence of the present modelling approach, a number of DDT simulations have been carried out for selected cases where experimental data or previous predictions are available for comparison.

7-1 Numerical simulation of DDT in 0.04 by 1 meter tube (compared with the predictions of Oran et al. [21])

The work of Oran et al. [21], which is also based on the ILES approach, is by far the most successful numerical study on DDT. In the previous chapter, a very similar Arrhenius reaction has been developed as the one suggested by them. It was decided as part of the validation exercise to see if the present model can reproduce their results.

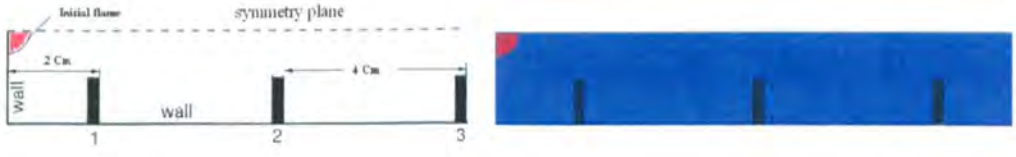

Figure 7-1 Schematic view of the 0.04 by 100 cm tube

The first case study involves flame acceleration and transition to detonation in a 1 m long and 0.04 m high duct which contains 1 cm high obstacles spaced 4 cm apart. A schematic of the computational domain is shown in Figure 7-1. The left image in Figure 7-1 shows the schematic view of the tube and the right image shows the numerical domain. Due to axisymmetric nature of the domain, only one half of the domain is simulated with a symmetric boundary condition imposed for the top side of the domain. The left side of the domain (the closed end of the tube), the bottom side and the obstacles are specified as wall boundaries with no slip condition imposed on the velocity field as well as constant temperature boundary condition for the temperature field. The DDT process normally occurs in a fraction of millisecond

so there is not enough time for any effective heat transfer happening through the tube walls. Therefore it is safe to assume that the walls temperature remain constant throughout the whole process so one can safely use fixed temperature boundary condition. For the other end of the tube at the far right, which is not depicted in Figure 7-1, an opening boundary condition is used.

The tube is filled with stoichiometric hydrogen-air mixture at atmospheric pressure. The numerical simulations are carried out at 2 different initial temperatures 273 K and 293 K for comparison. A uniform structured mesh is used. Based on the grid dependency analyses in previous chapter, a grid size of 10 micron should be kept in the domain. However, given the dimensions of the domain [$0.02\ m \times 1\ m$] this leads to a mesh with 200 M grid points. The following measures have hence been attempted to reduce the computational cost without compromising the accuracy.

7-1-1 Reducing the computational cost

The first treatment which is well developed and used in the scientific community is the adaptive mesh refinement (AMR) technique, which enables the solver to automatically refine the grids in regions with relatively high gradients of the targeted flow parameters, e.g. temperature or pressure. This practically means that the solver can identify what areas of the domain contain the flame front and refine the mesh only at those regions where higher resolution is required while keeping lower resolution at less important regions.

Implementation of this treatment in the current numerical code has encountered a set of difficulties which have been successfully resolved by the candidate. The implemented AMR allows two levels of refinement, i.e. an initial grid of 40 micron with help of AMR can result in a 10 micron resolution at the flame front and other regions with sharp pressure and temperature gradients. With the help of AMR, it has been possible to reduce the required number of grids to 20 M.

The second approach involves the use of multiple mesh blocks with different resolutions in different regions and then mapping the results from one mesh to another. In the present study, three different meshes were generated. In the first

mesh, the regions covering the first few obstacles have a very high resolution while the rest of the domain has lower resolution; the second mesh keeps high resolution around the obstacle in the middle of the tube and lower resolution in other areas and so on. The simulation starts from the first mesh therefore the regions around the initial flame fronts are benefiting from high resolution. As the flame moves forward and reaches the mid-tube obstacles, the results are mapped onto the second mesh and so on. This procedure helps to keep high resolution only in the areas where the flame or detonation front is located. With this approach, the number of the required grid points is further reduced to 10 M.

This is still a heavy computational case and numerical simulation of each case running on a high performance computational cluster with 32 cores running in parallel continuously takes about 2~4 month to finish. Consequently, only limited number of simulations could be carried out and presented here.

7-1-2 Single Step Chemistry and 273 K Initial Temperature

The first case shows the flame acceleration and DDT in the same geometry while the mixture is kept at 273 K initial temperature and the single step Arrhenius reaction in Eq. 7.1, derived in previous chapter is used for the chemistry.

$$\dot{\omega} = 6.85 \times 10^{12} \times exp\left(-\frac{112971}{RT}\right) \qquad 7.1$$

The predicted flame propagation and acceleration are illustrated in 10 frames in Figure 7-2 showing the temperature field and 10 frames in Figure 7-3 showing the pressure field. Due to limited space, it is not possible to show all stages of flame acceleration and only the time frames showing the transition to detonation are presented in Figures 7-2 and 7-3; however the detailed description of the process is included. Following the ignition, a laminar flame starts to propagate from the initial ignition centre towards the first obstacle. Initially, the flame propagates at laminar condition. Although the hydrogen laminar burning velocity which is about 3 m/s, due to the expansion of hot products behind the flame, the flame displacement velocity is significantly higher.

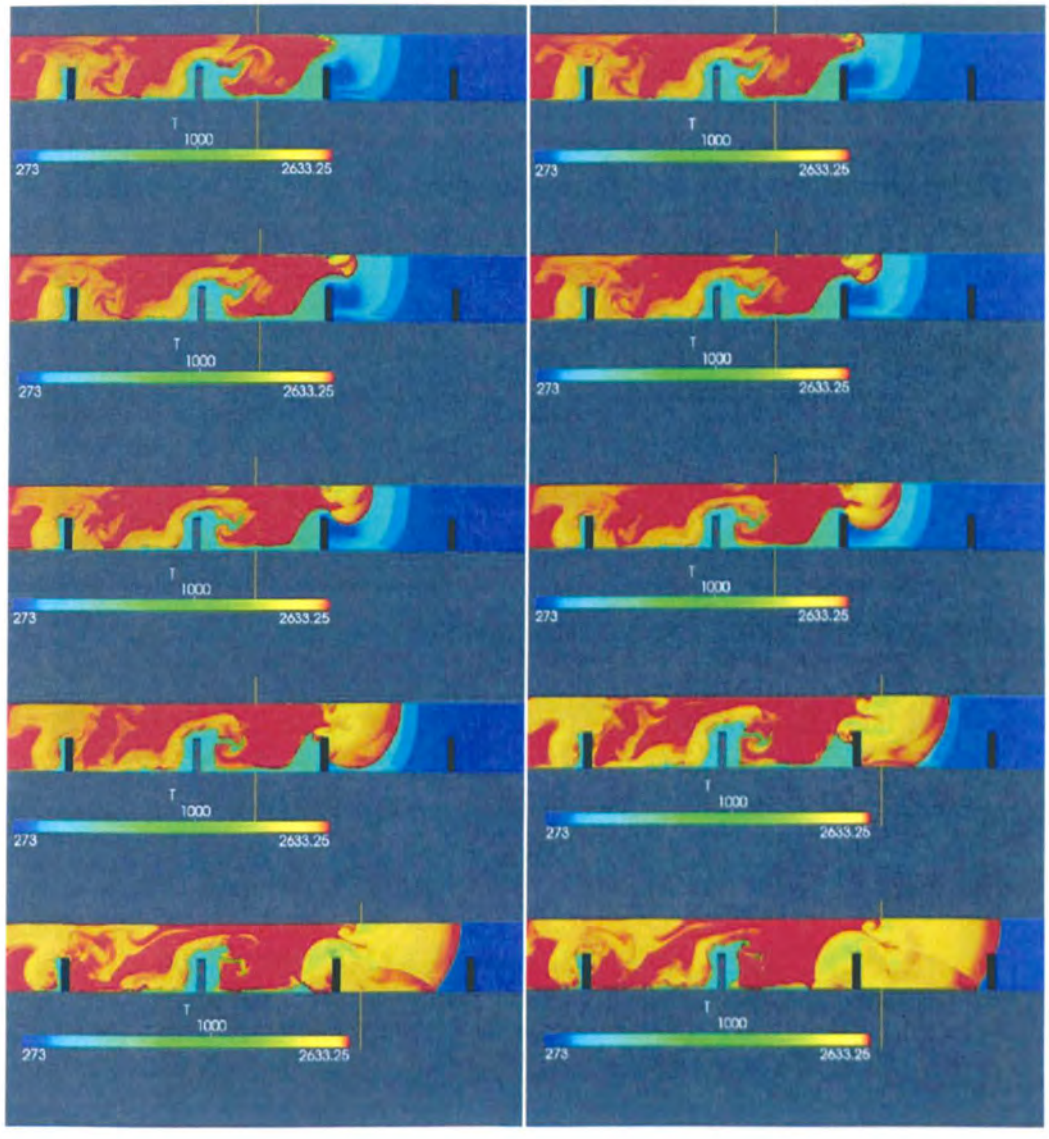

Figure 7-2 Temperature field for flame acceleration and DDT in H2-Air at 273K

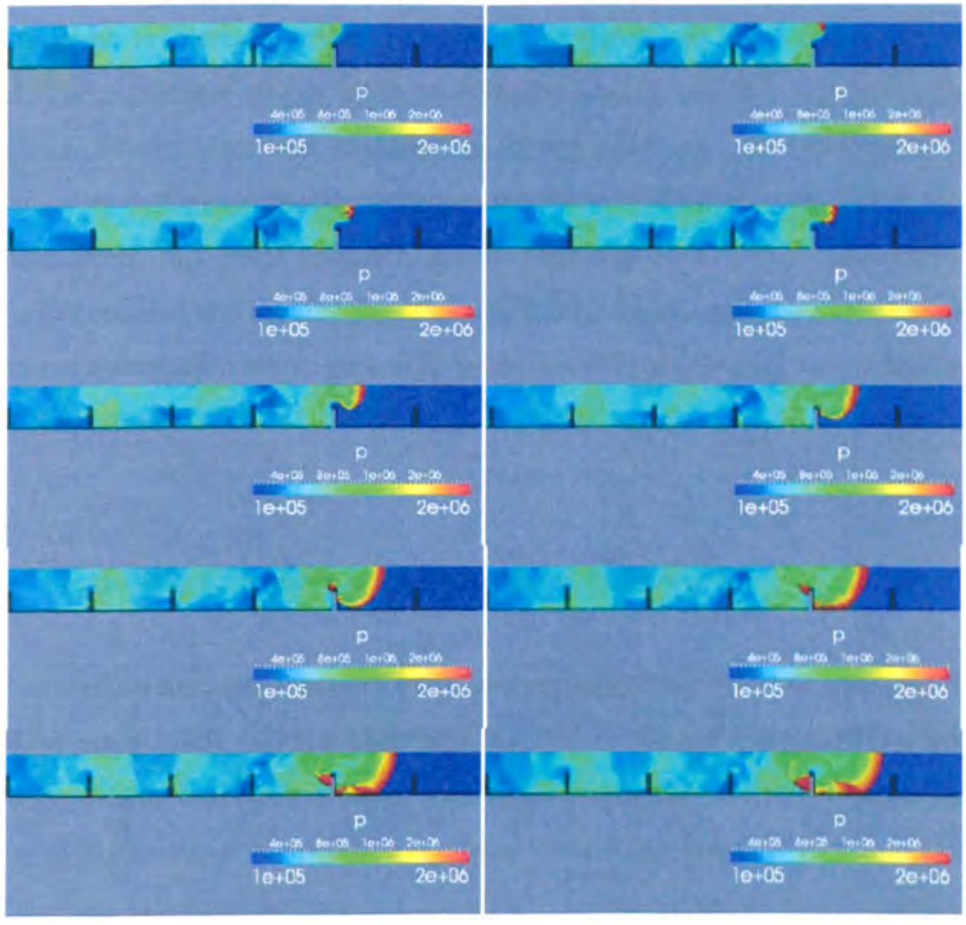

Figure 7-3 Pressure field for flame acceleration, hot spot formation and DDT in H2-Air at 273K

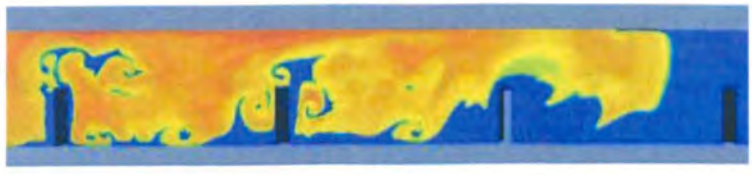

Figure 7-4 Flame wrinkling at flame acceleration stage

Gradually, the flame front starts to accelerate as the expansion of hot gases behind the flame pushes the flame front further away from the left side of the tube. The flame starts to wrinkle and accelerate further after it passes over the first obstacle. The flame front, right after the 4^{th} obstacle, becomes highly distorted. The increase in the flame surface area increases the rate of energy release which leads to further acceleration of the flame. After the flame passes the 6^{th} obstacle, the rate of energy release is so high that it generates several pressure waves ahead of the flame. When

the flame passes over the 8th obstacle several notable pressure waves are moving ahead of the flame. Reflected pressure wave from the obstacle hits the flame front. As the flame accelerates further, more pressure waves are generated ahead of the flame. These pressure waves catch up with the leading pressure wave and further amplify it. Finally, localised explosion is formed right over the 13th obstacle. The high velocity deflagration wave undergoes transition to detonation right over the 13th obstacle. From this point onwards, the leading shock wave and the combustion region are coupled and moving together at a local velocity of about 1990 m/s, at the same time a retonation wave, generated by the localised explosion, moves backwards in the burnt products.

7-1-3 Single Step Chemistry and 293 K Initial Temperature

The simulations are carried out with the same settings as the previous case except for the initial temperature which is increased to *293 K to study the effect of the mixture* initial condition. The same reaction mechanism as before, Eq. 7.1 is used. In this case with higher initial temperature the flame accelerates faster. Figure 7-5 includes 10 snapshots showing the pressure field right before transition to detonation and onset of detonation. Analysing the temperature field for this case reveals that the flame starts to accelerate faster compared to the previous case and the flame area is more wrinkled, in almost the same way as before stronger pressure waves are generated as the flame accelerates. These waves hit the obstacles and reflect back they also reflect from the tube wall and move vertical to the direction of flame propagation forming transverse waves. There is a complex combination of several reflected and transverse waves hitting one another and hitting the flame front. The most notable changes occur when the reflected waves from the obstacles hit the reflected waves from the tube walls. This leads to regions of very high pressure. The temperature, turbulence intensity and reactivity of the mixture ahead of the flame is elevated due to the passage of the leading pressure waves, therefore the high pressure points formed by collision of the reflected waves has the potential to create a localised explosion point. In this particular case the first hot spot, shown in the first frame in Figure 7-5, is formed attached to the tube's bottom wall right before the 10th obstacle where the reflected shocks from the 10th obstacle and the tube wall collide.

However this hot spot is not strong enough to form a self sustained detonation. The second hot spot is formed when the remaining strong pressure wave from the first hot spot collides with a reflected wave from the bottom wall right before the 11^{th} obstacle. This collision forms a much stronger localised explosion which can persist long enough to catch up with leading shock wave to trigger a detonation wave. The persistence of the second hot spot is apparent in the third frame onward. However, before the second hot spot catches up with the leading wave, the collision of two reflected shocks, one from 11^{th} obstacle and one from top tube wall with the remains of the first hot spot forms a third strong explosion point right over the 11^{th} obstacle and consequently this hot spot forms an over driven detonation wave which catches up with the leading pressure wave and later on stabilises as a self sustained detonation wave.

Figure 7-5 Pressure field and formation of localised explosions which finally lead to DDT in H2-Air mixture at 293 K initial temperature.

Figure 7-6 shows the temperature field for this test case at the same time instances as in Figure 7-6. Formation of hot spots is distinguishable in the frames; however this is clearer in pressure counters. The dark red regions show high temperature areas which are mainly the areas where several shocks have collided and increased the temperature. The light blue regions ahead of the flame, in the first snapshots, show the locations of the leading pressure waves. These pressure waves elevate the mixture temperature ahead of the flame; that is why they can be distinguished in the temperature contours; the stronger the leading shocks get the lighter the colour becomes, this is evident in the presented frames. As the flame moves further ahead the shock-heated region ahead of the flame becomes clearer. The last frame in Figure 7-6 shows that the combustion region caches up with the leading shock wave and they move together (there is no light blue area ahead of the flame anymore). This is evidence showing the detonation wave is successfully triggered at this point

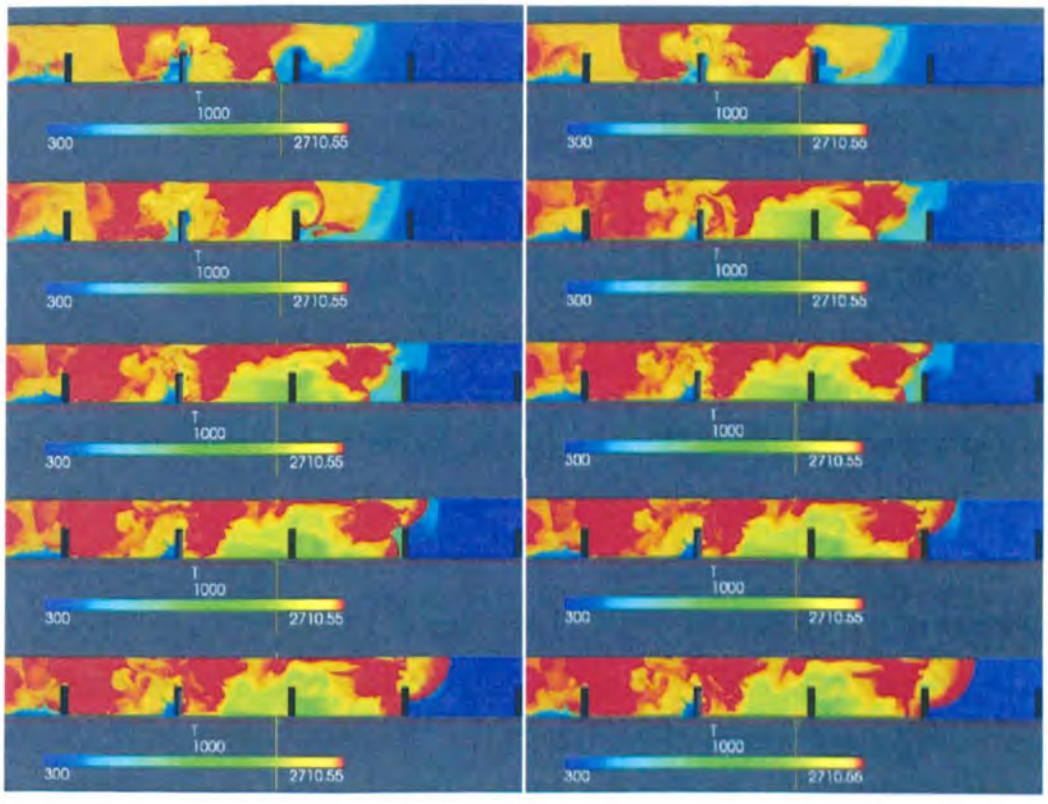

Figure 7-6 Temperature field and formation of localised explosions which finally lead to DDT in H2-Air mixture at 293 K initial temperature

The predictions compare well with Oran's predictions in terms of the DDT location as they predicted the 12th obstacle as the location where the transition to detonation

occurs first. However the details of the transition mechanism are slightly different in their predictions. Oran et al. observed that DDT occurs in most cases as a result of a strong leading pressure wave hitting the obstacles and forming a localised explosion right at the corner where the obstacle meets the tube wall [21].

The predicted behaviour in the current work for DDT and onset of detonation appears to be more complex and formation of several hot spots at unpredictable locations is observed. The predicted mechanism for transition to detonation in the present work matches well with the SWACER mechanism proposed by Lee [18], which suggested that a sequence of coherent waves amplify each other and eventually trigger a detonation wave.

Comparing the predictions for run-up distance in sections 7-1-2 and 7-1-3 reveals that increasing the temperature has reduced the run-up distance by 15%.

This is, however, contradictory to the experimental observations of Ciccarelli et al. [126], who found in their experiments with different tube dimensions that increasing the mixture temperature from 300K to 500K increased the run up distance from 3 m to 7 m (134%).

7-1-4 21 Step Chemistry and 293 K Initial Temperature

A third set of simulations is carried out using a 21-step detailed chemistry proposed by Williams' [124] for Hydrogen-Air autoignition simulations While all the other settings are the same as the previous case.

Figure 7-7 shows the pressure field for the case with detailed reaction and includes 18 frames showing the pressure waves from the early stages of the flame acceleration up to the point where a stable detonation wave is established. The colour spectrum in Figure starts from black (low pressure) and ends in yellow-white (high pressure, the mid-range pressure is red colure. Therefore, the obstacles inside the tube may not be distinguishable at the areas where the pressure waves have not been magnified yet and are having low pressures, because the obstacles also have black colour. Later on, as the stronger pressure waves pass over the obstacles they can be clearly distinguished within the domain.

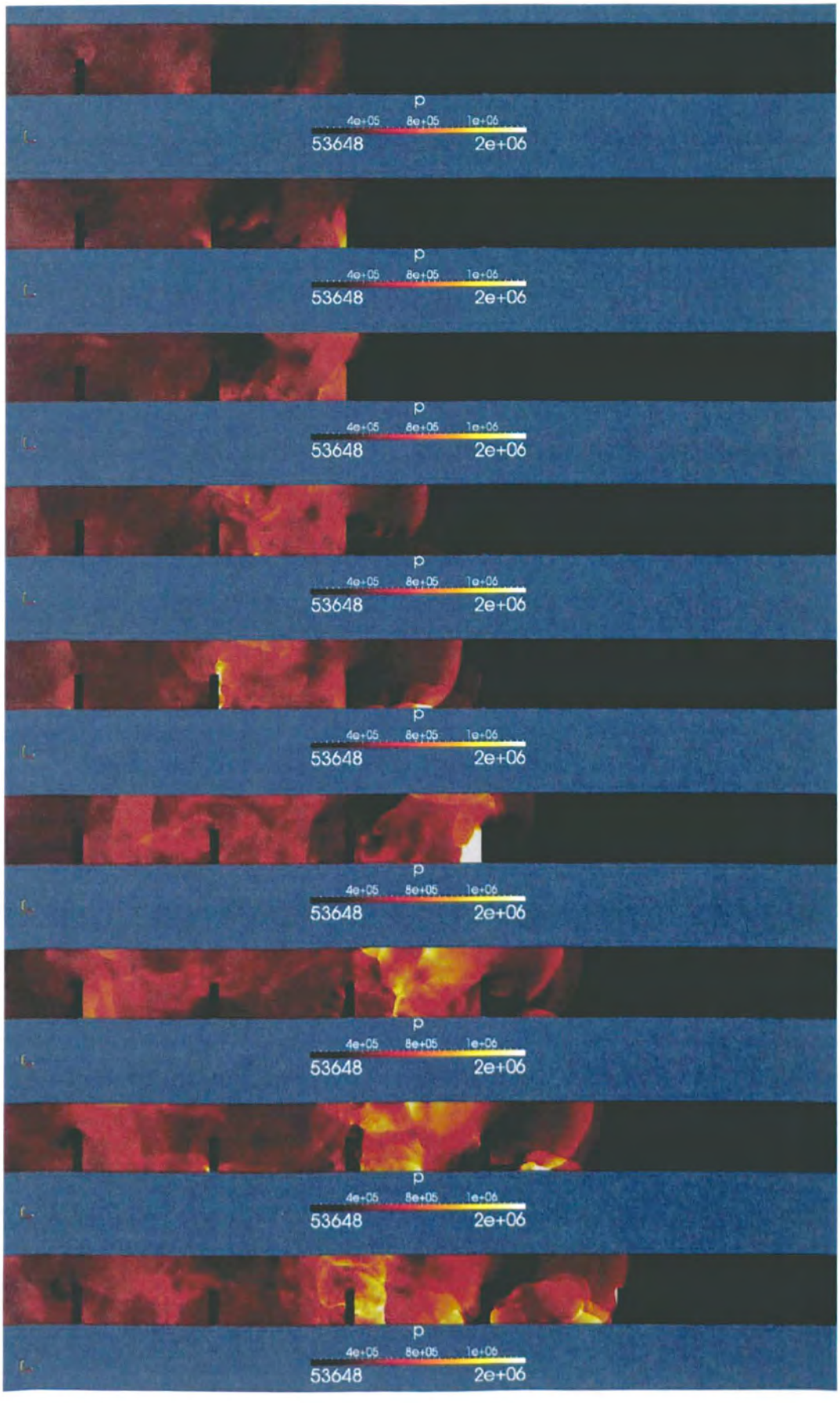
p
4e+05 8e+05 1e+06
53648 2e+06

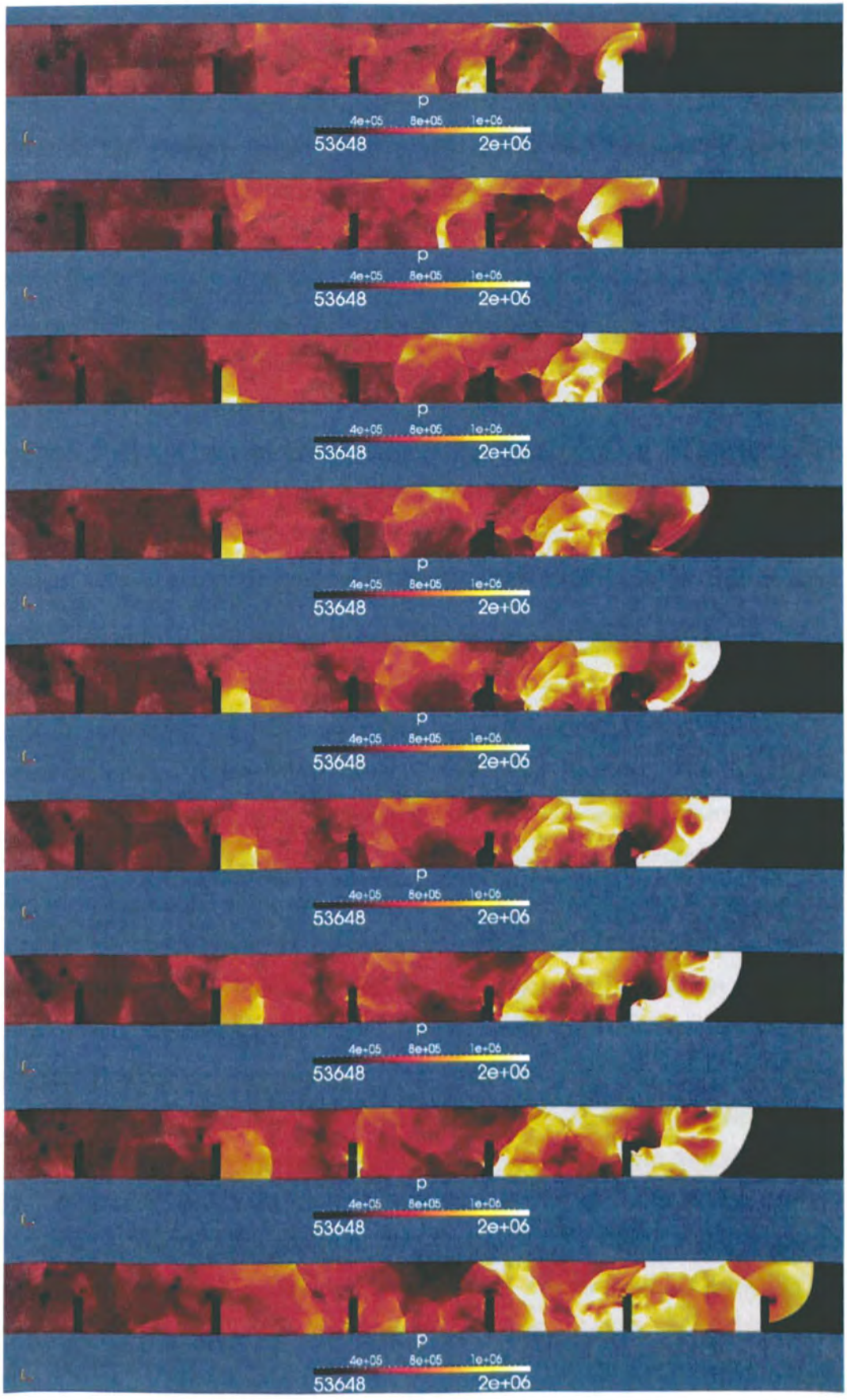

Figure 7-7 Pressure field showing the FA and DDT, predicted using 21 step reaction.

At the early stages of the flame acceleration the generated pressure waves are very weak, the dark red colour associated with these waves and represented in first few slides confirms that these waves are not strong enough to cause any hazardous situation yet. However as the flame propagates forward the pressure waves get stronger and stronger *illuminating the domain with a lighter* spectrum of colours. The most notable event happens at the 6^{th} frame where the leading pressure wave and reflected pressure wave from the 13^{th} obstacle collide and make a high pressure region but this collision is not strong enough to create a hot spot and damps quickly as it is evident in the 7^{th} frame. Similar shock collision happens right before the 14^{th} obstacle, although the shock collision region experiences a very high pressure at this instance, it cannot initiated the detonation at that location yet but the remains of this strong shock moves towards the leading flame front and catches up with the flame front in between the 14^{th} and 15^{th} obstacle. At this point, presented in 12^{th} and 13^{th} frames, a strong hot spot is generated which effectively initiates the detonation wave.

The most interesting observation here is that the hot spot appears in form of a curved line covering the whole surface of the flame front, meaning that in this particular case the detonation wave does not spread from one point to the rest of domain but rather it initiates at the whole flame surface at one instance. This observation suggests that the flame is experiencing a critical condition at this instance and is, more or less, uniformly conditioned to undergo transition to detonation. The two last frames in Figure 7-7 show that at the instance when DDT is occurring, the peak pressure magnitude is notably higher than CJ values, above 20 atm. This observation suggests that, when transition to detonation is happening, initially an overdriven detonation is generated which later, as presented in the last frame, stabilises at a peak pressure of about 15-17 atm which is in agreement with CJ predictions. The location of DDT occurrence in this case is delayed compared to the single step reaction results as well as Oran's predictions. In this case the DDT occurs between 14^{th} and 15^{th} obstacles whereas in the singles step reaction results DDT appears right over the 11^{th} obstacle and Oran has predicted DDT happening at 12^{th} obstacle. Analysing the results obtained using the detailed chemistry reveals that the predicted flame is lazier compared to the predictions of the simple reaction, as a consequence DDT is delay until the 15^{th} obstacle. It is generally difficult to conclude which result is more accurate because there is no experimental measurement available for this case to

verify the results, however the detailed reaction is derived and tested under a specific condition (for auto ignition) and there is no guarantee that it works well for every stage of flame acceleration and detonation, whereas the single step reaction is tested and tuned for both flames and detonation. Oran commented in an informal discussion with the candidate that they did not have a reasonable prediction using detailed reaction mechanisms which is believed to be a consequence of the limited applicability of detailed reaction mechanisms.

7-2 Numerical simulation of the DDT test of Teodorczyk et al. [120])

The experiments of Teodorczyk et al. [120] are one of the very few tests available on deflagration to detonation transition in hydrogen air mixtures and have hence be chosen as the benchmark case to validate the present model. The numerical domain is designed carefully to resemble the experimental setup.

The experimental equipment is schematically shown in Figure 7-8. The rig was equipped with four pressure transducers and four ion probes (P_1 to P_4) to record the pressure history. The domain is a 2 m long and 0.08 m high shock tube. The tube is filled with obstacle with 3 different blockage ratios and obstacle spacing. Only one case with 50% blockage ratio and 0.16 m obstacle spacing is simulated.

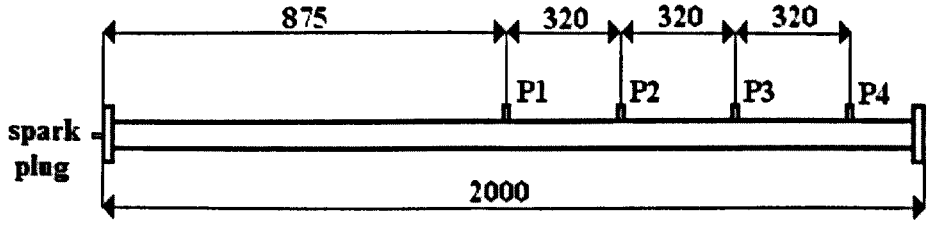

Figure 7-8 Experimental setup by Teodorczyk et al., the spacing between sensors is 32 cm (reproduced from [120])

Given the dimensions of the domain 80 mm×2000 mm, if 10 micron grid resolution is used, the total number of computational cells would be 1.6 billion. This is way above the maximum affordable number of grids even by using the largest

supercomputers. The two approaches explained in the previous section are used again to reduce the total number of the grid points.

By employing AMR with two levels of refinement, 40 micron grid resolution would give the same accuracy as a 10 micron one. This helps to reduce the total number of grid points to 100 M. The second approach is further used. The domain is divided into 6 mesh zones and fine grids are then used for different regions during different stages of the simulation. Depending on where the flame front is, the results are mapped from one mesh to the next one to carry on the simulations while keeping high resolution only at the areas covering the deflagration front. This has helped to reduce the total number of grid points to about 40 M. In the numerical simulations wall boundaries (no-slip reflecting boundaries) are used for obstacles and the tube walls. The mixture is stoichiometric hydrogen-air at 0.1 MPa and 293 K initial pressure and temperature.

7-2-1 Mild initiation of the Deflagration

As there is no information about the ignition size and energy in Teodorczyk et al. [120], it is decided to initiate the flame by setting a small (hemispherical shape with 0.0025 m radius) region of high temperature (2000 K) burnt products. This is the mildest way to initiate a laminar flame.

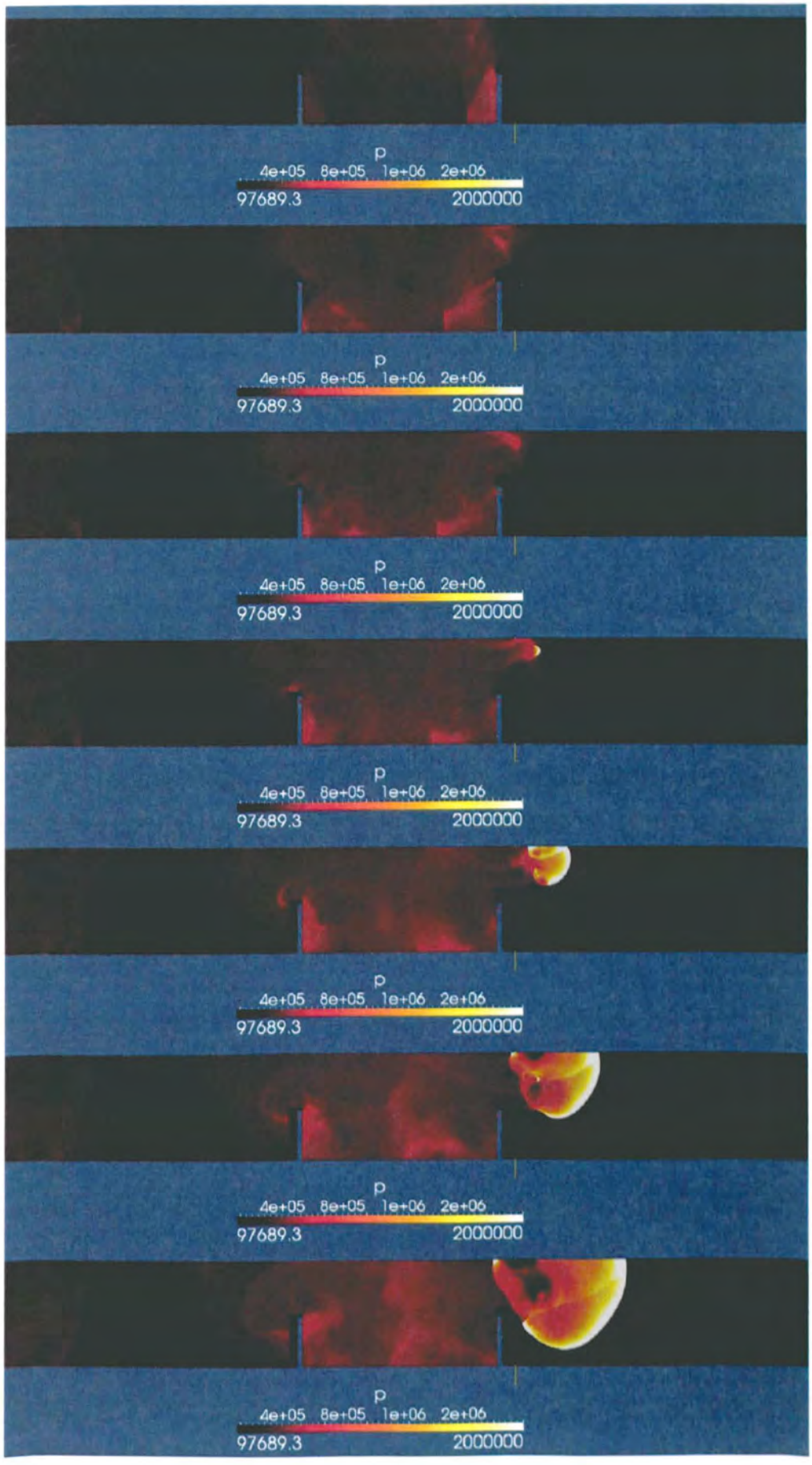
p
4e+05 8e+05 1e+06 2e+06
97689.3 2000000
p
4e+05 8e+05 1e+06 2e+06
97689.3 2000000
p
4e+05 8e+05 1e+06 2e+06
97689.3 2000000
p
4e+05 8e+05 1e+06 2e+06
97689.3 2000000
p
4e+05 8e+05 1e+06 2e+06
97689.3 2000000
p
4e+05 8e+05 1e+06 2e+06
97689.3 2000000
p
4e+05 8e+05 1e+06 2e+06
97689.3 2000000

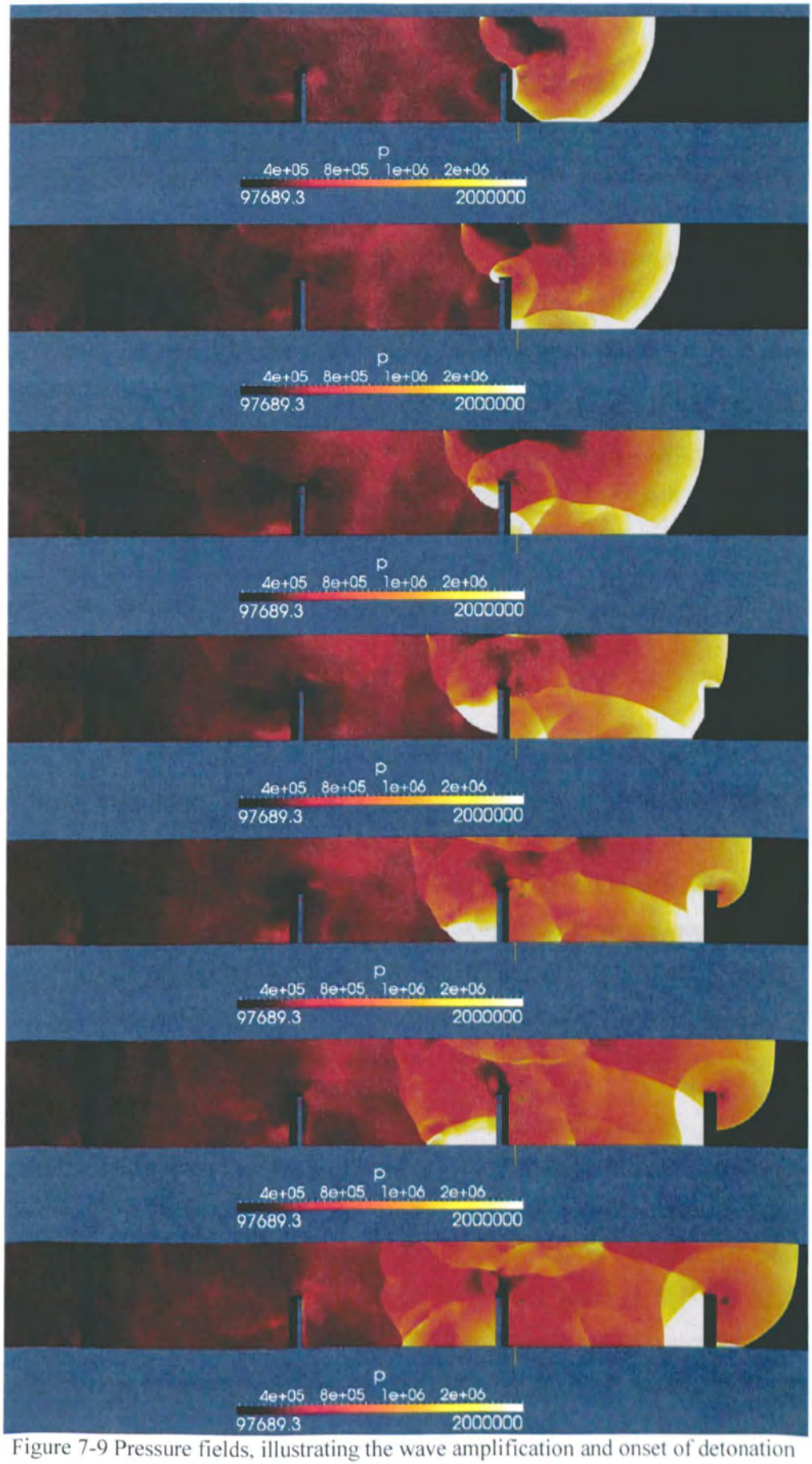

Figure 7-9 Pressure fields, illustrating the wave amplification and onset of detonation

Figure 7-9 shows the simulated pressure field illustrating the amplification of the pressure waves and onset of detonation. It shows 14 instances of the pressure filed. The timing between the presented frames is not equal because the initial stages are very slow compared to the stage when DDT occurs and it would be difficult to keep even time intervals for the images. At the initial frames, as expected, the pressure waves are weak, however the shock amplification and collision of the shocks happens continuously. The first sign of a hot spot formation appears in the 4^{th} frame where a small high pressure region starts to develop.

The hot spot continues to grow until it completely expands and catches up with the leading pressure waves. Consequently, a well established detonation wave starts to propagate from this point onwards.

These observations show that the first hot spot formed in this simulation was strong enough to cause the onset of detonation and the resulting detonation is self sustained and keeps propagating through the rest of the domain.

Similar to the previous simulation, the initially induced detonation wave is an overdriven detonation. This can be distinguished from the colour spectrum in the presented snapshots. Upon formation of the hot spot and onset of detonation, a retonation wave also propagates backwards into the burnt products. However the retonation wave damps quickly as it is propagating through a non-reactive mixture and do not have the energy to sustain it for a long distance. To analyse the details of transition to detonation in this case, pressure and temperature fields at the same time steps are presented at 8 different instances in Figure 7-10.

The third row of frames shows the initiation of the localised explosion. The pressure and temperature contours do not suggest any significant shock-shock or shock-flame collision at this point. However, the mixture is shock-heated and conditioned to ignite. This could be indicating that the flame is utterly fast in this case. The violent mixture ahead is well conditioned by the previous shock waves so that it is ready to auto-ignite. Then the regions very close to the flame brush or right at the flame brush auto-ignite simply by the slightest further actuation induced by the flame. This happens even before any shock-shock or shock-flame interaction causes auto-

ignition in the mixture. The hot spot initiated at the third frame successfully grows bigger and induces a self sustained detonation wave through the rest of the domain.

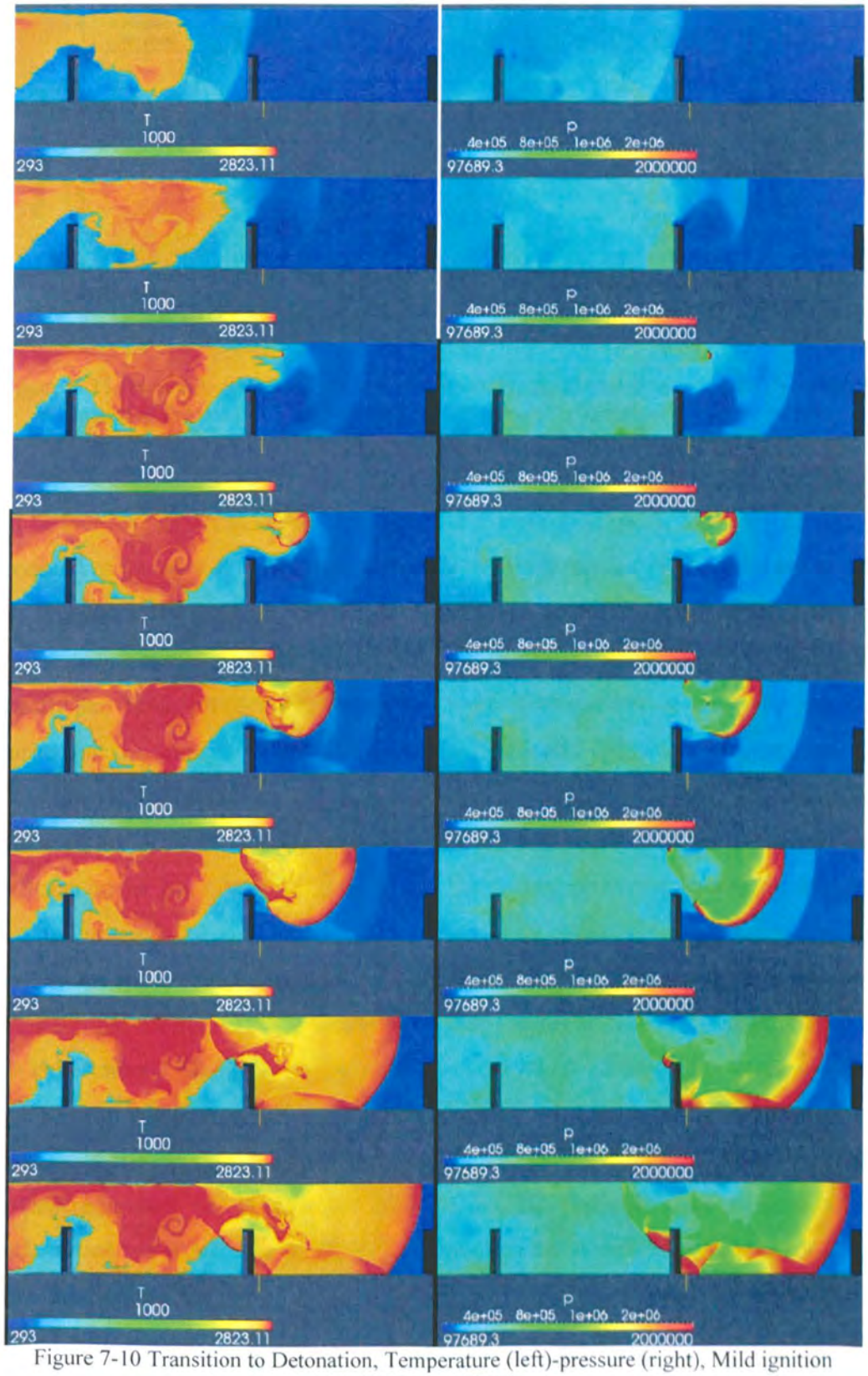

Figure 7-10 Transition to Detonation, Temperature (left)-pressure (right), Mild ignition (0.0025m, 2000K)

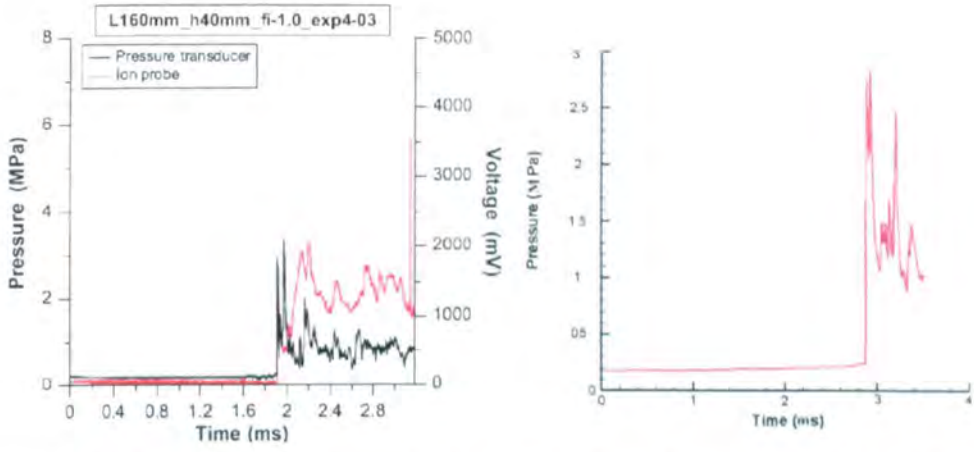

Figure 7-11 Recorded pressure history for location P3, Teodorczyk result [120] (left image) compared to the present work result (right image) - Mild ignition (0.0025m, 2000K)

To further investigate these observations and analyse the results, the pressure history recorded at location P_3 (as in Figure 7-8) from Teodorczyk [120] is compared with the predictions in the current work in Figure 7-11 where the left image shows the experimental results and the right image shows the predicted pressure history for exactly the same location in the present work. Comparison of the peak pressure shows that the strength of the shock wave is consistent with the measurements, but the numerical predictions show a slightly lower peak pressure. However the predicted time for detonation arrival to the P_3 location is delayed for about one millisecond in the numerical predictions. In the experimental measurements, the detonation reaches P_3 at about 1.9 milliseconds after ignition, whereas the numerical predictions show detonation reaches P_3 at about 2.9 milliseconds after ignition. This suggests that the transition to detonation occurs at about one millisecond earlier in the experiments. The delay in the predictions could be partially due to the ignition type used in the simulations. As mentioned earlier there is no information about the strength of the ignition source in the experiments. In the numerical simulations, the mildest approach for starting an initially laminar flame is used to initiate the deflagration wave whereas in the experiments a more violent electrical spark could have accelerated the initial flame development stages. It was even possible that it started with initially turbulent flame which would have led to shorter time for the deflagration wave to undergo transition to detonation.

Figure 7-12 shows the experimental observation of Teodorczyk et al. [127] in a different tube configuration. Although this shows a different case setting, the qualitative comparison of the results shows similar trend on the formation of a localised ignition centre at the flame brush (second frame in Figure 7-12) and transition to detonation.

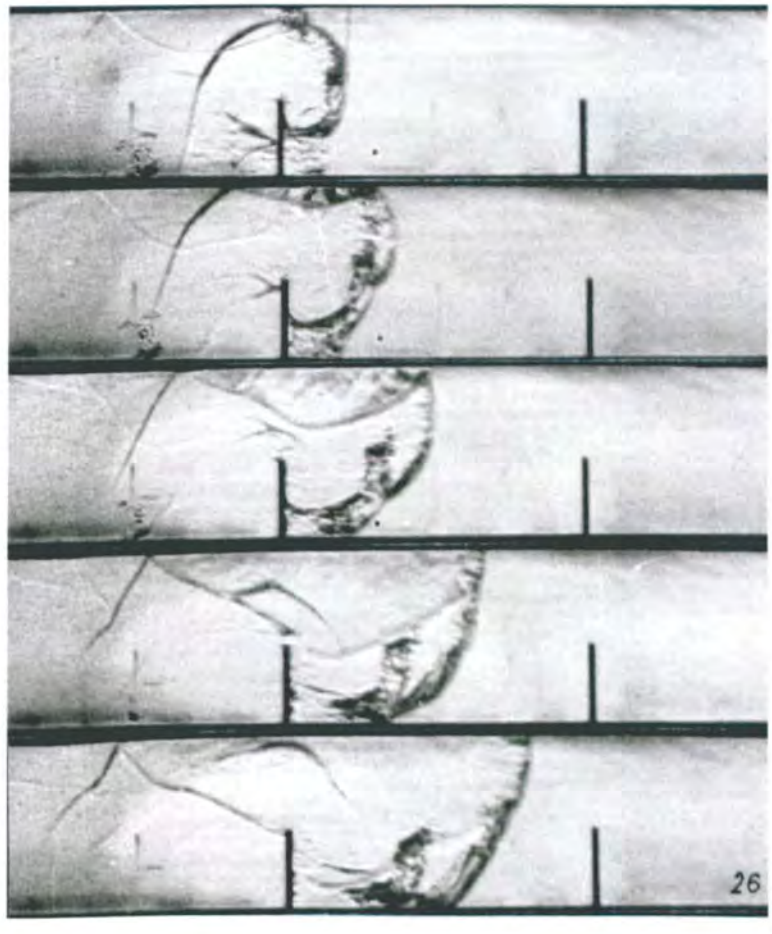

Figure 7-12 Sequence of schlieren photographs of a detonation wave propagating past an obstacle (reproduced from Teodorczyk et al., 1991 [127])

7-2-2 Stronger initiation of the Deflagration

Nevertheless the above discrepancy motivated the candidate to repeat the simulations with a stronger ignition source. As each simulation takes 6-8 month to finish, the simulation was only repeated once with a stronger ignition source. In this attempt, the size of the initial burnt kernel was doubled to 0.005 m and the initial ignition

temperature is increased to 3000K. This would form a stronger initiation for the initial flame but still keeping it laminar. If one wants to start a more violent ignition, it would be advisable to use a small amount of unburned mixture within the initial flame kernel. This would cause rapid burning of the un-reacted gases in the kernel and more violent and possibly turbulent growth of the initial flame kernel.

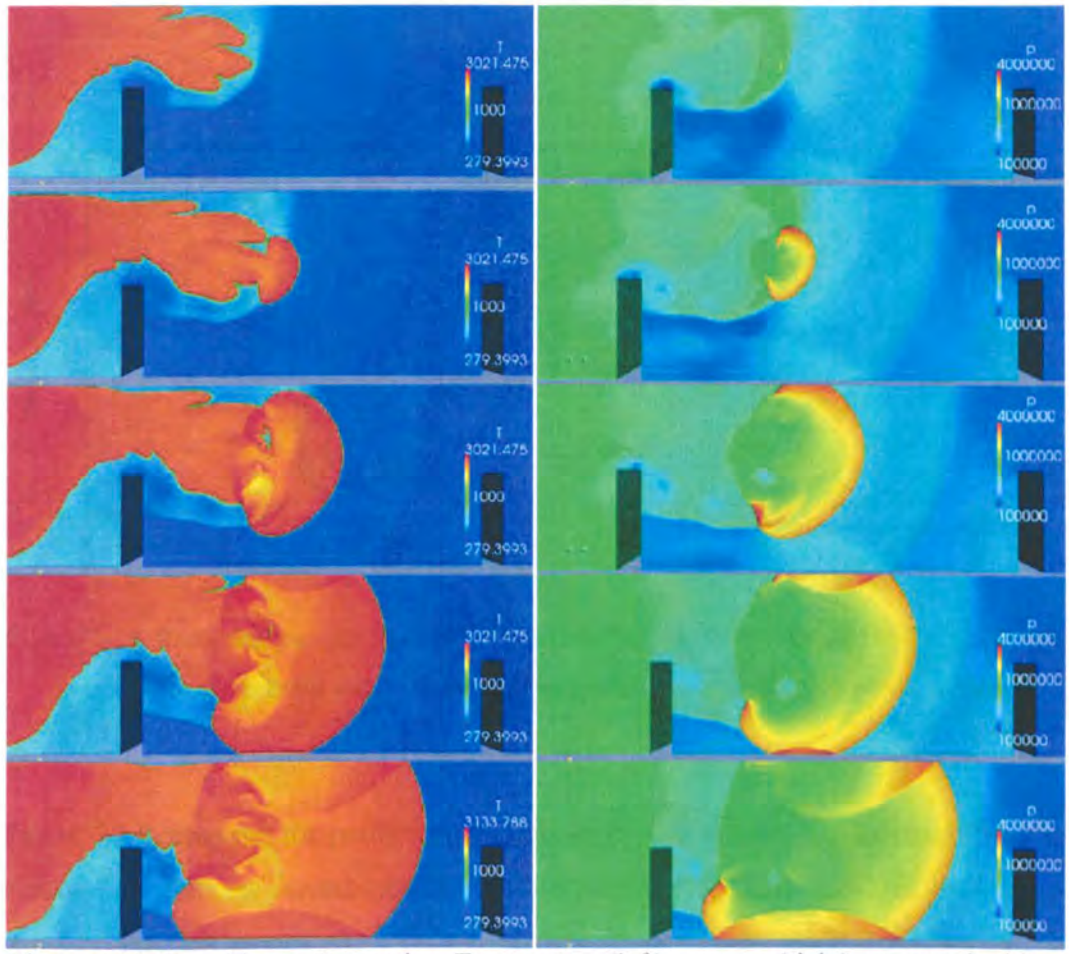

Figure 7-13 Transition to Detonation, Temperature (left)-pressure (right), stronger ignition (0.005m, 3000K)

Figure 7-13 shows pressure and temperature fields at the same time steps (for each row of frames) presented at 5 different time instances. Comparison of the pressure and temperature fields at the times when DDT is about to happen shows that, although the whole process is accelerated, the transition mechanism is very similar to the pervious case with milder ignition. This suggests that the mixture ahead of the flame is shock-heated by previous shock waves and conditioned to ignite, the flame

is utterly fast and violent so that the regions very close to the flame brush or right at the flame brush auto-ignite by the slightest further actuation induced by the reaction zone of the flame. This could be simply aligned with the SWACER mechanism implying that the sequence of energy release in the reaction zone is coherent with the leading pressure wave (in this case the flame front has almost caught up with leading pressure wave) so the sequence of energy feedings from the flame to the leading wave triggers the mixture to auto-ignite and transit to detonation.

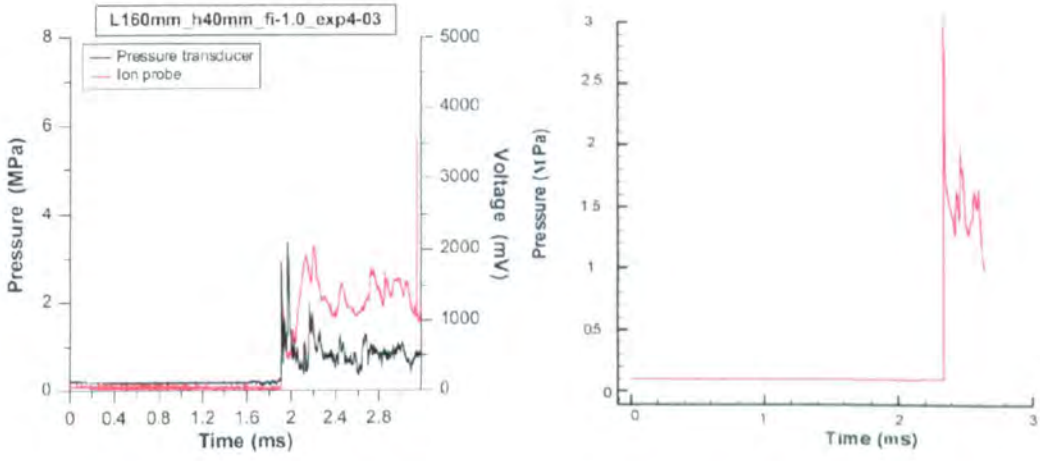

Figure 7-14 Recorded pressure history for location P3, Teodorczyk result [120] (left image) compared to the present work result (right image) stronger ignition (0.005m, 3000K)

Figure 7-14 compares the predicted the pressure history recorded at location P_3 (as in Figure 7-8) with the measurements of Teodorczyk [120]. It is seen that by using a stronger ignition source the detonation arrival time to pressure transducer P_3 is reduced to about 2.4 milliseconds whereas in the case of the mild ignition the recorded time is about 2.9 milliseconds. Although the timing still does not match the experimental measurement, it is promising in the sense that it confirms the influence of ignition source on the deviation of numerical predictions with experimental measurements. This confirms that the strength of the ignition source has considerable effect on the time for DDT and could affect the agreement between the predictions and the measurements.

This finding suggests that the effects of different ignition sources in combination with different initial conditions can be studied in the context of safety to assess the

potential hazards of DDT in practical applications. Following this thought, it will be possible to conduct numerical tests to develop guidance on the propensity, run-up distance and severity of DDT in different scenarios.

Chapter 8

Summary and Conclusions

8-1 Summary and Conclusions

The present work is concerned with numerical simulation of detonation as well as deflagration to detonation transition using two new solvers, DetoFOAM and DDTFOAM, developed within the OpenFOAM CFD toolbox.

Firstly in order to gain insight of flame acceleration, several numerical simulations of laminar and turbulent flames using the flame wrinkling model and coherent flame model (CFM) and large eddy simulations are carried out. The laminar burning velocity plays an important role in the combustion models and the overall behaviour of the reactive flow. A new correlation for hydrogen burning velocity has been developed from experimental data and implemented in the code. It predicts the burning velocity, which is required as input in the CFM, as a function of equivalence ratio, pressure and temperature of the mixture. The predictions of flame radii for spherically expanding flames in laminar and turbulent flows have compared favourably with the measurements.

Numerical simulations have then been carried out for a number of scenarios involving flame propagation and acceleration in obstructed channels. A grid size of about 1mm is used in these simulations. Despite good agreement with the experimental data, the flame pattern does not exactly mimic the measurements. Although the predictions reproduced some global flow parameters well, they missed the fine features of the flow. The deviations are attributed to the relatively large grid size and inadequacy of combustion and turbulent models to capture the underlying physics. For example, it is questionable whether the concept of flame thickness and the fundamentals of flamelet models are still valid at the vicinity of the obstacles without substantial modification. Furthermore a 1mm grid size would cut off a large portion of energy containing eddies and may obliterate some important dynamic effects in the flow such as formation of localised explosions in highly turbulent deflagration waves. The results revealed that the deviations of predictions from measurements are more evident in fast and highly turbulent flames. Based on these studies, it was decided that the traditional combustion models are only reliable at slow or medium velocities. They are not suitable for handling turbulent flames in the

presence of obstacles. It is also concluded that a much finer grid size is required to better resolve the flame front and the energy containing eddies.

For detonation studies, the diffusive effects are negligible and the Euler equations are solved. Based on the candidate's own experience as well as previously publishes investigations, the single step reaction mechanism was found to be capable of reproducing the detonation parameters well. The literature also suggests that detailed reactions are desirable only if one requires to monitor the traces of different species e.g. NO_X in the flow. A detonation solver, DetoFOAM, based on reactive Euler equations and single step Arrhenius reaction is developed within the OpenFOAM toolbox.

Predictions in both 2-D and 3-D have been carried out for several detonation propagations in small, medium and large scale geometries.

Firstly, detonation propagation in a very small domain using a 5 micron grid size is carried out. This is equivalent to having 33 grid points across the half reaction length. The predictions have captured the detonation structure which consists of mach stem, incident shock, transverse wave and the triple point. The formation of detonation cellular structure has also been captured accurately. The predicted detonation velocity of D=1997m/s further confirms the validity of the predictions. Further simulations in medium scale geometries are carried out and compared well against experimental results.

For large industrial scale detonations, it was necessity to re-tune the reaction mechanism based on the grid size as a comprise to limit computational time. Grid sizes of about 1~10 cm are used. These are well above the detonation wave thickness. At such large scale it is impossible to achieve grid independent results simply because it is impossible to resolve the detonation front (resolving detonation front requires ~10^{-5} m grid size). This problem was resolved by tuning the reaction mechanism in a way that the detonation front is artificially thickened. If the detonation front is thickened enough to contain 10~20 grid point within half reaction length, the artificially thickened detonation wave would be resolved using the available gird spacing. This approach predicts the detonation behaviour, pressure and propagation velocity correctly. However the fine details of detonation waves cannot be captured using this method. Using this approach, both validation and application

oriented studies have been conducted. In particular, the simulations of detonation scenario related to the Buncefield explosions are in line with the forensic evidence and support one of the investigation group's hypotheses that there were localised transitions from deflagration to detonation in the accident. The drag impulse generated from high velocity backward moving detonation products in large scale detonations can have more significant and destructive effects compared to the pressure impulses.

For comparison, a new solver based on the CJ programmed burn method, which is being more widely used in industry, has been programmed. Predictions for detonation propagation in a hypothetical vapour cloud filled with obstacles are compared with the predictions of DetoFoam. It was found that the CJ programmed burn approach is unable to predict the dynamics of detonation waves especially detonation failure and re-initiation at the vicinity of obstacles. Neglecting these effects led to under-predictions of pressure impulse and discrepancies in the predicted peak pressures and wave arrival timings.

For DDT simulations, a fully compressible solver, DDTFOAM, which solves the full Navier-Stokes equations has been developed also within the frame of OpenFOAM. A single step Arrhenius type reaction was designed in a way that ensures reproduction of flame properties, e.g. flame thickness and velocity as well as detonation properties, e.g. detonation thickness and velocity accurately. The grid independency test suggested that 10 micron grid, equivalent of 20 grid points across half reaction length, suffices for the simulations. Adaptive Mesh Refinement (AMR) and multistep mapping of results on multiple meshes with partially refined grids in regions of high gradients have been developed and used to reduce computational cost.

A 21 step detailed reaction mechanism for hydrogen and single step reaction were used to reproduce the numerical work of Oran et al. [21]. It is observed that the detailed reaction predicts a delayed DDT occurrence in comparison with the single step reaction. The results obtained from single step reaction are closer to the predictions of Oran et al. [21]. Generally, it is difficult to conclude which result is more accurate because there is no experimental measurement available to verify the results. The detailed reaction is derived and tested under a specific condition (for

auto ignition). There is no guarantee that it works well for every stage of flame acceleration and detonation, whereas the single step reaction is tested and tuned for both flames and detonation conditions. Therefore the results obtained from the single step reaction should be more reliable in this instance.

More simulations are carried out for the DDT case tested by Teodorczyk et al. [120]. It is observed that the transition to detonation occurred right at the flame brush while the flame is passing over one of the obstacles. This was in qualitative agreement with the experimental observations of Teodorczyk et al. In contrary with the numerical predictions of Oran et al. [21], which always predicted trigging DDT at the obstacle corners where the leading shock hits the obstacle.

The detonation arrival to a predetermined monitoring point was predicted with 1 ms delay compared to Teodorczyk measurements. This delay can be possibly attributed to the lack of information about the initial spark in the experiment and possibility of the numerical spark being too mild. The simulations are re-run using a more violent ignition source. The stronger ignition reduced the time discrepancy to 0.5 ms and supports the above suggestion.

8-2 Suggestions for future work

Lack of sufficient computational power is one of the main limiting aspects of the present work therefore the author recommend further work on AMR technique and incorporating more refinement levels in the simulations.

It would also be to develop two step and even more detailed reactions for DDT simulations to uncover more details throughout the simulations. However tuning multi-step reactions to correctly reproduce flame and detonation properties could be challenging.

The author also recommends further studies about the effects of various ignition sources on DDT run-up distance and run-up time.

Having a closer look at the whole DDT process reveals that it consists of four main stages, the initially low velocity deflagration wave, highly turbulent deflagration wave, the transition region and the final detonation wave. Solving all these 4 steps by using Navier stokes equations on an extremely fine grid is not cost effective, therefore the author recommends developing a new solver which can switch between three modes:

- Initial stages of the flame acceleration are solved using a combustion model on a relatively coarser grid (the traditional combustion models suffer from some shortcoming which are discussed earlier and must be addressed at this stage)
- The second stage comes into effect when the flame is getting highly turbulent and fast. At this stage the results are mapped from the previously coarser mesh to a much finer mesh and Navier stokes equations with properly tuned reaction models are solved until transition to detonation occurs.
- The third stage solves reactive Euler equations for simulating the final detonation wave (right after DDT stage) on a much coarse gird (due to lack of necessity for high resolution when we are dealing with a stabilised detonation wave only)

The suggested tree-step solver significantly reduces the computational cost in the simulations of the initial flame acceleration and the final detonation wave and spends the computational power on the DDT stage only where all the complexities lay. Despite being very challenging, combining these tree solvers and developing such a new solver could be a breakthrough towards fast and accurate simulation of deflagration to detonation transition in future.

References

1 H.D. Ng, J.H.S. Lee, "*Comments on explosion problems for hydrogen safety*", Journal of Loss Prevention in the Process Industries, 2007.

2 J. H. Lee, "*Initiation of gaseous detonation*", Ann. Rev. Phys. Chem., 28, 75–104, 1977.

3 E. Studer, P. Galon, "*Hydrogen Combustion Loads-plexus calculations*", Nuclear Engineering and Design 174, 119-134, 1997.

4 W.C. Reynolds, *The Element Potential Method for Chemical Equilibrium Analysis: Implementation in the Interactive Program STANJAN,* technical report, Stanford University, Dept. of Mechanical Engr., 1986.

5 S. Gordon, B.J. McBride, "*Computer Program for Calculations of Complex Chemical Equilibrium Compositions, Rocket Performances, Incident and Reflected Shocks, and Chapman-Jouguet Detonations*", NASA, Tech. Rep. SP-273, 1971.

6 J. H. S. Lee, "*The Detonation Phenomenon*", Cambridge University Press, ISBN-13: 978-0521897235, 2008.

7 E. S. Oran, "*Numerical Simulation of Reactive Flow*", Second edition, Cambridge University Press, 2000.

8 J.H.S. Lee, "*Dynamic parameters of gaseous detonations*", Ann Rev Fluids Mech 16, pp. 311–336, 1984.

9 T. Kratzel, E. Pantow and H. Eichert, "*Modelling of hydrogen combustion: Turbulent flame acceleration and detonation*", International Journal of Hydrogen Energy Volume 21, Issue 5, Pages 407-414, 1996.

10 N. N. Smirnov, I. I. Panfilov, M. V. Tyurnikov, A. G. Berdyuguin, V. R. Dushin and Yu. P. Presnyakov, "*Theoretical and experimental investigation of combustion to detonation transition in chemically active gas mixtures in closed vessels*", Journal of Hazardous Materials, Volume 53, Issues 1-3, Pages 195-211, 1997.

11 A. M. Khokhlov and E. S. Oran, "*Numerical simulation of detonation initiation in a flame brush: the role of hot spots*", Combustion and Flame, Volume 119, Issue 4, Pages 400-416, 1999.

12 A. M. Khokhlov, E. S. Oran, A. Y. Chtchelkanova, J.C. Wheeler, "*Interaction of a shock with a sinusoidally perturbed flame*", Combustion and Flame, Volume 117, Issues 1-2, Pages 99-116, 1999.

13 A.M. Khokhlov, E.S. Oran, G.O. Thomas, "*Numerical simulation of deflagration-to-detonation transition: the role of shock–flame interactions in turbulent flames*", Combustion and Flame, Volume 117, Issues 1-2, Pages 323-339, 1999.

14 E. S. Oran and V. N. Gamezo, "*Origins of the deflagration-to-detonation transition in gas-phase combustion*", Combustion and Flame, Volume 148, Issues 1-2, Pages 4-47, 2007.

15 J.H.S. Lee and I.O. Moen, "*The mechanism of transition from deflagration to*

detonation in vapour cloud explosions", Progress in Energy and Combustion Sciences 6, pp. 359–389, 1980.

16 K. Vaagsaether, V. Knudsen, D. Bjerketvedt "*Simulation of flame acceleration and DDT in H2-air mixture with a flux limiter centred method*", International Journal of Hydrogen Energy Volume 32, Issue 13, Pages 2186-2191, 2007.

17 A. M. Khokhlov, E. S. Oran and J. C. Wheeler, "*A theory of deflagration-to-detonation transition in unconfined flames*", Combustion and Flame, Volume 108, Issue 4, Pages 503-517, 1997.

18 J.H. Lee, R. Knystautas, N. Yoshikawa, "*Photochemical initiation of gaseous detonations*", Acta Astronautica, 1978.

19 Y. Mahmoudi, K. Mazaheri, "*High resolution numerical simulation of the structure of 2-D gaseous detonations*", Proceedings of the Combustion Institute, Volume 33, Issue 2, Pages 2187-2194, 2011.

20 E. Schultz, J. Shepherd, "*Detonation Diffraction Through a Mixture Gradient*", Explosion Dynamics Laboratory Report FM00-1, February 8, 2000.

21 V. N. Gamezo, T. Ogawa, E. S. Oran, "*Numerical simulations of flame propagation and DDT in obstructed channels filled with hydrogen–air mixture*", Proceedings of the Combustion Institute, Volume 31, Issue 2, Pages 2463-2471, 2007.

22 T. D. Aslam, D. Scott Stewart "*Detonation shock dynamics and comparisons with direct numerical simulation*", Los Alamos National Laboratory and University of Illinois, 1998.

23 C. Wang, "*One-Step Chemistry model for Large-Scale detonation simulation*", Centre for Fire and Explosion Studies, Kingston university, internal report, 2011.

24 S.P.M Bane, J. L. Ziegler and J.E. Shepherd. "*Development of One-Step Chemistry Model for flame and ignition simulation*". GALCIT Report GALTCITFM: 2010.002, 2010.

25 Z. Huang, Y. Zhang, K. Zeng, B. Liu, Q. Wang, D. Jiang, "*Measurements of laminar burning velocities for natural gas–hydrogen–air mixtures*", Combustion and Flame, 146, 1-2, 302-311, 2006.

26 S. Verhelst, R. Woolley, M. Lawes, R. Sierens, "*Laminar and unstable burning velocities and Markstein lengths of hydrogen-air mixtures at engine-like conditions*", proceeding of combustion Institute, 2005.

27 X. Qin, H. Kobayashi, T. Niioka, "*Laminar burning velocity of hydrogen–air premixed flames at elevated pressure*", Experimental Thermal and Fluid Science, 21, 1-3, 58-63, 2000.

28 N. Lamoureux, N. Djeba, Chaumeix, C. E. Paillard, "*Laminar flame velocity determination for H2–air–He–CO2 mixtures using the spherical bomb method*", Experimental Thermal and Fluid Science, 27, 385-393, 2003.

29 C. W. Kang, C. H. Chung , "*A suggestion for Hydrogen flame speed correlation under severe Accidents*", Journal of the Korean Nuclear Society, Volume 26, Number 1, 1994.

30 D. D. S. Liu, R. MacFarlane, "*Laminar Burning velocities of Hydrogen-Air and Hydrogen-Air-Steam Flames*", Combustion and Flame, 49: 59-71, 1983.

31 G. W. Koroll, R. K. Kumar and E. M. Bowles, "*Burning velocities of Hydrogen-air mixture*", *Combustion and Flames*, 94: 330-340, 1993.

32 M. Ilbas, A.P. Crayford, I. Yılmaz, P.J. Bowen, N. Syred, "*Laminar-burning velocities of hydrogen–air and Hydrogen–methane–air mixtures: An experimental study*", International Journal of Hydrogen Energy, 31, 1768 – 1779, 2006.

33 L. Mangani, "*Development and Validation of an Object Oriented CFD Solver for Heat Transfer and Combustion Modelling in Turbomachinery Applications*", PhD Thesis, Universita degli studi di Firenze, 2008.

34 F. M. White, "*Viscous Fluid Flow*", McGraw-Hill, 1991.

35 "*OpenFoam User Guide*", version 2.0.0, OpenCFD Co., accessed 2011.

36 S.V. Patankar, "*Numerical heat transfer and fluid flow*", Hemisphere Publishing Corporation, 1981.

37 H. Jasak, "*Error Analysis and Estimation for the Finite Volume Method with Applications to Fluid Flows*", PhD Thesis, Imperial College of Science, Technology and Medicine 1996.

38 Harten, Ami, "*High resolution schemes for hyperbolic conservation laws*", J. Comput. Phys. 49: 357–393, doi:10.1006/jcph.1997.5713, 1983.

39 Anderson, jr., J. D. "*Computational Fluid Dynamics, the basic with applications*", McGraw-Hill, US, 1995.

40 R.I. Issa, "*Solution of the implicitly discretized fluid flow equations by operator-splitting*", Journal of. Comp. Physics, 62:40:65, 1986.

41 S. R. Turns, "*An Introduction to Combustion*", McGraw-Hill, 2000.

42 K.K. Kuo, "*Principles of Combustion*", JOHN WILEY & SONS, 2005.

43 T. Poinsot, D. Veynante, "*Theoretical and Numerical Combustion*", Edwards, 2005.

44 M. C. Potter, D. C. Wiggert, "*Mechanics of Fluids*", Prentice-Hall International Inc, 1997.

45 J. H. Spurk, "*Fluid Mechanics*", Springer, 1997.

46 H. K. Versteeg, "*An Introduction to Computational Fluid Dynamic: The Finite Volume Method*", Harlow Longman, 1995.

47 J. H. Ferziger, M. Peric, "*Computational Methods for Fluid Dynamic*", Springer, 2002.

48 http://www.engineeringtoolbox.com/adiabatic-flame-temperature-d_996.html, "*flame temperatures*", access: date June 2008.

49 O. L. Gulder, "*Correlations of laminar combustion data for SI engine fuels*", SAE Technical Paper Series, 1984.

50 A. A. Boretti, M. J. Brear, H. C. Watson, "*Experimental and numerical study of hydrogen fuelled I.C. engine fitted with the hydrogen assisted jet ignition engine*", 16th Australian fluid mechanics conference, crown plaza, Gold coast, Australia, 2-7, 2007.

51 Z. Huang, Y. Zhang, K. Zeng, B. Liu, Q. Wang, D. Jiang, "*Measurements of laminar burning velocities for natural gas–hydrogen–air mixtures*", Combustion and Flame, 146, 1-2, 302-311, 2006.

52 S. Verhelst, R. Woolley, M. Lawes, R. Sierens, "*Laminar and unstable burning velocities and Markstein lengths of hydrogen-air mixtures at engine-like conditions*",

proceeding of combustion Institute, 2005.

53 X. Qin, H. Kobayashi, T. Niioka, "*Laminar burning velocity of hydrogen–air premixed flames at elevated pressure*", Experimental Thermal and Fluid Science, 21, 1-3, 58-63, 2000.

54 N. Lamoureux, N. Djeba, Chaumeix, C. E. Paillard, "*Laminar flame velocity determination for H2–air–He–CO2 mixtures using the spherical bomb method*", Experimental Thermal and Fluid Science, 27, 385-393, 2003.

55 C. W. Kang, C. H. Chung , "*A suggestion for Hydrogen flame speed correlation under severe Accidents*", Journal of the Korean Nuclear Society, Volume 26, Number 1, 1994.

56 D. D. S. Liu, R. MacFarlane, "*Laminar Burning velocities of Hydrogen-Air and Hydrogen-Air-Steam Flames*", Combustion and Flame, 49: 59-71, 1983.

57 G. W. Koroll, R. K. Kumar and E. M. Bowles, "*Burning velocities of Hydrogen-air mixture", Combustion and Flames*, 94: 330-340, 1993.

58 M. Ilbas, A.P. Crayford, I. Yılmaz, P.J. Bowen, N. Syred, "*Laminar-burning velocities of hydrogen–air and Hydrogen–methane–air mixtures: An experimental study*", International Journal of Hydrogen Energy, 31, 1768 – 1779, 2006.

59 H. G. Weller, G. Tabor, "*Large Eddy Simulation of Premixed Turbulent Combustion Using Ξ Flame Surface Wrinkling Model*", Flow, Turbulence and Combustion, 72, 1, 2004.

60 H.G. Weller, G. Tabor, A.D. Gosman, C. Fureby, "*Application of a flame-wrinkling les combustion model to a turbulent mixing layer*", Symposium (International) on Combustion, 27, 1, 899-907, 1998.

61 H.G. Weller, "*The development of a new flame area combustion model using conditional averaging*", thermo-fluid section report, TF/9307, Imperial college of science technology and medicine, 1993.

62 Y.J. Zhu, J. Chao, J.H.S. Lee "*An experimental investigation of the propagation mechanism of critical deflagration waves that lead to the onset of detonation*", Proceedings of the Combustion Institute 31, 2007.

63 S. Richard, O. Colin, O. Vermorel, A. Benkenida, C. Angelberger, D. Veynante, "*Towards large eddy simulation of combustion in spark ignition engines*", Proceedings of the Combustion Institute, Volume 31, Issue 2, Pages 3059-3066, 2007.

64 D. Veynante, L. Vervisch, "*Turbulent combustion modelling*", Progress in Energy and Combustion Science, Volume 28, Issue 3, Pages 193-266, 2002.

65 P. Boudier, S. Henriot, T. Poinsot, T. Baritaud, "*A model for turbulent flame ignition and propagation in spark engines*", Proceedings of the Combustion Institute. 24: 503–510, 1992.

66 J. Duclos, D. Veynante, T. Poinsot, "*A comparison of flamelet models for premixed turbulent combustion*", Combustion and Flame, 95 : 101–117, 1993.

67 E. Salzano, F.S. Marra, G. Russo, J.H.S. Lee, "*Numerical simulation of turbulent gas flames in tubes*", Journal of Hazardous Materials, A95, 233–247, 2002.

68 R. Knystautas, J. Lee, J. E. Shepherd, A. Teodorczyk, "*Flame Acceleration and Transition to Detonation in Benzene–Air Mixtures*", Combustion and Flame, Volume 115, pp. 424-436, 1998.

69 S. N. D. H. Patel, S. Jarvis, S. S. Ibrahim, G. K. Hargrave, "*an experimental and numerical investigation of premixed flame deflagration in a semi confined explosion chamber*", Proceedings of the Combustion Institute, 29, 1849–1854, 2002.

70 K. Vaagsaether, V. Knudsen, D. Bjerketvedt, "*Simulation of flame acceleration and DDT inH2-air mixture with a flux limiter centred method*", International Journal of Hydrogen Energy 32, 2186 – 2191, 2007.

71 B. Renou, A. Boukhalfa, "*An experimental study of freely propagating premixed flames at various Lewis numbers*", Combust. Sci. And Tech, 162, 347-370, 2001.

72 S. Richard, O. Colin, O. Vermorel, A. Benkenida, C. Angelberger, D. Veynante, "*Towards large eddy simulation of combustion in spark ignition engines*", Proceedings of the Combustion Institute 31, 3059–3066, 2007.

73 A. Patel, S.S. Ibrahim, M.A. Yehia, G.K. Hargrave, "*Investigation of premixed turbulent combustion in a semi-confined explosion chamber*" Experimental Thermal and Fluid Science, Volume 27, Issue 4, April, Pages 355-361, 2003.

74 F.A. Abel, "*Researches on Guncotton – On the manufacture and composition of gun cotton*" Phil. Trans. R. Soc. 159:489–516. 1869. Also, C. R. Acad. Sci. Paris 69:105–121, 1869.

75 P. Boudier, S. Henriot, T. Poinsot, T. Baritaud, "*A model for turbulent flame ignition and propagation in spark engines*", Proceedings of the Combustion Institute. 24: 503–510, 1992.

76 I. Matsukov, M. Kuznetsov, V. Alekseev, S. Dorofeev, "*Photographic study of the characteristic regimes of turbulent flame propagation, local and global quenching in obstructed areas*", Report No. 315/20088504/INR, prepared for FZK-INR, 1998.

77 I. Matsukov, M. Kuznetsov, V. Alekseev, S. Dorofeev, "*Photographic study of unstable turbulent flames in obstructed channel*", Proc. the 17th international colloquium on the dynamics of explosions and reactive systems, July 25–30, Heidelberg, Germany, ISBN 3-932217-01-2, Universitat Heidelberg, 1999.

78 N. Lamoureux, N. Djeba, N. Chaumeix, C.E. Paillard, "*Laminar flame velocity determination for H2–air–He–CO2 mixtures using the spherical bomb method*", Experimental Thermal and Fluid Science, 27, 385-393, 2003.

79 G. Ciccarelli, S. Dorofeev, "*Flame acceleration and transition to detonation in ducts*", Progress in Energy and Combustion Science, Volume 34, Issue 4, Pages 499-550, 2008.

80 J. Wen, A. Heidari, V.H.Y. Tam, "*Numerical simulation of propane detonation in medium and large scale geometries*", Journal of Loss Prevention in the Process Industries, 2010.

81 A. Heidari, S.A. Ferraris, J. Wen, V.H.Y. Tam, "*Numerical simulation of large scale hydrogen detonation*", International Journal of Hydrogen Energy, 2010.

82 A. Heidari, K. Mazaheri, "*Determination of the Equilibrium parameters of Gaseous Detonation using a Genetic Algorithm*", Iranian Journal of Chemical Engineering, 2007.

83 A. Heidari, J.X. Wen, "*Flame acceleration and transition from deflagration to detonation in hydrogen explosions*", 4th International Conference on Hydrogen Safety, ICHS 2011, San Francisco, California-USA, 2011.

84 A. Heidari, J.X. Wen, V.H.Y.Tam, "*Numerical simulations of large scale hemispherical and pancake cloud detonation*", International Colloquium on the Dynamics of Explosions and Reactive systems (ICDERS), University of California, Irvine, 2011.

85 A. Heidari, J. M. Pereira, J.X. Wen, V.H.Y.Tam, H.Ghasemnejad, H.A. Shariff, T Donchev, D.M. Johnson, "*Towards understanding the Buncefield Explosion Mechanism through advanced numerical analysis and large scale experiments*", Hazards XXII - process safety and environmental protection, 2011.

86 J. Wen, A. Heidari, M. Rao, S.A. Ferraris, V.H.Y. Tam, "*Simulating Flame Propagation in Obstructed Channels with OpenFOAM*", 6th International Seminar on Fire and Explosion Hazards, 2010.

87 J.X. Wen, A. Heidari, V.H.Y. Tam, "*Numerical simulation of propane detonation in medium and large scale geometries*", The 33rd International Symposium on Combustion, Beijing, China, 2010.

88 A. Heidari, S.A. Ferraris, J. Wen, V.H.Y. Tam, "*Numerical simulation of large scale hydrogen detonation*", Proc. 3rd International Conference on Hydrogen Safety, Sep., 2009, Corsica, France, 2009.

89 A. Heidari, S.A. Ferraris, J. Wen, V.H.Y. Tam, "*Predicting Flame Acceleration Using a Coherent Flame Model*", 22nd International Colloquium on the Dynamics of Explosions and Reactive Systems, 2009.

90 M. Rao, A. Heidari, J. Wen, V.H.Y. Tam, "*Numerical Study of Large Scale Hydrogen Explosions and Detonation*", Hazards XXI - Process safety and environmental protection, 2009.

91 A. Heidari, K. Mazaheri, "*Determination of Detonation Equilibrium Parameters using Genetic Algorithm*", ISME, 2007.

92 A. Heidari, K. Mazaheri, "*Determining the Equilibrium Composition of Combustion Products using Genetic Algorithm*", 11th National Congress of Chemical Engineering, 2006.

93 A. Heidari, "*Determining Detonation Speed and Comparing with Experimental Data*", Master Thesis, Tarbiat Modares University of Iran, 2007.

94 E. Schultz, "*Detonation diffraction trough an abrupt area expansion*", Ph.D. thesis, California Institute of Technology, 2000.

95 J. E. Shepherd, I. O. Moen, S. B. Murray, P. A. Thibault, "*Analyses of the cellular structure of detonation*", In 21st Symposium (Intl) on Combustion, pp. 1649-1658. The Combustion Institute, 1986.

96 M. Arienti, "*A Numerical and Analytical Study of Detonation Diffraction*" PhD Thesis, California Institute of Technology, 2003.

97 C. B. Laney, "*Computational Gas dynamics*", Cambridge University Press, 2008.

98 H. K. Versteeg, "*An Introduction to Computational Fluid Dynamic: The Finite Volume Method*", Harlow Longman, 1995.

99 R. Deiterding, "*Detonation Structure Simulation with AMROC*", California Institute of Technology, 2005.

100 R. Deiterding "*Numerical Structure Analysis of Regular Hydrogen-Oxygen Detonations*", SSCI Meeting, Session 03F-28, 2003.

101 R. Deiterding, "*High-resolution numerical simulation and analysis of Mach reflection structures in detonation waves in low-pressure H2 - O2 - Ar mixtures: a summary of results obtained with the adaptive mesh refinement framework AMROC*", Journal of Combustion, 2011: 738969, 2011.

102 M.I. Radulescu, G.J. Sharpe, J.H.S. Lee, C.B. Kiyand, A.J. Higgins, R.K. Hanson. "*The ignition mechanism in irregular structure gaseous detonations*", Proceedings of the Combustion Institute 30, 1859–1867, 2005.

103 C. J. Wang, S. L. Xu, C. M. Guo, "*Study on gaseous detonation propagation in a bifurcated tube*", Journal of Fluid Mechanics 25 599, pp 81-110, 2008.

104 A. Efimenko, A. Gavirkov, "*Large scale Hydrogen-Air detonation experiments. The effect of ignition location and hydrogen concentration on loads*", laboratory of induced chemical reactions Russian research centre, Kurchatov institute, Description of HySafe SBEP V13, www.hysafe.org, 2007.

105 A. Kotchourko, "*safety of hydrogen as an Energy carrier*", compilation report on SBEPs results of the 4th period, HYSAFE, http://www.hysafe.org/documents?kwd=SBEP, 2007.

106 S.M. Frolov, V.S. Aksenov, I.O. Shamshin, "*Reactive shock and detonation propagation in U-bend tubes*" Journal of Loss Prevention in the Process Industries 20, 501–508, 2007.

107 M. Groethe, E. Merilo, J. Colton, S. Chiba, Y. Sato, H. Iwabuchi, "*Large-scale hydrogen deflagrations and detonations*", International Journal of Hydrogen Energy 32, 2125 – 2133, 2007.

108 G.O. Thomas, R.L. Williams, "*Detonation interaction with wedges and bends*", Shock Waves, Volume 11, Number 6, 481-492, 2002.

109 Buncefield Explosion Mechanism Advisory Group report, http://www.buncefieldinvestigation.gov.uk/reports/buncefieldagr.pdf, 2007.

110 G. M. Makhviladze, S. E. Yakush, 2009, "*Buncefield Explosion Mechanism Phase 1*", HSE, Proc. Combust Inst, Vol. 29, pp. 195–210, 2002.

111 G. Atkinson, S. Gant, D. Painter, L. Shirvill, A. Ungut, "*Liquid dispersal and vapour production during overfilling incidents*", Hazards XX: Process Safety and Environmental Protection, Harnessing Knowledge, Challenging Complacency (Symposium Series 154), Institution of Chemical Engineers, 15, 2008.

112 M. Sichel, J. C. Foster, "*The ground impulse generated by a plane fuel-air explosion with side relief*", Acta Astronautica, 293-256, 1979.

113 B. Fishburn, N. Slagg, P. Lu, "*Blast effect from a pancake shaped fuel drop—air cloud detonation (theory and experiment)*", Journal of Hazardous Materials, Volume 5, Issues 1-2, , Pages 65-75, 1981.

114 E. D. Giroux, "*HEMP Users Manual*", UCRL-51079, Lawrence Livermore Laboratory, University of California, Livermore, California, 1971.

115 Ufa train disaster, http://en.wikipedia.org/wiki/Ufa, 2010.

116 G. M. Makhviladze, S. E. Yakush, "*Large-scale unconfined fires and explosions*", Proc. Combust Inst, Vol. 29, pp. 195–210, 2002.

117 R. B. Corr, V. H. Y. Tam, "*Gas explosion generated drag loads in offshore installations*", BP Exploration UK, 2000.

118 T. D. Aslam, D. S. Stewart, "*Detonation shock dynamics and comparisons with direct numerical simulation*", Los Alamos National Laboratory and University of Illinois, 1998.

119 A. K. Kapila, J. B. Bdzil, D. S. Stewart, "*On the Structure and Accuracy of Programmed-Burn*", Combustion Theory and Modelling, 2006.

120 A. Teodorczyk, P. Drobniak, A. Dabkowski, "*Fast turbulent*

deflagration and DDT of hydrogen–air mixtures in small obstructed channel" International Journal of Hydrogen Energy, Volume 34, Issue 14, Pages 5887-5893, 2009.

121 A. Teodorczyk, "*Scale effects on hydrogen–air fast deflagrations and detonations in small obstructed channels*", Journal of Loss Prevention in the Process Industries, Volume 21, Issue 2, Pages 147-153, 2008.

122 P. Moin, K. Mahesh. "*Direct numerical simulation: A tool in turbulence research*", Annual Reviews of Fluid Mechanics 30:539–578, 1998.

123 P. Vuillermoz, E. S. Oran, "*Mixing regimes in a spatially confined two-dimensional compressible mixing layer*", Proceedings of the Royal Society, London, A, 449:351–380, 1995.

124 F. A. Williams, "*Detailed and reduced chemistry for hydrogen autoignition*", Journal of Loss Prevention in the Process Industries, Volume 21, Issue 2, 2008.

125 Ya. B. Zeldovich, V. B. Librovich, G. M. Makhviladze, G. I. Sivashinsky, "*On the onset of detonation in a nonuniformly heated gas*" Acta Astron., 15, 313, 1970.

126 G Ciccarelli, J L Boccio, T Ginsberg, H. Tagawa, "*The Influence of initial temperature on flame acceleration and deflagration to detonation transition*", International Symposium on Combustion Volume: 26, Issue: 2, Pages: 2973-2979, 1996.

127 A. Teodorczyk, J.H.S. Lee, R. Knystautas, "*The structure of fast turbulent flames in very rough, obstacle-filled channels*", International Symposium on Combustion, Volume 23, Issue 1, Pages 735-741, 1991.

128 J.A. Domaradzki, "*Analysis of sub-grid scale eddy viscosity with the use of the results from direct numerical simulations*", Physics of Fluids A 4(9):2037–2045. 1992.

129 Yeung, P.K., and J.G. Brasseur, "*The response of isotropic turbulence to isotropic and anisotropic forcing at the large scales*",Physics of Fluids A 3(5):884–896. 1991.

130 David C Wilcox, "*Turbulence Modelling for CFD*" (Third Edition), Dcw Industries, Incorporated, 2006.

131 F. Grinstein, L. Margolin, W. Rider (Eds.), "*Implicit Large Eddy Simulation: Computing Turbulent Flow Dynamics*", Cambridge University Press, Cambridge, UK, 2007.

132 J. Chao, A. T. Hu, G. C. Karris, E. W. Phillips, H. Prophet, "*JANAF thermochemical tables, first addendum*", NASA-CR-83718, PB-168-370-1, Feb 17, 2009.

133 W. Sutherland, "*The viscosity of gases and molecular force*", Philosophical Magazine, S. 5, 36, pp. 507-531, 1893.

134 PA. Urtiew, A. K. Oppenheim, "*Experimental observation of the transition to detonation in an explosive gas.*" Proc of Roy Soc A 295:1328, 1966.

135 O. Peraldi, R. Knystautas, J. H. Lee, "*Criteria for transition to detonation in tubes*". 22nd Symposium (Int.) on Combustion. The Combustion Institute, Pittsburgh, pp 1629–1637, 1988.

136 J. H. Lee, R. Knystautas, C. K. Chan, "*Turbulent flame propagation in obstacle-filled tubes*". 20th Symposium (Int.) on Combustion, The Combustion Institute, Pittsburgh, PA, pp 1663–1672, 1984.

137 Y. B. Zeldovich, "*On the theory of the propagation of detonations in gaseous systems*", Zh. Eksp. Teor. Fiz. 10, 542–568, 1940.

138 J. von Neumann, "*Theory of detonation waves*" in: A.J. Taub. (Ed.), John von Neumann, Collected Works, vol. 6, Macmillan, New York, 1942.

139 W. Doring, "*On detonation processes in gases*", Ann. Phys. 43, 421–436, 1943.

140 M. Zbikowski, D. Makarov, V. Molkov, "*LES model of large scale hydrogen–air planar detonations: Verification by the ZND theory International Journal of Hydrogen Energy*", Volume 33, Issue 18, Pages 4884-4892, 2008.

141 A. Uranga, "*Investigation of transition to turbulence at low Reynolds numbers using Implicit Large Eddy Simulations with a Discontinuous Galerkin method*", Ph.D. Thesis, Massachusetts Institute of Technology, 2011.

141 L.Li, H. Liao, L. Qi, "*An improved r-factor algorithm for TVD schemes*", International Journal of Heat and Mass Transfer 51, 610–617, 2008.